

**Bone Tissue Regeneration by Using Melt Electrospinning Writing
(MEW)**

Author

Abbasi, Naghmeh

Published

2020-05-05

Thesis Type

Thesis (PhD Doctorate)

School

School of Dentistry&Oral Hlth

DOI

[10.25904/1912/2776](https://doi.org/10.25904/1912/2776)

Downloaded from

<http://hdl.handle.net/10072/393981>

Griffith Research Online

<https://research-repository.griffith.edu.au>

Bone Tissue Regeneration by Using Melt Electrospinning Writing (MEW)

Naghmeh Abbasi

BSc, MSc

School of Dentistry & Oral Health

Faculty of Health



**Submitted in fulfilment of the requirements
of the degree of**

Doctor of Philosophy

Dec 2019

Abstract

Biomaterial scaffolds engineered to facilitate osteogenesis which can subsequently remodel in a similar fashion to that of natural tissue, is an ideal clinical strategy for treating bone defects in the maxillofacial region. This study has developed, using a novel melt electrowriting (MEW) technique, various graded porous polycaprolactone (PCL) scaffolds able to imitate the bimodal structure of cortical and cancellous bone tissue in terms of their morphological pore structure. These scaffolds were subsequently shown to facilitate the proliferation of osteoblasts with significant alkaline phosphatase (ALP) activity. Scaffolds with a staggered architecture i.e. those where the corresponding fibers in different layers are offset horizontally during the printing process, increases the number of contact points, enables larger pores, facilitates cell attachment and creates a highly porous structure with interconnected networks favourable for improved cell migration and vascularization.

MEW is a relatively new technology that fills a gap between conventional fused deposition modelling (FDM) 3D printing and solution electrospinning by affording significantly better control over the fabrication of the porosity in scaffolds. This is due to the high-resolution during printing of the fibers which enables small pore sizes in the desired porosity. PCL polymer with its advantages of less immunoreactivity following implantation and mechanically suitability for the support of bone cells, has flexibility in design and is widely used in bone applications. However poor bioactivity and cellular affinity as well as long-term degradation issues with PCL have been reported.

A promising solution to overcome these drawbacks is fiber surface modification such as coating with bioactive inorganic components. hydroxyapatite (HAP) is the most stable form of calcium phosphate (CaP) used to improve the hydrophobic characteristics of PCL and enhance the binding affinity to the host tissue and promote new bone growth.

Furthermore, CaP coating also accelerates the degradation rate of PCL. While the CaP can directly regulate the bone regeneration process through the release of phosphate and calcium ions, to our knowledge, no study has compared the differing methodologies used to prepare PCL fibers for CaP coating. Similarly, there is limited research evaluating the influence of offset and gradient porosity structured scaffolds during bone healing and vascularization.

Therefore in the first experimental part of this thesis (Chapter 2), we evaluated the stability of CaP coated MEW PCL scaffolds following pretreatment with either Argon-Oxygen (Ar-O₂) plasma or sodium hydroxide (NaOH). In our study, Ar-O₂ plasma modification of the PCL prior to immersion in simulated body fluid for 1 hr, resulted in a uniform coating of CaP on the electrowritten fibers. This improved the mechanical properties of the scaffolds by increasing the tensile modulus. Regarding the structure of the coating, halite (NaCl) crystals were found in the coated scaffolds pretreated with NaOH whereas a mixture of HAP and tetracalcium phosphate (TTCP) crystals were found following plasma treatment. This confirmed the stability of the CaP minerals would be higher than NaOH pre-treated coated scaffolds due to the lower solubility of the TTCP and HAP in comparison to the halite structures. This study showed that the plasma modification is more applicable for further study of MEW PCL scaffolds in bone regeneration applications.

The second part of the study (Chapter 3) aimed to first examine the physical and mechanical properties of MEW CaP-coated PCL scaffolds with various homogeneous (250, 500 and 750 μm) and heterogeneous (offset.30.70, offset.50.50 and gradient) pore structures. We also evaluated the scaffold biocompatibility and the effect of these porous architectures on human osteoblast growth and proliferation. Physically, the offset.30.70 scaffold was shown to significantly increase the surface area while 250 μm homogeneous scaffolds were shown to improve the mechanical properties of the MEW scaffolds with

the offset.50.50 scaffold having the highest elongation at break result. The scaffold with a 250 μm pore size stimulated cell seeding efficiency however the highest levels of cell infiltration and proliferation were observed in the gradient scaffold structures following 30 days of culture. This study demonstrated that the architectures of offset and graded porosity scaffolds can be efficient in aiding the migration and proliferation of osteoblasts on MEW PCL scaffolds.

In Chapter 4, we assessed the impact of heterogeneous and homogeneous porous scaffolds on osteoblast mineralization and the expression of bone-associated markers. The gradient porous architecture significantly increased ALP activity in osteoblasts cells. In addition, significant expression of osteocalcin was observed by immunostaining. Moreover, the human osteoblast cells were shown to enhance matrix mineralization in offset.50.50 scaffolds. In particular, the expression of associated genes linked to mineralized-tissue formation stage, including osteocalcin and osteopontin were elevated in offset and gradient scaffold structures, thereby able to support the maturation of osteoblast cells essential for initial osteogenesis and mineralization.

Based on these findings, the final section of this project (Chapter 5) was designed to study the capability of these coated scaffolds to promote osteogenesis *in vivo*. Offset.50.50, 250 μm , 500 μm and two gradient (250top-500middle-750bottom and 750top-500middle-250bottom) scaffold structures were implanted into 5 mm calvarial defects created in Wistar rats to evaluate the neovascularization and bone formation after 4 and 8 weeks of healing. Micro-CT and histological analysis revealed the highest bone volume in the grad.250top scaffold. Having the larger pores facing the dura mater lead to better permeability of O_2 and nutrients in the that resulted in better cell migration, vascularization and bone growth compared to the 500 μm scaffolds and the grad.750top scaffolds. More soft tissue and incomplete newly formed bone was seen in the scaffolds with smaller pore sizes (250 μm and offset.50.50) 8 weeks post-implantation. Although

subsequent immunohistochemical investigation showed the expression of all bone markers examined (ALP, Col I, BMP-2, OCN, OPN) in all the scaffold groups, intense staining for osteocalcin was particularly observed in grad.250top and offset.50.50 scaffolds. The expression of vascular endothelial markers (VEGF, vWF, CD34) in all the scaffold groups along with low intensity CD105 expression confirmed angiogenesis and the remodeling phase of bone repair in the defect site.

In conclusion, our research has demonstrated that both homogeneous and heterogeneous porosity within MEW CaP-coated PCL scaffolds improved the mechanical properties of the scaffold structures and stimulated greater interaction and proliferation of osteoblast cells. The offset.50.50 scaffold was the most suitable candidate to increase mineralization *in-vitro*. Bone healing studies in the rat model showed bone regeneration also among the other porous scaffolds with the most bone formation and angiogenic action observed in the gradient.250top architecture scaffolds. Future studies are now required in large animal models to evaluate the osteogenic capacity of this gradient architecture in both load and non-load bearing applications.

Statement of Originality

I, Naghmeh Abbasi declare that this work has not previously been submitted for a degree or diploma in any university. To the best of my knowledge and belief, the thesis contains no material previously published or written by another person except where due reference is made in the thesis itself.

Naghmeh Abbasi

Table of Contents

Abstract.....	I
Statement of Originality	V
Table of Contents.....	VI
Table of Figures.....	XII
List of Tables	XV
List of Abbreviations Used.....	XVI
Acknowledgement	XX
Successful Grants and Other Output Arising from this Thesis	XXII
CHAPTER 1.....	1
INTRODUCTION AND LITERATURE REVIEW	1
ABSTRACT	3
INTRODUCTION	4
Review of the Literature	6
Methods for the Fabrication of Porous Scaffolds.....	6
Cell Behaviour in Porous Scaffolds	9
Role of Pore Size in Scaffold Osteogenicity	13
Homogeneous Pore Size.....	14
Heterogeneous Pore Size	16
Role of Pore Geometry in Scaffold Osteogenicity	17
Role of Porosity in Determining Scaffold Permeability.....	23
Role of Porosity in Scaffold Vascularisation	25
Role of Porosity in Determining Scaffold Mechanical Properties	33
Role of Porosity in Determining the Degradation Rate.....	40
CONCLUSIONS	41
Research Hypothesis.....	42

Aims.....	42
Significance and Innovation	43
References	45
CHAPTER 2.....	70
THE CALCIUM PHOSPHATE STABILITY ON MELT ELECTROWRITTEN (MEW) PCL SCAFFOLD.....	70
ABSTRACT	72
INTRODUCTION	73
MATERIALS AND METHODS.....	75
Melt Electrowriting (MEW)	75
Optimization of CaP Coating Process	76
Morphological Characterization.....	77
Energy Dispersive Spectrometry (EDS).....	77
Contact Angle.....	77
Mechanical Characterization	78
X-Ray Diffraction (XRD).....	78
Fourier-Transform Infrared Spectroscopy (FTIR)	78
Thermogravimetric Analysis (TGA)	78
Micro-Computed Tomography (μ -CT)	79
Statistical Analysis	79
RESULTS.....	79
Morphological Characterization of Scaffolds (SEM).....	79
Elemental Chemical Characterization (EDS).....	83
Surface Evaluation by Contact Angle	85
Mechanical Behaviour.....	86
X-Ray Diffraction (XRD) Analysis.....	88

FTIR Analysis	91
Thermal Analysis (TGA).....	93
Characterization of PCL Scaffolds Coated with CaP (Micro-Ct)	95
DISCUSSION	97
CONCLUSION	103
Acknowledgments	104
References	105
CHAPTER 3	114
EFFECT OF GRADIENT AND OFFSET ARCHITECTURES O THE MECHANICAL AND BIOLOGICAL PROPERTIES OF 3-D MELT ELECTROWRITTEN (MEW) SCAFFOLD	114
ABSTRACT	116
INTRODUCTION	117
MATERIALS AND METHODS	119
Melt Electrowriting (MEW)	119
CaP Coating.....	121
Scanning Electron Microscopy (SEM).....	121
Alizarin Red Staining	121
Water Contact Angle	122
Mechanical Properties	122
Micro-Computed Tomography (μ -CT)	123
Surface Area	123
Cell Culture	124
Confocal Microscopy	125
DNA Content Analysis.....	125
Statistical Analysis	126

RESULTS	127
Physical and Mechanical Characteristics of Fabricated Scaffolds	127
Scaffold Morphology and Architecture.....	127
CaP Coating.....	129
Hydrophobicity.....	131
Mechanical Properties	133
Micro-Computed Tomography Image Analysis.....	138
Surface Area	140
Osteoblast Activity	142
Morphological Analysis	142
Cell Proliferation	150
DISCUSSION	152
CONCLUSION	160
Acknowledgments	160
Supporting Information	161
References	176
CHAPTER 4	182
ROLE OF OFFSET AND GRADIENT ARCHITECTURES OF 3-D MELT ELECTROWRITTEN SCAFFOLD ON DIFFERENTIATION AND MINERALIZATION OF OSTEOBLASTS	182
ABSTRACT	184
INTRODUCTION	185
MATERIALS AND METHODS	187
Preparation of Microfibrous PCL Membrane.....	187
Cell Culture	187
Scanning Electron Microscopy (SEM).....	188

ALP Activity	188
Alizarin Red Staining (ARS).....	188
Micro-Computed Tomography (μ -CT) of Cell-Scaffold Construct.....	189
Real-Time PCR Analysis (q-PCR).....	189
Immunofluoresce Staining.....	190
Statistical Analysis	191
RESULTS	191
Cell-Scaffold Morphology.....	191
Impact of Porous Scaffolds on ALP Activity of Osteoblast Cells	198
Influence of Porous Scaffolds on Calcium Deposition by Osteoblast Cells	199
Impact of Porous MEW Scaffolds on Osteoblast Cells Mineralization	204
Effect of Porous Scaffolds on Osteoblast Gene Expression of Osteogenic Markers	206
Osteoblast-Related Protein Expression	215
DISCUSSION.....	223
CONCLUSION	228
Acknowledgments	228
References	229
CHAPTER 5.....	236
IN VIVO BONE REGENERATION STUDIES USING OFFSET AND	
GRADIENT MELT ELECTROWRITTEN (MEW) PCL SCAFFOLD	236
ABSTRACT	237
INTRODUCTION	238
MATERIALS AND METHODS	240
Animals.....	240
Surgical Procedures	240
Micro-CT Images Acquisition.....	242

Histomorphometric Preparation & Analysis	243
Immunohistochemistry (IHC)	243
Statistical Analysis	244
RESULTS	244
Micro-CT Evaluation of Newly Formed Bone.....	244
Histological Assessment (H&E Staining)	248
Collagen Type I (Col I) Immunostaining	252
Alkaline Phosphatase (Alp) Immunostaining.....	255
Bone Morphogenetic Protein - 2 (Bmp-2) Immunostaining	258
Osteocalcin (Ocn) Immunostaining.....	261
Osteopontin (Opn) Immunostaining.....	264
CD34 Immunostaining	267
CD105 Immunostaining	270
Vascular Endothelial Growth Factor (VEGF) Immunostaining.....	273
Von Willebrand Factor (vWf) Immunostaining	276
DISCUSSION	279
CONCLUSION	286
Acknowledgments	286
References	287
CHAPTER 6	295
DISCUSSION AND FUTURE DIRECTIONS	295
Future Directions	302
References	303

Table of Figures

Figure 1.1. Various porous scaffold fabrication techniques	7
Figure 1.2. Cell contraction	11
Figure 1.3. Computer-aided design model	20
Figure 1.4. SEM images of PCL scaffolds produced using a 3D plotting.....	22
Figure 1.5. The stiffness and topography of bone matrix.....	37
Figure 2.1. SEM micrographs of calcium phosphate.	81
Figure 2.2. The morphology of CaP coated scaffolds SEM images.....	82
Figure 2.3. The EDS analysis of CaP coated scaffolds	84
Figure 2.4. Water contact angle of PCL scaffolds.....	86
Figure 2.5. Mechanical properties of CaP coated and non-coated	88
Figure 2.6. X-ray diffraction spectra of coated and non-coated.....	90
Figure 2.7. Fourier-transform infrared spectrum of coated and non-coated.....	92
Figure 2.8. The TGA-DSC and TGA curves of CaP coated	94
Figure 2.9. Micro-CT analysis of coated and non-coated	96
Figure 3.1. Schematic illustrates the design of the different pore structured PCL.....	120
Figure 3.2. SEM images of the different pore structured	128
Figure 3.3. SEM images of PCL surfaces modified by treating with calcium.....	130
Figure 3.4. Qualitative and quantitative assessment of alizarin Red staining	131
Figure 3.5. Image of contact angle assessment and graph showing CaP coating.....	132
Figure 3.6. Typical Stress-strain curves under compression loading.	135

Figure 3.7. Mechanical properties of CaP coated melt electrowritten PCL scaffolds..	137
Figure 3.8. Images of Micro-CT analysis of the 3D porous PCL scaffolds	140
Figure 3.9. Mean specific surface area of the six different melt electrowritten	142
Figure 3.10. Confocal laser scanning microscopy images of osteoblast cells.....	149
Figure 3.11. The proliferation of osteoblasts in osteogenic and basal medium	151
Figure S1. SEM images of PCL surfaces modified by treating with NaOH	162
Figure S2. SEM images of mean fibre diameter of melt electrowritten PCL scaffold.	163
Figure S3. Qualitative and quantitative assessment of alizarin Red staining	164
Figure S4. Contact angle measurements on pore surfaces of NaOH treated PCL	165
Figure S5. Various contact angle measurements on different pore surfaces of PCL ...	166
Figure S6. The BET surface area calculated from argon adsorption–desorption.....	172
Figure S7. SEM cross section images of mean fibre diameter	173
Figure S8. Mean specific surface area of the melt electrowritten and FDM.....	173
Figure S9. The BET surface area calculated from argon adsorption–desorption.....	174
Figure S10. SEM micrographs of pore size distribution of FDM 3D printed	175
Figure 4.1. SEM image of the porous scaffold structures	193
Figure 4.2. SEM micrographs showing different magnification	197
Figure 4.3. ALP activity of osteoblasts in osteogenic	199
Figure 4.4. Alizarin Red staining of osteoblast cells seeded on porous PCL.....	203
Figure 4.5. ECM mineralization indicated in grey and the micro-CT images.	206
Figure 4.6. Gene expression pattern during mineralization of human osteoblast.	214

Figure 4.7. Immunocytochemistry analysis of osteogenitor markers.....	222
Figure 5.1. Photographs of the surgical procedures.	241
Figure 5.2. Schematic of the calvarial defects and the combination of melt.....	242
Figure 5.3. 3-D reconstructed Micro-CT image analysis showing the degree of bone	247
Figure 5.4. Quantitative micro-CT data analysis of bone volume to total volume....	248
Figure 5.5. Microscope images of H&E stained tissue sections.....	251
Figure 5.6. IHC analysis of collagen type I (Col I).	255
Figure 5.7. IHC analysis of alkaline phosphatase (Alp).....	258
Figure 5.8. IHC analysis of bone morphogenic protein-2 (Bmp-2).	261
Figure 5.9. IHC analysis of osteocalcin (Ocn).	264
Figure 5.10. IHC analysis of osteopontin (Opn).....	267
Figure 5.11. IHC analysis of CD34.	270
Figure 5.12. IHC analysis of endoglin (CD105).....	273
Figure 5.13. IHC analysis of Vascular endothelial growth factor (VEGF).....	276
Figure 5.14. IHC analysis of von Willebrand factor (vWF).....	279

List of Tables

Table 1.1. Best values for Young's modulus.....	39
Table 2.1. Nominal Ion Concentrations of SBF	77
Table 2.2. Element analysis by EDS of coated and non-coated	83
Table 2.3. Tensile strength of coated and non-coated	87
Table 2.4. The data of TGA-DSC analysis of CaP coated.....	93
Table 3.1. Compressive Young's Modulus mean values for the CaP treated PCL	135
Table 3.2. Tensile strength for the CaP treated PCL fibrous scaffolds.....	136
Table 3.3. Total surface area of coated PCL scaffolds obtained by BET.....	141
Table S1. Mean specific surface area of melt electrowritten NaOH treated PCL	161
Table S2. Total surface area of FDM 3D-printed and melt electrowritten PCL.....	161

List of Abbreviations used

Al	Aluminium
ALP	Alkaline Phosphatase
ANOVA	Analysis Of Variance
Ar	Argon
ARS	Alizarin Red Staining
BV/TV	Bone Volume to Total Volume
BET	Brunauer–Emmett–Teller
BFGF	Basic Fibroblast Growth Factor
BJH	Barrett-Joyner-Halenda analysis
BMPs	Bone Morphogenetic Proteins
BSP	Bone Sialoprotein
β -TCP	β -Tricalcium Phosphate
Ca	Calcium
CaP	Calcium Phosphates
CCD	Charge-Coupled Device
cDNA	Complementary DNA
CF4	Tetrafluoromethane
Ch-Al	Chitosan–Alginate
Cl	Chlorine
CNC	Computerized Numerical Control
CO	Carbonyl
COO	Carboxyl
CO ₂	Carbon Dioxide
Col-I	Collagen Type I
CPP	Calcium Polyphosphate
Cu	Copper
DAB	3,3'-Diaminobenzidine
DAC	Diamond Anvil Cell
DAPI	4',6-Diamidino-2-Phenylindole
DNA	Deoxyribonucleic Acid
ECFCs	Endothelial Colony Forming Cells
ECM	Extra Cellular Matrix

EDS	Energy Dispersive Spectrometry
EDTA	Ethylenediaminetetracetic Acid
EPCs	Endothelial Progenitor Cells
Erk1/2	Extracellular Signal-Regulated Kinases
FDM	Fused Deposition Modelling
FTIR	Fourier-Transform Infrared Spectroscopy
GAG	Glycosaminoglycan
G-Code	Programming Language
H&E	Haematoxylin and Eosin
HAP	Hydroxyapatite
H-CPP	Homogeneous Calcium Polyphosphate
HGFs	Human Gingival Fibroblasts
HIF-1 α	Hypoxia Inducible Factor-1 Alpha
HMDS	Hexamethyldisilazane
hOB	Human Osteoblasts
HRP	Horseradish Peroxidase
HUVECs	Human Umbilical Vein Endothelial Cells
IHC	Immunohistochemistry
IL	Interleukin
IUPAC	International Union of Pure and Applied Chemistry
K	Potassium
KDa	<i>Kilodaltons</i>
KV	Kilovolt
KVp	Peak Kilovoltage
M	Molar
MBG	Mesoporous Bioactive Glass
μ -CT	Micro-computed Tomography
MEW	Melt Electrowriting
Mg	Magnesium
MGP	Matrix Gla Protein
μ M	Micrometer
mm	Millimetre
MPa	Megapascal

MP	Microporous
MSCs	Mesenchymal Stem Cells
N	Newton
N ₂	Nitrogen
Na	Sodium
NaCl	Sodium Chloride
NAGEL	Nagelschmidite
NaOH	Sodium Hydroxide
OCN	Osteocalcin
OH	Hydroxide
OPN	Osteopontin
P	Phosphorus
PB-EPCs	Peripheral Blood-Derived Endothelial Progenitor Cells
PBS	Phosphate-Buffered Saline
PCL	Polycaprolactone
PDLLA	Poly (D, L-Lactide)
PDGF	Platelet-Derived Growth Factor
PEO	Polyethylene Oxide
PEOT/PBT	Poly (Ethylene Oxide Terephthalate)/Poly (Butylene Terephthalate)
PFA	Paraformaldehyde
PGA	Polyglycolic Acid
PGCPP	Porosity-Graded Calcium Polyphosphate
PLA	Poly(lactic Acid)
PLA/PEG	Poly (L-Lactide)-B-Poly (Ethylene Glycol)
PLGA	Poly (Lactic-Co-Glycolic Acid)
PLLA	Poly(lactic Acid) or Poly(lactide)
PO ₄	Phosphate
PTFE	Polytetrafluoroethylene
PVA	Polyvinyl Alcohol
q-PCR	Quantitative PCR or Real-Time PCR analysis
RBCs	Red Blood Cells
RNA	Ribonucleic Acid
RP	Rapid Prototyping
RT	Room Temperature

RUNX2	Runt-Related Transcription Factor 2
SBF	Simulated Body Fluid
SEM	Scanning Electron Microscope
SMCs	Smooth Muscle Cells
SPSS	Statistical Package for the Social Sciences
TCP	Tissue Culture Plate
TGA	Thermogravimetric Analysis
TGF- β	Transforming Growth Factor-Beta
3-D	Three-Dimensional
TiO ₂ /TCP	Titania/ Tricalcium Phosphate
TNF- α	Tumour Necrosis Factor α
TTCP	Tetracalcium Phosphate
VEGF	Vascular Endothelial Growth Factor
vWF	Von Willebrand Factor
Wnt	Wingless-Related Integration Site
XRD	X-Ray Diffraction

Acknowledgement

Dr. Stephen Hamlet, I would like to thank for being my principal supervisor with your experience in the publications and lending me invaluable assistance and guidance throughout my PhD journey.

In addition, a thank you to my Associate supervisors, Professor Robert M. Love, Professor Saso Ivanovski and Dr. Nathan Castro for guiding me in my PhD.

Also, I would like to express my appreciation towards Professor Nam-Trung Nguyen for sharing your wealth of knowledge and your experiences in the publications.

I also appreciate the Australian Dental Research Foundation (ADRF) and The school of Dentistry and Oral Health for funding my studies through the research grants and Griffith University for providing me with the scholarships and opportunity to undertake my research and facilitating my ambition of attaining my PhD degree.

Also, I appreciate Professor Bonnie Barber, Dean (Research), for his continuing support that give me much needed emotional and financial support during my research.

I thank Mr Christopher Philippa, Senior Scientist at Department of Pathology, Gold Coast University Hospital, Karan Gulati, Research Fellow at School of Dentistry, University of Queensland, Dr. Abdallah Abdal-Hay, Research Fellow at School of Dentistry, University of Queensland and Ms Elizabeth Graham, Senior Technologist at Central Analytical Research Facility, Queensland University of Technology, Gardens Point Campus for their help in this PhD project.

A very special heartfelt and the most deserved acknowledgement goes to my parents, Ali and Farzaneh who gave me my life, and whose sacrificial care for me made it possible to finish my degree. It is because of your wholehearted support and efforts that you have put into giving me the life I have now. You both truly silence me when it comes

down to describing how much I love and thank you. As for my lovely sister, Nasim, for her motivation to keep me trying and working better to complete this work.

Successful Grants and Other Output Arising from this Thesis

Acknowledgement of Published and Unpublished Papers included in this Thesis

Section 9.1 of the Griffith University Code for the Responsible Conduct of Research (“Criteria for Authorship”), in accordance with Section 5 of the Australian Code for the Responsible Conduct of Research, states:

To be named as an author, a researcher must have made a substantial scholarly contribution to the creative or scholarly work that constitutes the research output, and be able to take public responsibility for at least that part of the work they contributed. Attribution of authorship depends to some extent on the discipline and publisher policies, but in all cases, authorship must be based on substantial contributions in a combination of one or more of:

- conception and design of the research project
- analysis and interpretation of research data
- drafting or making significant parts of the creative or scholarly work or critically revising it so as to contribute significantly to the final output.

Section 9.3 of the Griffith University Code (“Responsibilities of Researchers”), in accordance with Section 5 of the Australian Code, states:

Researchers are expected to:

- Offer authorship to all people, including research trainees, who meet the criteria for authorship listed above, but only those people.
- accept or decline offers of authorship promptly in writing.
- Include in the list of authors only those who have accepted authorship

- Appoint one author to be the executive author to record authorship and manage correspondence about the work with the publisher and other interested parties.
- Acknowledge all those who have contributed to the research, facilities or materials but who do not qualify as authors, such as research assistants, technical staff, and advisors on cultural or community knowledge. Obtain written consent to name individuals.

Appropriate acknowledgements of those who contributed to the research but did not qualify as authors are included in each paper.

Signed _____ Date: 10-Dec-2019

Name of Student: Nag

Countersigned _____ Date: 10-Dec-2019

Supervisor: Dr. Stephen Hamlet

Publications arising from this thesis

1. **Naghmeb Abbasi**, Abdalla Abdal-hay, Stephen Hamlet, Elizabeth Graham, Saso Ivanovski. Effects of Gradient and Offset Architectures on the Mechanical and Biological Properties of 3-D Melt electrowritten (MEW) scaffolds. ACS Biomaterials Science and Engineering Journal; 2019 May, <https://doi.org/10.1021/acsbiomaterials.8b01456> (IF: 4.511)

Manuscripts submitted for publication

2. **Naghmeb Abbasi**, Stephen Hamlet, Robert M. Love, Nam-Trung Nguyen. A review: Porous Scaffolds for Bone and Tissue Regeneration.(Submitted Nov 2019 in Journal of Science: Advanced Materials and Devices) (IF: 3.357)
3. **Naghmeb Abbasi**, Stephen Hamlet, Van Thanh Dau, Nam-Trung Nguyen. The calcium phosphate stability on melt electrowritten (MEW) PCL scaffold (Submitted Oct 2019 in Journal of Science: Advanced Materials and Devices) (IF: 3.357)
4. **Naghmeb Abbasi**, Saso Ivanovski, Karan Gulati, Robert M. Love, Stephen Hamlet. Role of Offset and Gradient Architectures of 3-D Melt electrowritten Scaffold on Differentiation and Mineralization of Osteoblasts (Submitted Oct 2019 in Biomaterials Research Journal) (IF: 4.831)

Publications arising during candidature

5. Abdalla Abdal-hay, **Naghmeb Abbasi**, Marcin Gwiazda, Stephen Hamlet, Saso Ivanovski. Novel polycaprolactone/hydroxyapatite nanocomposite fibrous scaffolds by direct melt-electrospinning writing. European Polymer Journal); 2018 Aug, 105(2018):257-264.
<https://doi.org/10.1016/j.eurpolymj.2018.05.034> (IF: 3.621)

Manuscripts in preparation

6. **Naghmeh Abbasi**, Stephen Hamlet. In vivo Bone regeneration studies using offset and gradient melt electrowritten (MEW) PCL scaffolds of osteoblasts.
(Under revision of authors)

Published Conference Abstracts

1. **Naghmeh Abbasi**, Stephen Hamlet, Ryan Lee, Robert M. Love, Saso Ivanovski, “Osteoconductive melt electrospun PCL scaffolds with gradient and offset structures”, 97th General Session & Exhibition of the IADR, June 2019, Vancouver, Canada. Journal of Dental Research (**IF: 5.125**)
2. **Naghmeh Abbasi**, Stephen Hamlet, Nathan Castro, Abdalla Ali, Saso Ivanovski, “The effect of structural offset and gradient pore size on Osteoblast differentiation in PCL scaffolds”, International Society for Stem Cells Research (ISSCR), Jun 2018, Melbourne, Australia. Stem Cells Reports Journal (**IF: 5.597**)

Oral Presentations

1. **Naghmeh Abbasi**, Stephen Hamlet, Ryan Lee, Saso Ivanovski, “Bone Regeneration using Offset and Gradient Melt Electrowritten PCL Scaffolds”, 4th Meeting of the International Association for Dental Research Asia-Pacific Region 2019. Nov 2019, Brisbane, Australia.
2. **Naghmeh Abbasi**, Stephen Hamlet, Ryan Lee, Saso Ivanovski, “Bone Regeneration in Calvaria Defects in a Rat Model by Implantation of Offset and Gradient Melt Electrowritten PCL Scaffolds”, 5th annual Griffith School of Dentistry Research Day, Griffith University, Aug 2019, Gold Coast, Australia.
3. **Naghmeh Abbasi**, Stephen Hamlet, R. M. Love, Saso Ivanovski, “The role of biomimetic scaffold structures on bone tissue regeneration”, 58th Annual Scientific Meeting of International Association of Dental Research (IADR), ANZ, Sep 2018, Perth, Australia. (Accepted for both Oral & Poster presentation).
4. **Naghmeh Abbasi**, Saso Ivanovski, “The role of biomimetic scaffold structures on bone tissue regeneration”, 4th annual Griffith School of Dentistry Research Day, Griffith University, Sep 2018, Gold Coast, Australia.
5. **Naghmeh Abbasi**, Saso Ivanovski, “Bone tissue regeneration by using Melt Electrospinning Writing (MEW)”, 3th annual Griffith School of Dentistry Research Day, Griffith University, June 2017, Gold Coast, Australia.

Scientific Posters

1. **Naghmeh Abbasi**, “Bone Regeneration by Melt Electrowritten PCL Scaffolds”, Griffith Health Higher Degree Research End of Year Event, Griffith University, Nov 2019, Gold Coast, Australia.

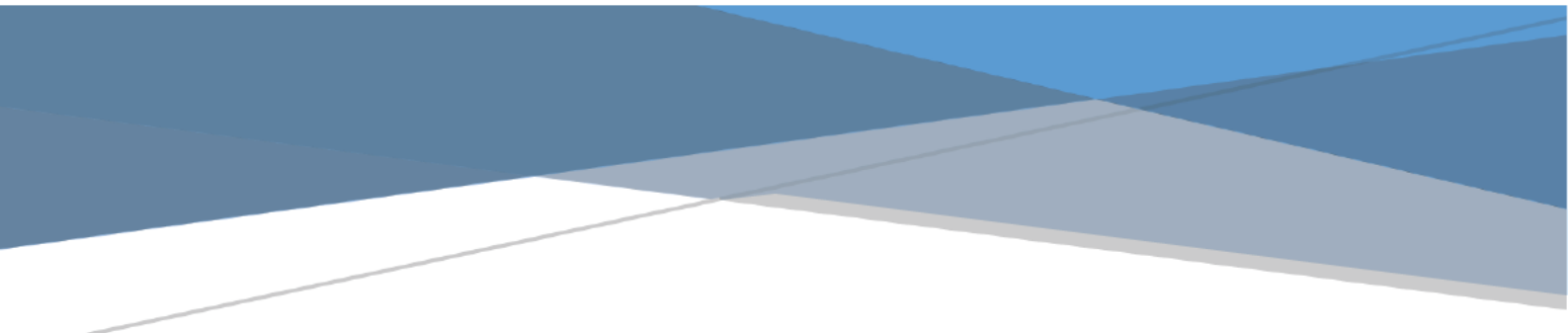
2. **Naghmeh Abbasi**, “Bone Regeneration by Melt Electrowritten PCL Scaffolds”, Griffith Health Higher Degree Research End of Year Event, Griffith University, Nov 2019, Gold Coast, Australia. (Accepted for both Oral & Poster presentation).
3. **Naghmeh Abbasi**, Stephen Hamlet, R. M. Love, Saso Ivanovski, “The role of biomimetic scaffold structures on bone tissue regeneration”, 58th Annual Scientific Meeting of International Association of Dental Research (IADR), ANZ, Sep 2018, Perth, Australia.
4. **Naghmeh Abbasi**, Stephen Hamlet, Cedryck Vaquette, Abdalla Abdal-hay, Ho-Jin Moon, Saso Ivanovski, “The mechanical properties and cell cultural response of melt electrospun scaffolds with controlled offset and gradient pore size”, International Conference on Bio Nano Innovation (ICBNI), University of Queensland, Sep 2017, Brisbane, Australia.

Competitive Research Grants

1. Bone regeneration in calvarial defects in a rat model by implantation of offset and gradient melt electrospun PCL scaffolds. Australian Dental Research Foundation grant (INC) - 2019-2020 (**\$6712**).
2. Bone regeneration in calvarial defects in a rat model by implantation of offset and gradient melt electrospun PCL scaffolds. DOH Research Grant 2018-2019 (**\$5000**).
3. Bone tissue regeneration by using Melt Electrospinning Writing (MEW). DOH Research Grant 2017-2018 (**\$4000**).

Academic Honours and Awards

1. 2th Place of 2019 Publication of the Year Award Griffith University HDR Health Group (Nov 2019).
2. Griffith University HDR Travel Grant to attend IADR Conference in Vancouver, Canada (June 2019).
3. Runner up in the IADR ANZ division Colgate Poster competition (Senior division) at Perth, Australia (Sep 2018)
4. Colgate travel award to attend IADR meeting in Perth, Australia (Sep 2018).



CHAPTER 1

INTRODUCTION AND LITERATURE REVIEW

STATEMENT OF CONTRIBUTION TO CO-AUTHORED PUBLISHED PAPER

This chapter includes a **published** co-authored paper. The bibliographic details of the co-authored paper, including all authors, are:

Naghmeh Abbasi, Stephen Hamlet, Robert M Love, Nam-Trung Nguyen. Porous Scaffolds for Bone Regeneration. Journal of Science: Advanced Materials and Devices; 2020 January, <https://doi.org/10.1016/j.jsamd.2020.01.007> (IF: 3.357)

My contribution to the paper involved:

Designing of the project, provision of the data, the preliminary analysis and categorisation of the data into a usable format and providing direction on the scope and structure of the analysis, interpretation of results and drafting of paper.



Naghmeh Abbasi

Date 10-Dec-2019



Corresponding author of paper: Prof. Nam-Trung Nguyen

Date 10-Dec-2019



Supervisor: Dr. Stephen Hamlet

Date 10-Dec-2019

ABSTRACT

Bone fracture caused by osteoporosis is a global disease that occurs every 20 seconds throughout the world in people aged 50 years. The concept of regenerative medicine comprises gene and cell-based therapies to producing the artificial organs through tissue engineering. The objective of tissue engineering is to use biomaterial scaffolds to stimulate and guide the regeneration of damaged tissue that cannot heal spontaneously. Scaffolds provide a three-dimensional network that mimics the extra cellular matrix (ECM) environment by supporting the viability, attachment, growth and migration of cells in vitro and regulating cell behaviour and maintaining the structure of regenerated tissue in vivo. The osteogenic capability of the scaffold is influenced by the interconnections between the scaffold pores, which facilitate cell distribution, integration with the host tissue and capillary ingrowth. To be effective, the scaffold must allow physiological mechanical loading, and hard tissue regeneration of tissue such as bone requires an appropriate porous scaffold. Hence, the preparation of bone scaffolds with applicable pore size and interconnectivity is a significant issue in bone tissue engineering. This review focuses on the relationships between porosity and the pore size of scaffolds, their mechanical and biological properties, induction of osteogenesis, vascularisation and degradation of scaffolds in bone regeneration.

INTRODUCTION

The gold standard for conventional clinical reconstruction of a bone defect caused by trauma or cancer metastasis is a graft of autogenous bone from a donor site (1). This method is limited by the ability to extract autogenous tissue in adequate quantity and morbidity at the donor region (2). Tissue engineering to produce biocompatible scaffolds populated with autogenous cells has recently been shown to be an ideal alternative method to provide bone substitutes (3). Tissue engineering to create an artificial construct *in vitro* requires the combination of live cells, a scaffold to act as the ECM and growth factors. All three of these must be provided as the basis of artificial construct in a coordinated fashion to recover the geometry at the injury site in an individual patient (4, 5).

Unlike many other tissues, minor bone tissue damage can regenerate by itself (6). However, the bone's ability for self-repair of massive defects is limited because of deficient of blood supply or in the presence of systemic disease as in pathological and infectious cases (7).

Bone tissue typically has four cell types, each of which has a different role: osteocytes, osteoblasts, osteoclasts and bone-lining cells. Bone-lining cells are responsible for matrix preservation, mineralisation and resorption, and serve as precursors of osteoblasts (8).

The penetration, proliferation, differentiation and migration abilities of these cells are affected by the size and geometry of scaffold pores and the vascularisation (9). The composition of bone matrix includes osteopontin (OPN), transforming growth factor-beta (TGF- β), collagen type I (COL-I), osteocalcin (OCN), bone sialoprotein (BSP), HAP, bone morphogenetic proteins (BMPs) and matrix Gla protein (MGP) (10).

Three steps are involved in osteoblast differentiation: (i) proliferation, when TGF- β , procollagen I and fibronectin are able to be characterised; (ii) maturation of the matrix, which is accompanied by the highest level of ALP; and (iii) mineralisation of the matrix,

which involves the expression of bone sialoprotein, osteopontin and osteocalcin genes and proteins and the sedimentation of calcium (11).

Bone tissue engineering requires a suitable architecture for the porous scaffold, which provides an environment to promote cell infiltration and nutrient flow to the tissue while being able to withstand external loading stresses (12). The pore distribution strongly influences the rate of scaffold degradation, which must be balanced with that of bone growth after implantation (13). Therefore, materials of ultra-high molecular weight that do not degrade in the body have limited use as bone graft materials (14).

Adequate porosity and appropriate interconnectivity are essential aspects of the scaffold that influence subsequent vascularisation and angiogenesis. (15). These materials must also have an appropriate interval until they are degraded that is compatible with the maturation and regeneration of artificial tissue when the new natural tissue is formed after transplantation *in vivo*. The products of the degradation process must be non-toxic and not stimulate the inflammatory response (16). In addition, the scaffolds must be designed with sufficient porosity of suitable size and interconnections between the pores to allow for cell penetration and migration (17). The ability of cells to penetrate, proliferate and differentiate is affected by the size and geometry of scaffold pores and subsequent vascularisation (18).

The ideal candidate scaffolds are thought to require proper pore system architecture to ensure the appropriate distribution and transportation of nutrients and oxygen, removal of waste materials, vascularisation and ultimately host integration (19). Appropriate physical and chemical surface properties are an inherent requirement for promoting the attachment, infiltration, growth, proliferation and migration of cells (20, 21).

Review of the Literature

Methods for the Fabrication of Porous Scaffolds

A few methods are used to controlling the porosity of a scaffold (Figure 1.1). The combination of the freeze-drying and leaching template techniques generates porous structures. In this method, the pore size can be adjusted by controlling the gap space of the leaching template, temperature changes and varying the density or the viscosity of the polymer solution concentration during freeze drying technique (22-24) . A high concentration of polymer solution inhibits filling the voids in the templates and increases the compression modulus at higher temperatures (25). It is not clear whether scaffolds with uniform pore distribution and homogeneous size are more efficient in tissue regeneration than those with varying pore size distribution. Supercritical CO₂ foaming and melt processing is another method to produce porous scaffolds with different pore sizes. In this method, the molecular weight of the polymer component is changed, which affects the pore architecture (26).

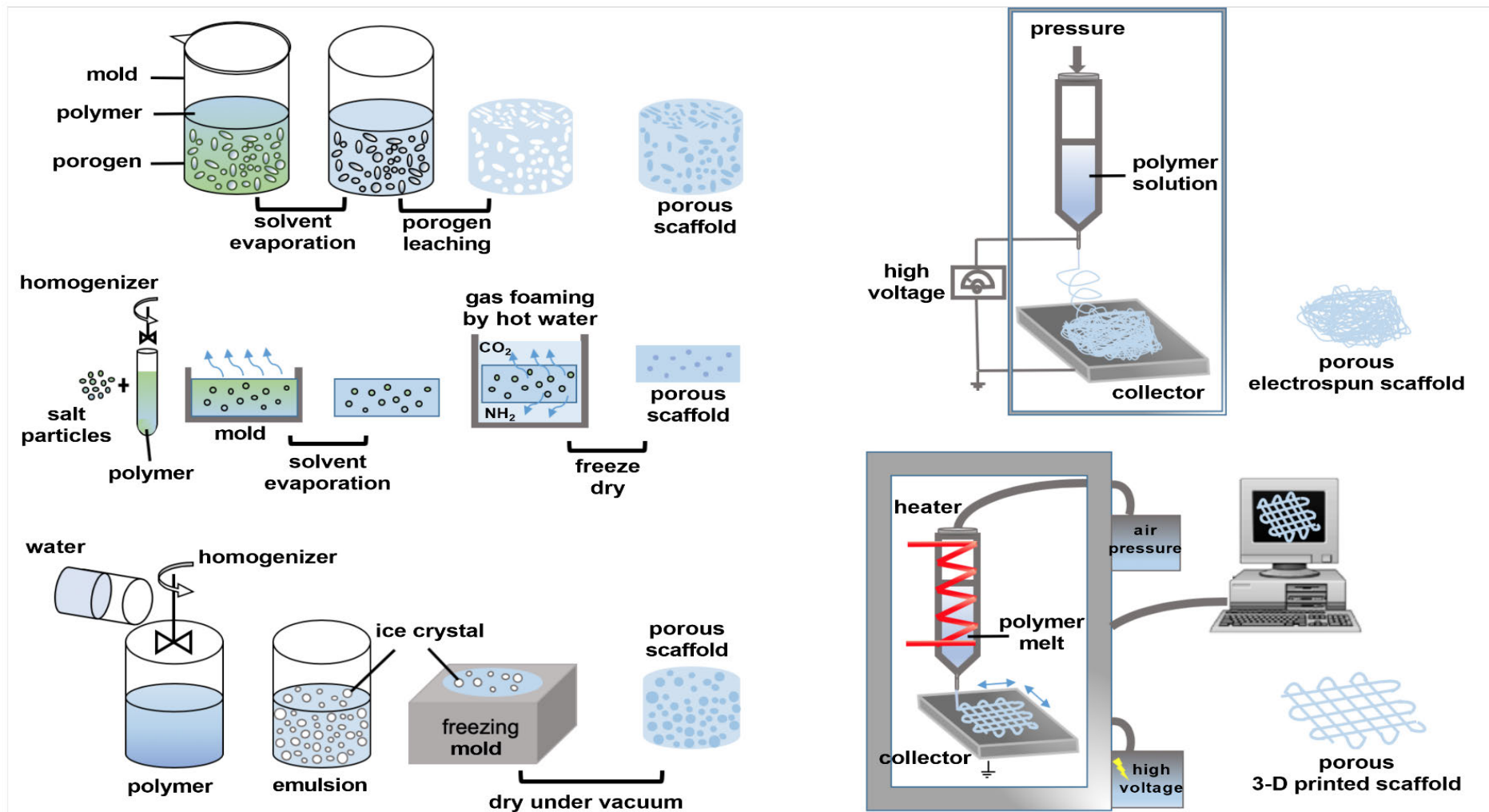


Figure 1.1. Various porous scaffold fabrication techniques

The other fabrication methods for creating porous scaffolds in macroscale dimensions are rapid prototyping, immersion precipitation, freeze drying, salt leaching and laser sintering (17). Scaffolds with high interconnectivity and heterogeneous (large and small) pores can be obtained by using melt mixing of the two polymers, which are immiscible because of their different sizes or amounts of water-leachable porogen particles (27). Of these methods, the direct melt electrospinning technique is the appropriate candidate for generating homogeneous porous biomaterials with large ordered pore size ($>100\ \mu\text{m}$). Electrospinning can provide a suitable substrate to enable cells to penetrate sufficiently by controlling the filament deposition on the patterned stainless steel collector containing the diamond and the use of cubic or circular holes as the template for spongy constructs (28-30).

The instability of the electrostatically drawn jet causes the jet to whip and to deposit the fibre randomly (31). The drawn filament diameter depends on the nozzle size and the high voltage to the nozzle. The higher the voltage, the smaller the filament diameter. The dimension of fibres generating by melt electrospinning ranges from 270 nm to 350 μm (28, 30). Electrospinning delivers fibres with nanometre dimensions because of the high surface-area-to-volume ratio, a property that is exploited to ensure a suitable surface for cell adhesion.

The formation of ordered structures by controlling the fibre placement is one challenge of electrospinning. The repulsed charges of the electrospun fibres can produce firmly compressed nonwoven mesh with very small pore sizes, which prevents cell infiltration (32). Modified patterned collectors allow for the production of macroporous architecture scaffolds with an adequately large pore size to allow cell infiltration. The fibre diameter of melt electrospun scaffolds is typically in the range of 5 to 25 μm (33, 34). Three main material-based and instrument-based parameters for the reduction of

fibre diameter are high voltage, low distance from the needle tip to the collector and low flow rate (35).

The placement of a fibre in a particular location is influenced by the direction and speed of the collector (36). The morphology of the scaffold is a key aspect that affects the migration of cells (37). The key parameters to consider when optimising this scaffold morphology to create a scaffold with balanced biological and physical properties include the total porosity, pore morphology, pore size and pore distribution in the scaffold (38).

Cell Behaviour in Porous Scaffolds

The size of osteoblasts is 10–50 μm (39). However, to be effective after implantation, the pore sizes in the scaffold must be $>100 \mu\text{m}$ to permit macrophages to infiltrate to eliminate bacteria and to induce the infiltration of other cells involved in colonisation, migration and vascularisation *in vivo* (40). In contrast to macropores, micropores provide a greater surface area, favourable protein adhesion, greater reactivity, supply of nutrients and removal of waste products, and cell attachment on the scaffold (41).

Effective osteointegration is accompanied by the creation of a strong chemical bond with the bone tissue environment. A macroporous interconnected network (100–600 μm) is a better candidate than micropores ($<100 \mu\text{m}$) (42). Lim et al. reported in 2010 that pore size in the range of 200–350 μm is optimal for osteoblast proliferation. A larger pore size (500 μm) does not affect cell attachment or promote cell infiltration (43). O'Brien et al. suggested that the best pore size for initial cell adhesion is 95 μm (44). The ideal pore size varies between materials (45). Osteoblasts prefer a coarse surface for adherence because the roughness provides points for anchorage of the cells inside and on the surface of the scaffold (46).

The interconnectivity needs to be large enough for cell infiltration. For instance, ceramic-based coralline scaffold has a pore size of 500 μm , which is optimal for cell penetration. Restricted pore size and lack of space for infiltration forces cells to differentiate instead of proliferate (47, 48). The behaviour of cells differs between larger and small pore sizes. For example, chondrocytes produce the most amount of GAG and collagen II in 400 μm pores, whereas they proliferate in 200 μm pores appropriately. In another words, larger pores allow cells to agglomerate and produce proteoglycan, but they cause less proliferation. A larger pore size permits the cells to be accommodated in a larger space and does not limit cell–cell interaction and cell aggregation (49).

Cells proliferate and fill the pores from the corners, and this growth develops as a circular pattern, leading to round corners until the remaining pore space is filled by the tissue completely (Figure 1.2) (50-52). Rumpler et al. reported that the cells amplification of regenerated tissue in the corners is lower in triangular pores followed by the square, and finally in hexagonal ones in three-dimensional (3-D) printed HAP scaffolds (53). This behaviour is associated with the slower nutrient transportation and curvature-driven growth (54). High growth rate is attributed to the high curvature that decreases from hexagonal, square to triangular pores (50, 53). The reason for these differences is the short distance between the two struts and arches in the corners, particularly in hexagonal pores. This means that cell bridging happen faster in hexagonal than in rectangular and triangular pores, whose struts are further apart. In other words, more tissue is formed because of the smaller vertical spaces between the stuts (53-55).

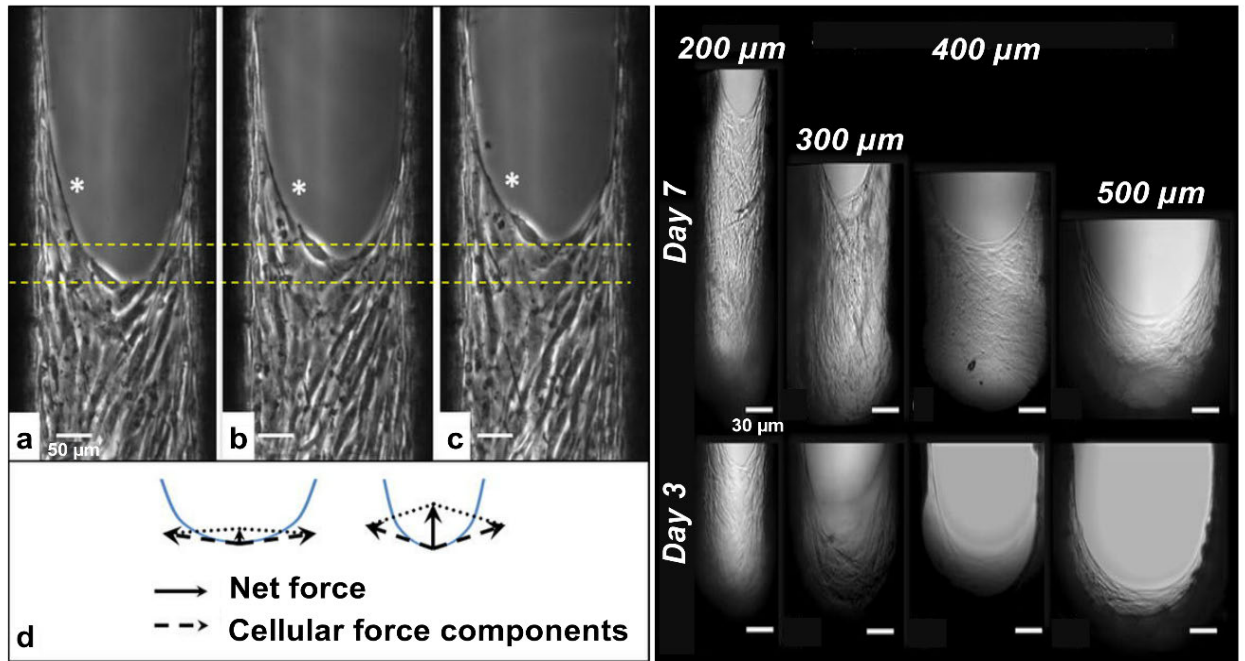


Figure 1.2. (a–c) Cell contraction. Examples of a leading cell shortening, indicated by the asterisk. Yellow lines indicate the extent the tissue was stretched because of cell-generated stresses. The interval between the images was 1 h 40. (d) Schematic representation of forces exerted by aligned cells at the tissue front on the underlying tissue, which can drive proliferation, increasing with curvature (image from Knychala et.al. doi: [10.1007/s10439-013-0748-z](https://doi.org/10.1007/s10439-013-0748-z) (50)).

The main driving force behind the cells' response to curvature is explained by the theory of contractile tensile stress and focal adhesion produced by the cells when they sense their physical surroundings and interact with the geometric features of the material surface (56). Cell contraction causes tissue stretching (50, 57). As cells grow on the surface, the regenerated tissue layers spread over flat and convex surfaces. Concave surfaces provide the room for cell alignment, whereas convex surfaces delay tissue growth (58, 59). Cell alignment is mediated through a cascade of events and is stronger in an environment with a smaller curvature (60). The average curvature and pore size are

related to the perimeter of the curve. Larger pores have a larger perimeter and less curvature (Figure 1.2) (61).

The relationship between tissue growth and surface curvature is influenced by mechanical forces. For instance, the magnitude of surface tension generated within multicellular aggregates (cell sheet) affects the spatial pattern available for the proliferation of cells (59, 62, 63). The template of mechanical stress produced by the contractions of the cell sheet against the substratum surface increases the traction stress, which is greater at the outer edge of circular pores and at the corner of square pores, triangular and rectangular pores. Therefore, the cell proliferation is higher around the periphery of a circular pore and in the corners and edges of the substrates compared with the central parts (63).

Rustom et al. (64) reported that bone formation in macro- and microporous (MP) scaffolds can increase bone volume and bone distribution by starting from the periphery of the scaffold. They measured micropore-induced capillarity after filling pores by dipping the scaffolds in phosphate-buffered saline (PBS) (MP-Wet) or using dry scaffolds without fluid immersion (MP-Dry). They found that induction of capillarity was suppressed in the MP-Wet condition. Bone density was greater near the central region of the scaffolds. Bone growth was accelerated in MP-Dry compared to MP-Wet, and a non-microporous scaffold (NMP) had low bone volume and a slower rate of cell distribution (64).

Similar results were reported by Nelson et al (63). They found that increasing cell growth corresponded with higher traction stress that concentrated at the borders and was maximum at the outer edges farthest from the core and inner area. The cellular mechanism involved includes Rho kinase signalling, which regulates the actomyosin cytoskeleton

and activates mechanical stress (65). In another study, greater proliferation was found at the short edges of rectangular pores than at the long edges (17).

Another factor that may explain the dependence of cell growth on the curvature layers is surface tension, which tends to minimise the surface area (66). However, there are no experimental data to support the hypothesis that minimum surface tension increases bone regeneration. This hypothesis is based on the stability and equilibrium of the cells to minimise their energy on a minimum surface area (67). Surface tension or surface energy comes from the attraction between molecules or cells to achieve a minimum energy (68). Closely packed molecules or cells have the least energy and are in the most stable state. This reflects the natural tendency of molecules to minimise their energy (69). Therefore, cells try to reduce their surface energy to the lowest possible level by reaching the most stable state. Thus, the cells select the corners of the pore to have more contact with other cells (70).

At the corners of a pore, the small angle of struts provides a suitable environment for cells to interact and to minimise their residual energy (71), whereas cells at the pore centre have the highest level of energy and are in an unsteady state. This may explain why greater cell proliferation and growth rate occur in triangular pores with smaller angles and higher curvatures compared with rectangular, square and hexagonal pores. As observed previously, “The tissue growth process prefers concave surfaces to convex ones” (72).

Role of Pore Size in Scaffold Osteogenicity

Pore sizes across a broad range play a crucial role in the proliferation and migration of cells (73). Cell activity is influenced by the porosity, pore size and pore interconnectivity of tissue-engineered scaffolds (74). Pore sizes smaller than hundreds of microns are relevant to cell attachment (75). Because the interactions between cells and the

biomaterial is mediated via transmembrane proteins, pores with few micron size are basically concerned with the protein adsorption on the scaffold surfaces (76).

Pore size also determines the destiny of stem cells and controls the cell actions (77) because limited interfacial area of biomaterials with larger pores inhibits cell bonding. Biomaterial scientists have categorised pore sizes of scaffolds as micropores ($<10\ \mu\text{m}$) and macropores ($>50\ \mu\text{m}$) (78). The maximum distance between cells and a blood vessel for ensuring sufficient delivery of nutrients and oxygen is $150\text{--}200\ \mu\text{m}$ (79). Hence, macroporosity allows cells to migrate, participate in vascularisation and ultimately integrate with the host tissue. Macroporous scaffolds allow for blood vessel ingrowth (19, 64). Murphy et al. reported that a pore size of $100\text{--}325\ \mu\text{m}$ is optimal for bone engineering scaffolds (80).

Homogeneous Pore Size

Previous studies have shown that cell infiltration is restricted by small pore size because of the greater surface area-to-volume ratio. Different pore sizes are required for optimal growth of various cell types (81). Osteoblasts prefer larger pores ($100\text{--}200\ \mu\text{m}$) for regenerating mineralised bone, whereas fibroblasts show better growth in smaller pores ($10\text{--}75\ \mu\text{m}$). The smaller pore size proceeds the growth of unmineralised osteoid tissue or presenting only fibrous tissue (40, 82-84). Although pore size $>50\ \mu\text{m}$ (macropores) has beneficial effects on osteogenic quality, pore size $<10\ \mu\text{m}$ (micropore) creates a larger surface area that stimulates greater ion exchange and bone protein adsorption (85, 86). The submicron and nanoscale surface roughness of the pore wall also promotes the differentiation and ingrowth of anchorage-dependent bone-forming cells (87). Rapid bone formation and substantial bone ingrowth have been reported for pore size from 290 to $310\ \mu\text{m}$ (88). Smaller pore size ($<100\ \mu\text{m}$) is associated with the growth of unmineralised osteoid tissue (89). The optimal size for vascularisation was noted to be $400\ \mu\text{m}$ (90).

Other work found that bone regeneration was similar when using the range of a pore size between 350 and 800 μm for interconnected solid free-form PCL scaffolds with cylindrical orthogonal pore geometry after subcutaneous implantation in mice for 8 weeks (91). The reason for the low bone formation rate may reflect the use of a subcutaneous implant instead of implantation into an orthotopic site or muscle (92). However, the mechanical properties were higher in the scaffold with pore size of 350 μm than 550 and 800 μm 4 weeks after implantation. This may reflect the larger volume of PCL or greater mineralisation in an empty scaffold and the degradation and weakening the scaffold following 8 weeks of implantation. The scaffold was filled with fibroblast, which prefer to be deposited in smaller pore sizes compared with bone cells, which prefer larger pores. Therefore, a pore size of 800 μm was considered to be more appropriate for bone formation to provide adequate space for cell ingrowth. This behaviour is different from that for finer pores, which are best for fibroblast penetration (91). Similar results were obtained by Cheng et al.(93), who fabricated porous magnesium (Mg) scaffolds with two pore sizes of 250 and 400 μm using the titanium wire space holder method.

Larger pore size leads to greater formation of mature bone by promoting vascularisation. The newly formed blood vessels supply sufficient oxygen tension and nutrients for osteoblastic activity in the implant site, which leads to the upregulation of OPN and collagen type I, which contribute to the generation of bone mass. Mg ions contained within the scaffold are not absorbed by the body and do not contribute to severe inflammatory reactions. These ions are excreted in the urine after degradation of scaffold without causing any side effects. Inflammatory cells such as macrophages and lymphocytes are present around the larger pore size of the Mg scaffold (400 μm). These cells participate in inflammatory reactions during the first 3 months after implantation because of the higher corrosion rate of scaffolds with large pore size compared with those

with smaller pore size. The reaction to the scaffolds as a foreign body decreases 4 months after implantation, when the scaffolds with different pore sizes are degraded completely and replaced by the new formed bone (93).

According to other studies, the large pore size is beneficial *in vivo* because of its stimulation of bone formation, whereas the smaller pores have advantages *in vitro*. Smaller pores are suitable for controlling cell aggregation and proliferation (87, 94). However, the exogenous hypoxic state stimulates endothelial cell proliferation (95). Previous studies have shown no correlation between oxygen concentration and the opening region in the middle of the pore space when it is filled by cells during the culture process (53, 96). Also, proinflammatory cytokines such as tumour necrosis factor α (TNF- α) and interleukin 6 (IL-6), IL-10, IL-12 and IL-13 are secreted at a high level in wider pores with a larger angle and can trigger bone regeneration response (97).

Heterogeneous Pore Size

Variation in bone density occurs in the axial direction in long bones, which display a gradient in porous structure from cortical bone to cancellous bone (98). Therefore, scaffolds with a gradient in porosity may be a good candidate for bone regeneration. According to Luca et al., gradient PCL scaffolds improved the osteogenic differentiation on human mesenchymal stem cells (MSCs) by increasing the calcium content and ALP activity because of the better supply of oxygen and nutrients in larger pores (99). A perfect bone implant must be made of porous gradient biomaterials that mimic the properties of natural bone ECM and have a porosity-graded structure (100). Different pore size ranges are required for the optimal growth of various cell types (101). Osteoblasts prefer larger pores, whereas fibroblasts show better growth in smaller pores (102-104). The pore size range of 290 to 310 μm is associated with rapid bone formation, and the optimal size for vascularisation is 400 μm (75, 88, 105, 106).

One study showed the effect of a graded porous calcium polyphosphate (CPP) scaffold with 200–400 μm pore diameter used with three different porosity structures: dense, intermediate and highly porous. The more porous layer imitated light spongy cancellous bone, whereas the compact area simulated the stiff cortical human bone. The authors found greater cell growth and transport of nutrients and waste in the highly porous region because of its greater surface area. The dense layer was favourable for external mechanical loading. The mechanical properties indicated better compressive strength and non-brittle failure for the porosity-graded scaffold than for a homogeneous calcium polyphosphate (H-CPP) scaffold because of the increased degradation in H-CPP compared with the porosity-graded CPP, which exhibited slow degradation (107).

Sobral et al. evaluated cell-seeding efficiency of a human osteosarcoma cell in 3D poly (ϵ -caprolactone) scaffolds with two gradient pore sizes (100–700–100 μm and 700–100–700 μm) based on two pore sizes (100 and 700 μm). The pore-size gradient scaffolds exhibited better seeding efficiency, which increased from about 35% in the homogeneous scaffolds to about 70% in the gradient scaffolds under static culture conditions (108).

Role of Pore Geometry in Scaffold Osteogenicity

One of the geometric features that influences the bone regeneration rate is the geometry of the porous scaffold (72). Most scaffolds for tissue engineering have been designed with different pore morphologies through the salt leaching, gas foaming, freeze drying, rapid prototyping (RP) and 3D printing techniques to examine the effect geometry on the materials' biological and mechanical properties (23, 109-111). The pore geometry and surface curvature provide the 3D environment for the spatial arrangement and plays an important role in modulating tissue functions such as proliferation, differentiation and organisation (61).

The differences in pore width and curvature of the surface lead to variations in tissue morphology and growth rate (50, 53, 112). Cell motion is directed as traction forces provided by the actin cytoskeleton network (113). Internal forces, such as cell contraction, are associated with the pore configuration, which regulates the growth, progression and migration of cells (114). The larger the volume of tissue generated, mineralisation process, the angiogenesis and the growth of blood vessels favour concave surfaces compared with flat and convex regions. Because there is the greater cell stress in concave areas and density of actin and myosin fibres in these surfaces (115, 116). The stiffness of the biomaterial is associated with variations in the curvature (117). As a result, the pre-osteoblasts have a higher proliferation rate on a stiffer substrate than on a pliable substrate because of the higher traction strength on rigid materials (118, 119). Engler et al. confirmed that osteon cells differentiate the most on unyielding substrates, muscle tissue on stiffer substrates and neural cells on the soft matrices (120).

According to Van Bael et al. (52), Ti_6Al_4V scaffolds produced by the selective laser melting method have three distinct pore geometries and two pore sizes. The stiffness of scaffolds with the rectangular and triangular pores approached that of trabecular bone. The hexagonal design has the smallest pore size and mechanical stiffness close to those of cancellous bone. In addition, the compressive stiffness was lower in materials with pore size of 500 μm compared with 1,000 μm . This study normalised the metabolic activity, measured DNA content and used microcomputed tomography (μ -CT) to quantify the scaffold surface to estimate the rate and speed of cell growth. Hexagonal pores showed the lowest cell growth in the corners, followed by square pores. Triangular pores had the greatest tissue growth because of the largest curvature. The rates of growth and cell invasion into the pores are faster in materials with smaller pores (50, 53).

According to Boccaccio et al., the use of rectangular and elliptic pores leads to a larger bone volume than square and circular pores. These authors also evaluated the effect of pore distribution on the amount of bone generated by comparing aligned elliptic pores with pores in a staggered pattern. Aligned elliptic pores generated a larger quantity of bone under low mechanical loading on the scaffold. By contrast, the scaffolds with staggered pores were occupied by a larger bone volume under high mechanical loading. The authors also optimised the pore number numerically using staggered elliptic pores, 3×3 pores per unit area, aligned elliptic pores, and 4×4 and 5×5 pores per unit area (Figure 1.3). They predicted the greatest bone formation for scaffolds with a higher pore number by loading beyond 3 MPa and with a lower pore number with mechanical loads of 0.1–1.0 MPa. However, the pore number had no a significant effect on the quantity of bone formation (72, 121).

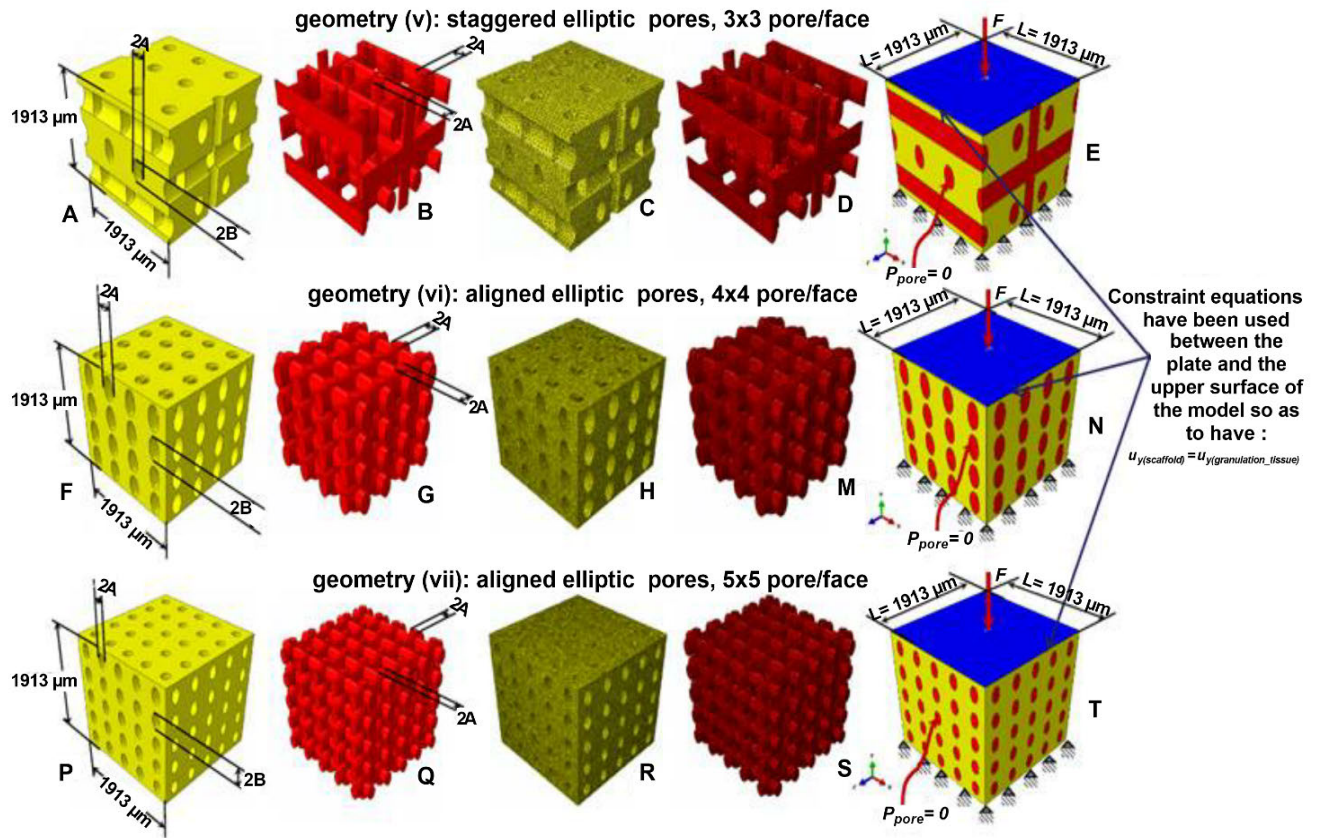


Figure 1.3. Computer-aided design model (A–B, F–G, P–Q) and finite element mesh (C–D, H–M, R–S) of the scaffold (A, C, F, H, P, R) and of the granulation tissue (B, D, G, M, Q, S) in the case of: (A–E) elliptic staggered pores, 3×3 pore/face; (F–N) elliptic (aligned) pores, 4×4 pore/face; and elliptic (aligned) pores, 5×5 pore/face (P–T). (E, N, T) Boundary and loading conditions acting on the model. In this model, a force to generate an apparent pressure is applied vertically via a rigid plate. The pore pressure p_{pore} on the outer surfaces of the granulation tissue was set to zero to simulate the free exudation of fluid (image from Boccaccio et al. doi:10.7150/ijbs.13158 (72)).

Xu et.al reported that different pore shapes also affect the rate of ALP activity. The authors compared 3D-printed macroporous nagelschmidtite (NAGEL, $\text{Ca}_7\text{Si}_2\text{P}_2\text{O}_{16}$) bioceramic scaffolds to β -tricalcium phosphate (β -TCP) bioceramic discs. Both materials contain three pore morphologies (triangular, square and parallelogram). The pore size for three geometries was 500–1000 μm . It was seen that the attachment was about 70% for

all groups. With an increasing culture time, the parallelogram and triangular NAGEL exhibited a greater proliferation than the square morphology. The parallelogram morphology had the highest ALP activity in the NAGEL scaffold compared with the other pore morphologies and β -TCP scaffolds. Among the pore morphologies, the square pore provided a higher modulus, greater mechanical strength and faster degradability and scaffold weight loss (122).

The ability to control the architecture, pore shape and scaffold strength can be achieved using 3D printing and RP techniques to create a scaffold directly from the digitised and scanned image of the defect site (67). Yilgor et al. designed and constructed four complex structures of porous PCL scaffold by changing the configuration of the deposited fibres within the architecture (basic, basic-offset, crossed and crossed-offset) (Figure 1.4). Greater cell proliferation was observed for the basic offset scaffolds compared with the crossed scaffolds. Greater mesenchymal stem cells (MSCs) differentiation and ALP activity were observed in crossed-offset scaffolds. These findings suggest that designing the architecture using different shapes and sizes, and at micro- and macroscales, can alter the cell behaviour, proliferation and differentiation. The basic-offset scaffolds (homogeneous structure) allowed cells to grow homogeneously because of the higher numbers of anchorage points. Interconnected struts created the angles, which differed from those in basic scaffolds and increased differentiation (123).

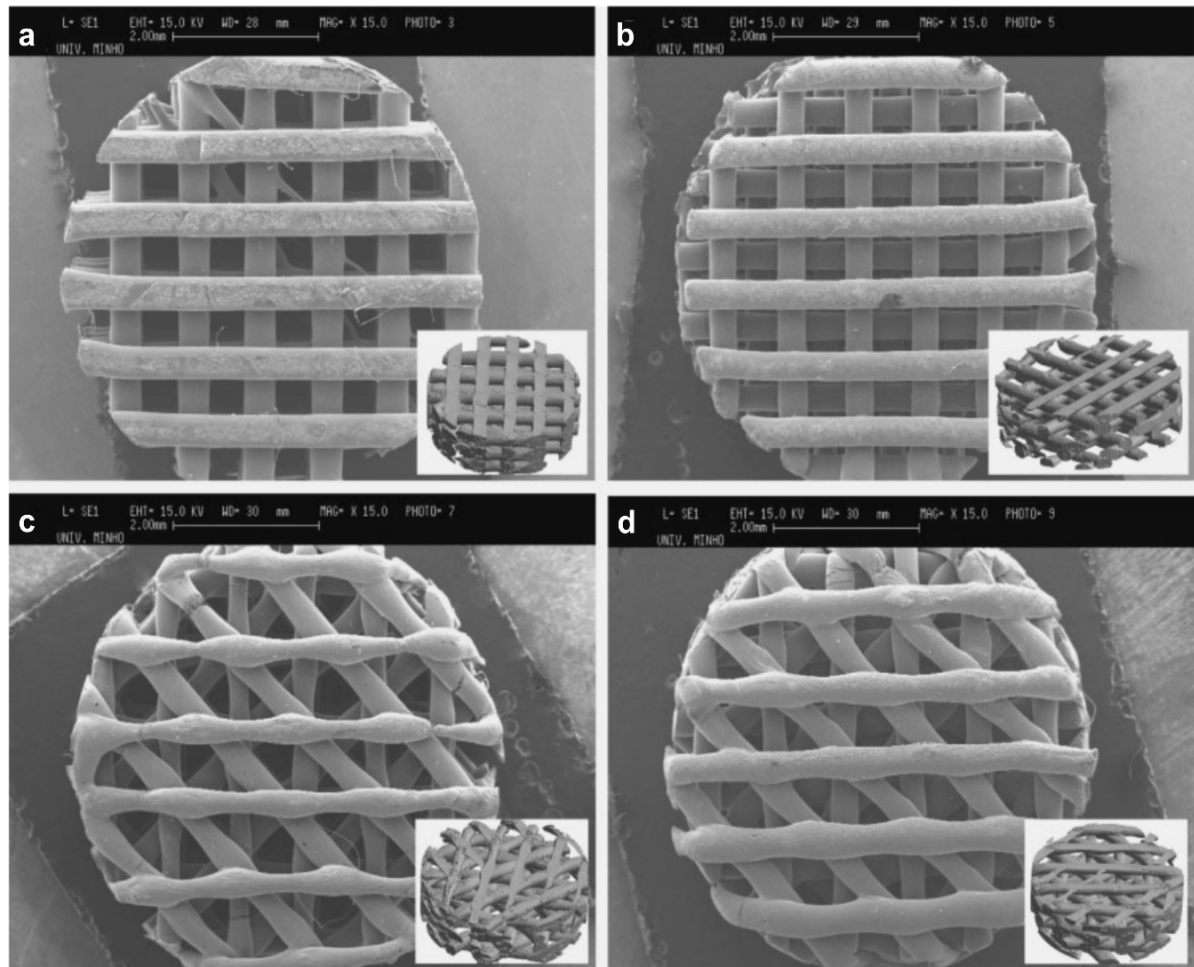


Figure 1.4. SEM images of PCL scaffolds produced using a 3D plotting technique with different architecture: a) basic, b) basic-offset, c) crossed and d) crossed-offset, including μ -CT images (bars represent 2 mm) (image from Yilgor et al. doi:[000258909100012](https://doi.org/10.1002/258909100012) (123)).

In a similar study, Yeo et al. fabricated various PCL- β -TCP (20 wt%) scaffolds with similar porosity (62%), 100% pore interconnectivity and a square pore shape, but with five pore sizes of different offset values (0%, 25%, 50%, 75% and 100%). They found superior cell differentiation and proliferation efficacy for calcium deposition and ALP activity (up to 50%), cell viability (increase to about 60%), cell seeding and higher bending modulus for scaffolds with offset values of 50% and 100% (124). These findings

suggest that designing the architecture with different offset values can alter the cell behaviour, proliferation and differentiation.

Role of Porosity in Determining Scaffold Permeability

The highly vascularised bone structure provides for greater mass transport in the 3D porous scaffold, which supports further bone regeneration (125). The ability of the scaffold to deliver nutrients to and remove waste from the regenerated site is key to successful bone tissue engineering (126). Permeability is defined as the ability of a porous environment to conduct fluid mobility and depends on important parameters such as porosity, pore orientation, pore size and distribution, pore interconnection and the organisational depth (127). Higher permeability improves the amount of bone ingrowth and inhibits the formation of cartilaginous tissue in the regenerated site (128). The permeability of a material can be normalised by the fluid viscosity (129). Permeability decreases with increasing organisational depth which allows for the development of the calcified layer and increased collagen content (130). Fluid flow is affected by the surface area of the scaffold and decreases with larger pore size (131). Permeability enhances in the scaffold by increasing the average pore size (132).

Mitsak et al. reported that higher permeability of BMP-7-transduced Human gingival fibroblasts (HGFs) seeded into a PCL scaffold increased bone regeneration and the mechanical properties of PCL–bone constructs after implantation into mice for 2 months (133). O’Brien et al. reduced the permeability by decreasing the pore size of collagen–GAG scaffolds, and this was accompanied by increased compressive strain (134).

Cell attachment depends on the scaffold permeability, and a larger pore size leads to a higher flow velocity of the cell suspension. Therefore, more time is needed for cells to attach to the surface (135). The highly open pore architecture does not permit cell

entrapment but instead makes the cells pass through the length of scaffold and settle at the bottom of scaffold without binding between the cells and the surface-adsorbed proteins (136). Hence, the greatest seeding efficiency is obtained by using the smallest pore size (137). A larger pore size is preferred for cell growth and proliferation because the pores will be occluded later than smaller pores during progressive growth and will therefore provide open space for nutrient and oxygen supply and further vascularisation (138). However, the interconnectivity of pores must also be considered when trying to create sufficient permeability to prolong the time of pore occlusion before the cells overgrow and nutrient and oxygen transportation becomes limited (139).

Melchels et al. examined that the porous salt-leached poly (D, L-lactide) (PDLLA)–dimethacrylate scaffold and found few cells in the central part of the scaffold. They attributed this to total blockade of small interconnections in the deeper sections of the scaffold because of matrix deposition that obstructed the pores and decreased permeability. However, the porous rapid prototyped gyroid scaffold contained the open pore network without clear boundaries in the pore intervals, and this delayed the pore blockage and kept free parts of the scaffold accessible for tissue diffusion. The authors used A4-4 cells that expressed luciferase enzyme to estimate the oxygen concentration in different pore interconnectivity scaffolds. They found that luciferase expression per cell, which reflected the availability of oxygen in the extracellular environment, was higher in scaffolds with smaller pore sizes during the early culture period. Not all of the scaffold's outside area was available for tissue diffusion after 20 days of culture (140). Therefore, pores with a smaller dimension may not be appropriate for encouraging bone formation and ontogenesis, because they may create a hypoxic state and stimulate chondrogenesis instead of osteogenesis (141, 142).

Xu et al. reported that the release of Ca, P and Si ionic products from nagelschmidite (NAGEL, $\text{Ca}_7\text{Si}_2\text{P}_2\text{O}_{16}$) ceramic scaffolds accelerated the proliferation of human umbilical vein endothelial cells (HUVECs) in at high concentrations (12.5 mg ml^{-1}) of NAGEL extracts by promoting angiogenesis via the nodes, which are mesh-like circles and tubular structures that are characteristic of endothelial cells (122). This conclusion agrees with the findings of previous studies that proposed that Si ions induce pro-angiogenesis and osteogenesis, and that Ca stimulates proliferation of endothelial cells (143, 144).

Role of Porosity in Scaffold Vascularisation

Engineered tissue with desirable properties has been achieved for thin or avascular tissues (145). Insufficient vascularity in complex or thick tissues such as bone limits spontaneous regeneration of these parts. Damage disrupts the vascular supply, leading to slow ingrowth of vessels and unsustainable remodelling and repair of tissues (146). The bone architecture showed a high vascularity, that the vessels are deposited in the inner region of trabecular structures such as the haversian system, which contains the blood and nerve supply (147). Extraosseous vascularisation starts 3–6 weeks after the onset of osteogenesis, when the mineral nodules generate the disconnected fine plate-like woven bone with high porosity, low density and scattered orientation. Extraosseous vascularisation becomes more following bone plates come together to form the highly oriented trabecular bone and it accompanies with medullary vascularisation from this stage of bone-forming process to the last step in configuring lamellar bone (148).

A fracture in natural bone produces a hypoxic environment, which leads to upregulation of angiogenesis and eventually creates a vascular network (149). This process is followed by the differentiation of (MSCs) located in the medullar cavity to cartilage (150). The newly formed cartilage is then calcified and hardened into bone. Because of the inability of the impermeable inner cartilage to transport nutrients, the

cartilage cells start to die, which creates cavities and allows the vessels to invade these cavities and the vascular mesh to develop. Osteoclasts, osteoblasts, lymphocytes and nerve cells also penetrate into the cavity, and the remaining cartilage starts to collapse after secretion of osteoid by osteoblasts and osteoclasts, which arrange the spongy bone (151).

The hypoxic situation stimulates the hypoxia-inducible factor 1 (HIF-1) pathway, which regulates vascular endothelial growth factor (VEGF) activation (152, 153). The presence of VEGF is required for angiogenesis and participates in bone generation and callus mineralisation (154). The hypoxic zones actuate the tips of endothelial cells, which behave like oxygen sensors and migrate toward the oxygen-deficient area. Stalk cells begin to sprout and branch to create vessel channels (154). Most of these cells reside within 100–200 μm from capillary tubes (155).

The risk of tissue necrosis is reduced by effective angiogenesis in the central parts of the defect, particularly in large scars. Some tissue-engineered bone products regenerate aneural and avascular bone tissue. The delivery of oxygen and nutrients to the cells located inside the scaffolds is limited in bone with a thickness of more than few hundred micrometres, and this impairs cell viability and bone regeneration. Several weeks are needed after implantation for complete vascularisation (156). The maximum distance from cells to the blood vein or artery required to stay alive is 150–200 μm (157), and cells beyond this distance will die because of nutrient deficiency and hypoxia. A distance of more than 25–200 μm is tolerable for only chondrocytes (158). Neovascularisation ensures nutrition supply and subsequent cell colonisation and survival. Therefore, creating the optimal conditions for the tissue to be pre-vascularised is essential before implantation (159).

One strategy for creating *in vivo* preformed vessels that needs two-step surgery, which is the implantation of a cell scaffold into a well-vascularised spot such as beneath the panniculus carnosus muscle before the next implantation at the injury site (160, 161).

Another approach focuses on co-culturing endothelial cells within other cell types on the scaffold construct (162). This method encourages the intercommunication of host blood vessel branches and the pre-vascularised construct. It also requires a shorter time because the host tissue vessel network is required to only cover the outer areas of the graft, which means that multiple surgeries are not required (163).

Techniques for creating vascularised constructs include perfusion of pro-angiogenic growth factors into the scaffold (basic fibroblast growth factor (bFGF), VEGF and Platelet-derived growth factor (PDGF)), channelling the scaffold, using a bioreactor system for nutrient exchange, creating branching endothelial microvascular networks and co-culturing of different cell types such as (MSCs), adipose-derived stem cells, osteoblasts and femur-derived stem cells with endothelial cells, vascular smooth muscle cells (SMCs) and immune cells (164, 165).

Growth factors can be encapsulated within the scaffold and release using a time-dependent controlled delivery system or immobilised by covalent binding or binding of intermediate biological molecules on the surface of the scaffold (166). Angiogenesis happens automatically after bone graft implantation as part of the inflammatory response, which stimulates vascularisation (167). Inflammatory response initiates the release of PDGF and VEGF by activating platelets, and these factors stimulate lymphocytes, monocytes–macrophages, fibroblasts and endothelial cells as part of the inflammatory response leading to activation of cytokine signalling (IL-1, IL-6, TNF- α , TGF- β). The secretion of pro-angiogenic VEGF by osteoprogenitor and phagocyte cells stimulates angiogenesis and blood vessel formation (168). The speed of neovascularisation is 1 mm per day.

The size of the construct will depend on the size of the defect. Larger defects need larger constructs, which greater supply of oxygen and nutrients; if these are inadequate, spontaneous vascularisation will be insufficient and the vascular network will not

penetrate into the implant (145). Incorporation of different cell types in bone tissue engineering provides options according to their resilience in different environments. For instance, in an environment with low concentration of oxygen or glucose because of limited blood supply, adipose tissue-derived stem cells are better able to survive in biofabricated bone structures (169).

Jin et al. showed that an HA scaffold with 300 μm pores loaded with VEGF increased MSC differentiation to endothelial cells and induced vascularisation. Multilayers of collagen and heparin can also be used to cover the scaffold structure to imitate the ECM of endothelial cells and may promote cell differentiation and stimulate new vessel formation (170). Heparin sulfate or heparin have been identified as bioactive elements that modify the binding of VEGF to its receptors and potentiate the stability of inchoate vascular networks by binding to the other growth factors and proteins of the ECM (166, 170). They improve the growth and differentiation of cells during osteogenesis by augmenting the bone-inducing growth factors such as bFGF (171).

Another important point for angiogenesis is the high cell density needed for better vasculogenic differentiation. Cell interactions and matrix elasticity affect endothelial differentiation (172). Approaches to improve the angiogenic properties of biomaterials include co-culture of osteoblasts and endothelial cells, and integration of VEGF, bFGF, PDGF into the biomaterials (102, 173). These pro-angiogenic growth factors can be supplemented within the scaffold by loading or simple coating (136, 174). The respective functions of VEGF, bFGF and PDGF are initiation of capillary formation, stimulation of endothelial cell proliferation and promotion of vessel maturation (175).

The dual delivery of two growth factors in combination speeds the maturation of the vascular network towards full development even in larger constructs compared with the single-factor delivery (163, 176). Since PDGF plays an effective role in progression of endothelial cells during the final stages of vessel formation (177), multiple delivery

must be optimised so that the distinct release rate performs for every factor in the regions of need. Multiple drug delivery requires the co-culture of two cell types that require different growth factors to proliferate and to mature into blood vessels (178). For example, PDGF can be encapsulated into polymer microspheres to provide a suitable environment for mixed culture of endothelial cells and SMCs. In this system, VEGF can be deposited on the surface through mixing with the polymer scaffold during its formation (166).

The fusion of the growth factor–polymer and growth factor–polymer microspheres provides a localised delivery system to release VEGF rapidly enough to initiate and sustain primitive angiogenesis in the first days. PDGF is released by slowly and induces vessel maturation and prevents apoptosis and regression of endothelial cell by encouraging SMCs to cover the newly formed vasculature and increase vessel density. A continuous, homogeneous matrix with more even distribution throughout the scaffold can be generated using microspheres. The release rate can be regulated by altering the molecular weight or formulation of the polymer microspheres to obtain various degradation times (179).

Growth factor gradients within channelled scaffolds can influence the rate, length and direction of vascular sprouting by controlling cell alignment and migration, and vascular conductance (180, 181). When engineering new bone tissue, prevascularisation and osteogenesis can be induced by combining endothelial cells and osteoblasts, which will display synergistic communication (182). Pore size also plays a significant role by supporting vessel invasion into the scaffold structure. Ensuring sufficient and homogeneous cell delivery are other obstacles that must be considered in cell-based strategy (183). The cell population should be adequate to cover the porous structure according to the shape and dimension of scaffold (184).

Amini et al. [184] studied vasculogenic and osteogenic growth of MSCs together with peripheral blood-derived endothelial progenitor cells (PB-EPCs) on cylinder-shaped oxygen tension-controlled matrices measuring 15 mm in height and 5 mm in diameter. The scaffold was fabricated by mixing poly (lactic-co-glycolic acid) (PLGA) microspheres (425–600 μm in diameter) and NaCl crystals as the porogen (200–300 μm in diameter) to create a large pore volume for bone regeneration *in vivo*. Co-culture at a 1-to-1 ratio of MSC-derived osteoblasts and EPCs, with a total of 250,000 cells per scaffold, produced the highest levels of collagen and vascular formation after 8 weeks of implantation. In this report, the maximum bone formation occurred with equal amounts of blood and bone cell incorporation. Adipose tissue was observed in acellular scaffolds because of the absence of the osteo/angiogenic environment. By contrast, the EPC-seeded scaffold was the more effective for mineralisation and collagen deposition compared with the MSC-seeded scaffold group because of a greater vascular inductive effect and support during early osteogenesis. The EPC-seeded scaffold also contained the least amount of fibrous and adipose tissues compare with the scaffold alone and MSC-seeded scaffold (156).

The usage of inorganic bioactive elements has advantages such as cost effectiveness, stability during storage and process, and low-dose functionality associated with their long-term activity after implant (3). The instability, high cost and a short half-life of growth factors *in vivo* inhibit their usefulness in clinical translation (185, 186). Cobalt (Co) ions are used as a cofactor for metalloproteins, which are required for the formation of the HIF-1 α complex, which comprises a highly conserved transcription factor that activates and regulates VEGF and numerous angiogenic genes (102, 187).

Zhao et al integrated Co nanograins measuring 30–60 nm at different concentrations coated on the surface of TiO₂/TCP microporous structure with a diameter pore size of 3–4 μm . They assessed the osteogenesis and angiogenesis behaviours of rat

bone marrow stem cells. The different doses of Co coating did not significantly alter the surface wettability, roughness or protein adsorption. However, the spreading and attachment of the cells was greatly improved because of cell anchorage to the micropores of the TCP construct. Cell proliferation was best in the low Co range of 10 ppm. A higher Co concentration (>15 ppm) caused cell cytotoxicity and reduced cell proliferation. By contrast, gene and protein expression relating to angiogenic factors (VEGF and HIF-1a) was increased by addition of Co incorporation amount. In this study, Co dose enhancement had positive effects on osteogenesis as shown by increased collagen secretion, ALP activity and ECM mineralisation (188).

Because of the scarcity of autologous tissue sources and potential for immune activation against allogenic cell lines, one study examined an acellular scaffold for making tissue-engineered constructs to treat bone or cartilage defects (189). Macro- and microstructures induced the influx and distribution of cells and blood uptake into the scaffold (190). Highly hydrophilic chitosan–alginate (Ch-Al) scaffolds were made using 3D-printed moulds with high porosity created through 1 and 3 mm scale cylindrical macrochannels and micro pores with 100 and 300 μm pores located in the internal region and the areas around the macrochannel edges. Micropores appeared in the densely fibrous architecture containing holes oriented perpendicular to the z-axis at the top of the scaffold, as randomly oriented spherical pores in the transitional or middle zone, and as interconnected columnar or lamellar pores in the residual height of the scaffold or deep zone.

The pore orientation design described in the preceding paragraph imitates the zonal configuration of collagen fibre orientation that occurs from the natural articular cartilage to subchondral bone, that includes superficial zone (perpendicular), middle zone (spherical) and deep zone (align to z axis) respectively. This orientation can be obtained by increasing or reducing the cooling rate during freezing using a directional freezing

technique that alters the ice crystal growth. Inadequate low temperature during lyophilisation causes the matrix interface between the scaffold and air to collapse because of the interfacial tension. Faster supercooling freezing or a faster cooling rate at the interface leads to instability of the Ch-Al slurry particles and concentrates the crystals, which allows faster crystal growth that creates the transitional or cellular zone. The pore formation generated by growing the lamellar ice crystal in the articular or deep zone through the slow cooling regime. Therefore, the microstructure was scaled up and the lamellar pores were formed by increasing the pore thickness.

The combined aligned micro- and macro channelled architecture of the Ch-Al scaffold improves the distribution of the cell suspension throughout the entire height and width of the scaffold. In addition, it accelerated the blood and aqueous solution volumetric flow rate from 18.2 ± 0.45 to $440.9 \pm 0.5 \text{ mm}^3 \text{ s}^{-1}$ and from 291.4 ± 89.5 to $1782.1 \pm 48 \text{ mm}^3 \text{ s}^{-1}$, respectively, compared with scaffolds without macrochannels. The wicking rate for blood is less than that for aqueous solution because of the viscosity difference. However, the flow rate is fast enough to prevent the activation of plasma coagulation, which requires 25–30 s and may hinder cells infiltration *in vivo*. This multiscale porous scaffold creates a greater surface area-to-volume ratio and interconnected pores with less tortuosity, which all increase the cell seeding and penetration and blood uptake (190).

According to Rustom et al., biphasic CaP scaffolds with a micropores ($<20 \text{ }\mu\text{m}$) size of $2.2 \text{ }\mu\text{m}$ and macropores ($>300 \text{ }\mu\text{m}$) with a size range of $650\text{--}750 \text{ }\mu\text{m}$ ensures a homogeneous cell distribution and bone volume fraction throughout the scaffold via the capillarity mechanism. The scaffold increases the capacity of cells to migrate throughout the microporous network. Better bone distribution improves the load-bearing of the repaired bone defect. This study reported that the capillarity process increased the bone distribution uniformly and incorporated a variety of cells such as vascular and blood cells,

which had aggregated in the micropores after implantation. Red blood cells (RBCs) cannot migrate because they lack a cell nucleus, and the capillarity forces driven by the scaffold architecture caused the RBCs to pass through the microporous network. The capillarity rate depends on the empty dry regions of micropores and how much the micropores are vacant or devoid of any kind of fluids, which may occupy the pore space and prevent or decrease capillarity. As shown in this study, submersion of pores in fluid decreases the capillarity rate and penetration, as well as cell spreading that cause the consequent minor homogeneous bone distribution in these structures (64). The gradient concentration of physiological fluid containing biomolecules, growth factors and nutrients contributes to the effectiveness and extent of regeneration (191).

Maintaining capillarity and providing a consistent capillary force to stimulate cell diffusion and vascularisation after implantation need to be considered for bone engineering. Because the macro-and microporous scaffolds which are inserted into the defect site, might be already filled with the initial biomolecules and endogenous cells from physiological fluid in the early stages of implantation. The saturation may prevent or slow continued flow of liquid (18). The surface tension combined with adhesion forces between the inner wall of the surface tube and the liquid can draw the liquid column upwards (192).

Role of Porosity in Determining Scaffold Mechanical Properties

One effective factor for regulating the mechanical properties of a scaffold is the porosity rate. The mechanical properties of the scaffold tend to deplete exponentially with increasing porosity (193, 194). Although cell delivery requires a highly porous scaffold (>90% porosity), porosity >80% is not recommended for implantation of a polymeric scaffold into bone defects (195, 196). The porous surface of the scaffold improves the stability of the mechanical interconnections between the implant biomaterial and the

natural tissue (197). The polymer molecular weight can affect the porosity, interconnectivity, pore sizes and mechanical properties of a scaffold (17).

The value of Young's modulus and mechanical properties are affected by modification of the biomaterials homogeneity or heterogeneity of the pores, morphology of the pores, pore alignment or random direction, and the model for pore size distribution (198). For example, Serra et al. reported that poly (L-lactide)-b-poly (ethylene glycol) (PLA/PEG) with composite material of CaP glass and molar composition $44.5\text{P}_2\text{O}_5-44.5\text{Ca}_2\text{O}-6\text{Na}_2\text{O}-5\text{TiO}_2$ coded G5 (PLA/PEG/G5) scaffolds with orthogonal structure exhibited greater compression strength than those with displaced double-layer patterns. Both scaffolds were fabricated using a RP technique. Although the presence of glass in PLA/PEG/G5 increased the compressive modulus, tolerance of mechanical stress decreased because of the large pore sizes created by the double-layer dissociation (199).

Ma et al. produced 3D biodegradable porous PLLA and PLGA scaffolds using a solvent cast technology. Their mechanical analysis showed that smaller pores increased the compressive modulus of the scaffolds. However, smaller pore size reduced the compressive modulus by extending the time required for the heat treatment of paraffin spheres, which introduced spaces between the pores of the scaffolds (200). Maximum supported stress has been achieved by using uniform small pores, although heterogeneous porous patterns containing both small and large pore sizes produced better mechanical properties. The construct with only one large pore size had a lower Young modulus and poorer mechanical properties (201, 202).

There are some contradictions between *in vitro* and *in vivo* studies related to the mechanical properties subject. According to the study of Roosa et al., the mechanical properties are better in scaffolds with a pore size of 350 μm without cells compared with the cell-scaffold structure. This may be related to the larger PCL volume or more

mineralisation in empty scaffolds after 8 weeks of implantation because the scaffold was weakened. This process may have been affected by fibroblasts, which prefer to be deposited in smaller pore sizes compared with the bone cells, which localise to larger pores. Therefore, a pore size of 800 μm was observed to be more appropriate for bone formation in animal models because it provides adequate spaces for bone cells ingrowth as opposed to smaller pores that encourage fibroblast penetration (91).

The correlation between mechanical properties and pore size is not linear (203). Intermediate stiffness occurs in scaffolds with a gradient of pore sizes. Other factors such as fibre positioning and orientation also play an important role in determining the ultimate mechanical properties. The simple architecture of homogeneous scaffolds is prone to collapse under high stress. The complexity of non-uniform porous scaffolds allows them to recover after deformation and maintain their elastic state, which is critical for the effective use of implanted biomaterials and biomedical applications (108). The orientation of pores is another parameter that directly affects the mechanical properties of scaffolds (204). Arora et al. reported maximum mechanical properties and a doubled Young modulus for aligned pores *in vitro* and when implanted into an injury site (205, 206).

The complex heterogeneous and hierarchical structure of bone tissue creates variations in compressive strength and tensile values in different regions of bone (207). There is a linear relationship between the resistance to mechanical loading and bone density or toughness. This relationship can be modified by the presence of cement, formation of mineral phase crystal or osteon infiltration (208). A reduction in bone mass increases the susceptibility to fracture (209). Cortical bone has a great mass-to-surface area ratio. Cortical bone contains 20% porosity along the transverse axis and has a load bearing capacity of 8–20 GPa parallel to the osteon direction which forms packets of

osteons, whose cortex shell contains concentric rings of bone matrix surrounding the central channel, which contains nerve and blood vessels. Therefore, cortical bone generates compact bone which is denser than cancellous bone (210, 211).

Cancellous or spongy bone had >90% porosity and is found next to joints that are highly vascular. In cancellous bone, cells exchange Ca ions, exert metabolic activity and produce blood cell (called haematopoiesis) (212). Cancellous bone has greater flexibility and its young's modulus is 100 MPa, which is lower than that in cortical bone (213). The vascular integrity is preserved by the local mechanical stability (214). The mechanical forces can be translated into cellular and tissue responses and bone remodelling (215).

CaP scaffolds is an osteoconductive material that has been used in bone tissue engineering because of its similarities in osteointegration potential and inorganic mineral phase crystals found in bone (216). Bone matrix topography and stiffness influence the deposition, adhesion, migration and differentiation of osteoblasts (217). Coarse surfaces increase focal adhesion strength, which ensures a high resistance and cytoskeletal organisation (46). The formation of localised stresses through the surface roughness at the point on the cell membrane changes the nuclear shape, which induces modification of gene expression. These modifications are transmitted via the focal adhesion. The signalling pathways are triggered by actin filaments and integrin receptors (Figure 1.5) (218). According to Gharibi et al., mechanical loading on CaP scaffolds activates transcription factors, which upregulate the genes controlling osteoblast differentiation and proliferation such as *ERK1/2* and *RUNX2* and eventually and augment mineralisation *in vitro* (219).

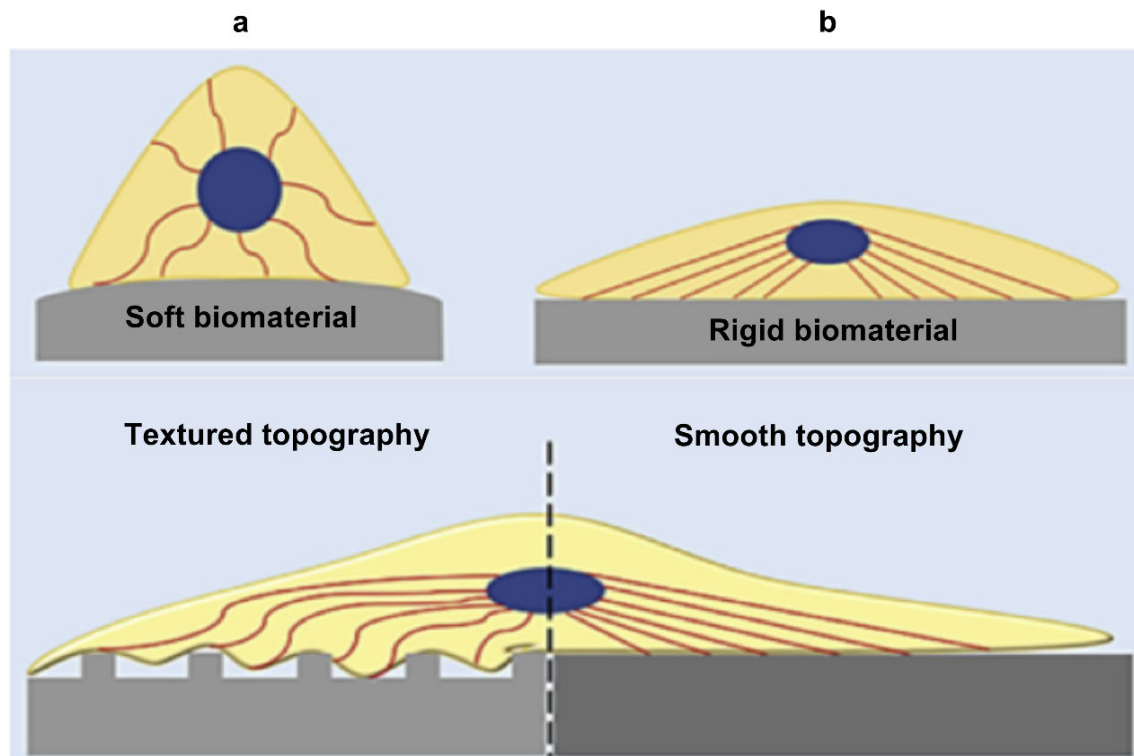


Figure 1.5. The stiffness and topography of bone matrix affect new bone deposition by osteoblasts. (a) Substrate rigidity influences cell adhesion, spreading, and differentiation patterns. Soft surfaces provide low resistance, reducing focal adhesion strength and cytoskeletal organisation (shown in red) relative to more rigid surfaces. Changes in the nuclear shape induce changes in gene expression. (b) Similarly, surface roughness, spacing and randomness in the nanotopography of scaffolds can influence cell adhesion and formation of localised stresses along the cell membrane. Such differences are transmitted via actin filaments (shown in red) to the nucleus, which leads to changes in gene expression and cell fate (image from Hung et al. doi:[10.1186/scrt158](https://doi.org/10.1186/scrt158) (218)).

The morphology of the selective organic or mineral porogen and pores affects the mechanical properties and structure of the scaffold (220). A more complex morphological architecture has greater compressive strength (221). For example, Young's modulus was reported as 9.81 MPa for a bio-scaffold with a diagonal morphology, 7.43 MPa for that with a stagger morphology, and 6.05 MPa for that with a lattice morphology. The

scaffolds were prepared using a multi-head deposition system for blended PCL/PLGA (222). Other studies by Zhang et al. and Ma et al. reported that spherical pores in a PLGA scaffold had better mechanical properties than cubic pores (109, 200).

The optimal values for Young's modulus for forming the greatest amount of bone were predicted using a computed algorithm design for different scaffold geometries and then tested with compression loads (0.001 to 5 MPa) (Table 1.1). For example, applying a load of about 0.05 MPa maximised bone formation for aligned circular pores with a 3 × 3 pore/face and the Young's modulus was 1500 MPa. The load decreased to 0.005 MPa for a scaffold with a Young's modulus of 500 MPa. In general, oriented pores permit greater bone regeneration than non-aligned pores. Oriented pores allow for a greater bone production at low load values, whereas staggered pores have a better capacity to induce a larger bone volume against a high load. However, scaffolds with higher Young's modulus and smaller pore size are preferred for greater loads.

Table 1.1. Best values for Young’s modulus (expressed in MPa) for different scaffold geometries and compression loads (image from Boccaccio et.al. doi: [10.7150/ijbs.13158](https://doi.org/10.7150/ijbs.13158) (72)).

Scaffold geometry/pressure [MPa]	0.01	0.05	0.1	0.5	1.0	2.0	3.0	4.0	5.0
(i) Aligned elliptic pores, 3×3 pore/face	500	1000	1500	1500	1500	1500	1500	1500	1500
(ii) Aligned circular pores, 3×3 pore/face	500	1000	1500	1500	1500	1500	1500	1500	1500
(iii) Aligned rectangular pores, 3×3 pore/face	500	1500	1500	1500	1500	1500	1500	1500	1500
(iv) Aligned square pores, 3×3 pore/face	500	1500	1500	1500	1500	1500	1500	1500	1500
(v) Staggered elliptic pores, 3×3 pore/face	500	500	500	1000	1500	1500	1500	1500	1500
(vi) Aligned elliptic pores, 4×4 pore/face	500	1000	1500	1500	1500	1500	1500	1500	1500
(vii) Aligned elliptic pores, 5×5 pore/face	500	1000	1500	1500	1500	1500	1500	1500	1500

Boccaccio et al. and Kim et al. suggested that a larger pore dimension is better in low compression environments (220) and oriented and smaller pores are appropriate for higher loads (72).

Role of Porosity in Determining the Degradation Rate

The pore size plays an important role in the pattern of scaffold degradation (223). Although greater porosity leads to further permeability, which ultimately results in faster degradation, other parameters such as the homogeneity of pores, morphology and pore size influence the degeneration of porous biomaterials (224). For example, Wu et al. investigated the *in vitro* degradation rate of 3D porous scaffolds composed of PLGA85/15 (poly (D,L-lactide-co-glycolide)) with a porosity of 80–95% and pore size of 50–450 μm in PBS at 37°C for 26 weeks. The scaffolds with larger pore size and lower porosity degraded faster than those with smaller pore size and higher porosity. This finding was attributed to the effect of the smaller surface area in the scaffolds with larger pore size, which reduced the diffusion of acidic degradation products during the incubation period and lead to a stronger acid-catalysed hydrolysis (225).

Pore size and porosity regulate the rate of degradation in PLA scaffolds with a pore size of 0–500 μm from solid to highly porous scaffolds with porosity >90%. Faster degradation occurred in scaffolds with a larger pore size and in solid films because the degradation products were trapped in isolated pores as a result of autocatalysed degradation. Intermediate degradation behaviour was observed in scaffolds with pore sizes between the maximum and minimum range mentioned above. The morphology of pores changed to sharp pore edges with larger pore size and decreasing or closed pore cavities with subsequent a solid surface formation on the top in scaffolds with a smaller pore size (226-228).

CONCLUSIONS

This review examined the importance of pore size and porosity to cell behaviour during ossification and angiogenesis, as well as how porosity determines the mechanical properties of biomaterial scaffolds. Various techniques have been developed to produce porous scaffolds. Of these methods, additive manufacturing technology is more successful for fabricating 3D custom-designed scaffolds with the best configuration to control the pore size. Macroporous scaffolds allow better integration with the host bone tissue and subsequent vascularisation, and interconnected pore sizes between 100 and 600 μm are optimal for bone distribution. Large pores are more favourable for bone formation and mineralisation, but small pores are more suitable for soft tissue ingrowth. With respect to their mechanical properties, a greater compressive modulus is associated with smaller pore sizes and scaffolds with gradient porosity as well as with staggered orientated pores.

The major advantage of using graded porosity scaffolds is their ability to maintain and recover their elastic properties after deformation. The geometry of the structure is another major requirement for the effective manufacture of scaffolds. Triangular, rectangular and elliptic pores support angiogenesis and cause faster cell migration compared with other pores because the surface has greater curvature and the staggered and offset pores help to produce a larger bone volume compared with scaffolds with aligned patterns. The advantage of square pores is that they can help to improve the stable mechanical strength among the other pores shape. Increasing the pore size increases the permeability, which increases bone ingrowth.

The combination of endothelial cells and osteoblasts in an equal ratio plays a pivotal role in pre-vascularisation during osteogenesis and homogeneous bone distribution in macroporous scaffolds. A faster degradation rate is attributed to a larger pore size because

of the greater dispersal of acidic products after degradation. Although several reports have shown the effects of pore size, shape and porosity on ossification, few have reported on the influence of heterogeneous porosity on degradation, mechanical properties and angiogenesis after implantation to stimulate bone healing. As a consequence, there is an extensive scope of research in this field of bone tissue engineering.

Research Hypothesis

However, there are some reports supporting the effect of pore size of scaffold on osteogenesis and angiogenesis, the Offset and gradient pore size heterogeneous porous architectures in melt electrowritten scaffolds is not clear. Consequently, this PhD has focused on the influence of offset and gradient design structures during bone differentiation both *in vitro* and *in vivo*. Furthermore, it is proposed that CaP has been shown to promote the bone mineralization, thereby the CaP stability has important role to affect the pore size and fibre dimension of melt electrowritten scaffolds.

We hypothesise that the offset and gradient architectures of MEW scaffold improve bone regeneration in an osseous defect compared to homogeneous porous structures. Using an appropriate etching of 3-D printed PCL scaffold before CaP coating activates the bonding strength of the mineral coatings to the scaffold surface, thereby enhances the quality of uniform and stable CaP coating.

Aims

1. Development of three-dimensional PCL scaffolds with different pore sizes using a MEW technique and evaluation of the different surface modifications of the scaffold with bioactive CaP materials which influence on physicochemical properties of the construct.
2. Determine the effect of various offset and gradient pore structures on scaffold's mechanical properties, as well as attachment and proliferation of human osteoblast cells *in vitro*.

3. Evaluation of various offset and gradient pore structures on bone matrix mineralization of human osteoblast cells *in vitro*.
4. Evaluate the *in vivo* effect of the designed offset and gradient porous scaffolds on osteogenesis and angiogenesis after implanting into a rat calvarial osseous defect.

Significance and Innovation

Organ and tissue transplantation, a vital life-saving treatment option, is often hampered by problems with morbidity, immune rejection, immunosuppressive therapy and the shortage of donor organs. To address this problem, synthetic tissues with unique properties can be created by biomedical engineering which utilizes a scaffold to serve as a template for specific tissue formation that is subsequently seeded with cells and growth factors to stimulate cell growth. These three-dimensional scaffolds mimic the actual microenvironment of real tissue *in vivo*, therefore they are more suitable compared to two-dimensional substrates for the investigation of cellular characteristics such as, morphology, proliferation, gene and protein expression and drug sensitivity.

A porous scaffold with porosity-graded architecture is an ideal template to mimic the natural bone ECM. Adequate porosity is necessary to promote cell infiltration, nutrient fluids to the structure, subsequent vascularization and angiogenesis through the appropriate interconnectivity and to withstand external loading stress. As the stress and strain distributions within the scaffolds will be changed by the scaffold architecture, it's important to understand the relationship between biophysical signals which are sent from the scaffold through deformation that are received by the cells to adjust their behaviour accordingly. There are some theories to support the notion that specific tissue formation is stimulated by mechano-regulation factors. As previous studies have shown that cell differentiation is influenced by porosity, elasticity and dissolution rate of the scaffold, by predicting the strain and stress distribution in the scaffold, we are able to optimize the

scaffold design parameters such as porosity, structure and type of material that will be coupled with the tissue formation and cell differentiation.

This study will investigate the role of pore size and porous scaffold architecture in osteogenesis, cell-scaffold interaction and growth and development, which will provide a better understanding of these processes and their potential for vascularization and bone formation. In this study, two different scaffold structures; homogeneous pore size (250 um, 500 um, 750 um) and heterogeneous architecture including gradient scaffolds with different pore sizes (from top 250um, middle 500um, bottom 750um) and offset scaffolds in which layers are printed with various offset values of 30% and 50% compared to the previous layer.

References

1. Winkler T, Sass FA, Duda GN, Schmidt-Bleek K. A review of biomaterials in bone defect healing, remaining shortcomings and future opportunities for bone tissue engineering THE UNSOLVED CHALLENGE. *Bone Joint Res.* 2018;7(3):232-43.
2. Sakkas A, Wilde F, Heufelder M, Winter K, Schramm A. Autogenous bone grafts in oral implantology-is it still a "gold standard"? A consecutive review of 279 patients with 456 clinical procedures. *Int J Implant Dent.* 2017;3.
3. de Grado GF, Keller L, Idoux-Gillet Y, Wagner Q, Musset AM, Benkirane-Jessel N, et al. Bone substitutes: a review of their characteristics, clinical use, and perspectives for large bone defects management. *J Tissue Eng.* 2018;9.
4. Chen FM, Liu XH. Advancing biomaterials of human origin for tissue engineering. *Prog Polym Sci.* 2016;53:86-168.
5. Kamm RD, Bashir R, Arora N, Dar RD, Gillette MU, Griffith LG, et al. Perspective: The promise of multi-cellular engineered living systems. *Apl Bioeng.* 2018;2(4).
6. Talebian S, Mehrali M, Taebnia N, Pennisi CP, Kadumudi FB, Foroughi J, et al. Self-Healing Hydrogels: The Next Paradigm Shift in Tissue Engineering? *Adv Sci.* 2019;6(16).
7. Oryan A, Alidadi S, Moshiri A, Maffulli N. Bone regenerative medicine: classic options, novel strategies, and future directions. *J Orthop Surg Res.* 2014;9.
8. Owen R, Reilly GC. In vitro Models of Bone Remodelling and Associated Disorders. *Front Bioeng Biotech.* 2018;6.
9. Efraim Y, Schoen B, Zahran S, Davidov T, Vasilyev G, Baruch L, et al. 3D Structure and Processing Methods Direct the Biological Attributes of ECM-Based Cardiac Scaffolds. *Sci Rep-Uk.* 2019;9.

10. Foster BL, Ao M, Salmon CR, Chavez MB, Kolli TN, Tran AB, et al. Osteopontin regulates dentin and alveolar bone development and mineralization. *Bone*. 2018;107:196-207.
11. Kasperk C, Wergedal J, Strong D, Farley J, Wangerin K, Gropp H, et al. Human Bone Cell Phenotypes Differ Depending on Their Skeletal Site of Origin. *J Clin Endocr Metab*. 1995;80(8):2511-7.
12. Limmahakhun S, Oloyede A, Sitthiseripratip K, Xiao Y, Yan C. 3D-printed cellular structures for bone biomimetic implants. *Addit Manuf*. 2017;15:93-101.
13. Wissing TB, Bonito V, Bouten CVC, Smits AIPM. Biomaterial-driven in situ cardiovascular tissue engineering-a multi-disciplinary perspective. *Npj Regen Med*. 2017;2.
14. Kashirina A, Yao YT, Liu YJ, Leng JS. Biopolymers as bone substitutes: a review. *Biomater Sci-Uk*. 2019;7(10):3961-83.
15. Honda M, Hariya R, Matsumoto M, Aizawa M. Acceleration of Osteogenesis via Stimulation of Angiogenesis by Combination with Scaffold and Connective Tissue Growth Factor. *Materials*. 2019;12(13).
16. Saberi A, Jabbari F, Zarrintaj P, Saeb MR, Mozafari M. Electrically Conductive Materials: Opportunities and Challenges in Tissue Engineering. *Biomolecules*. 2019;9(9).
17. Babaie E, Bhaduri SB. Fabrication Aspects of Porous Biomaterials in Orthopedic Applications: A Review. *Acs Biomater Sci Eng*. 2018;4(1):1-39.
18. Zhang K, Fan YB, Dunne N, Li XM. Effect of microporosity on scaffolds for bone tissue engineering. *Regen Biomater*. 2018;5(2):115-24.
19. Marrella A, Lee TY, Lee DH, Karuthedom S, Sylva D, Chawla A, et al. Engineering vascularized and innervated bone biomaterials for improved skeletal tissue regeneration. *Mater Today*. 2018;21(4):362-76.

20. Bhattarai DP, Aguilar LE, Park CH, Kim CS. A Review on Properties of Natural and Synthetic Based Electrospun Fibrous Materials for Bone Tissue Engineering. *Membranes*. 2018;8(3).
21. Jenkins TL, Little D. Synthetic scaffolds for musculoskeletal tissue engineering: cellular responses to fiber parameters. *Npj Regen Med*. 2019;4.
22. Mehrasa M, Asadollahi MA, Nasri-Nasrabadi B, Ghaedi K, Salehi H, Dolatshahi-Pirouz A, et al. Incorporation of mesoporous silica nanoparticles into random electrospun PLGA and PLGA/gelatin nanofibrous scaffolds enhances mechanical and cell proliferation properties. *Mat Sci Eng C-Mater*. 2016;66:25-32.
23. Eltom A, Zhong GY, Muhammad A. Scaffold Techniques and Designs in Tissue Engineering Functions and Purposes: A Review. *Adv Mater Sci Eng*. 2019.
24. Bodenberger N, Kubiczek D, Abrosimova I, Scharm A, Kipper F, Walther P, et al. Evaluation of methods for pore generation and their influence on physio-chemical properties of a protein based hydrogel. *Biotechnol Rep (Amst)*. 2016;12:6-12.
25. Savina IN, Ingavle GC, Cundy AB, Mikhalovsky SV. A simple method for the production of large volume 3D macroporous hydrogels for advanced biotechnological, medical and environmental applications. *Sci Rep-Uk*. 2016;6.
26. Kosowska K, Henczka M. The Influence of Supercritical Foaming Conditions on Properties of Polymer Scaffolds for Tissue Engineering. *Chem Process Eng-Inz*. 2017;38(4):535-41.
27. Scaffaro R, Lopresti F, Maio A, Sutera F, Botta L. Development of polymeric functionally graded scaffolds: a brief review. *J Appl Biomater Func*. 2017;15(2):E107-E21.
28. Brown TD, Edin F, Detta N, Skelton AD, Hutmacher DW, Dalton PD. Melt electrospinning of poly(epsilon-caprolactone) scaffolds: Phenomenological observations associated with collection and direct writing. *Mat Sci Eng C-Mater*. 2014;45:698-708.

29. Soares S, Silva A, Correia I. Porous Bioglass Scaffold for Orthopedics Applications. *Mater Sci-Medzg*. 2016;22(2):279-84.
30. Zaiss S, Brown TD, Reichert JC, Berner A. Poly(epsilon-caprolactone) Scaffolds Fabricated by Melt Electrospinning for Bone Tissue Engineering. *Materials*. 2016;9(4).
31. Hamed A, Shehata N, Elosairy M. Investigation of Conical Spinneret in Generating More Dense and Compact Electrospun Nanofibers. *Polymers-Basel*. 2018;10(1).
32. Din FU, Aman W, Ullah I, Qureshi OS, Mustapha O, Shafique S, et al. Effective use of nanocarriers as drug delivery systems for the treatment of selected tumors. *Int J Nanomed*. 2017;12:7291-309.
33. Muerza-Cascante ML, Haylock D, Hutmacher DW, Dalton PD. Melt Electrospinning and Its Technologization in Tissue Engineering. *Tissue Eng Part B-Re*. 2015;21(2):187-202.
34. Kim M, Yun HS, Kim GH. Electric-field assisted 3D-fibrous bioceramic-based scaffolds for bone tissue regeneration: Fabrication, characterization, and in vitro cellular activities. *Sci Rep-Uk*. 2017;7.
35. Liu Z, Ju KY, Wang ZQ, Li W, Ke HZ, He JH. Electrospun Jets Number and Nanofiber Morphology Effected by Voltage Value: Numerical Simulation and Experimental Verification. *Nanoscale Res Lett*. 2019;14(1).
36. Hrynevich A, Elci BS, Haigh JN, McMaster R, Youssef A, Blum C, et al. Dimension-Based Design of Melt Electrowritten Scaffolds. *Small*. 2018;14(22).
37. Bobbert FSL, Zadpoor AA. Effects of bone substitute architecture and surface properties on cell response, angiogenesis, and structure of new bone. *J Mater Chem B*. 2017;5(31):6175-92.

38. Mohammadzadehmoghadam S, Dong Y, Davies IJ. Modeling electrospun nanofibers: An overview from theoretical, empirical, and numerical approaches. *Int J Polym Mater Po.* 2016;65(17):901-15.
39. Sugawara Y, Kamioka H, Honjo T, Tezuka K, Takano-Yamamoto T. Three-dimensional reconstruction of chick calvarial osteocytes and their cell processes using confocal microscopy. *Bone.* 2005;36(5):877-83.
40. Iviglia G, Kargozar S, Baino F. Biomaterials, Current Strategies, and Novel Nano-Technological Approaches for Periodontal Regeneration. *J Funct Biomater.* 2019;10(1).
41. Abbasi N, Abdal-hay A, Hamlet S, Graham E, Ivanovski S. Effects of Gradient and Offset Architectures on the Mechanical and Biological Properties of 3-D Melt Electrowritten (MEW) Scaffolds. *Acs Biomater Sci Eng.* 2019;5(7):3448-61.
42. Thavornnyutikarn B, Chantarapanich N, Sittthiseripratip K, Thouas GA, Chen Q. Bone tissue engineering scaffolding: computer-aided scaffolding techniques. *Prog Biomater.* 2014;3:61-102.
43. Lim TC, Chian KS, Leong KF. Cryogenic prototyping of chitosan scaffolds with controlled micro and macro architecture and their effect on in vivo neo-vascularization and cellular infiltration. *J Biomed Mater Res A.* 2010;94a(4):1303-11.
44. Murphy CM, O'Brien FJ. Understanding the effect of mean pore size on cell activity in collagen-glycosaminoglycan scaffolds. *Cell Adhes Migr.* 2010;4(3):377-81.
45. Gunathilake TMSU, Ching YC, Ching KY, Chuah CH, Abdullah LC. Biomedical and Microbiological Applications of Bio-Based Porous Materials: A Review. *Polymers-Basel.* 2017;9(5).
46. Ermis M, Antmen E, Hasirci V. Micro and Nanofabrication methods to control cell-substrate interactions and cell behavior: A review from the tissue engineering perspective. *Bioact Mater.* 2018;3(3):355-69.

47. Im GI, Ko JY, Lee JH. Chondrogenesis of Adipose Stem Cells in a Porous Polymer Scaffold: Influence of the Pore Size. *Cell Transplant*. 2012;21(11):2397-405.
48. Vitale-Brovarone C, Baino F, Miola M, Mortera R, Onida B, Verne E. Glass-ceramic scaffolds containing silica mesophases for bone grafting and drug delivery. *J Mater Sci-Mater M*. 2009;20(3):809-20.
49. Lien S-M, Ko L-Y, Huang T-J. Effect of pore size on ECM secretion and cell growth in gelatin scaffold for articular cartilage tissue engineering. *Acta biomaterialia*. 2009;5(2):670-9.
50. Knychala J, Bouropoulos N, Catt CJ, Katsamenis OL, Please CP, Sengers BG. Pore geometry regulates early stage human bone marrow cell tissue formation and organisation. *Ann Biomed Eng*. 2013;41(5):917-30.
51. Gariboldi MI, Best SM. Effect of Ceramic Scaffold Architectural Parameters on Biological Response. *Front Bioeng Biotechnol*. 2015;3:151.
52. Van Bael S, Chai YC, Truscetto S, Moesen M, Kerckhofs G, Van Oosterwyck H, et al. The effect of pore geometry on the in vitro biological behavior of human periosteum-derived cells seeded on selective laser-melted Ti6Al4V bone scaffolds. *Acta Biomater*. 2012;8(7):2824-34.
53. Rumpler M, Woesz A, Dunlop JW, van Dongen JT, Fratzl P. The effect of geometry on three-dimensional tissue growth. *J R Soc Interface*. 2008;5(27):1173-80.
54. Guyot Y, Papantoniou I, Chai YC, Van Bael S, Schrooten J, Geris L. A computational model for cell/ECM growth on 3D surfaces using the level set method: a bone tissue engineering case study. *Biomech Model Mechan*. 2014;13(6):1361-71.
55. Sanaei P, Cummings LJ, Waters SL, Griffiths IM. Curvature- and fluid-stress-driven tissue growth in a tissue-engineering scaffold pore. *Biomech Model Mechan*. 2019;18(3):589-605.

56. Zadpoor AA. Bone tissue regeneration: the role of scaffold geometry. *Biomater Sci-Uk*. 2015;3(2):231-45.
57. Wang WY, Davidson CD, Lin D, Baker BM. Actomyosin contractility-dependent matrix stretch and recoil induces rapid cell migration. *Nat Commun*. 2019;10.
58. Ma JL, van den Beucken JJJP, Pan JL, Cui FZ, Chen S. Bone regeneration using coculture of mesenchymal stem cells and angiogenic cells. *Front Mater Sci*. 2014;8(1):32-8.
59. Bidan CM, Wang FM, Dunlop JW. A three-dimensional model for tissue deposition on complex surfaces. *Comput Methods Biomech Biomed Engin*. 2013;16(10):1056-70.
60. Hosseini V, Kollmannsberger P, Ahadian S, Ostrovidov S, Kaji H, Vogel V, et al. Fiber-assisted molding (FAM) of surfaces with tunable curvature to guide cell alignment and complex tissue architecture. *Small*. 2014;10(23):4851-7.
61. Vetsch JR, Muller R, Hofmann S. The influence of curvature on three-dimensional mineralized matrix formation under static and perfused conditions: an in vitro bioreactor model. *J R Soc Interface*. 2016;13(123).
62. Matamoro-Vidal A, Levayer R. Multiple Influences of Mechanical Forces on Cell Competition. *Curr Biol*. 2019;29(15):R762-R74.
63. Nelson CM, Jean RP, Tan JL, Liu WF, Sniadecki NJ, Spector AA, et al. Emergent patterns of growth controlled by multicellular form and mechanics. *P Natl Acad Sci USA*. 2005;102(33):11594-9.
64. Rustom LE, Boudou T, Lou SY, Pignot-Paintrand I, Nemke BW, Lu Y, et al. Micropore-induced capillarity enhances bone distribution in vivo in biphasic calcium phosphate scaffolds. *Acta Biomater*. 2016;44:144-54.
65. Alfieri R, Vassalli M, Viti F. Flow-induced mechanotransduction in skeletal cells. *Biophys Rev*. 2019;11(5):729-43.

66. Ehrig S, Schamberger B, Bidan CM, West A, Jacobi C, Lam K, et al. Surface tension determines tissue shape and growth kinetics. *Sci Adv.* 2019;5(9):eaav9394.
67. Chocholata P, Kulda V, Babuska V. Fabrication of Scaffolds for Bone-Tissue Regeneration. *Materials.* 2019;12(4).
68. Macis M, Lugli F, Zerbetto F. Modeling Living Cells Response to Surface Tension and Chemical Patterns. *ACS Appl Mater Inter.* 2017;9(23):19552-61.
69. Tsuda A, Konduru NV. The role of natural processes and surface energy of inhaled engineered nanoparticles on aggregation and corona formation. *Nanoimpact.* 2016;2:38-44.
70. Ponsonnet L, Reybier K, Jaffrezic N, Comte V, Lagneau C, Lissac M, et al. Relationship between surface properties (roughness, wettability) of titanium and titanium alloys and cell behaviour. *Mat Sci Eng C-Bio S.* 2003;23(4):551-60.
71. Van Liedekerke P, Palm MM, Jagiella N, Drasdo D. Simulating tissue mechanics with agent-based models: concepts, perspectives and some novel results. *Comput Part Mech.* 2015;2(4):401-44.
72. Boccaccio A, Uva AE, Fiorentino M, Lamberti L, Monno G. A Mechanobiology-based Algorithm to Optimize the Microstructure Geometry of Bone Tissue Scaffolds. *Int J Biol Sci.* 2016;12(1):1-17.
73. da Cunha DALV, Neto PI, Micocci KC, Bellani CF, Selistre-de-Araujo HS, Silveira ZC, et al. Fabrication and Characterization of Scaffolds of Poly(epsilon-caprolactone)/Biosilicate (R) Biocomposites Prepared by Generative Manufacturing Process. *Int J Biomater.* 2019.
74. Parisi L, Toffoli A, Ghiacci G, Macaluso GM. Tailoring the Interface of Biomaterials to Design Effective Scaffolds. *J Funct Biomater.* 2018;9(3).
75. Kapat K, Srivas PK, Rameshbabu AP, Maity PP, Jana S, Dutta J, et al. Influence of Porosity and Pore-Size Distribution in Ti6Al4 V Foam on Physicomechanical

Properties, Osteogenesis, and Quantitative Validation of Bone Ingrowth by Micro-Computed Tomography. *Acs Appl Mater Inter.* 2017;9(45):39235-48.

76. Ferrari M, Cirisano F, Moran MC. Mammalian Cell Behavior on Hydrophobic Substrates: Influence of Surface Properties. *Colloid Interfac.* 2019;3(2).

77. Donnelly H, Salmeron-Sanchez M, Dalby MJ. Designing stem cell niches for differentiation and self-renewal. *J R Soc Interface.* 2018;15(145).

78. Sampath UGTM, Ching YC, Chuah CH, Sabariah JJ, Lin PC. Fabrication of Porous Materials from Natural/Synthetic Biopolymers and Their Composites. *Materials.* 2016;9(12).

79. Place TL, Domann FE, Case AJ. Limitations of oxygen delivery to cells in culture: An underappreciated problem in basic and translational research. *Free Radical Bio Med.* 2017;113:311-22.

80. Murphy CM, Haugh MG, O'Brien FJ. The effect of mean pore size on cell attachment, proliferation and migration in collagen-glycosaminoglycan scaffolds for bone tissue engineering. *Biomaterials.* 2010;31(3):461-6.

81. Persson M, Lehenkari PP, Berglin L, Turunen S, Finnila MAJ, Risteli J, et al. Osteogenic Differentiation of Human Mesenchymal Stem cells in a 3D Woven Scaffold. *Sci Rep-Uk.* 2018;8.

82. Liu J, Chen G, Xu H, Hu K, Sun JF, Liu M, et al. Pre-vascularization in fibrin Gel/PLGA microsphere scaffolds designed for bone regeneration. *Npg Asia Mater.* 2018;10:827-39.

83. Miculescu F, Maidaniuc A, Voicu SI, Thakur VK, Stan GE, Ciocan LT. Progress in Hydroxyapatite-Starch Based Sustainable Biomaterials for Biomedical Bone Substitution Applications. *Acs Sustain Chem Eng.* 2017;5(10):8491-512.

84. Nava MM, Draghi L, Giordano C, Pietrabissa R. The effect of scaffold pore size in cartilage tissue engineering. *J Appl Biomater Func.* 2016;14(3):E223-E9.

85. Morejon L, Delgado JA, Ribeiro AA, de Oliveira MV, Mendizabal E, Garcia I, et al. Development, Characterization and In Vitro Biological Properties of Scaffolds Fabricated From Calcium Phosphate Nanoparticles. *Int J Mol Sci.* 2019;20(7).
86. Diaz-Rodriguez P, Sanchez M, Landin M. Drug-Loaded Biomimetic Ceramics for Tissue Engineering. *Pharmaceutics.* 2018;10(4).
87. Chen XN, Fan HY, Deng XW, Wu LN, Yi T, Gu LX, et al. Scaffold Structural Microenvironmental Cues to Guide Tissue Regeneration in Bone Tissue Applications. *Nanomaterials-Basel.* 2018;8(11).
88. Gao CD, Peng SP, Feng P, Shuai CJ. Bone biomaterials and interactions with stem cells. *Bone Res.* 2017;5.
89. Sha JJ, Kanno T, Miyamoto K, Bai YP, Hideshima K, Matsuzaki Y. Application of a Bioactive/Bioresorbable Three-Dimensional Porous Uncalcined and Unsintered Hydroxyapatite/Poly-d/l-lactide Composite with Human Mesenchymal Stem Cells for Bone Regeneration in Maxillofacial Surgery: A Pilot Animal Study. *Materials.* 2019;12(5).
90. Li L, Li YX, Yang LF, Yu F, Zhang KJ, Jin J, et al. Polydopamine coating promotes early osteogenesis in 3D printing porous Ti6Al4V scaffolds. *Ann Transl Med.* 2019;7(11).
91. Roosa SMM, Kempainen JM, Moffitt EN, Krebsbach PH, Hollister SJ. The pore size of polycaprolactone scaffolds has limited influence on bone regeneration in an in vivo model. *J Biomed Mater Res A.* 2010;92a(1):359-68.
92. Lin SC, Lee YC, Yu G, Cheng CJ, Zhou X, Chu K, et al. Endothelial-to-Osteoblast Conversion Generates Osteoblastic Metastasis of Prostate Cancer. *Dev Cell.* 2017;41(5):467-+.

93. Cheng MQ, Wahafu TEHJ, Jiang GF, Liu W, Qiao YQ, Peng XC, et al. A novel open-porous magnesium scaffold with controllable microstructures and properties for bone regeneration. *Sci Rep-Uk*. 2016;6.
94. Karageorgiou V, Kaplan D. Porosity of 3D biomaterial scaffolds and osteogenesis. *Biomaterials*. 2005;26(27):5474-91.
95. Bianco S, Mancardi D, Merlino A, Bussolati B, Munaron L. Hypoxia and hydrogen sulfide differentially affect normal and tumor-derived vascular endothelium. *Redox Biol*. 2017;12:499-504.
96. Schafer M, Ewald N, Schafer C, Stapler A, Piper HM, Noll T. Signaling of hypoxia-induced autonomous proliferation of endothelial cells. *FASEB J*. 2003;17(3):449-51.
97. Mukherjee S, Darzi S, Paul K, Werkmeister JA, Gargett CE. Mesenchymal stem cell-based bioengineered constructs: foreign body response, cross-talk with macrophages and impact of biomaterial design strategies for pelvic floor disorders. *Interface Focus*. 2019;9(4).
98. Estermann SJ, Scheiner S. Multiscale Modeling Provides Differentiated Insights to Fluid Flow-Driven Stimulation of Bone Cellular Activities. *Front Phys*. 2018;6.
99. Di Luca A, Ostrowska B, Lorenzo-Moldero I, Lapedda A, Swieszkowski W, Van Blitterswijk C, et al. Gradients in pore size enhance the osteogenic differentiation of human mesenchymal stromal cells in three-dimensional scaffolds. *Sci Rep*. 2016;6:22898.
100. Boccaccio A, Uva AE, Fiorentino M, Mori G, Monno G. Geometry Design Optimization of Functionally Graded Scaffolds for Bone Tissue Engineering: A Mechanobiological Approach. *Plos One*. 2016;11(1).

101. Zaharin HA, Rani AMA, Azam FI, Ginta TL, Sallih N, Ahmad A, et al. Effect of Unit Cell Type and Pore Size on Porosity and Mechanical Behavior of Additively Manufactured Ti6Al4V Scaffolds. *Materials*. 2018;11(12).
102. Scaffaro R, Lopresti F, Botta L, Rigogliuso S, Ghersi G. Melt Processed PCL/PEG Scaffold With Discrete Pore Size Gradient for Selective Cellular Infiltration. *Macromol Mater Eng*. 2016;301(2):182-90.
103. Orciani M, Fini M, Di Primio R, Mattioli-Belmonte M. Biofabrication and Bone Tissue Regeneration: Cell Source, Approaches, and Challenges. *Front Bioeng Biotech*. 2017;5.
104. Egan PF. Integrated Design Approaches for 3D Printed Tissue Scaffolds: Review and Outlook. *Materials*. 2019;12(15).
105. Lo Re G, Lopresti F, Petrucci G, Scaffaro R. A facile method to determine pore size distribution in porous scaffold by using image processing. *Micron*. 2015;76:37-45.
106. Dorozhkin SV. Nanodimensional and Nanocrystalline Calcium Orthophosphates. *Developments and Applications of Calcium Phosphate Bone Cements*. 2018;9:355-448.
107. Wang QB, Wang QG, Wan CX. Preparation and evaluation of a biomimetic scaffold with porosity gradients in vitro. *An Acad Bras Cienc*. 2012;84(1):9-16.
108. Sobral JM, Caridade SG, Sousa RA, Mano JF, Reis RL. Three-dimensional plotted scaffolds with controlled pore size gradients: Effect of scaffold geometry on mechanical performance and cell seeding efficiency. *Acta Biomater*. 2011;7(3):1009-18.
109. Zhang JC, Wu LB, Jing DY, Ding JD. A comparative study of porous scaffolds with cubic and spherical macropores. *Polymer*. 2005;46(13):4979-85.
110. Baino F, Vitale-Brovarone C. Mechanical properties and reliability of glass-ceramic foam scaffolds for bone repair. *Mater Lett*. 2014;118:27-30.

111. Pina S, Ribeiro VP, Marques CF, Maia FR, Silva TH, Reis RL, et al. Scaffolding Strategies for Tissue Engineering and Regenerative Medicine Applications. *Materials*. 2019;12(11).
112. Ambu R, Morabito AE. Modeling, Assessment, and Design of Porous Cells Based on Schwartz Primitive Surface for Bone Scaffolds. *ScientificWorldJournal*. 2019;2019:7060847.
113. Nathan AS, Baker BM, Nerurkar NL, Mauck RL. Mechano-topographic modulation of stem cell nuclear shape on nanofibrous scaffolds. *Acta Biomaterialia*. 2011;7(1):57-66.
114. Bashirzadeh Y, Liu AP. Encapsulation of the cytoskeleton: towards mimicking the mechanics of a cell. *Soft Matter*. 2019.
115. Bianchi M, Edreira ERU, Wolke JGC, Birgani ZT, Habibovic P, Jansen JA, et al. Substrate geometry directs the in vitro mineralization of calcium phosphate ceramics. *Acta Biomaterialia*. 2014;10(2):661-9.
116. Moss J, Gebara E, Bushong EA, Sanchez-Pascual I, O'Laoi R, El M'Ghari I, et al. Fine processes of Nestin-GFP-positive radial glia-like stem cells in the adult dentate gyrus ensheath the local synapses and vasculature. *P Natl Acad Sci USA*. 2016;113(18):E2536-E45.
117. Pieuchot L, Marteau J, Guignandon A, Dos Santos T, Brigaud I, Chauvy PF, et al. Curvotaxis directs cell migration through cell-scale curvature landscapes. *Nat Commun*. 2018;9.
118. Zhang YY, Xing YH, Li J, Zhang ZQ, Luan HQ, Chu ZW, et al. Osteogenesis-Related Behavior of MC3T3-E1 Cells on Substrates with Tunable Stiffness. *Biomed Res Int*. 2018.
119. Zhang T, Lin SY, Shao XR, Zhang Q, Xue CY, Zhang S, et al. Effect of matrix stiffness on osteoblast functionalization. *Cell Proliferat*. 2017;50(3).

120. Engler AJ, Sen S, Sweeney HL, Discher DE. Matrix elasticity directs stem cell lineage specification. *Cell*. 2006;126(4):677-89.
121. Boccaccio A, Uva AE, Fiorentino M, Monno G, Ballini A, Desiate A. Optimal Load for Bone Tissue Scaffolds with an Assigned Geometry. *Int J Med Sci*. 2018;15(1):16-22.
122. Xu MC, Zhai D, Chang J, Wu CT. In vitro assessment of three-dimensionally plotted nagelschmidite bioceramic scaffolds with varied macropore morphologies. *Acta Biomaterialia*. 2014;10(1):463-76.
123. Yilgor P, Sousa RA, Reis RL, Hasirci N, Hasirci V. 3D plotted PCL scaffolds for stem cell based bone tissue engineering. *Macromol Symp*. 2008;269:92-9.
124. Yeo M, Simon CG, Kim G. Effects of offset values of solid freeform fabricated PCL-beta-TCP scaffolds on mechanical properties and cellular activities in bone tissue regeneration. *J Mater Chem*. 2012;22(40):21636-46.
125. Dang M, Saunders L, Niu XF, Fan YB, Ma PX. Biomimetic delivery of signals for bone tissue engineering. *Bone Res*. 2018;6.
126. De Witte TM, Fratila-Apachitei LE, Zadpoor AA, Peppas NA. Bone tissue engineering via growth factor delivery: from scaffolds to complex matrices. *Regen Biomater*. 2018;5(4):197-211.
127. Castejon P, Habibi K, Saffar A, Ajji A, Martinez AB, Arencon D. Polypropylene-Based Porous Membranes: Influence of Polymer Composition, Extrusion Draw Ratio and Uniaxial Strain. *Polymers-Basel*. 2018;10(1).
128. Turnbull G, Clarke J, Picard F, Riches P, Jia LL, Han FX, et al. 3D bioactive composite scaffolds for bone tissue engineering. *Bioact Mater*. 2018;3(3):278-314.
129. Sivanapillai R, Steeb H. Fluid Interfaces during Viscous-Dominated Primary Drainage in 2D Micromodels Using Pore-Scale SPH Simulations. *Geofluids*. 2018.

130. Maity D, Li YZ, Chen Y, Sun SX. Response of collagen matrices under pressure and hydraulic resistance in hydrogels. *Soft Matter*. 2019;15(12):2617-26.
131. Offeddu GS, Ashworth JC, Cameron RE, Oyen ML. Structural determinants of hydration, mechanics and fluid flow in freeze-dried collagen scaffolds. *Acta Biomater*. 2016;41:193-203.
132. Li J, Chen DS, Luan HQ, Zhang YY, Fan YB. Numerical Evaluation and Prediction of Porous Implant Design and Flow Performance. *Biomed Res Int*. 2018.
133. Mitsak AG, Kempainen JM, Harris MT, Hollister SJ. Effect of Polycaprolactone Scaffold Permeability on Bone Regeneration In Vivo. *Tissue Eng Pt A*. 2011;17(13-14):1831-9.
134. O'Brien FJ, Harley BA, Waller MA, Yannas IV, Gibson LJ, Prendergast PJ. The effect of pore size on permeability and cell attachment in collagen scaffolds for tissue engineering. *Technol Health Care*. 2007;15(1):3-17.
135. Egan PF, Gonella VC, Engelsperger M, Ferguson SJ, Shea K. Computationally designed lattices with tuned properties for tissue engineering using 3D printing. *Plos One*. 2017;12(8).
136. Wang ZM, Wang ZF, Lu WW, Zhen WX, Yang DZ, Peng SL. Novel biomaterial strategies for controlled growth factor delivery for biomedical applications. *Npg Asia Mater*. 2017;9.
137. Wysocki B, Idaszek J, Szlajak K, Strzelczyk K, Brynk T, Kurzydowski KJ, et al. Post Processing and Biological Evaluation of the Titanium Scaffolds for Bone Tissue Engineering. *Materials*. 2016;9(3).
138. Kang YQ, Chang J. Channels in a porous scaffold: a new player for vascularization. *Regen Med*. 2018;13(6):704-15.

139. Ran QC, Yang WH, Hu Y, She XK, Yu YL, Xiang Y, et al. Osteogenesis of 3D printed porous Ti6Al4V implants with different pore sizes. *J Mech Behav Biomed.* 2018;84:1-11.
140. Melchels FPW, Barradas AMC, van Blitterswijk CA, de Boer J, Feijen J, Grijpma DW. Effects of the architecture of tissue engineering scaffolds on cell seeding and culturing. *Acta Biomaterialia.* 2010;6(11):4208-17.
141. Lin TH, Wang HC, Cheng WH, Hsu HC, Yeh ML. Osteochondral Tissue Regeneration Using a Tyramine-Modified Bilayered PLGA Scaffold Combined with Articular Chondrocytes in a Porcine Model. *Int J Mol Sci.* 2019;20(2).
142. Cunniffe GM, Diaz-Payno PJ, Sheehy EJ, Critchley SE, Almeida HV, Pitacco P, et al. Tissue-specific extracellular matrix scaffolds for the regeneration of spatially complex musculoskeletal tissues. *Biomaterials.* 2019;188:63-73.
143. Li HY, Chang J. Stimulation of proangiogenesis by calcium silicate bioactive ceramic. *Acta Biomaterialia.* 2013;9(2):5379-89.
144. Hoppe A, Guldal NS, Boccaccini AR. A review of the biological response to ionic dissolution products from bioactive glasses and glass-ceramics. *Biomaterials.* 2011;32(11):2757-74.
145. Tomasina C, Bodet T, Mota C, Moroni L, Camarero-Espinosa S. Bioprinting Vasculature: Materials, Cells and Emergent Techniques. *Materials.* 2019;12(17).
146. Filipowska J, Tomaszewski KA, Niedzwiedzki L, Walocha J, Niedzwiedzki T. The role of vasculature in bone development, regeneration and proper systemic functioning. *Angiogenesis.* 2017;20(3):291-302.
147. Piroso A, Gottardi R, Alexander PG, Tuan RS. Engineering in-vitro stem cell-based vascularized bone models for drug screening and predictive toxicology. *Stem Cell Research & Therapy.* 2018;9.

148. Liu YC, Chan JKY, Teoh SH. Review of vascularised bone tissue-engineering strategies with a focus on co-culture systems. *J Tissue Eng Regen M.* 2015;9(2):85-105.
149. Sivaraj KK, Adams RH. Blood vessel formation and function in bone. *Development.* 2016;143(15):2706-15.
150. Su PH, Tian Y, Yang CF, Ma XL, Wang X, Pei JW, et al. Mesenchymal Stem Cell Migration during Bone Formation and Bone Diseases Therapy. *Int J Mol Sci.* 2018;19(8).
151. Breeland G, Menezes RG. Embryology, Bone Ossification. StatPearls. Treasure Island (FL)2019.
152. Germain S, Monnot C, Muller L, Eichmann A. Hypoxia-driven angiogenesis: role of tip cells and extracellular matrix scaffolding. *Curr Opin Hematol.* 2010;17(3):245-51.
153. Zhu HJ, Zhang SL. Hypoxia inducible factor-1/vascular endothelial growth factor signaling activation correlates with response to radiotherapy and its inhibition reduces hypoxia-induced angiogenesis in lung cancer. *J Cell Biochem.* 2018;119(9):7707-18.
154. Hu K, Olsen BR. Vascular endothelial growth factor control mechanisms in skeletal growth and repair. *Dev Dynam.* 2017;246(4):227-34.
155. Jain RK, Au P, Tam J, Duda DG, Fukumura D. Engineering vascularized tissue. *Nat Biotechnol.* 2005;23(7):821-3.
156. Amini AR, Xu TO, Chidambaram RM, Nukavarapu SP. Oxygen Tension-Controlled Matrices with Osteogenic and Vasculogenic Cells for Vascularized Bone Regeneration In Vivo. *Tissue Eng Pt A.* 2016;22(7-8):610-20.
157. Lei D, Yang Y, Liu ZH, Yang BQ, Gong WH, Chen S, et al. 3D printing of biomimetic vasculature for tissue regeneration. *Mater Horiz.* 2019;6(6):1197-206.
158. Dew L, English WR, Chong CK, MacNeil S. Investigating Neovascularization in Rat Decellularized Intestine: An In Vitro Platform for Studying Angiogenesis. *Tissue Eng Pt A.* 2016;22(23-24):1317-26.

159. Avolio E, Alvino VV, Ghorbel MT, Campagnolo P. Perivascular cells and tissue engineering: Current applications and untapped potential. *Pharmacol Therapeut.* 2017;171:83-92.
160. Kneser U, Polykandriotis E, Ohnolz J, Heidner K, Grabinger L, Euler S, et al. Engineering of vascularized transplantable bone tissues: Induction of axial vascularization in an osteoconductive matrix using an arteriovenous loop. *Tissue Eng.* 2006;12(7):1721-31.
161. Warnke PH, Springer ING, Wiltfang J, Acil Y, Eufinger H, Wehmoller M, et al. Growth and transplantation of a custom vascularised bone graft in a man. *Lancet.* 2004;364(9436):766-70.
162. Inomata K, Honda M. Co-Culture of Osteoblasts and Endothelial Cells on a Microfiber Scaffold to Construct Bone-Like Tissue with Vascular Networks. *Materials (Basel).* 2019;12(18).
163. Sarker MD, Naghieh S, Sharma NK, Chen XB. 3D biofabrication of vascular networks for tissue regeneration: A report on recent advances. *J Pharm Anal.* 2018;8(5):277-96.
164. Inglis S, Christensen D, Wilson DI, Kanczler JM, Oreffo ROC. Human endothelial and foetal femur-derived stem cell co-cultures modulate osteogenesis and angiogenesis. *Stem Cell Res Ther.* 2016;7.
165. Mitchell GM, Morrison WA. In Vivo Vascularization for Large-Volume Soft Tissue Engineering. *Vascularization: Regenerative Medicine and Tissue Engineering.* 2015:343-62.
166. Sarker MD, Naghieh S, Sharma NK, Ning LQ, Chen XB. Bioprinting of Vascularized Tissue Scaffolds: Influence of Biopolymer, Cells, Growth Factors, and Gene Delivery. *J Healthc Eng.* 2019.

167. Anghelescu VM, Neculae I, Dinca O, Vladan C, Socoliuc C, Cioplea M, et al. Inflammatory-Driven Angiogenesis in Bone Augmentation with Bovine Hydroxyapatite, B-Tricalcium Phosphate, and Bioglasses: A Comparative Study. *J Immunol Res*. 2018.
168. Eckardt H, Ding M, Lind M, Hansen ES, Christensen KS, Hvid I. Recombinant human vascular endothelial growth factor enhances bone healing in an experimental nonunion model. *J Bone Joint Surg Br*. 2005;87b(10):1434-8.
169. Phillips MD, Kuznetsov SA, Cherman N, Park K, Chen KG, McClendon BN, et al. Directed Differentiation of Human Induced Pluripotent Stem Cells Toward Bone and Cartilage: In Vitro Versus In Vivo Assays. *Stem Cell Transl Med*. 2014;3(7):867-78.
170. Jin K, Li B, Lou LX, Xu YF, Ye X, Yao K, et al. In vivo vascularization of MSC-loaded porous hydroxyapatite constructs coated with VEGF-functionalized collagen/heparin multilayers. *Sci Rep-Uk*. 2016;6.
171. Li B, Wang H, Qiu GX, Su XL, Wu ZH. Synergistic Effects of Vascular Endothelial Growth Factor on Bone Morphogenetic Proteins Induced Bone Formation In Vivo: Influencing Factors and Future Research Directions. *Biomed Res Int*. 2016.
172. van Esterik FAS, Zandieh-Doulabi B, Kleverlaan CJ, Klein-Nulend J. Enhanced Osteogenic and Vasculogenic Differentiation Potential of Human Adipose Stem Cells on Biphasic Calcium Phosphate Scaffolds in Fibrin Gels. *Stem Cells Int*. 2016.
173. Kant RJ, Coulombe KKK. Integrated approaches to spatiotemporally directing angiogenesis in host and engineered tissues. *Acta Biomater*. 2018;69:42-62.
174. Saberianpour S, Heidarzadeh M, Geranmayeh MH, Hosseinkhani H, Rahbarghazi R, Nouri M. Tissue engineering strategies for the induction of angiogenesis using biomaterials. *J Biol Eng*. 2018;12.
175. Moulisova V, Gonzalez-Garcia C, Cantini M, Rodrigo-Navarro A, Weaver J, Costell M, et al. Engineered microenvironments for synergistic VEGF - Integrin signalling during vascularization. *Biomaterials*. 2017;126:61-74.

176. Jiang J, Wang SH, Chai F, Ai CC, Chen SY. The study on vascularisation and osteogenesis of BMP/VEGF co-modified tissue engineering bone in vivo. *Rsc Adv.* 2016;6(48):41800-8.
177. Sweeney M, Foldes G. Takes Two: Endothelial-Perivascular Cell Cross-Talk in Vascular Development and Disease. *Front Cardiovasc Med.* 2018;5.
178. Kook YM, Jeong Y, Lee K, Koh WG. Design of biomimetic cellular scaffolds for co-culture system and their application. *J Tissue Eng.* 2017;8.
179. Richardson TP, Peters MC, Ennett AB, Mooney DJ. Polymeric system for dual growth factor delivery. *Nat Biotechnol.* 2001;19(11):1029-34.
180. Jafarkhani M, Salehi Z, Shokrgozar MA, Mashayekhan S. An optimized procedure to develop a 3-dimensional microfluidic hydrogel with parallel transport networks. *Int J Numer Meth Bio.* 2019;35(1).
181. Freeman FE, Kelly DJ. Tuning Alginate Bioink Stiffness and Composition for Controlled Growth Factor Delivery and to Spatially Direct MSC Fate within Bioprinted Tissues. *Sci Rep.* 2017;7(1):17042.
182. Liu X, Chen WC, Zhang C, Thein-Han W, Hu KV, Reynolds MA, et al. Co-Seeding Human Endothelial Cells with Human-Induced Pluripotent Stem Cell-Derived Mesenchymal Stem Cells on Calcium Phosphate Scaffold Enhances Osteogenesis and Vascularization in Rats. *Tissue Eng Pt A.* 2017;23(11-12):546-55.
183. Zhang W, Zhang K, Li G, Yan S, Cui L, Yin J. Effects of large dimensional deformation of a porous structure on stem cell fate activated by poly(l-glutamic acid)-based shape memory scaffolds. *Biomater Sci.* 2018;6(10):2738-49.
184. Neto AS, Ferreira JMF. Synthetic and Marine-Derived Porous Scaffolds for Bone Tissue Engineering. *Materials.* 2018;11(9).

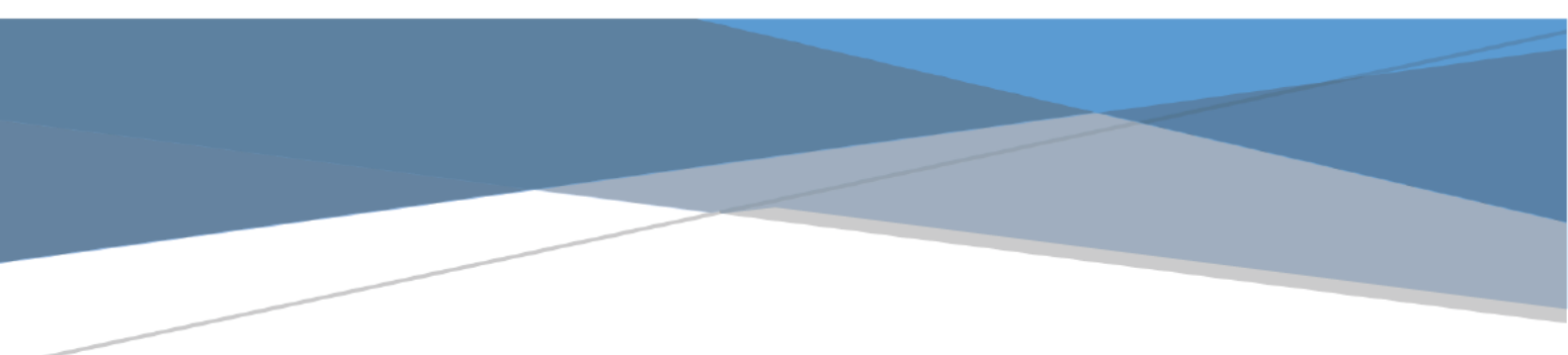
185. Tang D, Tare RS, Yang LY, Williams DF, Ou KL, Oreffo RO. Biofabrication of bone tissue: approaches, challenges and translation for bone regeneration. *Biomaterials*. 2016;83:363-82.
186. Yamakawa S, Hayashida K. Advances in surgical applications of growth factors for wound healing. *Burns & Trauma*. 2019;7.
187. Zhou JH, Zhao LZ. Hypoxia-mimicking Co doped TiO₂ microporous coating on titanium with enhanced angiogenic and osteogenic activities. *Acta Biomater*. 2016;43:358-68.
188. Zhao F, Yin YJ, Lu WW, Leong JC, Zhang WJ, Zhang JY, et al. Preparation and histological evaluation of biomimetic three-dimensional hydroxyapatite/chitosan-gelatin network composite scaffolds. *Biomaterials*. 2002;23(15):3227-34.
189. Porzionato A, Stocco E, Barbon S, Grandi F, Macchi V, De Caro R. Tissue-Engineered Grafts from Human Decellularized Extracellular Matrices: A Systematic Review and Future Perspectives. *Int J Mol Sci*. 2018;19(12).
190. Reed S, Lau G, Delattre B, Lopez DD, Tomsia AP, Wu BM. Macro- and micro-designed chitosan-alginate scaffold architecture by three-dimensional printing and directional freezing. *Biofabrication*. 2016;8(1).
191. Ho MH, Kuo PY, Hsieh HJ, Hsien TY, Hou LT, Lai JY, et al. Preparation of porous scaffolds by using freeze-extraction and freeze-gelation methods. *Biomaterials*. 2004;25(1):129-38.
192. Miller R, Loglio G, Tesei U, Neumann AW. Dynamics of adsorption layers at the liquid-fluid interface. *Prog Coll Pol Sci S*. 1993;93:319-.
193. Hollister SJ. Porous scaffold design for tissue engineering. *Nat Mater*. 2005;4(7):518-24.

194. Afghah F, Dikyol C, Altunbek M, Koc B. Biomimicry in Bio-Manufacturing: Developments in Melt Electrospinning Writing Technology Towards Hybrid Biomanufacturing. *Appl Sci-Basel*. 2019;9(17).
195. Sengers BG, Please CP, Taylor M, Oreffo ROC. Experimental-Computational Evaluation of Human Bone Marrow Stromal Cell Spreading on Trabecular Bone Structures. *Annals of Biomedical Engineering*. 2009;37(6):1165-76.
196. Liu MY, Lv YG. Reconstructing Bone with Natural Bone Graft: A Review of In Vivo Studies in Bone Defect Animal Model. *Nanomaterials-Basel*. 2018;8(12).
197. Maisani M, Pezzoli D, Chassande O, Mantovani D. Cellularizing hydrogel-based scaffolds to repair bone tissue: How to create a physiologically relevant micro-environment? *J Tissue Eng*. 2017;8.
198. Gaharwar AK, Cross LM, Peak CW, Gold K, Carrow JK, Brokesh A, et al. 2D Nanoclay for Biomedical Applications: Regenerative Medicine, Therapeutic Delivery, and Additive Manufacturing. *Adv Mater*. 2019;31(23):e1900332.
199. Serra T, Planell JA, Navarro M. High-resolution PLA-based composite scaffolds via 3-D printing technology. *Acta Biomater*. 2013;9(3):5521-30.
200. Ma PX, Choi JW. Biodegradable polymer scaffolds with well-defined interconnected spherical pore network. *Tissue Eng*. 2001;7(1):23-33.
201. Xiong QR, Baychev TG, Jivkov AP. Review of pore network modelling of porous media: Experimental characterisations, network constructions and applications to reactive transport. *J Contam Hydrol*. 2016;192:101-17.
202. Zhao S, Zhao JX, Han GZ. Advances in the study of mechanical properties and constitutive law in the field of wood research. *Iop Conf Ser-Mat Sci*. 2016;137.
203. Yuan JY, Chen XD, Shen N, Fan X, Lu J. Experimental study on the pore structure variation of self-compacting rubberised concrete under fatigue load. *Road Mater Pavement*. 2019.

204. Velasco MA, Lancheros Y, Garzon-Alvarado DA. Geometric and mechanical properties evaluation of scaffolds for bone tissue applications designing by a reaction-diffusion models and manufactured with a material jetting system. *J Comput Des Eng.* 2016;3(4):385-97.
205. Arora A, Kothari A, Katti DS. Pore orientation mediated control of mechanical behavior of scaffolds and its application in cartilage-mimetic scaffold design. *J Mech Behav Biomed Mater.* 2015;51:169-83.
206. Liu D, Savija B, Smith GE, Flewitt PEJ, Lowe T, Schlangen E. Towards understanding the influence of porosity on mechanical and fracture behaviour of quasi-brittle materials: experiments and modelling. *Int J Fracture.* 2017;205(1):57-72.
207. Morgan EF, Unnikrisnan GU, Hussein AI. Bone Mechanical Properties in Healthy and Diseased States. *Annu Rev Biomed Eng.* 2018;20:119-43.
208. Eliaz N, Metoki N. Calcium Phosphate Bioceramics: A Review of Their History, Structure, Properties, Coating Technologies and Biomedical Applications. *Materials.* 2017;10(4).
209. Sozen T, Ozisik L, Basaran NC. An overview and management of osteoporosis. *Eur J Rheumatol.* 2017;4(1):46-56.
210. Sottile J, Shi F, Rublyevska I, Chiang HY, Lust J, Chandler J. Fibronectin-dependent collagen I deposition modulates the cell response to fibronectin. *Am J Physiol-Cell Ph.* 2007;293(6):C1934-C46.
211. Setiawati R, Utomo DN, Rantam FA, Ifran NN, Budhiparama NC. Early Graft Tunnel Healing After Anterior Cruciate Ligament Reconstruction With Intratunnel Injection of Bone Marrow Mesenchymal Stem Cells and Vascular Endothelial Growth Factor. *Orthopaedic Journal of Sports Medicine.* 2017;5(6).

212. Moreira CA, Dempster DW, Baron R. Anatomy and Ultrastructure of Bone - Histogenesis, Growth and Remodeling. In: Feingold KR, Anawalt B, Boyce A, Chrousos G, Dungan K, Grossman A, et al., editors. Endotext. South Dartmouth (MA)2000.
213. Shi F, Harman J, Fujiwara K, Sottile J. Collagen I matrix turnover is regulated by fibronectin polymerization. *Am J Physiol-Cell Ph.* 2010;298(5):C1265-C75.
214. Discher DE, Janmey P, Wang YL. Tissue cells feel and respond to the stiffness of their substrate. *Science.* 2005;310(5751):1139-43.
215. Lozinsky VI. Cryogels on the basis of natural and synthetic polymers: Preparation, properties and application. *Usp Khim+.* 2002;71(6):559-85.
216. Bigi A, Boanini E. Functionalized biomimetic calcium phosphates for bone tissue repair. *J Appl Biomater Func.* 2017;15(4):E313-E25.
217. Yang Y, Wang K, Gu XS, Leong KW. Biophysical Regulation of Cell Behavior- Cross Talk between Substrate Stiffness and Nanotopography. *Engineering.* 2017;3(1):36-54.
218. Hung BP, Hutton DL, Grayson WL. Mechanical control of tissue-engineered bone. *Stem Cell Res Ther.* 2013;4.
219. Gharibi B, Cama G, Capurro M, Thompson I, Deb S, Di Silvio L, et al. Gene Expression Responses to Mechanical Stimulation of Mesenchymal Stem Cells Seeded on Calcium Phosphate Cement. *Tissue Eng Pt A.* 2013;19(21-22):2426-38.
220. Kim TR, Kim MS, Goh TS, Lee JS, Kim YH, Yoon SY, et al. Evaluation of Structural and Mechanical Properties of Porous Artificial Bone Scaffolds Fabricated via Advanced TBA-Based Freeze-Gel Casting Technique. *Appl Sci-Basel.* 2019;9(9).
221. Vetric M, Parizek M, Hadraba D, Kukackova O, Brus J, Hlidkova H, et al. Porous Heat-Treated Polyacrylonitrile Scaffolds for Bone Tissue Engineering. *Acs Appl Mater Inter.* 2018;10(10):8496-506.

222. Lee JS, Cha HD, Shim JH, Jung JW, Kim JY, Cho DW. Effect of pore architecture and stacking direction on mechanical properties of solid freeform fabrication-based scaffold for bone tissue engineering. *J Biomed Mater Res A*. 2012;100(7):1846-53.
223. Guo ZQ, Yang C, Zhou ZP, Chen S, Li F. Characterization of biodegradable poly(lactic acid) porous scaffolds prepared using selective enzymatic degradation for tissue engineering. *Rsc Adv*. 2017;7(54):34063-70.
224. Qin L, Zhai C, Liu SM, Xu JZ. Factors controlling the mechanical properties degradation and permeability of coal subjected to liquid nitrogen freeze-thaw. *Sci Rep-Uk*. 2017;7.
225. Wu LB, Ding JD. Effects of porosity and pore size on in vitro degradation of three-dimensional porous poly(D,L-lactide-co-glycolide) scaffolds for tissue engineering. *J Biomed Mater Res A*. 2005;75a(4):767-77.
226. Odelius K, Hoglund A, Kumar S, Hakkarainen M, Ghosh AK, Bhatnagar N, et al. Porosity and Pore Size Regulate the Degradation Product Profile of Polylactide. *Biomacromolecules*. 2011;12(4):1250-8.
227. Diaz E, Puerto I, Ribeiro S, Lanceros-Mendez S, Barandiaran JM. The Influence of Copolymer Composition on PLGA/nHA Scaffolds' Cytotoxicity and In Vitro Degradation. *Nanomaterials-Basel*. 2017;7(7).
228. Zhu DY, Handschuh-Wang S, Zhou XC. Recent progress in fabrication and application of polydimethylsiloxane sponges. *J Mater Chem A*. 2017;5(32):16467-97.



CHAPTER 2

THE CALCIUM PHOSPHATE STABILITY ON MELT ELECTROWRITTEN (MEW) PCL SCAFFOLD

STATEMENT OF CONTRIBUTION TO CO-AUTHORED PUBLISHED PAPER

This chapter includes a **published** co-authored paper. The bibliographic details of the co-authored paper, including all authors, are:

Naghmeh Abbasi, Stephen Hamlet, Van Thanh Dau, Nam-Trung Nguyen. Calcium phosphate stability on melt electrowritten PCL scaffold. Journal of Science: Advanced Materials and Devices, 2020 January,
<https://doi.org/10.1016/j.jsamd.2020.01.001> (IF: 3.357)

My contribution to the paper involved:

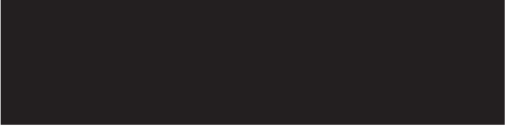
Designing of the project, provision of the data, the preliminary analysis and categorisation of the data into a usable format and providing direction on the scope and structure of the analysis, interpretation of results and drafting of paper.


_____ Date 10-Dec-2019

Naghmeh Abbasi


_____ Date 10-Dec-2019

Corresponding author of paper: Prof. Nam-Trung Nguyen


_____ Date 10-Dec-2019

Supervisor: Dr. Stephen Hamlet

ABSTRACT

CaP coating on melt electrowritten (MEW) substrates demonstrated itself as a potential candidate for bone regeneration due to mimick the natural bone tissue. It increased the osteoblast cells - implanted scaffolds interactions and improved bone ingrowth. This study aims to evaluate the stability and structural properties of CaP coating on melt electrowritten PCL scaffolds following pre-treatments of Ar- O₂ plasma and NaOH solution to improve the wettability.

The plasma-treated fibers were uniformly coated after one hour. The surface wettability enhanced through the mineralization of both plasma and NaOH pre-treated scaffolds. Mechanical properties of the scaffolds degraded through the plasma and NaOH treatment. However, tensile stability was improved following mineralization in plasma-treated scaffolds due to the smaller crystal size and a dense CaP layer, which leads to the higher solubility. The plasma pre-treated mineralized surface is stable enough to be potentially useful for the further development of bone regeneration.

INTRODUCTION

Two major performance indicators of the bone structure are its metabolic and mechanical functions. The bone metabolic function is determined by the availability of calcium and phosphate (1). A major part of bone tissue constitutes the crystalline form of calcium carbonate, HAP and CaP (2). Using the CaP coated scaffold has advantages of accelerating the bone reconstruction due to the strong bond between the bone and the coated implant. Implant surface with high roughness enhances the contact between the implant to the bone tissue and the subsequent bone connection (3). CaP has been demonstrated to affect the osteoinductivity and osteoconductivity of cells during the differentiation process towards bone lineage (4-6). The remodeling process of the hard tissue is directed by the protein adsorption via the extracellular matrix (ECM) and cell interactions which are influenced by the surface charge and chemistry of the implanted materials (7). Direct binding of bone cells to the implanted bone-like mineral surface stimulated significant bone growth and vascularization, also enclosed by the connective tissue (8, 9). Nandakuma et al. were able to improve the the bioactivity of the polymer successfully during *in vivo* bone regeneration by coating the electrospun poly(ethylene oxide terephthalate)–poly(buthylene terephthalate) (PEOT/PBT) scaffold with CaP (10). . Bone calcification and maturation can be stimulated by releasing calcium ions (11). The delivery of calcium and phosphorus ions adjusts the ion concentration and the local pH of the treating environment, which determines the protein adhesion and subsequent attachment of the osteoblast and its activation that have impact on the bone regeneration (12-14).

Crystal structure, surface area and the particle size of CaP, as well as the temperature, acidity and the fluid movement, can change the dissolution process (5, 15).

Besides, the increase of the pore size and pore number of CaP will enhance the body fluid convection because of the better contact between the surface area and the body fluids (16-18). On the other hand, the greater porosity resulted in poor mechanical properties and CaP displayed a weak load-bearing (19, 20).

PCL is a great candidate to use in bone tissue engineering applications (21). PCL polyester particularly in fibre form displayed hydrophobic surface properties, that reduced the cell adherence to the polymer surface (22). Surface activation and the substrate pre-treatment specifies the rate of coating formation (23). Various surface modifications were applied to obtain a suitable CaP deposition (24), such as O₂ plasma treatment (25), chemical treatment like tetrafluoromethane (CF₄), and sulphur hexafluoride (SF₆) (26), film deposition (27), thermal and lipase dependent surface modifications (28) and etching in alkaline and acidic solutions (29).

It has been shown that the NaOH and Ar-O₂ plasma treatment as the pre-treatment of surface activation improve the hydrophilicity of the scaffold by increasing the surface area. The treated scaffolds were dipped into simulated body fluid (SBF) at different time points. Ar plasma is preferred for surface cleaning in contrast to O₂ plasma because of minimum oxidative groups, less impact on the main material properties and removing the surface contamination by physical etching of ion emission (30). However, the composition of Ar-O₂ plasma mixture was found to be more efficient to eliminate the microorganisms and increase of sample roughness than Ar exclusively (31). Therefore, we selected Ar-O₂ plasma treatment for this study to create a more coarse surface as the adsorption of CaP is enhanced when the roughness increases (32).

The process of plasma spraying and etching by NaOH can alter the material properties before the immersion in SBF. In previous study, electrospun poly lactic-glycolic acid (PLGA) scaffolds were coated by bonelike CaP following surface modification with gelatin to produce positively charged groups before deposition into

SBF (33). Also, Zviagin1 et al, evaluated the improvement of CaP coating process by deposition of the electrospun PCL, poly(3-hydroxybutyrate) (PHB) and polyaniline (PANi) polymers scaffold into ethanol before soaking in the calcium solution (34).

Although the electrospun scaffolds were tested for wettability improvement by CaP coating, no study is available for MEW scaffolds to compare the solubility and the stability characteristics of the CaP following plasma and NaOH pre-treatment. Accordingly, the purpose of this study is to characterize the CaP properties and comparative effect of NaOH and Ar-O₂ plasma pre-treatment on the coated MEW PCL scaffold. As CaP stability is important to be controlled during bone remodeling and the desirable CaP properties need to be selected to be compatible with the appropriate applications.

MATERIALS AND METHODS

Melt Electrowriting (MEW)

The MEW printer used in this study contained a high voltage source (DX250R, EMCO, Hallein, Austria) controlled by a voltage divider (Digit Multimeter 2100, Keithley, Cleveland, USA), a pneumatically regulated melt feeding system (regulator, FESTO, Berkheim, Germany) and a planar movable aluminium collector plate (XSlide, Velmex, New York, USA) controlled by G-code (MACH 3 Computerized Numerical Control (CNC) software, ARTSOFT, Livermore Falls, USA). A proportional-integral-derivative controller was used to regulate the electrical heating system (TR400, Delta-t, Bielefeld, Germany) to assure a stable melt temperature profile.

An amount of 2.0 g of medical-grade 80 kDa PCL pellets (Corbion, Australia) was placed in a 2-ml syringe with a 21G nozzle, and heated to 80°C for 30 min to melt the PCL before insertion into the MEW heated head. The feed rate was 20 mL/h, which was controlled via compressed air. A threshold voltage between 5 and 7 kV was applied to create the charged polymer and to form a Taylor cone. The X-Y movement of the

collector platform was controlled using programmable software (G-code) that shapes the deposited polymer fibres in the desired pattern. The homogeneous pore size of 250 μm was designed and printed for this study.

Optimization of CaP Coating Process

The samples were cut into the dimension of 2 cm \times 2 cm and divided into five groups. All groups were placed in ethanol for 15 min under a vacuum to remove any residuals. The first group was not treated and considered as the control group (nC). The second group was immersed in pre-warmed 2 M NaOH at 37 $^{\circ}\text{C}$ for 30 min then washed 5 times with Milli Q water until the pH was neutralized (Na-nC). The third group was treated by Ar and O₂ radio frequency plasma cleaner (PDC-002-HP, Harrick Plasma, USA). Plasma discharge was used for the specimens with the setting of medium frequency power (10.15 W) for 7 minutes each side of the sample under the vacuum condition (Plas-nC). The fourth and fifth groups were treated by the separate NaOH and plasma consequently for etching the surface of the scaffold as explained above and then immersed into SBF10 solution used from Kokubo et al.'s protocol (Table 2.1) (35) at 37 $^{\circ}\text{C}$ for 0.5, 1, 3 and 6 hours (Na-C and Plas-C respectively). The SBF was replaced every 30 min. After washing the scaffolds in Milli Q water, they were immersed in 0.5 M NaOH at 37 $^{\circ}\text{C}$ for 30 min. Finally, the scaffolds were rinsed with distilled water then collected for freeze drying overnight.

Table 2.1. Nominal Ion Concentrations of SBF.

Reagent	Order	Amount (g)
		SBF 10
NaCl	1	58.430
KCl	2	0.373
CaCl ₂ .2H ₂ O	3	3.675
MgCl ₂ .6H ₂ O	4	1.016
Na ₂ HPO ₄	5	1.420
K ₂ HPO ₄	6	-
NaHCO ₃	7	Until pH=6

Morphological Characterization

To characterize the surface morphology of the MEW scaffolds, the samples were coated with gold and examined with Jeol JCM-5000 SEM at 15 kV accelerating voltage.

Energy Dispersive Spectrometry (EDS)

The element analysis was characterized with a JSM-7800 scanning electron microscope (Japan), equipped with INCA energy dispersive X-ray instrument mounted on the SEM. The scaffolds were cut by tissue biopsy puncher (kai Europe GmbH, Solingen, Germany) in 6-mm discs. The samples were coated by gold sputter and examined at 10 kV.

Contact Angle

A water contact angle test was accomplished using a FTA200 Contact Angle and Surface Tension instrument (Poly-Instruments Pty. Ltd., Australia). Three different locations of the sample were selected for the measurement of the angle between the surface and a liquid droplet (setting pump speed at 2 μ l/sec, needle diameter of 0.279 mm, water droplet diameter of 1.0 mm) using a lens mounted on a 3 viewing stage and the connected CCD video camera to capture the samples in real time and saved the images for further analysis.

Mechanical Characterization

To assess the influence of CaP particles, tensile strength tests were performed on all five groups of coated and non-coated PCL scaffolds using an electromechanical MicroTester machine (Instron 5848, Norwood, Ma) with 500 N load cell and a gauge length of 15 mm. The samples with 1-mm thickness were prepared in a rectangular shape and the dimensions of 45×10 mm and stretched at a speed rate of 15 mm/min until the break of the specimen. The slope of each stress-strain curve was analysed by average results of 5 samples in each group.

X-Ray Diffraction (XRD)

X-ray diffraction of the CaP-coated scaffold was recorded using a Cu-K α_1 source, $\lambda=1.5406 \text{ \AA}$ diffractometer (RigakuSmartLab, Germany) operating at 40 kV, 40 mA. The scanning range was performed on powder which was 10° to 40° with a step size of 0.04° and irradiation time of 0.96 s per step. The mean crystallite size was determined using DIFFRAC SUITE EVA software.

Fourier-Transform Infrared Spectroscopy (FTIR)

FTIR spectroscopy (Bruker Vertex 70 spectrometer) was applied to characterize the type of functional groups on the scaffolds. Four different points of the portion of a sample were deposited in a diamond anvil cell (DAC) and the image scans were analysed following the contact of the radius needle tip with the total area of the fibre scaffold.

Thermogravimetric Analysis (TGA)

Thermal behaviour of CaP coated PCL scaffolds (with NaOH and Ar-O₂ Plasma modification) was examined and compared with each other using a Netzsch Jupiter Simultaneous Thermal Analyser (Germany) with temperature range 25 to 600 °C at a heating rate 10 K/min with the sample mass of 20 mg.

Micro-Computed Tomography (μ -CT)

The porosity of the scaffolds and the distribution of CaP particles on the fibre structures was examined. A 6-mm disc of the scaffolds was placed inside the X-ray tube of a micro-CT scanner (μ CT40, SCANCO Medical AG, Brüttisellen, Switzerland) and exposed to a voltage of 55 kV X-rays with a current of 120 μ A and a greyscale threshold of 10 and resolution of 6 μ m. A suitable threshold composed of both fibres and particles was selected corresponding to the original grayscale images for porosity analysis. However, the fibres showing in grayscale images were eliminated to select the threshold for CaP particle distribution. The micro computed tomography (CT) software package was applied for 3D visualization of the scaffolds reconstructed from the 2D scanned slices.

Statistical Analysis

All data were expressed as mean \pm standard deviation. Comparisons between groups were analysed by analysis of variance (ANOVA, post hoc test: Tukey). The statistical software SPSS 17.0 for windows was used for calculations and $p < 0.05$ was considered to be statistically significant.

RESULTS

Morphological Characterization of Scaffolds (SEM)

Figures 2.1 show the SEM micrographs of post-treated coating samples at different treatment times. The topographical scaffold structures indicated that the scaffolds retained their porous structural confirmation after coating. The 0.5-hour SBF treatment seemed unable to fully cover the whole of fibres surface (Figure 2.1-A2, A4). While nucleation immersion for 1 hr could provide the uniform coating structures in both Na-C and Plas-C groups (Figure 2.1-B). However, after 3 and 6 h immersion in SBF, there was an increase in crystalline deposition and a thick layer of CaP particles encased the fibres which may affect the scaffold pore dimensions (Figure 2.1-C3, D3). The round CaP

fragments were spread in Na-C scaffold (Figure 2.1-B2). The CaP particles were distributed smoothly in Plas-C (Figure 2.1-B4). The incremental crystalline deposition was observed in Plas-C scaffold over the more extended period of 3 and 6 hours (Figure 2.1-C, D). The forming clusters had more spherical arrangement in Na-C (Figure 2.1-B2) in comparison with Plas-C (Figure 2.1-B4). It seemed extra level of Ca and P contents aggregated and merged on the surface layers which were already coated in the scaffolds which were immersed in the nucleation solution for 3 and 6 hours (Figure 2.1-C4, D4). The coating structure in Na-C scaffold showed some cracks and separated coated layer from the fibres (Figure 2.2-B1, yellow arrows). While, The images showed the denser and even coated layer in Plas-C group (Figure 2.2-D1). The SEM images proved that the NaOH and Ar-O₂ plasma treatment didn't have negative impact or substantial changes on the fibre diameter (Figure 2.2-C, E). However, the Na-nC scaffold appeared that the first layer of material dissolved and peeled off from the filaments (Figure 2.2-C2). Also, the surface of Plas-nC scaffold displayed relatively rough morphology with nanometre features on the surface of the fibres (Figure 2.2-E2).

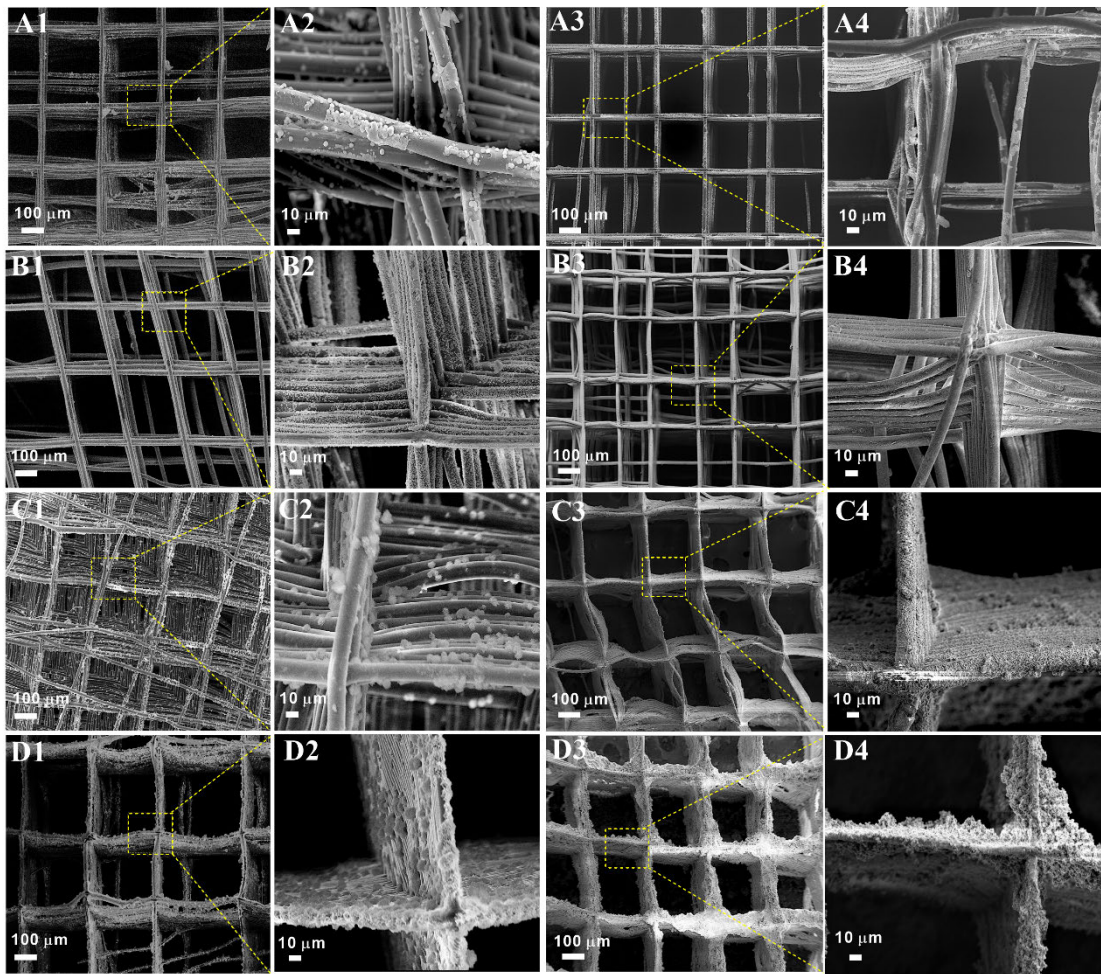


Figure 2.1. SEM micrographs of CaP coated scaffolds immersed in SBF for (A) 0.5, (B) 1, (C) 3 and (D) 6 hours with (1 and 3) lower and (2 and 4) higher magnifications; (1 and 2) Na-C; (3 and 4) Plas-C.

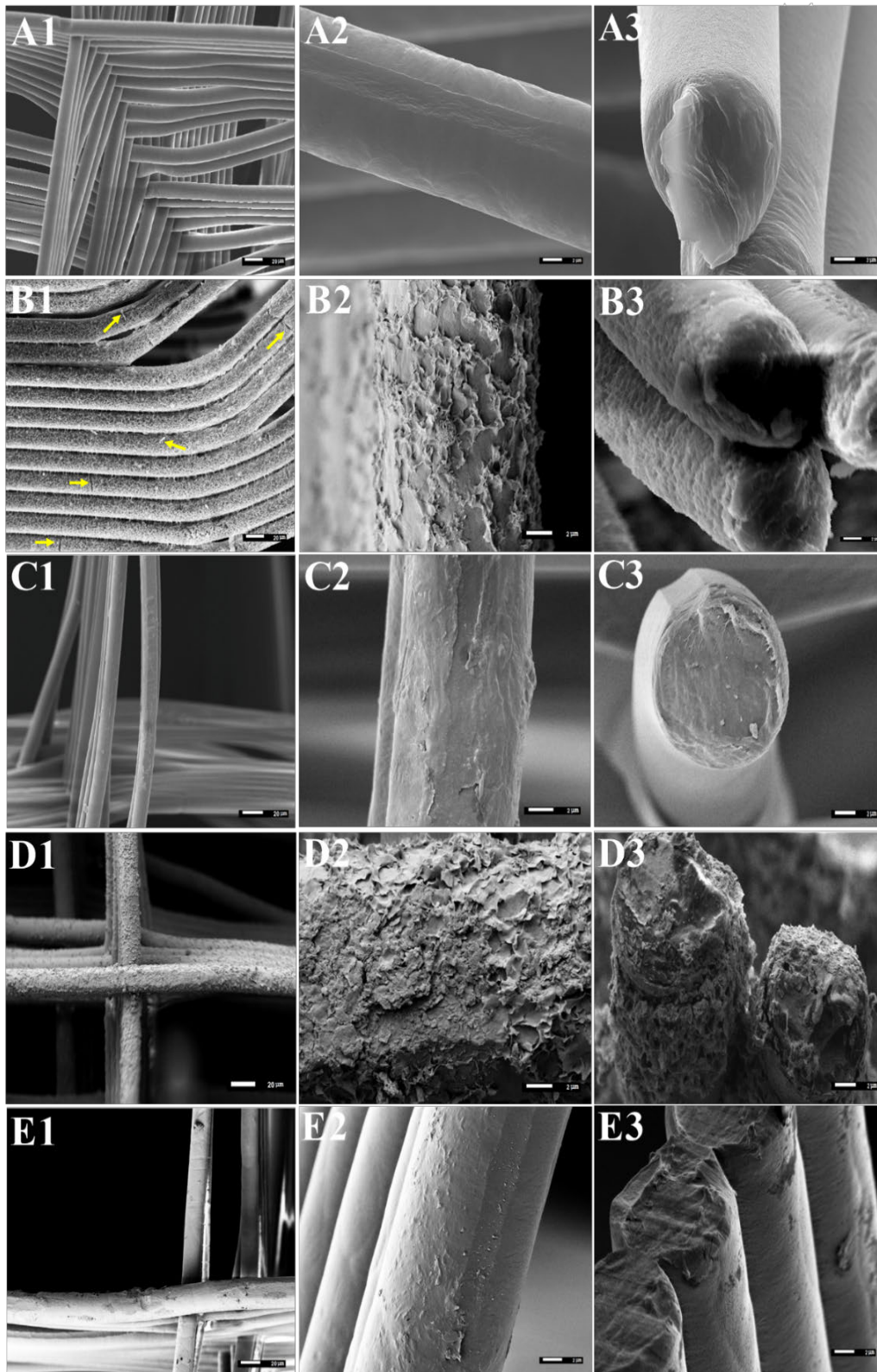


Figure 2.2. The morphology of CaP coated scaffolds SEM images immersed in SBF for 1 hour with (1) lower and (2,3) higher magnifications. (A) nC; (B) Na-C; (C) Na-nC; (D) Plas-C; (E) Plas-nC.

Elemental Chemical Characterization (EDS)

EDS analysis identified the proportion of elements found on the scaffold areas through percentage in weight. The results showed the presence of Ca ion on the surface of the fibrous scaffolds in both (Na-C and Plas-C groups (Figure 2.3, Table 2.2). The pre-treatment with Ar-O₂ plasma increased the Ca level to 6.7% in Plas-C compared to 2.7% in Na-C group. Also, P ion was not detected in Na-C scaffold whilst the level of P increased to 1.7% in Plas-C scaffold which demonstrated that the pre-treatment with Ar-O₂ plasma influenced on the Ca/P ratio. Instead, the amount of Na ion was greater in Na-C (7.0%) than Plas-C scaffold (2.2%). The presence of Cu ion was observed only in both Plas-nC and Plas-C scaffolds. The Plas-C scaffold indicated the presence of K and Mg ions which were not found on the other scaffold groups.

Table 2.2. Element analysis by EDS of coated and non-coated MEW PCL scaffolds: nC; Na-C; Na-nC; Plas-C; Plas-nC.

Element	nC Weight %	Na-C Weight %	Na-nC Weight %	Plas-C Weight %	Plas-nC Weight %
Al	8.0	1.8	100	2.1	6.9
Ca	-	2.7	-	6.7	-
Cl	-	13.9	-	12.4	-
Cu	-	-	-	1.3	0.4
K	-	-	-	1.5	-
Na	-	7.0	-	2.2	-
Mg	-	-	-	0.4	-
O	92.0	74.6	-	71.7	92.6
P	-	-	-	1.7	-

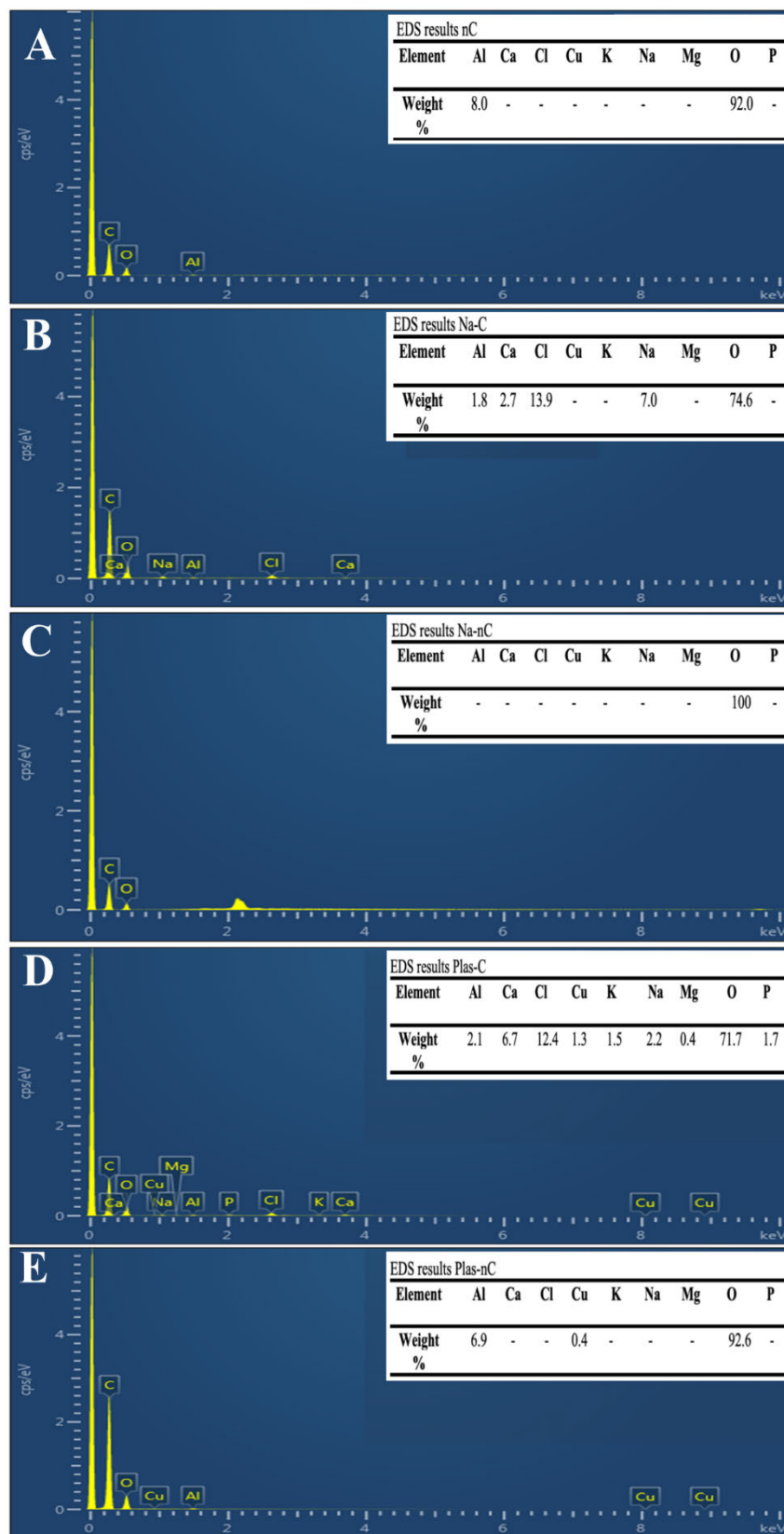


Figure 2.3. The EDS analysis of CaP coated scaffolds after 1 hour immersion in SBF. (AnC; (B) Na-C; (C) Na-nC; (D) Plas-C; (E) Plas-nC.

Surface Evaluation by Contact Angle

The hydrophilicity of the treated and untreated scaffolds was assessed by contact angle measurement (Figure 2.4). We observed that the drop of de-ionized water in the nC PCL scaffolds retained on the fibres surface and revealed the hydrophobic characteristic of the scaffolds with an average contact angle of $135^{\circ} \pm 4.9^{\circ}$ (Figure 2.4-A). The results showed that the hydrophilicity of the surface scaffold raised following CaP coating in both Na-C and Plas-C groups as the immediate adsorption and spreading of water (Figure 2.4-B, D). However, the contact angle value slightly decreased with the treatment of 1M NaOH in Na-nC scaffold with the range of $91^{\circ} \pm 12.4^{\circ}$ (Figure 2.4-C). The contact angle value indicated a significant reduction to 0° after plasma treatment without coating (Plas-nC) as compared to Na-nC (Figure 2.4-E).

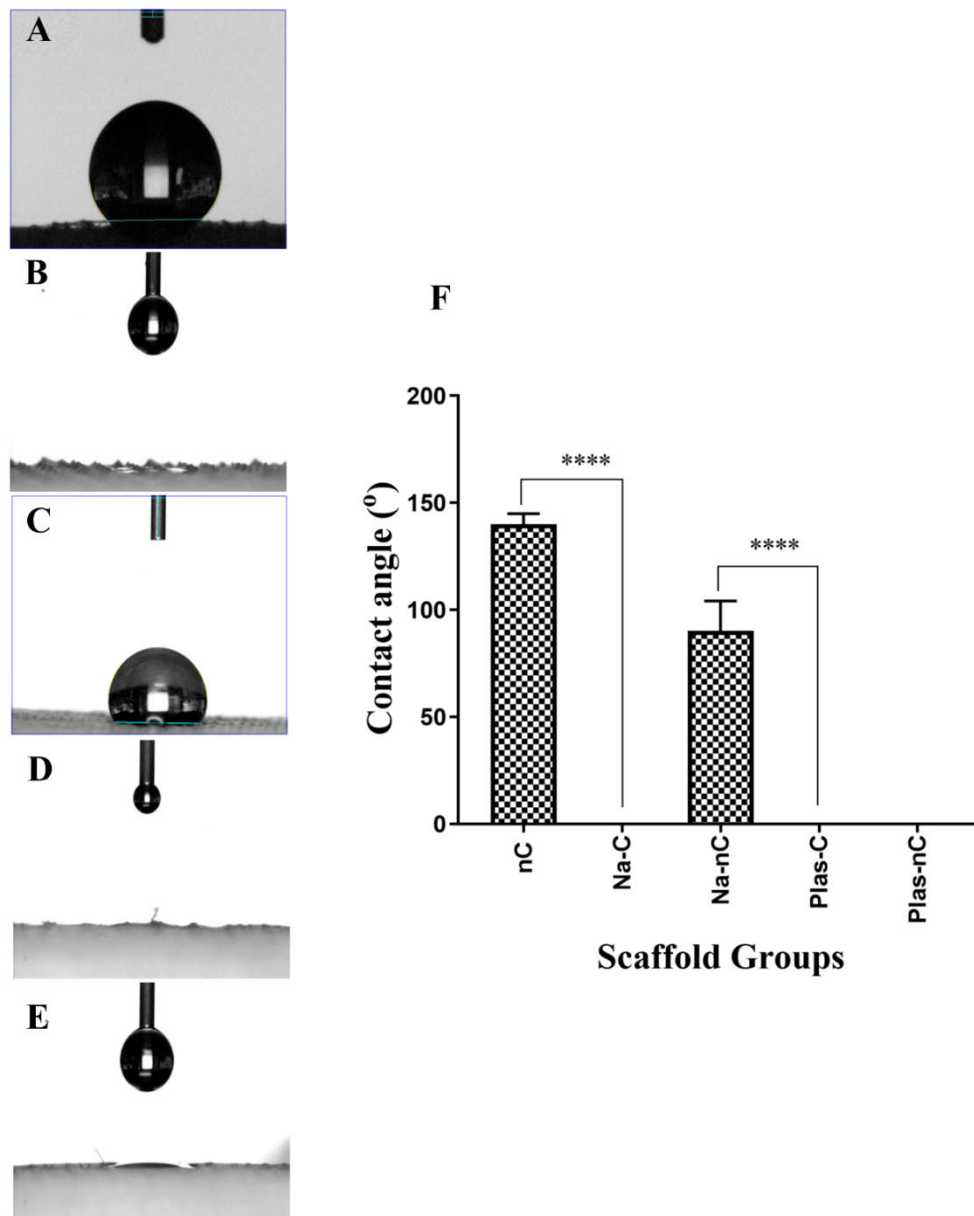


Figure 2.4. Water contact angle of PCL scaffolds: (A) nC; (B) Na-C; (C) Na-nC; (D) Plas-C; (E) Plas-nC; (F) Quantitative micro-CT analysis of coated and non-coated scaffolds.

Mechanical Behaviour

The assessment of the mechanical performance of treated and non-treated PCL scaffolds was carried out using mechanical tensile tests (Figure 2.5). Apparent stress-strain relationship was recorded (Figure 2.5-A) and the mechanical properties were calculated from the curve (Table 2.3). The Young's modulus of nC scaffolds was found to be

1.93±0.23 kPa, which is the maximum among the values of other groups. However, this value was not significant compared to Plas-C with a Young's modulus of 1.67±0.76 kPa. It was demonstrated that the Plas-C promoted the tensile modulus of the fibrous scaffold approximately 37% rather than the Na-C. The Plas-nC scaffold displayed the minimum modulus among the scaffold groups (Figure 2.5-C). The nC scaffold showed the higher ultimate tensile strength (UTS) (29.66±1.37 kPa) and the failure elongation (1088.2±121.4 %) compare to the other scaffolds; followed by Plas-C (685.42±59.6 %) (23.06±1.90 kPa), although these two mechanical properties were not significant in contrast to Na-C scaffolds (Figure 2.5-B, D, Table 2.2). Therefore, the nC and Plas-nC scaffolds showed the highest and the lowest potential to tolerate the tensile loading ($p \leq 0.002$), respectively.

Table 2.3. Tensile strength of coated and non-coated MEW PCL scaffolds: nC; Na-C; Na-nC; Plas-C; Plas-nC; a-c ($p=0.02$), d, e ($p < 0.0001$).

Sample	Young's Modulus (kPa)	Elongation at break (%)	Ultimate tensile strength (kPa)
nC	1.93±0.23 ^{a, c}	1088.2±121.4	29.66±1.37
Na-C	1.04±0.35 ^c	547.83±275.9 ^d	20.29±3.60
Na-nC	0.85±0.47 ^c	44±18.62 ^e	17.21±4.52
Plas-C	1.67±0.76 ^c	685.42±59.6 ^d	23.06±1.90
Plas-nC	0.57±0.27 ^{b, c}	3.08±0.95 ^e	0.63±0.23

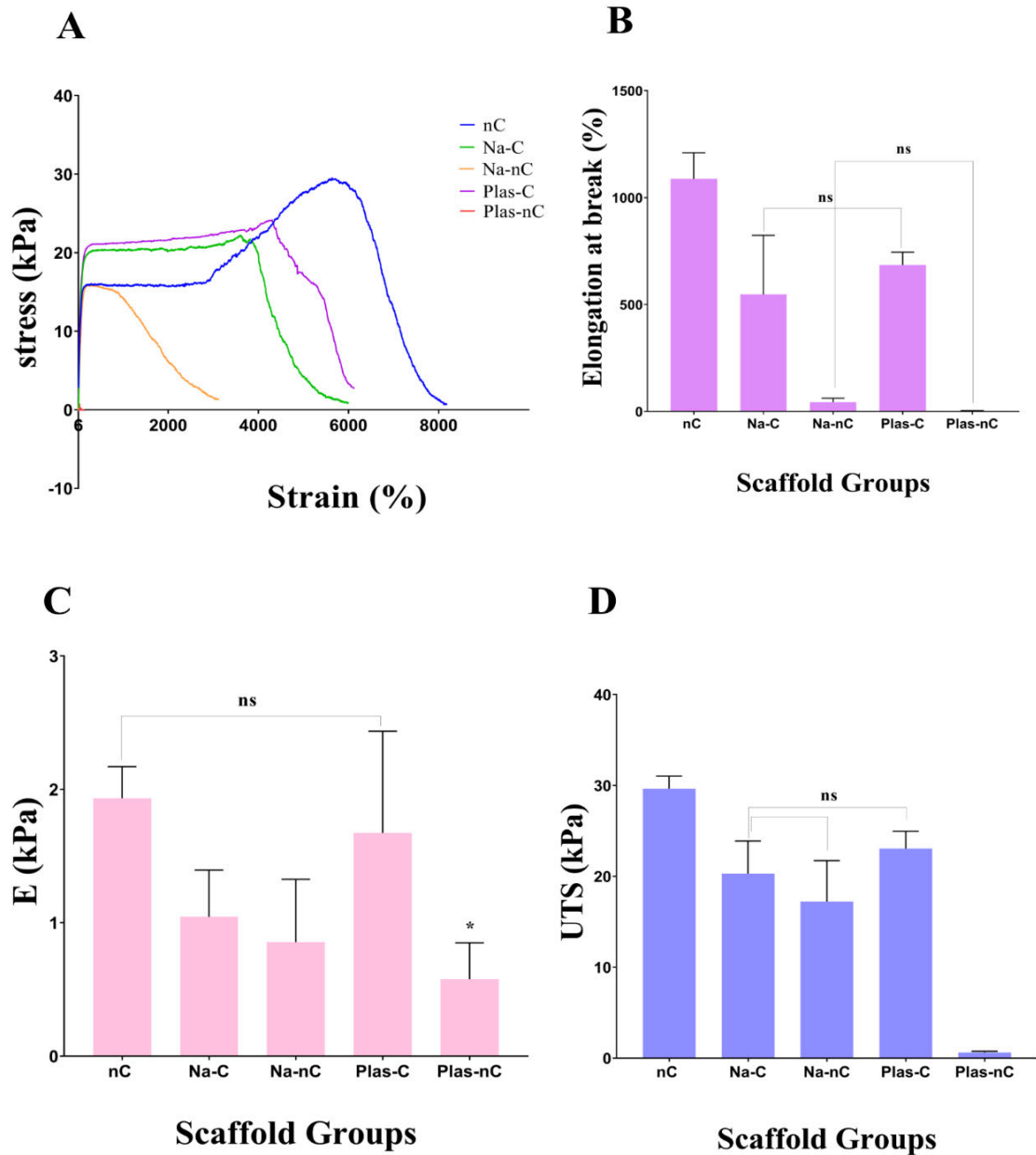


Figure 2.5. Mechanical properties of CaP coated and non-coated MEW PCL scaffolds. (A) tensile stress-strain curve; (B) Elongation at break; (C) Yong's modulus; (D) Ultimate tensile strength (UTS); nC; Na-C; Na-nC; Plas-C; Plas-nC; ns: nonsignificant; * $p \leq 0.002$.

X-Ray Diffraction (XRD) Analysis

XRD patterns of coated and non-coated scaffolds were obtained (Figure 2.6). The diffraction peaks at $2\theta = 21.60^\circ$ and 23.95° were attributed to PCL materials in all the

groups and assigned by the red asterisks. XRD analysis was performed on Na-nC and Plas-nC. The absence of crystalline CaP revealed that no coating materials were found in these specimens. Although some small crystalline structures were observed in Na-nC and Plas-nC scaffolds which showed a greater size than the nC PCL scaffold. The presence of major pattern peaks at $2\theta = 31.73^\circ$, 66.34° and 75.12° could be assigned to the halite structure of NaCl. Also, the diffraction peaks at $2\theta = 11.92^\circ$, 29.74° and 34.01° corresponding to the formation of brushite structure ($\text{HCa}(\text{PO}_4)_2(\text{H}_2\text{O})_2$) in coated scaffolds (Na-C and Plas-C). Both halite and brushite crystalline forms were distinguished in Plas-C and Na-C scaffolds with the difference in crystal orientation of 200 for Na-C and 220 for Plas-C scaffolds. In addition, the crystals looked sharp in shape and larger in size for Na-C scaffolds. Approximately 36.77% halite and 63.23 % brushite structures were found in Plas-C scaffolds. The crystal sizes of both coated Na-C and Plas-C scaffolds were determined by Scherrer's equation and the average crystal sizes were [PCL (11.72 ± 0.23 nm), halite (44.53 ± 2.76 nm), brushite (50.93 ± 14.44 nm)] for Plas-C scaffolds and [PCL (11.60 ± 0.12 nm), halite (237.27 ± 121.67 nm), brushite (41.63 ± 6.14 nm)] for Na-C scaffolds.

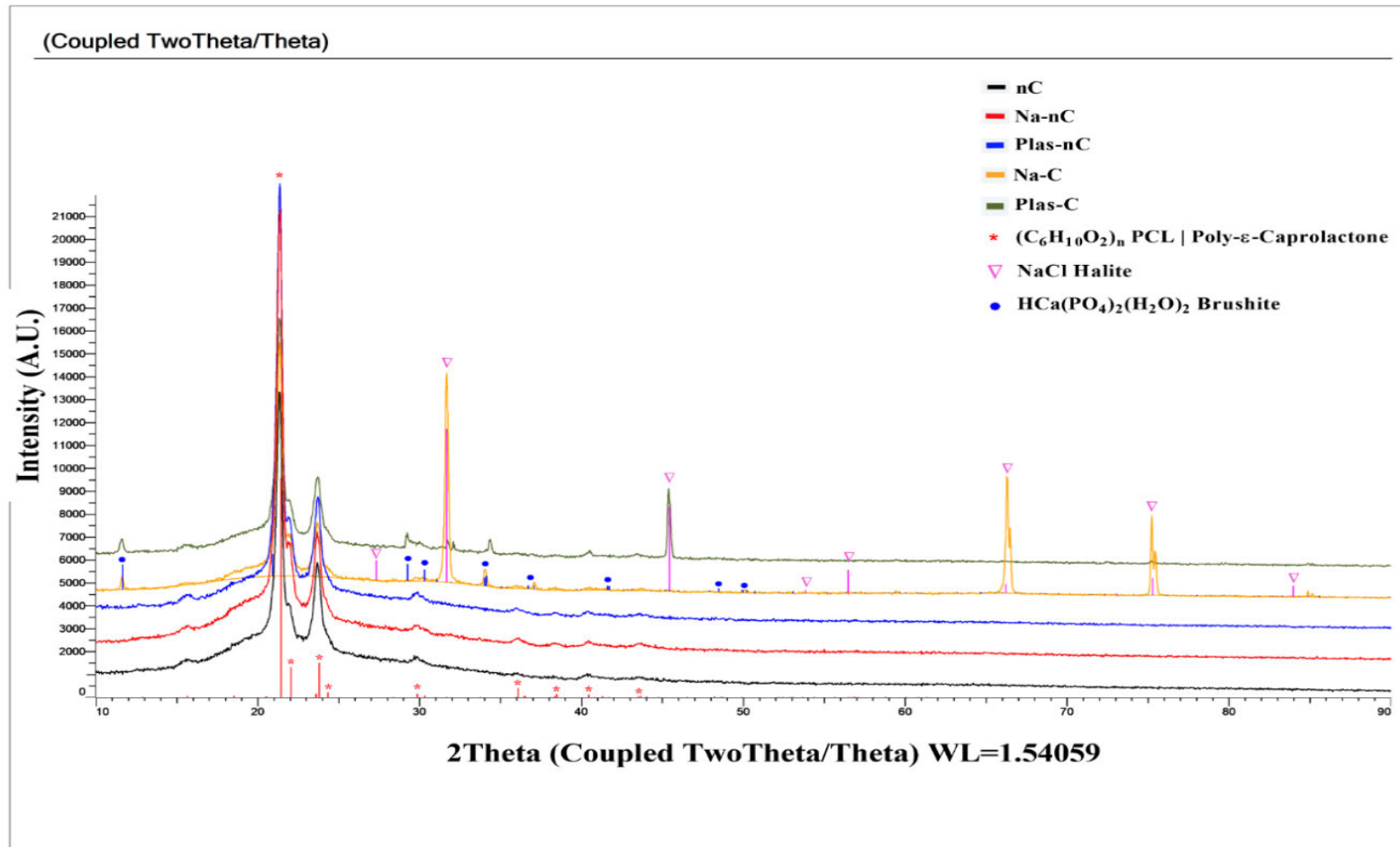


Figure 2.6. X-ray diffraction spectra of coated and non-coated MEW PCL scaffolds: nC; Na-nC; Plas-nC; Na-C; Plas-C.

FTIR Analysis

Figure 2.7 presents the FTIR spectra of PCL scaffolds of Na-nC, Plas-nC, Na-C, Plas-C and without any treatment (nC). The chemical identification on the nC PCL scaffold surface showed the following bands of C-O-C at $1,161\text{ cm}^{-1}$, C-O-C at $1,239\text{ cm}^{-1}$, C-O and C-C at $1,293\text{ cm}^{-1}$, carbonyl stretching at 1721 cm^{-1} and CH₂ stretching at $2,946\text{ cm}^{-1}$, and CH₂ stretching at $2,866\text{ cm}^{-1}$. Identification of the hydrophilic OH groups at $2,942\text{ cm}^{-1}$ indicated the surface of Na-nC scaffold. The FTIR of HAP on the surface of Na-C group, exhibited the bands of OH⁻ stretching at $3,341\text{ cm}^{-1}$, asymmetric PO₄³⁻ bend at 558 and 603 cm^{-1} , asymmetric PO₄³⁻ stretch at 1026 cm^{-1} and symmetric PO₄³⁻ stretch at 959 cm^{-1} . The hydrophilic OH bands placed at $2,943\text{ cm}^{-1}$ corresponded to the surface of Plas-nC scaffold. Regarding the FTIR of Plas-C scaffold the spectra was reported as follows: the absorption bands at 3366 cm^{-1} belonged to OH stretch, the bands at 564 cm^{-1} attributed to asymmetric PO₄³⁻ bend, the bands at 960 cm^{-1} was assigned to symmetric P-O stretch and the asymmetric PO₄³⁻ stretch was observed at 1045 cm^{-1} .

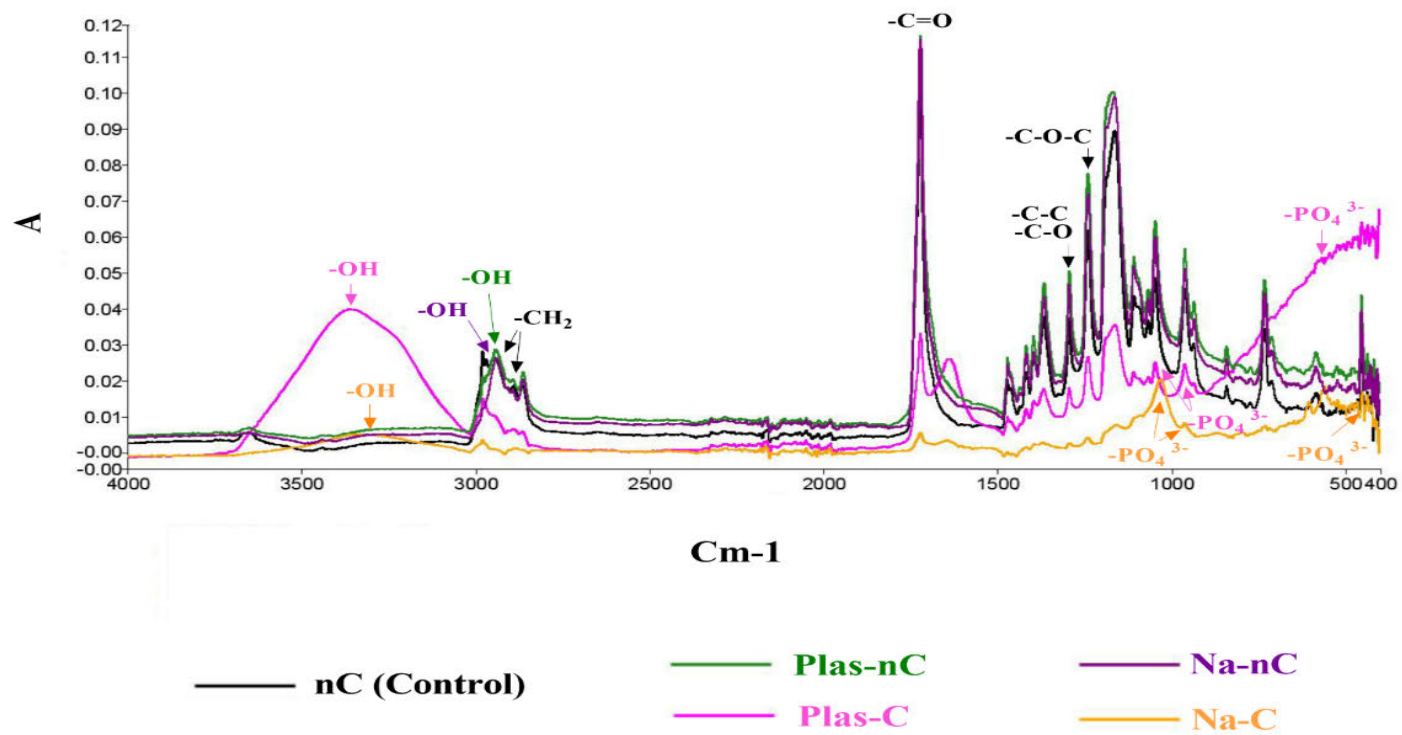


Figure 2.7. Fourier-transform infrared spectrum of coated and non-coated PCL scaffolds; nC ; Plas-nC; Plas-C; Na-nC; Na-C.

Thermal Analysis (TGA)

The TGA-DSC curves of the CaP coated scaffolds were obtained under N₂ atmosphere (Figure 2.8). We used TGA-DSC to compare the quantity of CaP particles on both CaP coated scaffolds Plas-C and Na-C. As the scaffold material will be degraded completely at decomposition temperature, above this temperature only the inorganic components (HA or TTCP) remain, we could show higher amounts of CaP deposition on the Plas-C scaffolds in contrast to Na-C. As this test relating to only CaP coated scaffolds, there was no need to do this test for the other scaffold groups were not processed for CaP coating. The weight loss happened through three steps according to the details listed in Table 2.4. The first step was associated with the mass loss of 0.45% for Na-C scaffold and 0.86% for Plas-C scaffold at the endothermic peak of 64.9 °C. The preliminary decomposition occurred at the range of 193.4 to 431 °C and the weight loss of 41.66% and 39.15% appeared for Na-C and Plas-C scaffolds respectively at the maximum peak temperature of 390.3 °C and 393.3 °C. Further decomposition exhibited between 431.5-600 °C with the highest exothermic peak of 517.9 and 514 °C for Na-c and Plas-C scaffolds. Following the complete degradation of the material, the residual CaP particles of Plas-C was 58.23% and 56.38% for Na-C scaffolds at 600 °C.

Table 2.4. The data of TGA-DSC analysis of CaP coated MEW PCL scaffolds.

Sample	Temperature range (°C)	Mass loss (wt %)	Total mass loss (mg)	DSC peak (°C)
Na-C	25-193.4	0.45		64.9
	193.4-431.5	41.66	6.46	390.3
	431.5-600	1.46		517.9
Plas-C	25-193.4	0.86		64.9

193.4-431.5	39.15	5.87	393.3
431.5-600	1.76		514

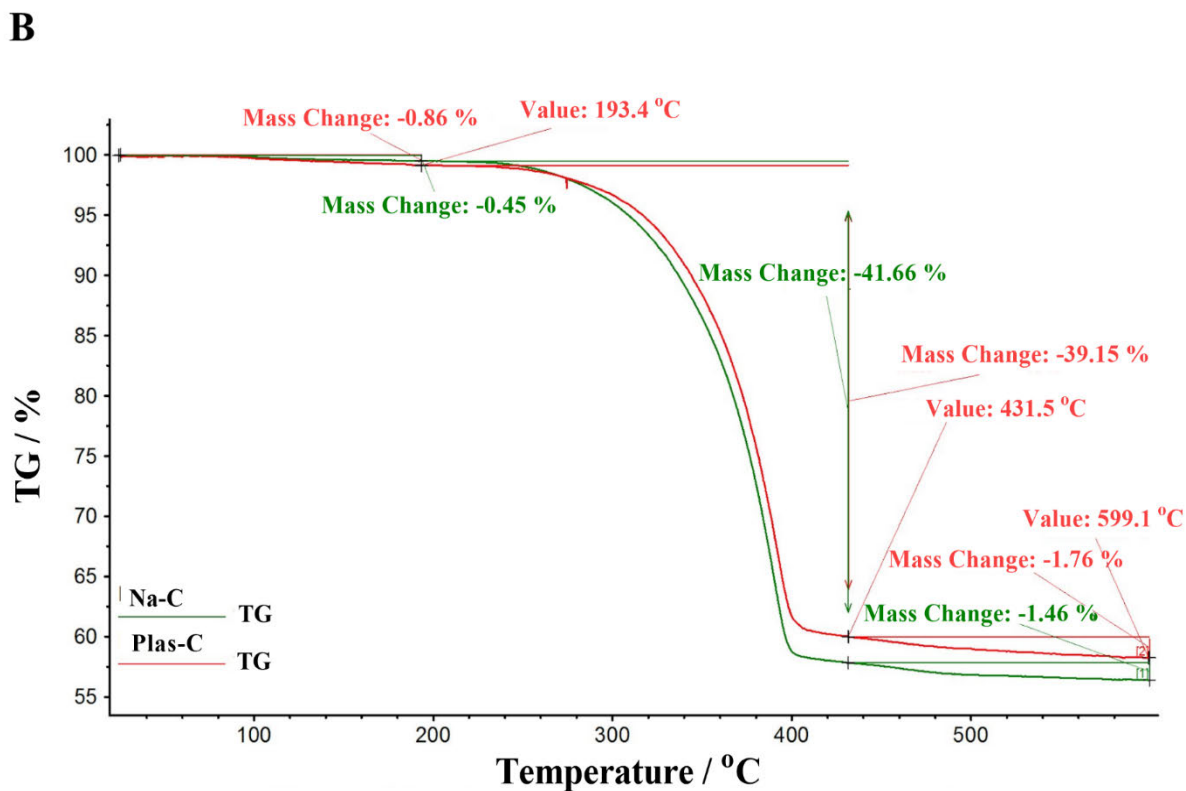
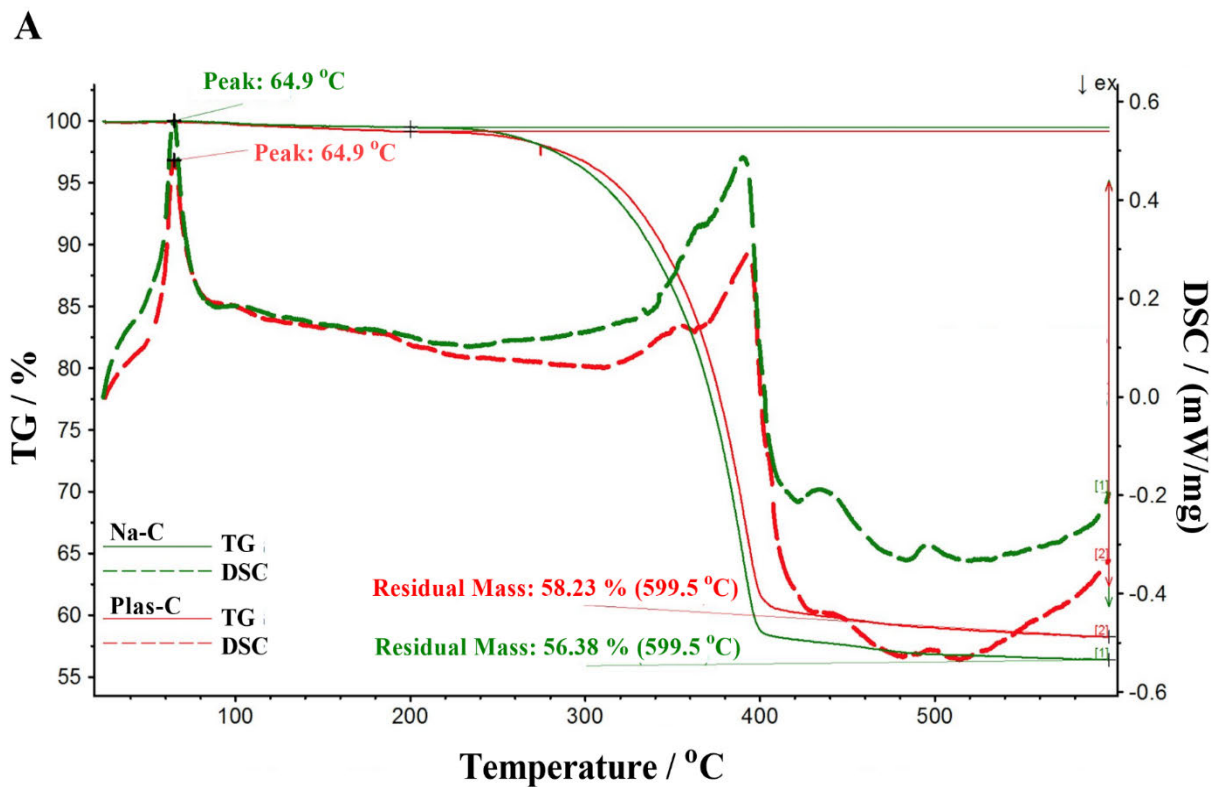


Figure 2.8. (A) The TGA-DSC and (B) TGA curves of CaP coated MEW PCL scaffolds: Na-C; Plas-C.

Characterization of PCL Scaffolds Coated with Cap (Micro-CT)

The effect of different coating treatments was evaluated using micro-CT to determine the distribution of CaP particles (Figure 2.9). The grey areas showed the CaP and the white and blue regions represented the lack of CaP. No CaP coating was identified for nC (Figure 2.9-A), Na-nC (Figure 9-C) and Plas-nC (Figure 2.9-E) groups. The Na-C scaffold exhibited a heterogeneous CaP distribution. Some areas contained more concentrated CaP, which were aggregated and created some large CaP clusters, whilst other regions are empty of the CaP particles (Figure 2.9-B). While, the observed Plas-C structures indicate an even distribution of CaP coating on the surface of the PCL scaffold struts that were spread throughout the inner and outer of scaffold structure (Figure 2.9-D). The total coated mineral volume was detected. The value significantly increased in Plas-C scaffold which was quantified at 40.21 mm³ in comparison with 31.54 mm³ in Na-C scaffold (Figure 2.9F).

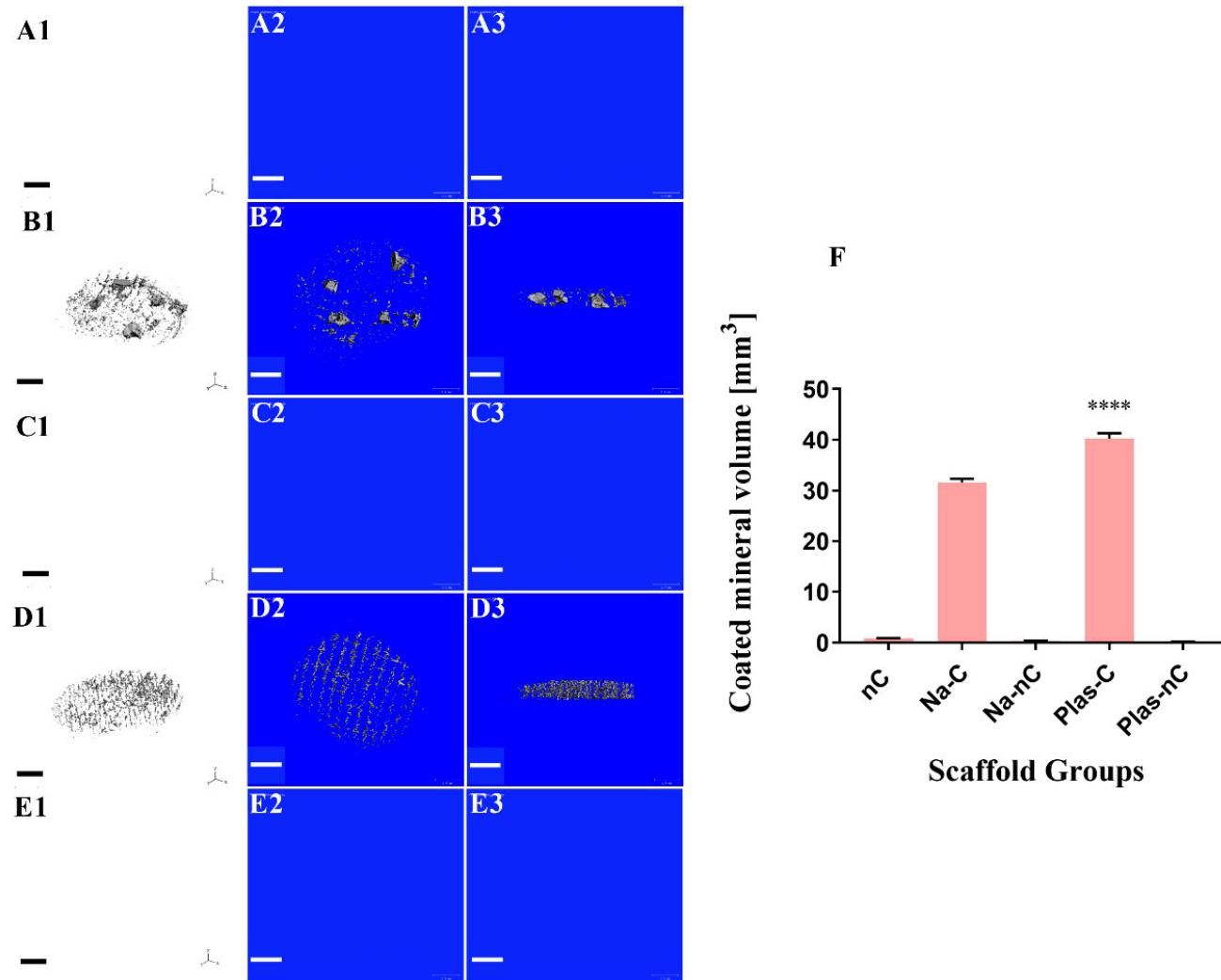


Figure 2.9. Micro-CT analysis of coated and non-coated PCL scaffolds (1,2) Top view; (3) Saggital section; (A) nC; (B) Na-C; (C) Na-nC; (D) Plas-C; (E) Plas-nC. (F) The total coated mineral volume was calculated using CTAn program. **** $p \leq 0.0001$.

DISCUSSION

Calcium phosphates as a bioactive material is commonly used for the treatment of human bones and dental applications since of superior initial rate of osseointegration (28). Because of the various nucleation potential of phosphate and calcium ions, there is a large demand for obtaining a firm and uniform coating of them on the material surface by surface activation through the alkali, acid or plasma pre-treatments (36, 37). .

Ar plasma is preferred for surface cleaning in contrast to O₂ plasma because of minimum oxidative groups, less impact on the main material properties and removing the surface contamination by physical etching of ion emission (38). However, the composition of Ar-O₂ plasma mixture was found to be more efficient to eliminate the microorganisms and increase of sample roughness than Ar exclusively (31). Therefore, we selected Ar-O₂ plasma treatment for this study to create a more coarse surface as the adsorption of CaP is enhanced when the roughness increases (39). The hydrophilicity of the PCL scaffolds increased significantly following surface plasma treatment and calcium phosphate (CaP) coating. This is associated with the polar components (-C-O-, C=O, and -COOH) on the polymeric chains induced by the surface modifications.

The greater hydrophilicity of the plasma pre-treatment (Plas-nC) compared to NaOH alkaline treatment (Na-nC) was attributed to the additional hydroxyl (-OH) and carboxylate (-COO⁻) groups on the scaffold surface. The surface chemical composition measured by EDS also reflected this. The level of O in Plas-nC scaffold was noticeably higher than that of Na-nC group. This explained why the Plas-nC scaffold was wholly wetted compared to the Na-nC scaffold. Additionally, more wettability was obtained after CaP coating exhibited a greater Ca/P atomic ratio in Plas-C and Na-C scaffolds. The surface hydrophilicity and wettability of the CaP coated PCL scaffold were enhanced prominently when it was initially pre-treated by NaOH and subsequently modified by CaP.

According to the SEM data, using Ar-O₂ plasma treatment seems to create a roughness on the surface of Plas-nC compared to the smooth surface of nC PCL scaffold. This is in agreement with the previous study of Cvelbar et al., reporting that the surface roughness of graphite/polymer composite increased by O₂ plasma etching (40), as well as the study of Kosorn et al. showing the rough surface of porous PCL scaffolds due to the plasma treatment (41). The mild condition of alkaline pre-treatment is beneficial in contrast to acidic treatment to generate less harsh undesirable by-product formation (42, 43). Accordingly, the dilute NaOH was preferred in this study as its low cost as to other related alkaline agents.

The corrosive behavior of NaOH made the surface layer of the fibres peel off and created the rough surface compared to nC PCL scaffold. This was in accordance to the study of Luickx et al. that showed a similar effect of NaOH (1M) on electrospun PCL scaffold (44). However, no removal of 3D printed PCL/Graphene surface Scaffolds was seen by dipping in 5M NaOH for 3 hours (45). This means the modification and cleaved carboxyl and hydroxyl chains of PCL polymer in mesh-like structure promoted severely in comparison with 3D-printed fibre printed by FDM. However, Li et al. showed the micro-size pores and rough surface of 3D-printed PCL scaffold following ethanolic sodium hydroxide (30% 0.25 M NaOH: 70% absolute ethanol) treatment for 2 min (46).

Our SEM data indicate that the Plas-C scaffolds have a uniform coating density without any cracks or fracture compared to brittle coated layers in Na-C scaffolds. Our results show an enhancement compared to the studies of Luickx et. al. (44), Araujo et al. (47) and Yu et al. (48) where the non-uniform surface activation and subsequent uneven CaP deposition after NaOH treatment. This resulted in the larger CaP crystals on the surface of Na-C scaffolds which were aggregated non-uniform versus Plas-C ones as shown in micro-CT evaluation. Differences in crystal morphology are due to the different surface treatments. Surface activation by NaOH in Na-C scaffolds relied upon diffusion of the

aqueous NaOH solution into the pores which were already filled with air thus hindering homogeneous surface activation. Also, the resultant morphology of the fibers was changed after immersion in NaOH solution and surface of the PCL fibers was not homogeneously activated. Therefore, the CP deposits appear as local precipitation and accumulations in those areas of scaffold and created a more spherical arrangement than seen in Na-C scaffolds.

It is not fully understood which main factors of physical (Van der Waals), chemical or mechanical interactions influence on coating adhesion to the substrate (49). The surface of PCL polymer becomes super-active by the active carbonyl ($-\text{CO}-$), carboxyl ($-\text{COO}-$) and hydroxyl ($-\text{OH}$) anions. These negatively charged groups are ready to attract the soluble positive calcium ions of the SBF solution (50, 51). Hence, the reason of unsteady CaP coated layer in Na-C scaffolds might be associated to the scaffold pores, which were already filled by the air and were not able to take up the aqueous NaOH solution. In contrast, the plasma pre-treatment could overcome this limitation by stimulating a homogeneous activation on MEW PCL scaffolds prior to immersion in SBF solution.

Following NaOH and Ar-O₂ plasma treatment, the samples with negatively charged surface had potential to interact with the releasing positively charged Ca²⁺ ions of SBF by immersion for 1 hour. As the EDS analysis demonstrated, the Ca²⁺ contents enhanced in both Na-C and Plas-C scaffolds by attachment of Ca²⁺ ions. However, the percentage of Ca²⁺ ion was higher in Plas-C scaffold compared to Na-C scaffolds. However, the positive charge would appear by accumulation of Ca²⁺ ions and ready to interact to the opposite charged of PO₄³⁻ ions. Poorly crystallized CaP and no phosphorus element was detected by precipitates analyses of EDS for Na-C scaffolds. This was a consistent observation of the study having been repeated multiple times. Furthermore, the SBF pH was stabilized in all samples prior to treatment and the same SBF was used for coating

both groups of Na-C and Plas-C scaffolds. CaP coating of scaffolds can be influenced by a broad range of factors, especially pH and thus while further studies may be required to determine the precise reason for our observations, a number of possibilities exist.

Our study showed that NaOH surface modification did not allow homogeneous precipitation of CaP from SBF onto Na-C scaffolds due to inherent limitations with the aqueous NaOH solution treating scaffold pores which were filled with air. This difference in subsequent CaP precipitation is reflected in the differing trace amounts of various elements detected by EDS in the Na-C and Plas-C scaffolds. Moreover, Ca-P nucleation on the substrates is promoted by the chemical affinities, which are related to the surface charge of the scaffold. Quantitative variation of the elements presents in the SBF during etching time and with pH changes have been shown by Barrere et al. to effect CaP coating (52). In the absence of Mg^{2+} content in SBF solution, no Ca-P trace was detected. So the presence of Mg^{2+} is essential for Ca-P coating formation. Mg^{2+} ion influences on the Ca-P crystal size and the high concentration of Mg^{2+} ion reduces the Ca-P crystal growth and creates the stabilized and uniform coating on the substrate. This was similar to our result, since we found Mg element in Plas-C scaffold group showing evenly smooth coated layer and not detected in our Na-C scaffolds that might influence on the nucleation of Ca-P and the absence of ion P in this group.

The degree of ion exchange during the reaction in SBF depends on the pH value (53). Dissolution of the surface material following NaOH pre-treatment is shown in Figure 2.2-C2 and although the samples were washed with distilled water several times following NaOH pre-treatment, the pH of the scaffolds is acidic due to air contact and dissolution of carbon dioxide gas which creates a dilute solution of carbonic acid. These pH changes may then promote different deposition of ions from SBF.

Finally another factor which influences the pH level is the residue of carboxyl and hydroxyl chains of PCL polymer compositions which degraded following NaOH etching

and release during the immersion of scaffolds in the SBF solution that might lead to the pH changes and creates unexpected ion deposition and different CaP crystals compared to plasma modification which does not have these issues.

Apart from copper (Cu) and aluminum (Al), the source of all of the other elements such as Ca, Cl, K, Na, Mg, O and P are contained within the SBF solution used (Table 2.1) (35) that detected on the Plas-C scaffolds. There is no Al element in SBF solution. Therefore, it should indicate the material of pin stubs which is aluminum and accommodated the scaffold samples for SEM observation and the EDS analysis that detected in all the groups. As there is no Cu present in the SBF solution, Cu deposition suggests a contaminant obtained from the equipment during plasma modification process, as was indicated in only Plas-C and Plas-nC scaffolds. Although we wiped the chamber by the ethanol before starting the test.

The presence of most intense peaks of XRD analysis were labeled for large deposits of halite structure (NaCl) that was obtained for Na-C scaffolds. Furthermore, EDS results demonstrated the high concentration of Na⁺ (7.0%) in Na-C scaffolds in contrast to the Na⁺ (2.2%) in Plas-C scaffolds. Although the same concentrations of Na⁺ and Cl⁻ (1:1 molar ratio) represents for the mineral form Halite which was different to our findings, which showed the molar ratio Na/Cl of 0.50 for Na-C scaffolds and 0.17 for Plas-C groups. The molar ratio of Na/Cl less than 1 indicated the removal of Na⁺ ions in both scaffold groups.

According to the XRD graphs, the main structures of the Plas-C samples were brushite (CaHPO₄, 2H₂O), and HAP. Although the equal ratio of calcium and phosphate ions represents the brushite structure, the Ca/P ratio was found 3.94 for Plas-C scaffolds, which was approximately close to biphasic combinations of HAP (Ca/P: 1.67) + TTCP (Ca/P: 2.00). The mixture of phases of particles resulted in different morphologies of coated pieces that influenced the solubility depending on the crystallinity and its size. The

changing structures can be associated with the different pH and temperature conditions. As the previous studies showed the stability of the crystal particles of coated scaffold can be modified according to the pH and temperature of the implanted site (54). The brushite structure of the Plas-C scaffolds tends to form to HAP or TTCP, by changing the acidity or basicity of the environment. For example, in a neutral state, TCP can convert to HAP. But under acidic pH, TCP will change to brushite structure (55). However, the most stable phase of CaP at neutral pH of human body is HAP which is the main constituent of bone tissues (56).

Among the different crystal structures, crystal with larger size has lower solubility because of the reduction of surface area (57). Although both Plas-C and Na-C - scaffolds contained halite and brushite crystal structures, the smaller crystal size was found for Plas-C scaffolds than Na-C ones. Regarding the previous studies that showed the low crystallinity and finer crystal size can increase the solubility (58), Plas-C scaffolds might have more solubility in contrast to Na-C scaffolds.

The stability and solubility of the CaP minerals reduce from brushite, TTCP and HAP orderly (59-62). However, Jang et al. reported the more stability of brushite in acidic media compared to the neutral environment or when the pH goes towards to basic as it transforms to apatitic calcium phosphate (Ap-CaP) (63). Previous studies demonstrated the advantages of brushite within b-TCP (b-tricalcium phosphate, $b\text{-Ca}_3(\text{PO}_4)_2$) and MCPM [monocalcium phosphate monohydrate, $\text{Ca}(\text{H}_2\text{PO}_4) \cdot 2\text{H}_2\text{O}$] for using starting materials for dental paste formulations and injectable orthopedic because of the high solubility of brushite. Also, the combination of brushite matrix and b-TCP granules microstructures confirmed the rapid bone formation in contrast to the HAP cements in the market (64). In addition, the cubic halite (NaCl) crystals were detected in both Plas-C and Na-C scaffolds in larger size for Na-C scaffolds in comparison to Plas-C scaffolds.

However, the Plas-C scaffolds illustrated the higher percentage of brushite crystals enriched in Ca and P elements confirmed by EDS and XRD.

In addition, other findings showed that the larger NaCl crystal in size which results from the lower temperature, reduction of free energy of the solution and the high concentration of solution can cause the lower solubility since of less contact surface area with the solution (65, 66). Releasing the calcium and phosphate minerals decreases by the greater crystal size and higher crystallinity (67).

Therefore, there would be higher solubility of CaP coating for Plas-C scaffolds in comparison to Na-C ones, due to smaller crystal size. Since the average crystal size has an impressive effect on mechanical properties of the coated scaffolds, the tensile strength of Plas-C scaffolds showed greater value between all the treated samples. Previous reports demonstrated the weak compressive strength of brushite in comparison to HAP because of more resorbable properties (67).

Both Plas-C and Na-C scaffolds exhibited a meaningful increase of tensile modulus with regard to the Plas-nC and Na-nC scaffolds that was similar to the study of Al-Munajjed et al. that reported the higher mechanical properties of the collagen/calcium-phosphate composite scaffold compared to the collagen scaffold (68). Although Plas-C samples indicated the formed brushite crystal structures, the smaller average crystal size in these scaffolds than Na-C ones created the dense layer of calcium phosphate, which lead to better mechanical properties. This is in agreement with the study of Obayi et al. who reported the mechanical tensile strength of samples increased with decreasing crystallized iron size due to the Hall-Petch relationship (69).

CONCLUSION

The apatite mineral layer was precipitated on the surface of melt electrowritten PCL scaffolds through the O₂-Ar plasma and NaOH surface modification by immersing them in simulated body fluids. We found that the plasma pre-treatment after 1hr of SBF

incubation provides uniform and homogeneous CaP coating with thin layer of mineral deposition. Although XRD analysis showed that both Plas-C and Na-C scaffolds include the brushite and halite structures, the halite structure (NaCl) mostly was found in Na-C scaffolds and a mixture of brushite structure and biphasic combinations of HAP and TTCP were in Plas-C scaffolds. However, the crystal size was smaller in Plas-C scaffolds than Na-C ones. The mechanical characterization indicated Plas-C scaffolds was stronger among all other treated scaffolds, but not more than nC. Plas-C scaffolds might have more stability of the CaP minerals due to the higher percentage of brushite and HAP than Na-C scaffolds. We conclude that the plasma treatment is suitable for further development of drugs incorporation in the MEW fibres for bone application.

Acknowledgments

Naghmeh Abbasi was sponsored by a scholarship from Griffith University, Australia. This study is part of her PhD research project being carried out at Griffith University. The authors would like to express their gratitude to Institute of Health and Biomedical Innovation (IHBI) and the Central Analytical Research Facility (CARF) of QUT, Australia, for providing some facilities and technical support for this study, along with Dr. Abdalla Abdal-hay for his advice and general supervision of this research. We want to acknowledge and thank Alan White and Niloofar Ordou for their technical support.

References

1. Jeong J, Kim JH, Shim JH, Hwang NS, Heo CY. Bioactive calcium phosphate materials and applications in bone regeneration. *Biomater Res.* 2019;23:4.
2. Fragozeorgi EA, Rouchota M, Georgiou M, Velez M, Bouziotis P, Loudos G. In vivo imaging techniques for bone tissue engineering. *J Tissue Eng.* 2019;10.
3. Marenzi G, Spagnuolo G, Sammartino JC, Gasparro R, Rebaudi A, Salerno M. Micro-Scale Surface Patterning of Titanium Dental Implants by Anodization in the Presence of Modifying Salts. *Materials.* 2019;12(11).
4. Samavedi S, Whittington AR, Goldstein AS. Calcium phosphate ceramics in bone tissue engineering: a review of properties and their influence on cell behavior. *Acta biomaterialia.* 2013;9(9):8037-45.
5. Ambard AJ, Mueninghoff L. Calcium phosphate cement: review of mechanical and biological properties. *J Prosthodont.* 2006;15(5):321-8.
6. Puttini IO, Poli PP, Maiorana C, Vasconcelos IR, Schmidt LE, Colombo LT, et al. Evaluation of Osteoconduction of Biphasic Calcium Phosphate Ceramic in the Calvaria of Rats: Microscopic and Histometric Analysis. *Journal of functional biomaterials.* 2019;10(1).
7. Moran MC, Ruano G, Cirisano F, Ferrari M. Mammalian cell viability on hydrophobic and superhydrophobic fabrics. *Materials science & engineering C, Materials for biological applications.* 2019;99:241-7.
8. Baranowski A, Klein A, Ritz U, Gotz H, Mattyasovszky SG, Rommens PM, et al. Evaluation of Bone Sialoprotein Coating of Three-Dimensional Printed Calcium Phosphate Scaffolds in a Calvarial Defect Model in Mice. *Materials.* 2018;11(11).
9. Huang L, Zhou B, Wu HY, Zheng L, Zhao JM. Effect of apatite formation of biphasic calcium phosphate ceramic (BCP) on osteoblastogenesis using simulated body

fluid (SBF) with or without bovine serum albumin (BSA). *Mat Sci Eng C-Mater.* 2017;70:955-61.

10. Nandakumar A, Yang L, Habibovic P, van Blitterswijk C. Calcium Phosphate Coated Electrospun Fiber Matrices as Scaffolds for Bone Tissue Engineering. *Langmuir.* 2010;26(10):7380-7.

11. Wasilewski GB, Vervloet MG, Schurgers LJ. The Bone-Vasculature Axis: Calcium Supplementation and the Role of Vitamin K. *Front Cardiovasc Med.* 2019;6:6.

12. Meng D, Dong L, Yuan Y, Jiang Q. In vitro and in vivo analysis of the biocompatibility of two novel and injectable calcium phosphate cements. *Regen Biomater.* 2019;6(1):13-9.

13. Kelder C, Bakker AD, Klein-Nulend J, Wismeijer D. The 3D Printing of Calcium Phosphate with K-Carrageenan under Conditions Permitting the Incorporation of Biological Components-A Method. *J Funct Biomater.* 2018;9(4).

14. Gustavsson J, Ginebra MP, Planell J, Engel E. Osteoblast-like cellular response to dynamic changes in the ionic extracellular environment produced by calcium-deficient hydroxyapatite. *Journal of materials science Materials in medicine.* 2012;23(10):2509-20.

15. Oberbek P, Bolek T, Chlanda A, Hirano S, Kusnieruk S, Rogowska-Tylman J, et al. Characterization and influence of hydroxyapatite nanopowders on living cells. *Beilstein J Nanotechnol.* 2018;9:3079-94.

16. Zhu XD, Zhang HJ, Fan HS, Li W, Zhang XD. Effect of phase composition and microstructure of calcium phosphate ceramic particles on protein adsorption. *Acta biomaterialia.* 2010;6(4):1536-41.

17. Rouahi M, Champion E, Gallet O, Jada A, Anselme K. Physico-chemical characteristics and protein adsorption potential of hydroxyapatite particles: influence on

in vitro biocompatibility of ceramics after sintering. *Colloids and surfaces B, Biointerfaces*. 2006;47(1):10-9.

18. Beaufile S, Rouillon T, Millet P, Le Bideau J, Weiss P, Chopart JP, et al. Synthesis of calcium-deficient hydroxyapatite nanowires and nanotubes performed by template-assisted electrodeposition. *Materials science & engineering C, Materials for biological applications*. 2019;98:333-46.

19. Li X, Song T, Chen X, Wang M, Yang X, Xiao Y, et al. Osteoinductivity of Porous Biphasic Calcium Phosphate Ceramic Spheres with Nanocrystalline and Their Efficacy in Guiding Bone Regeneration. *ACS applied materials & interfaces*. 2019;11(4):3722-36.

20. Lee JB, Maeng WY, Koh YH, Kim HE. Porous Calcium Phosphate Ceramic Scaffolds with Tailored Pore Orientations and Mechanical Properties Using Lithography-Based Ceramic 3D Printing Technique. *Materials (Basel)*. 2018;11(9).

21. Chocholata P, Kulda V, Babuska V. Fabrication of Scaffolds for Bone-Tissue Regeneration. *Materials*. 2019;12(4).

22. Recek N. Biocompatibility of Plasma-Treated Polymeric Implants. *Materials*. 2019;12(2).

23. Huynh V, Ngo NK, Golden TD. Surface Activation and Pretreatments for Biocompatible Metals and Alloys Used in Biomedical Applications. *International journal of biomaterials*. 2019;2019:3806504.

24. Moghadas H, Saidi MS, Kashaninejad N, Nguyen NT. A high-performance polydimethylsiloxane electrospun membrane for cell culture in lab-on-a-chip. *Biomicrofluidics*. 2018;12(2).

25. Ghobeira R, Philips C, Declercq H, Cools P, De Geyter N, Cornelissen R, et al. Effects of different sterilization methods on the physico-chemical and bioresponsive properties of plasma-treated polycaprolactone films. *Biomed Mater*. 2017;12(1).

26. Lin WC, Razali NAM. Temporary Wettability Tuning of PCL/PDMS Micro Pattern Using the Plasma Treatments. *Materials*. 2019;12(4).
27. Phiri RR, Oladijo OP, Nakajima H, Rattanachata A, Akinlabi ET. Structural and morphological dataset for rf-sputtered WC-Co thin films using synchrotron radiation methods. *Data Brief*. 2019;25.
28. Jaroszewicz J, Idaszek J, Choinska E, Szlajak K, Hyc A, Osiecka-Iwan A, et al. Formation of calcium phosphate coatings within polycaprolactone scaffolds by simple, alkaline phosphatase based method. *Mat Sci Eng C-Mater*. 2019;96:319-28.
29. Chen W, Liu YP, Yang LX, Wu JT, Chen QS, Zhao Y, et al. Difference in anisotropic etching characteristics of alkaline and copper based acid solutions for single-crystalline Si. *Sci Rep-Uk*. 2018;8.
30. Yamamoto M, Matsumae T, Kurashima Y, Takagi H, Suga T, Itoh T, et al. Comparison of Argon and Oxygen Plasma Treatments for Ambient Room-Temperature Wafer-Scale Au-Au Bonding Using Ultrathin Au Films. *Micromachines-Basel*. 2019;10(2).
31. Desmet T, Morent R, De Geyter N, Leys C, Schacht E, Dubruel P. Nonthermal Plasma Technology as a Versatile Strategy for Polymeric Biomaterials Surface Modification: A Review. *Biomacromolecules*. 2009;10(9):2351-78.
32. Khlusov IA, Dekhtyar Y, Sharkeev YP, Pichugin VF, Khlusova MY, Polyaka N, et al. Nanoscale Electrical Potential and Roughness of a Calcium Phosphate Surface Promotes the Osteogenic Phenotype of Stromal Cells. *Materials*. 2018;11(6).
33. Li XR, Xie JW, Yuan XY, Xia YN. Coating Electrospun Poly(epsilon-caprolactone) Fibers with Gelatin and Calcium Phosphate and Their Use as Biomimetic Scaffolds for Bone Tissue Engineering. *Langmuir*. 2008;24(24):14145-50.
34. Zviagin AS, Chernozem RV, Surmeneva MA, Pyeon M, Frank M, Ludwig T, et al. Enhanced piezoelectric response of hybrid biodegradable 3D poly(3-hydroxybutyrate)

scaffolds coated with hydrothermally deposited ZnO for biomedical applications. *Eur Polym J.* 2019;117:272-9.

35. Kokubo T, Yamaguchi S. Simulated body fluid and the novel bioactive materials derived from it. *J Biomed Mater Res A.* 2019;107(5):968-77.

36. Pierre C, Bertrand G, Rey C, Benhamou O, Combes C. Calcium phosphate coatings elaborated by the soaking process on titanium dental implants: Surface preparation, processing and physical-chemical characterization. *Dent Mater.* 2019;35(2):E25-E35.

37. Nguyen-Trig P, Altiparmak F, Nguyen N, Tuduri L, Ouellet-Plamondon CM, Prud'homme RE. Robust Superhydrophobic Cotton Fibers Prepared by Simple Dip-Coating Approach Using Chemical and Plasma-Etching Pretreatments. *ACS Omega.* 2019;4(4):7829-37.

38. Yamamoto M, Matsumae T, Kurashima Y, Takagi H, Suga T, Itoh T, et al. Comparison of Argon and Oxygen Plasma Treatments for Ambient Room-Temperature Wafer-Scale Au(-)Au Bonding Using Ultrathin Au Films. *Micromachines.* 2019;10(2).

39. Khlusov IA, Dekhtyar Y, Sharkeev YP, Pichugin VF, Khlusova MY, Polyaka N, et al. Nanoscale Electrical Potential and Roughness of a Calcium Phosphate Surface Promotes the Osteogenic Phenotype of Stromal Cells. *Materials (Basel).* 2018;11(6).

40. Sabu Thomas MMUCPS, K.M P, Elsevier All Access Books, eBook - Materials Science 2018 [EBCMS18]. Non-Thermal Plasma Technology for Polymeric Materials. S.l.: Elsevier; 2019. 1 online resource p.

41. Lin WC, Mohd Razali NA. Temporary Wettability Tuning of PCL/PDMS Micro Pattern Using the Plasma Treatments. *Materials (Basel).* 2019;12(4).

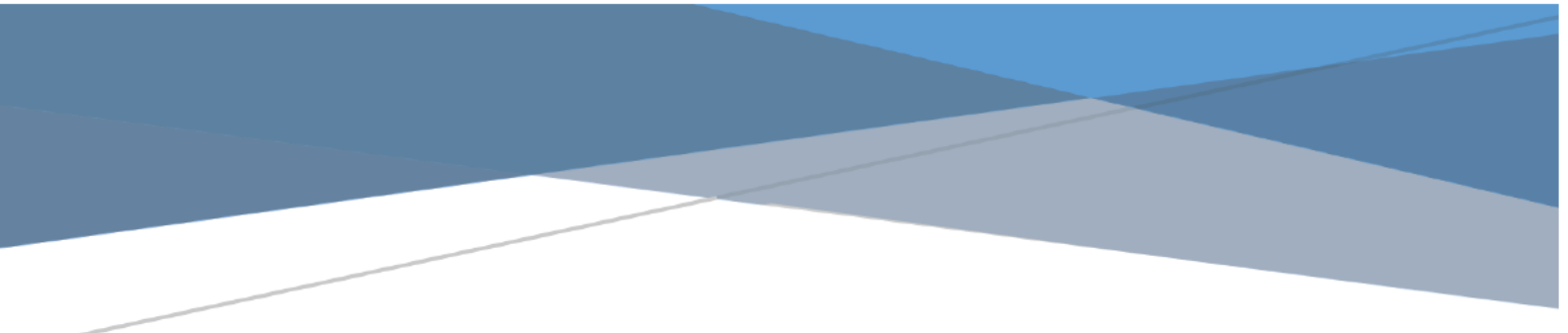
42. Cheng C, Gupta M. Surface functionalization of 3D-printed plastics via initiated chemical vapor deposition. *Beilstein journal of nanotechnology.* 2017;8:1629-36.

43. Kumar AK, Sharma S. Recent updates on different methods of pretreatment of lignocellulosic feedstocks: a review. *Bioresources and bioprocessing*. 2017;4(1):7.
44. Luickx N, Van den Vreken N, D'Oosterlinck W, Van der Schueren L, Declercq H, De Clerck K, et al. Optimization of the activation and nucleation steps in the precipitation of a calcium phosphate primer layer on electrospun poly(ϵ -caprolactone). *Journal of biomedical materials research Part A*. 2015;103(2):511-24.
45. Wang W, Caetano G, Ambler WS, Blaker JJ, Frade MA, Mandal P, et al. Enhancing the Hydrophilicity and Cell Attachment of 3D Printed PCL/Graphene Scaffolds for Bone Tissue Engineering. *Materials (Basel)*. 2016;9(12).
46. Li J, Chen M, Wei X, Hao Y, Wang J. Evaluation of 3D-Printed Polycaprolactone Scaffolds Coated with Freeze-Dried Platelet-Rich Plasma for Bone Regeneration. *Materials (Basel)*. 2017;10(7).
47. Araujo JV, Martins A, Leonor IB, Pinho ED, Reis RL, Neves NM. Surface controlled biomimetic coating of polycaprolactone nanofiber meshes to be used as bone extracellular matrix analogues. *Journal of biomaterials science Polymer edition*. 2008;19(10):1261-78.
48. Yu HS, Jang JH, Kim TI, Lee HH, Kim HW. Apatite-mineralized polycaprolactone nanofibrous web as a bone tissue regeneration substrate. *Journal of biomedical materials research Part A*. 2009;88(3):747-54.
49. Kobayashi A, Kuroda T, Kimura H, Inoue A. Effect of Zr on microstructure of metallic glass coatings prepared by gas tunnel type plasma spraying. *Journal of nanoscience and nanotechnology*. 2012;12(6):4883-6.
50. Li Y, Liao C, Tjong SC. Synthetic Biodegradable Aliphatic Polyester Nanocomposites Reinforced with Nanohydroxyapatite and/or Graphene Oxide for Bone Tissue Engineering Applications. *Nanomaterials (Basel)*. 2019;9(4).

51. Harito C, Bavykin DV, Yuliarto B, Dipojono HK, Walsh FC. Polymer nanocomposites having a high filler content: synthesis, structures, properties, and applications. *Nanoscale*. 2019;11(11):4653-82.
52. Barrere F, van Blitterswijk CA, de Groot K, Layrolle P. Nucleation of biomimetic Ca-P coatings on Ti6Al4V from a SBF x 5 solution: influence of magnesium. *Biomaterials*. 2002;23(10):2211-20.
53. Lyutova E, Borilo L, Izosimova E. The effect of sodium and magnesium ions on the properties of calcium-phosphate biomaterials. *Progress in Biomaterials*. 2019;8(2):127-36.
54. Chocholata P, Kulda V, Babuska V. Fabrication of Scaffolds for Bone-Tissue Regeneration. *Materials (Basel)*. 2019;12(4).
55. Morejon L, Delgado JA, Antunes Ribeiro A, Varella de Oliveira M, Mendizabal E, Garcia I, et al. Development, Characterization and In Vitro Biological Properties of Scaffolds Fabricated From Calcium Phosphate Nanoparticles. *International journal of molecular sciences*. 2019;20(7).
56. Mohd Pu'ad NAS, Koshy P, Abdullah HZ, Idris MI, Lee TC. Syntheses of hydroxyapatite from natural sources. *Heliyon*. 2019;5(5):e01588.
57. Zheng K, Lin Z, Capece M, Kunnath K, Chen L, Dave RN. Effect of Particle Size and Polymer Loading on Dissolution Behavior of Amorphous Griseofulvin Powder. *Journal of pharmaceutical sciences*. 2019;108(1):234-42.
58. Pan X, Julian T, Augsburger L. Increasing the dissolution rate of a low-solubility drug through a crystalline-amorphous transition: a case study with indomethacin [correction of indomethicin]. *Drug development and industrial pharmacy*. 2008;34(2):221-31.
59. Dorozhkin SV, Epple M. Biological and medical significance of calcium phosphates. *Angew Chem Int Ed Engl*. 2002;41(17):3130-46.

60. Barralet JE, Lilley KJ, Grover LM, Farrar DF, Ansell C, Gbureck U. Cements from nanocrystalline hydroxyapatite. *Journal of materials science Materials in medicine*. 2004;15(4):407-11.
61. Shaddel S, Ucar S, Andreassen JP, Osterhus SW. Enhancing efficiency and economics of phosphorus recovery process by customizing the product based on sidestream characteristics - an alternative phosphorus recovery strategy. *Water science and technology : a journal of the International Association on Water Pollution Research*. 2019;79(9):1777-89.
62. Mekmene O, Rouillon T, Quillard S, Pilet P, Bouler JM, Pezenec S, et al. Effects of citrate and NaCl on size, morphology, crystallinity and microstructure of calcium phosphates obtained from aqueous solutions at acidic or near-neutral pH. *J Dairy Res*. 2012;79(2):238-48.
63. Jang HL, Zheng GB, Park J, Kim HD, Baek HR, Lee HK, et al. In Vitro and In Vivo Evaluation of Whitlockite Biocompatibility: Comparative Study with Hydroxyapatite and beta-Tricalcium Phosphate. *Adv Healthc Mater*. 2016;5(1):128-36.
64. Apelt D, Theiss F, El-Warrak AO, Zlinszky K, Bettschart-Wolfisberger R, Bohner M, et al. In vivo behavior of three different injectable hydraulic calcium phosphate cements. *Biomaterials*. 2004;25(7-8):1439-51.
65. Tran RT, Naseri E, Kolasnikov A, Bai X, Yang J. A new generation of sodium chloride porogen for tissue engineering. *Biotechnol Appl Biochem*. 2011;58(5):335-44.
66. Sun L, Berndt CC, Khor KA, Cheang HN, Gross KA. Surface characteristics and dissolution behavior of plasma-sprayed hydroxyapatite coating. *J Biomed Mater Res*. 2002;62(2):228-36.
67. Abou Neel EA, Aljabo A, Strange A, Ibrahim S, Coathup M, Young AM, et al. Demineralization-remineralization dynamics in teeth and bone. *Int J Nanomedicine*. 2016;11:4743-63.

68. Al-Munajjed AA, O'Brien FJ. Influence of a novel calcium-phosphate coating on the mechanical properties of highly porous collagen scaffolds for bone repair. *J Mech Behav Biomed Mater.* 2009;2(2):138-46.
69. Obayi CS, Tolouei R, Mostavan A, Paternoster C, Turgeon S, Okorie BA, et al. Effect of grain sizes on mechanical properties and biodegradation behavior of pure iron for cardiovascular stent application. *Biomatter.* 2016;6:e959874.



CHAPTER 3

**EFFECT OF GRADIENT AND OFFSET
ARCHITECTURES ON MECHANICAL AND
BIOLOGICAL PROPERTIES OF 3-D MELT
ELECTROWRITTEN (MEW) SCAFFOLD**

STATEMENT OF CONTRIBUTION TO CO-AUTHORED PUBLISHED PAPER

This chapter includes a **published** co-authored paper. The bibliographic details of the co-authored paper, including all authors, are:

Naghmeh Abbasi, Abdalla Abdal-hay, Stephen Hamlet, Elizabeth Graham, Saso Ivanovski. Effects of Gradient and Offset Architectures on Mechanical and Biological Properties of 3-D Melt electrowritten (MEW) scaffolds. ACS Biomaterials Science and Engineering Journal; 2019 May, <https://doi.org/10.1021/acsbiomaterials.8b01456> (IF: 4.511)

My contribution to the paper involved:

Designing of the project, provision of the data, the preliminary analysis and categorisation of the data into a usable format and providing direction on the scope and structure of the analysis, interpretation of results and drafting of paper.


_____ Date 10-Dec-2019

Naghmeh Abbasi


_____ Date 10-Dec-2019

Corresponding authors of paper: Prof. Saso Ivanovski


_____ Date 10-Dec-2019
Supervisor: Dr. Stephen Hamlet

ABSTRACT

This study describes the fabrication and characterization of three-dimensional (3-D) PCL scaffolds with defined pore architectures prepared using MEW technique. Three homogeneous pore sized (250, 500 and 750 μm) scaffolds, two fibre offset (30/70 and 50/50) and a three-layered (250 μm bottom – 500 μm middle – 750 μm top) gradient pore sized scaffold were designed and printed with ~ 10 μm fibres.

The mechanical properties (tensile and compression tests), total surface area, porosity of these scaffolds and their ability to promote the attachment and proliferation of human osteoblasts were then compared. All scaffolds induced good tensile properties however they reacted differently during compressive testing. The offset 30/70 scaffold had the highest surface area to volume ratio which enhanced osteoblast attachment after 3 days of cell culture.

While the highest initial level of osteoblast attachment at day 1 was found on the 250 μm homogenous scaffold, the highest degree of cell proliferation and infiltration at day 30 was observed in the three-layered graded porosity scaffold.

In terms of physical and biological properties to support bone cell distribution and migration through the entire structure of the scaffold, our results suggest that melt electrowritten offset and gradient scaffolds are good candidate platforms for cell infiltration and growth compared to homogeneous scaffolds.

INTRODUCTION

Organ and tissue transplantation is often hampered by problems with morbidity, immune rejection, immunosuppressive therapy and the shortage of donor organs. To address this problem, scaffolds that can be seeded with cells and growth factors to stimulate cell growth are widely used as templates for specific tissue formation (1). The physical structure of the ideal scaffold needs a pore system architecture that will ensure the appropriate distribution and transportation of nutrients and oxygen as well as removing waste materials to promote cell attachment, infiltration, growth, proliferation, migration and ultimately integration with the host (2, 3).

Many methods have been used to design 3-D porous scaffolds such as additive manufacturing, immersion precipitation, freeze drying, salt leaching, laser sintering and electrospinning (4). However, in order to create a homogenous porous structure with large ordered pore size ($> 100 \mu\text{m}$) which can provide a suitable substrate that favours tissue infiltration, a direct MEW technique which controls filament deposition during the spinning process is an excellent candidate (5, 6). More recently, MEW has been shown to be able to control the diameter and deposition of fibres within the scaffold during the printing process resulting in customisable pore shapes and overall control of the scaffold architecture (7).

Previous studies suggest that osteoblasts prefer scaffolds with a defined range of pore sizes to facilitate the regeneration of mineralized tissue e.g. scaffold pore sizes between 200 to 350 μm appear to be an optimal platform for osteoblast proliferation and promote rapid bone formation and substantial bone ingrowth (8). In contrast, larger pore sizes (500 μm) did not enhance cell attachment or promote cell infiltration (9, 10). Similarly, a scaffold pore size below 100 μm was associated with fibroblast differentiation and non-mineralized soft tissue infiltration (11).

Apart from pore size, 3D-printed scaffolds with different strut offsets particularly those

with values of 50% and 100%, can allow cells to grow homogeneously due to a higher number of anchorage points and higher uptake ability, while interconnected struts create the angles which can influence cell function through mechanotransduction. Previous studies have suggested that cell proliferation and seeding efficiency is also increased in offset scaffolds because of the higher contact time between the scaffold surface area and the fluid containing cells (12).

Since the ECM of natural bone displays a gradient porous architecture from the cortical bone to the cancellous bone, we propose that a porous scaffold with a porosity-graded architecture would be a good template to mimic natural bone ECM. A combination of a highly porous region should afford more cell growth and nutrient-waste flow transport because of the greater surface area, while a lower porous layer provides mechanical support for external loading (13, 14). The present study therefore aimed to design and compare the mechanical properties of offset and gradient porous 3-D scaffolds using MEW and to investigate the role of pore size and gradient architecture on cell growth and cell-scaffold interactions in order to identify suitable architectures for scaffold assisted bone regeneration.

MATERIALS AND METHODS

Melt Electrowriting (MEW)

The MEW printer used in this study contained a high voltage source (DX250R, EMCO, Hallein, Austria) controlled by a voltage divider (Digit Multimeter 2100, Keithley, Cleveland, USA), a pneumatically regulated melt feeding system (regulator, FESTO, Berkheim, Germany) and a planar movable aluminium collector plate (XSlide, Velmex, New York, USA) controlled by G-code (MACH 3 Computerized Numerical Control (CNC) software, ARTSOFT, Livermore Falls, USA). A proportional-integral-derivative controller was used to regulate the electrical heating system (TR400, Delta-t, Bielefeld, Germany) to assure a stable melt temperature profile.

2.0 g of medical-grade 80 kDa PCL pellets (Corbion, Australia) were placed in a 2 ml syringe with a 21G nozzle, and heated to 80°C for 30 min to melt the PCL before insertion into the MEW heating head. The feed rate was 20 mL/h which was controlled via compressed air. A threshold voltage between 5 and 7 kV was applied to create the charged polymer and form a Taylor cone. The X-Y movement of the collector platform was controlled using programmable software (G-code) that afforded polymer fibre deposition in the desired pattern. Three different pore size homogeneous scaffolds (250 µm, 500 µm and 750 µm), two displaced offset scaffolds (Offset 30/70, Offset 50/50) with 30% and 50% lay down patterns respectively, as well as a gradient scaffold of three different pore sizes in the one scaffold (top layer 750 µm, middle layer 500 µm, bottom layer 250 µm) were designed and printed (Figure 3.1). The distance between the tip and collector was 10 mm. All designed scaffolds were fabricated in a 1 mm thick mesh structure with a 0 - 90° lay-down pattern. A 6 mm diameter tissue biopsy punch (kai Europe GmbH, Solingen, Germany) was used to prepare standard circular shaped scaffolds for the *in vitro* experiments.

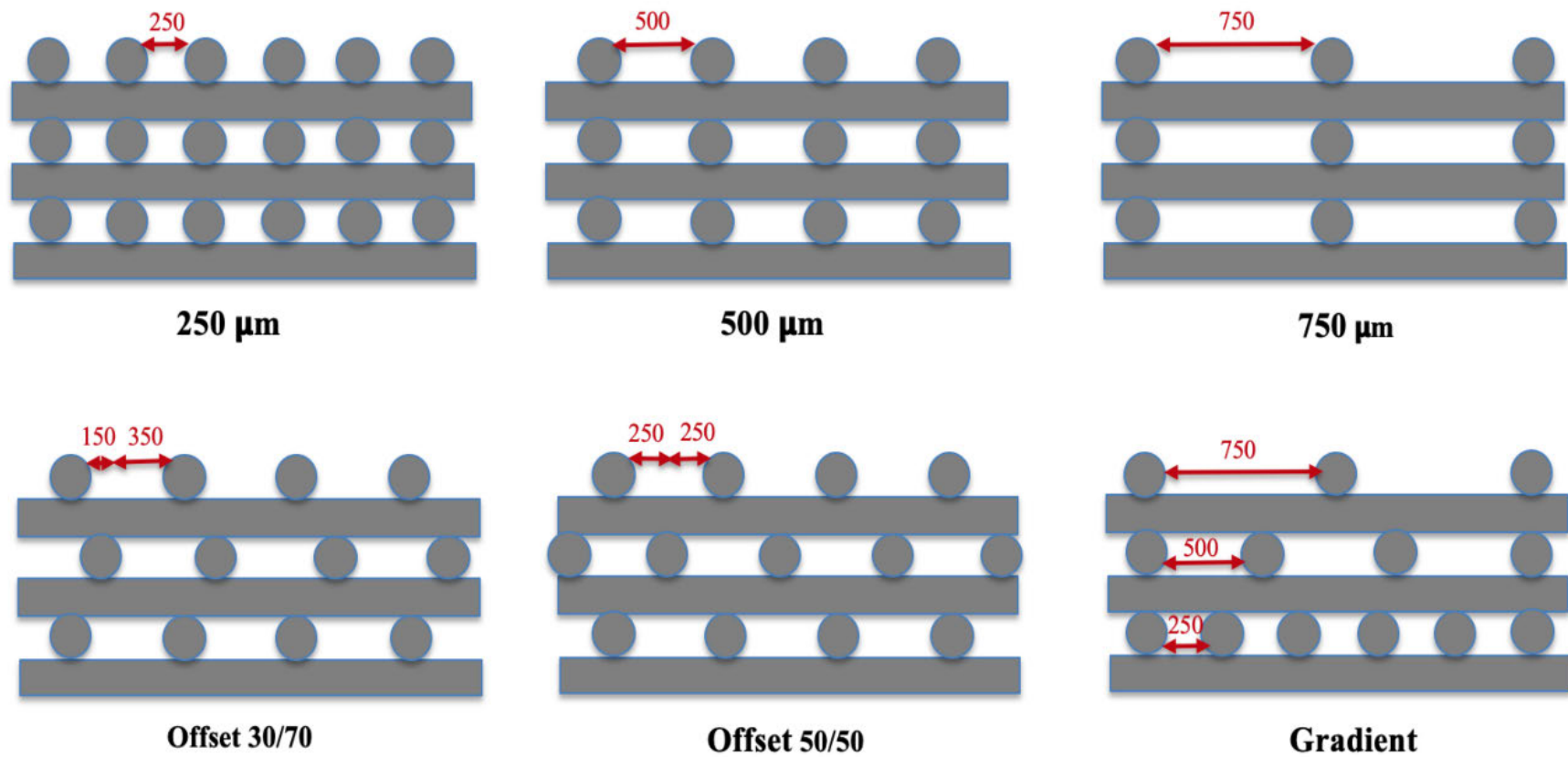


Figure 3.1. Schematic illustrates the design of the different pore structured PCL scaffolds: homogeneous pore size constructs of 250, 500, 750 μm; offset 30/70; offset 50/50; gradient pore structure.

CaP Coating

CaP was deposited on the fibre surfaces by immersion in 10x simulated body fluid (SBF) (15-18). Briefly, the punched scaffolds were placed in ethanol under a vacuum for 15 min to remove entrapped air bubbles. After that, the scaffolds were immersed in pre-warmed 2M NaOH at 37 °C for 30 min in a water bath. The scaffolds were washed 5 times with Milli Q water until the pH was neutralized. SBF solution was added to cover the scaffolds completely (50 mL in a Falcon tube containing 20 scaffolds). The Falcon tubes were kept under vacuum for 5 minutes then placed at 37°C for 30 min and were shaken every 10 min. After 30 min the SBF solution was removed and fresh SBF was placed in the same Falcon tubes containing the scaffolds for 30 min. After washing the scaffolds twice in Milli Q water, the scaffolds were immersed in 0.5 M NaOH at 37°C for 30 min. Finally, the scaffolds were rinsed with distilled water then left to dry at room temperature.

Scanning Electron Microscopy (SEM)

Scanning electron microscopy was used to investigate the morphology of the uncoated and CaP-coated MEW fabricated scaffolds. For this purpose, dried samples were mounted on copper stubs using adhesive carbon tapes and sputter coated with gold for 2 min. Images were captured using a Jeol JCM-5000 SEM at 15 kV accelerating voltage. Cross-sectional views of the specimens were obtained by fracturing the scaffolds in liquid nitrogen in order to visualise the internal structure.

Alizarin Red Staining

To assess CaP deposition on the alkali treated PCL scaffolds, alizarin red staining was performed. Specimens were covered in 500 µl of alizarin red solution for 20 min. The dye was eliminated by softly rinsing in pure water until only clear water remained. After washing the samples were immersed in cetylpyridinium chloride for 1 hour to solubilize the CaP precipitates. The solution was then placed into a 96-well plate (triplicates of 100

μl) and the optical density was measured at 562 nm. The results were normalised by the weight of scaffolds.

Water Contact Angle

The hydrophobicity of untreated and CaP-treated scaffolds was measured using a FTA200 Contact Angle and Surface Tension Instrument (Poly-Instruments Pty. Ltd., Australia). The angle between a liquid droplet and the solid surface was measured using a CCD video camera and lens mounted on a 3 viewing stage. A video capture card allowed observation of the samples in real time and saved the images for later measurement. A disposable syringe equipped with a needle diameter of 0.279 mm was filled with distilled water and was adjusted into the camera's field of view. The pump speed was set to $2\mu\text{l}$ per second so that a 1.0 mm diameter droplet of water was placed gently on the scaffold surface. Three measurements of each contact angle were performed on different parts of the scaffold.

Mechanical Properties

Compressive and tensile strength tests were performed on the CaP coated PCL (n=6) scaffolds using an Instron 5848 Micro Tester. For the compression tests, the measurements were performed at 37 °C in PBS. The samples were cut into 10x10 mm squares 2 mm thick. The static forces of a 5 N load cell was applied at 1mm/min until the scaffold reached 1mm displacement. The deformation (mm) and force F (N) were recorded by the Instron software for each sample. The Young's modulus (kPa) was estimated from the resultant stress-strain curve as the slope of the initial linear portion of the curve with any toe region due to the initial settling of the specimen neglected. Compressive strength at yield was defined as the intersection of the stress-strain curve with the modulus slope at an offset of 1.0% strain.

For the tensile strength tests, 2 mm thick PCL scaffolds were cut with a sharp blade into rectangles 45×10 mm. The thickness of the samples was measured in micrometers

(Mitutoyo IP 65, China) with $\pm 1 \mu\text{m}$ precision. Conventional macro-tensile measurements were performed using an electromechanical MicroTester machine (Instron 5848, Norwood, Ma). All the samples were mounted between two clamps at a gauge length of 15 mm instrumented with a 500 N load cell. Tensile testing was applied at a rate of 15 mm/min at room temperature until total failure of the specimen. The experimental load-elongation curves were recorded and the slope of each stress-strain curve in its elastic deformation region was calculated by the Instron software to obtain Young's modulus and strain at break (%).

Micro-Computed Tomography (μ -CT)

In order to measure the pore size and the porosity of the scaffolds, 1 cm diameter circular punches were located inside the x-ray tube of a micro-CT scanner (μ CT40, SCANCO Medical AG, Brüttsellen, Switzerland) and scanned using the following parameters; a current of 120 μA and a voltage of 55 kV at a greyscale threshold of 10 and resolution of 6 μm . 3D images of the scaffolds were reconstructed from the 2D scanned slices by the micro-CT system software package. Subsequently, a suitable threshold corresponding to the original grayscale images was selected, contour lines were drawn around the scaffold and 3D images were assessed. The average value of the pore size and porosity of specimens were measured using the quantitative 3D evaluation program included with the micro computed tomography (CT) software package.

Surface Area

Argon gas adsorption isotherms were collected on all scaffolds at 77 degrees Kelvin. The measurements were performed on a surface area analyser (ASAP 2020, Micromeritics Instrument Co, Norcross, USA). Scaffold sheets (40 mm \times 40 mm \times 1 mm \sim 0.2 g) were sliced and placed in a glass vacuum sample tube and evacuated to 3 μmHg . A series of freeze dry degassing steps were applied to remove absorbed impurities. A five point BET isotherm was collected (up to a pressure of 203.37 mmHg / pressure of \sim 0.2 bar) after

each freeze drying step, and this was repeated until a stable result was achieved. Two full Argon adsorption experiments were then performed at 77.45°K. The specific surface area (in m²/g) was obtained by measuring the total surface area and dividing by the total scaffold mass. The Brunauer–Emmett–Teller (BET) method was used to determine the surface area of the scaffold. Pore size distributions were determined using BJH analysis on the adsorption branch of the full isotherms.

Cell Culture

Human osteoblasts (hOB) previously isolated from the alveolar bone of a healthy 24-year-old female patient were used for all *in vitro* studies. Ethical approval for the use of this tissue was attained from the Griffith University Human Research Ethics Committee (ref# DOH/17/07/HREC). These cells have been shown to undergo differentiation in response to osteogenic conditions (19). hOB cells at 85% confluency were cultured in either basal (Dulbecco's modified Eagle's medium, Penicillin-Streptomycin 10,000 U/mL, Non-Essential Amino Acids 10 U/ml, 10% Foetal Bovine Serum, Life Technologies, Pty Ltd) or osteogenic supplemented medium (0.1 mM dexamethasone, 10 mM beta-glycerophosphate, and 50 mg/ mL L-ascorbic acid-2-phosphate (Gibco, St. Louis, MO, USA) for 1, 3, 14 and 30 days.

Scaffolds were inserted into the wells of a 6-well tissue culture plate and sterilized using 70% ethanol for 1 h and UV for 30 min. 2×10^4 hOB cells in 15 μ l of basal culture media were seeded onto each MEW scaffold. The scaffolds and cells were rehydrated every 30 min by adding 6 μ l of medium to feed the cells and prevent drying during incubation. After 6 hr incubation, the scaffolds were transferred to a new plate to ensure that only cells that attach to the scaffold are assessed during the study. 1 ml of medium was then added to each well. The scaffolds were cultured for 8 weeks in both basal and osteogenic medium. A total of fourteen experimental groups were assessed i.e. 6 different pore size / architectures; (1) 250 μ m, (2) 500 μ m, (3) 750 μ m, (4) Offset.30.70, (5) Offset.50.50,

(6) Gradient and a control (7) Tissue Culture Plate (TCP) in both basal and osteogenic supplemented medium.

Confocal Microscopy

The distribution and infiltration of the hOB cells into the 3-D fibrous scaffolds was assessed by confocal microscopy (Nikon, Eclipse-Ti, U.S.A). Constructs were fixed in 4% paraformaldehyde in PBS for 30 min at room temperature then washed in PBS three times. The hOB cell membrane was subsequently permeabilised using 0.1% triton X-100 solution for 5 min. After two rinses with PBS, the specimens were incubated in a mixture of red fluorescent phalloidin conjugate in 1% BSA (AAT Bioquest, USA) for 3 hours. The scaffolds were then rinsed twice more in PBS. To visualise the cell nuclei, scaffolds were stained with 4',6-diamidino-2-phenylindole (DAPI, Vector Laboratories, Burlingame, CA, USA) dye for 30 min at room temperature. The scaffolds were rinsed gently another three times in PBS to remove excess phalloidin conjugate and were placed on a glass slide for observation under a confocal microscope.

DNA Content Analysis

To quantify cell numbers, the scaffolds were transferred into 1.5 ml micro centrifuge tubes and digested with 500 μ l of 0.5 mg/mL Proteinase K (Invitrogen) in phosphate buffered EDTA, at 60°C for at least 24 hr until no visible scaffold material remained. The cells on the tissue culture plates were also incubated with Proteinase K at 37 °C for 24 hr. To precipitate any remaining proteins, the digested scaffolds were then centrifuged at 9000 rpm for 5 min and the purified supernatant was transferred to a new micro centrifuge tube. To calculate the final DNA content of the sample, a standard curve of known λ DNA concentrations ranging from 1 ng/mL to 1 μ g/mL was constructed. Then, 100 μ l of the purified supernatant and the diluted standard DNA were aliquoted in triplicate into black 96-well plates, and 100 μ l of PicoGreen (P11496, Invitrogen) working solution was added to obtain a total volume of 200 μ l. After 5 min incubation in the dark the fluorescence

(excitation 485 nm, emission 520 nm) was measured using a fluorescence plate reader (POLARstar Omega, BMG LABTECH, Germany). For the DNA analyses, 3 biological replicates were used.

Statistical Analysis

To assess the statistical significance of any differences, a one-way ANOVA was performed with post hoc analysis (Tukey) corrected for multiple comparisons. A p value of <0.01 was considered as statistically significant.

RESULTS

Physical and Mechanical Characteristics of Fabricated Scaffolds

Scaffold Morphology and Architecture

Six scaffolds with a square pore shape with a 0-90 ° pattern were successfully printed (Figure 3.2A-F). SEM images of the homogenous scaffolds (Figure 3.2A-C) showed good bonding between the fibres and pore dimensions as designed using the CNC software. Offset scaffolds were produced using a continuous offset value of 30% and 50% between consecutive layers (Figure 3.2-D, E). In addition, a gradient scaffold was created with three different layers of pore sizes (750/500/250 µm) in the one construct (Figure 3.2-F). NaOH treatment prior to CaP coating did not appear to have any significant effect on either the scaffold fibers (supplementary information Figure S1).

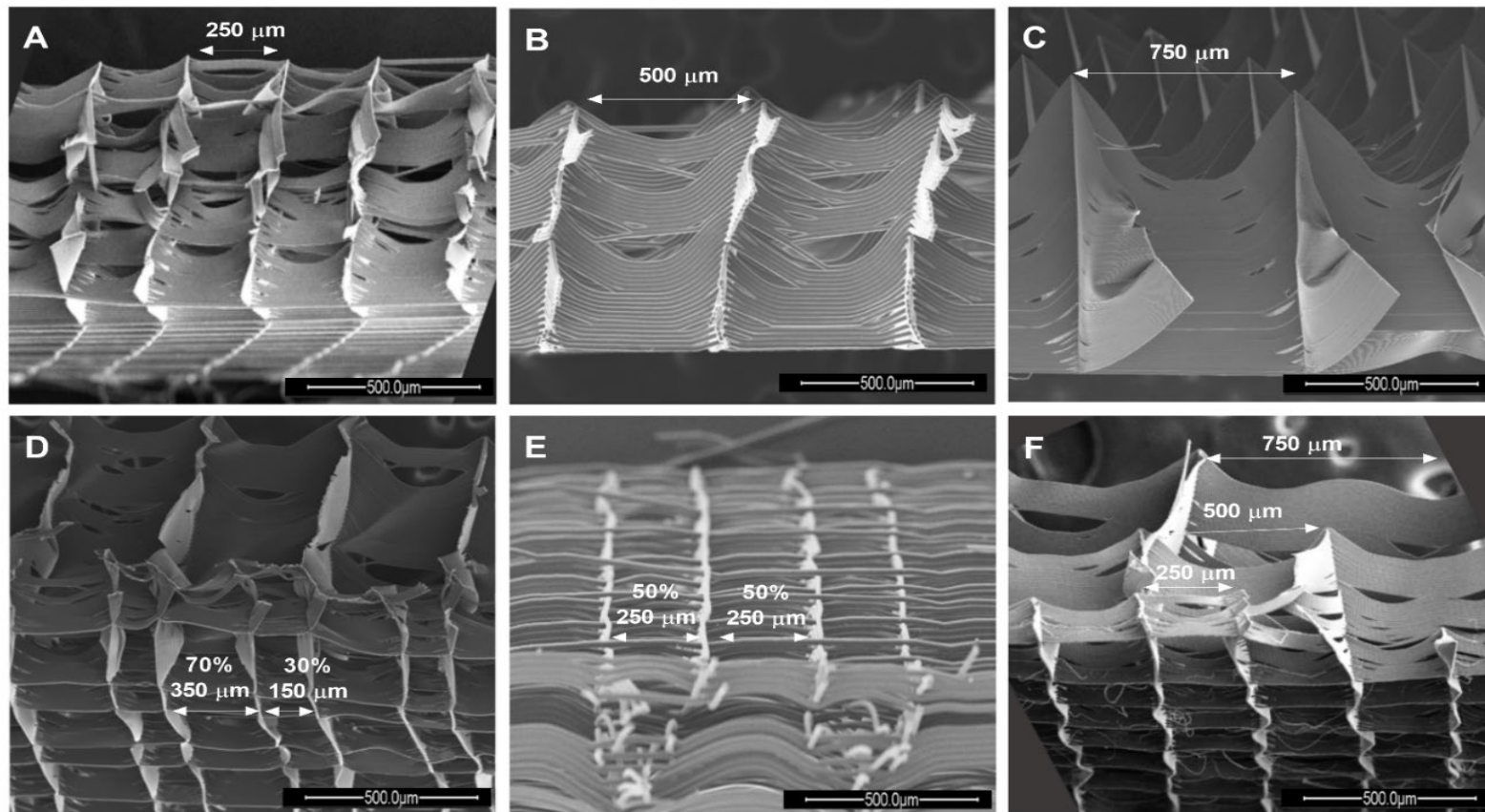


Figure 3.2. SEM images of the different pore structured PCL scaffolds fabricated using MEW; (A) 250 μm , (B) 500 μm , (C) 750 μm , (D) Offset.30.70, (E) Offset.50.50, (F) Gradient.

CaP Coating

Figure 3.3 shows the surface morphology of the PCL fibrous scaffold before (Figure 3.3-A, B) and after (Fig 3C-F) deposition of a thin layer of CaP onto the fibre surface. The nano-textured CAP coating appeared homogeneous without any evidence of cracking (Figure 3.3-D). The diameter of the pristine PCL fibres without any treatment was between 6-10 μm (Figure 3.3-B, S2) and as judged by the SEM observations, the CaP layer did not have a significant effect on the resultant fibre diameter or pore size. Alizarin red S staining subsequently confirmed deposition of CaP on the surface of the PCL fibrous scaffolds regardless of architecture (Figure 3.4). NaOH treatment prior to CaP coating did not appear to have any significant effect on Alizarin red S staining (supplementary information Figure S3).

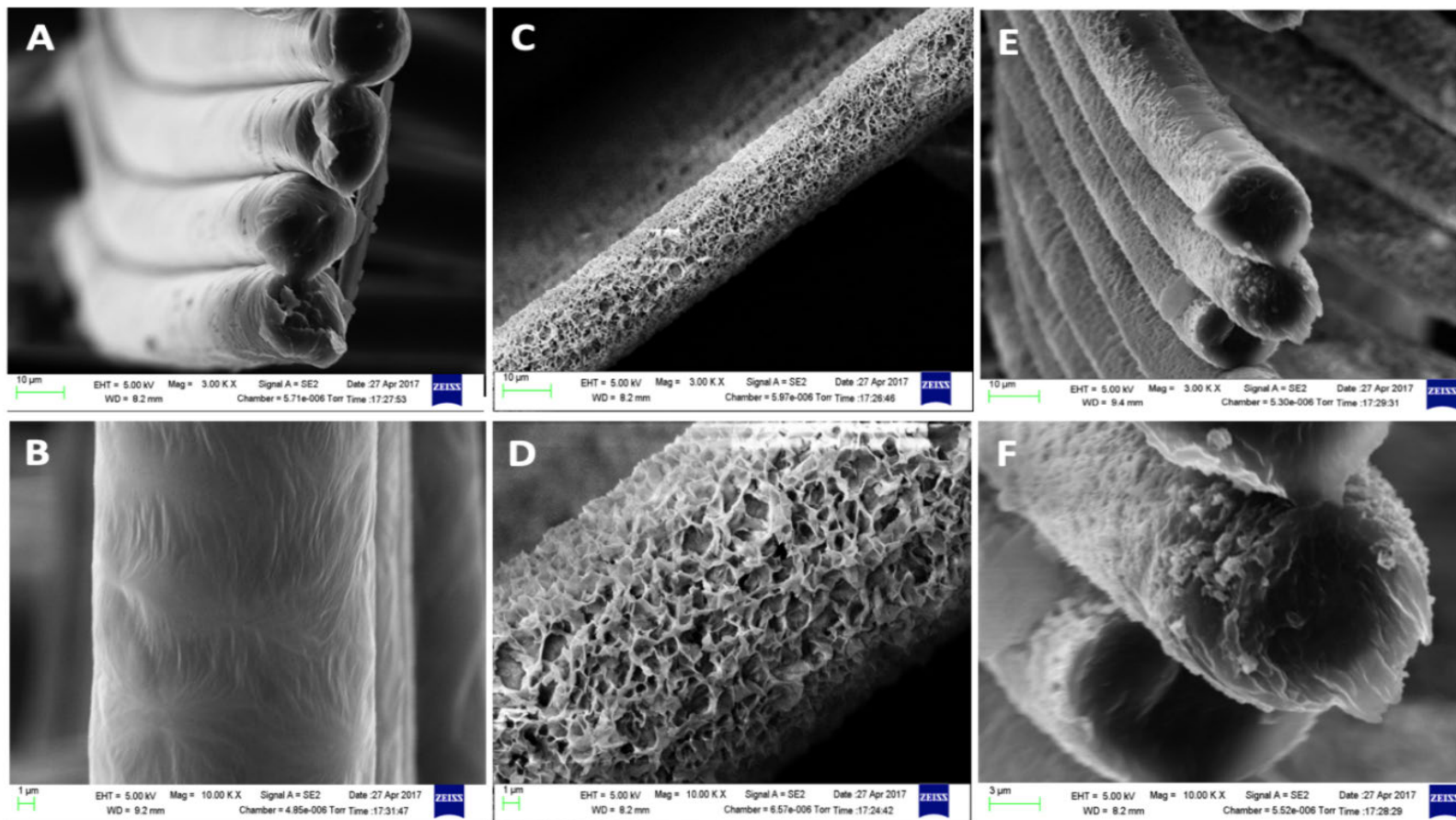


Figure 3.3. SEM images of PCL surfaces modified by treating with calcium phosphate: (A, B) non coated scaffold fibers, (C, D) CaP coated scaffold fibers, (E, F) Cross-sectional view of CaP-coated scaffold fibers.

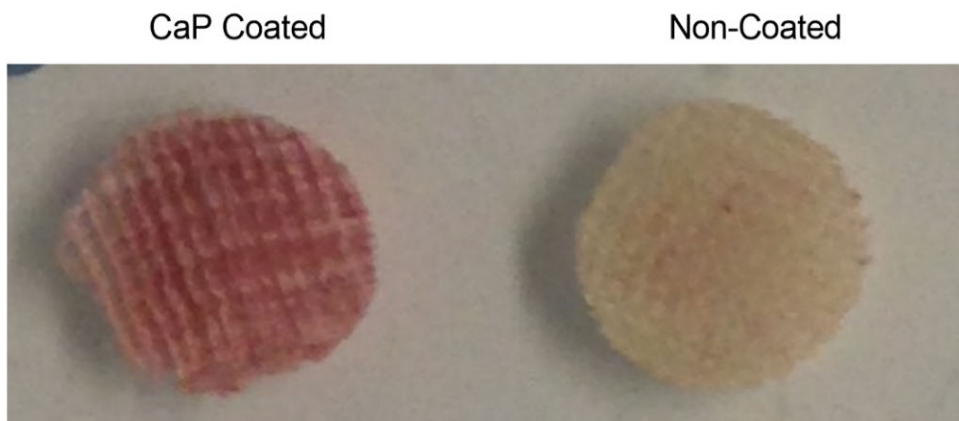
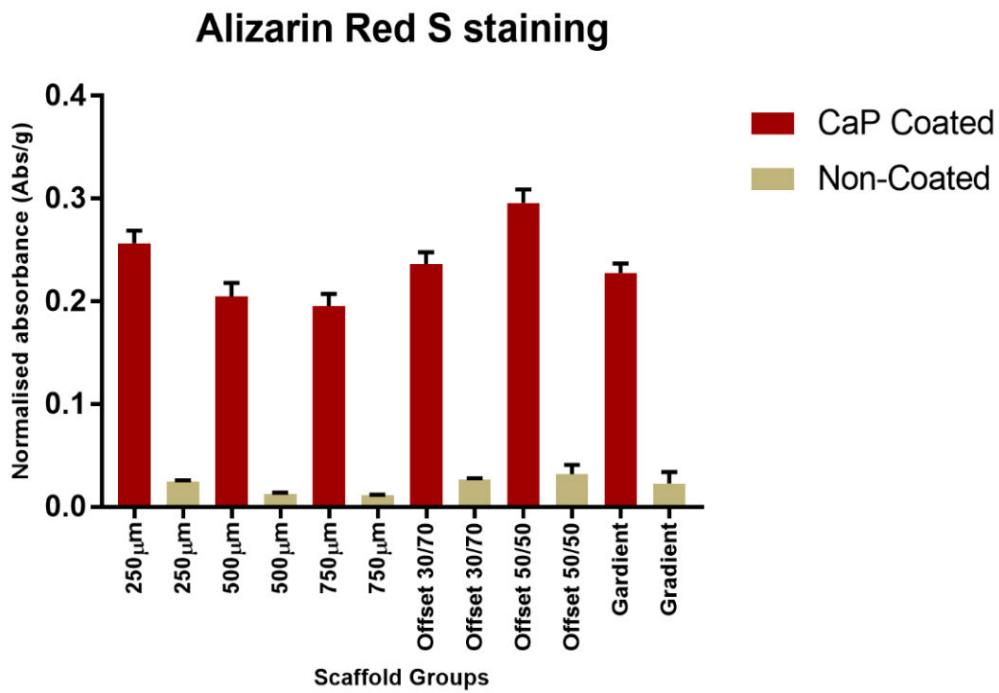


Figure 3.4. Qualitative and quantitative assessment of alizarin Red staining showed homogenous CaP coating on melt electrowritten PCL scaffolds. Pore architecture did not significantly affect the amount of CaP deposited. **** $p < 0.0001$ CaP coated scaffolds versus non coated scaffolds.

Hydrophobicity

The contact angles of the CaP-coated and non-coated PCL scaffolds are shown in Figure 3.5. CaP coating significantly reduced the hydrophobicity of the PCL scaffolds as shown

previously by our group (18). Again, NaOH treatment prior to CaP coating did not appear to have any significant effect on hydrophobicity except for offset 50/50 and the gradient scaffolds (supplementary information Figure S4 & S5).

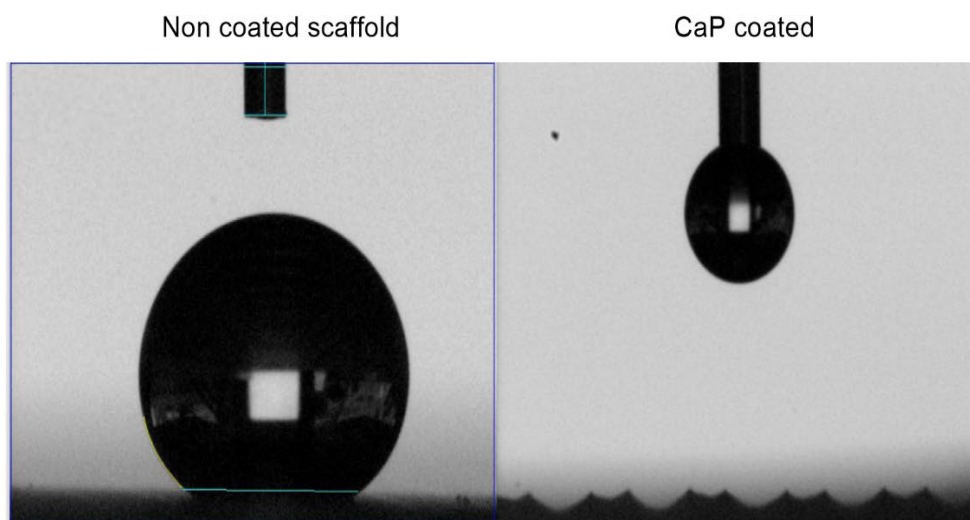
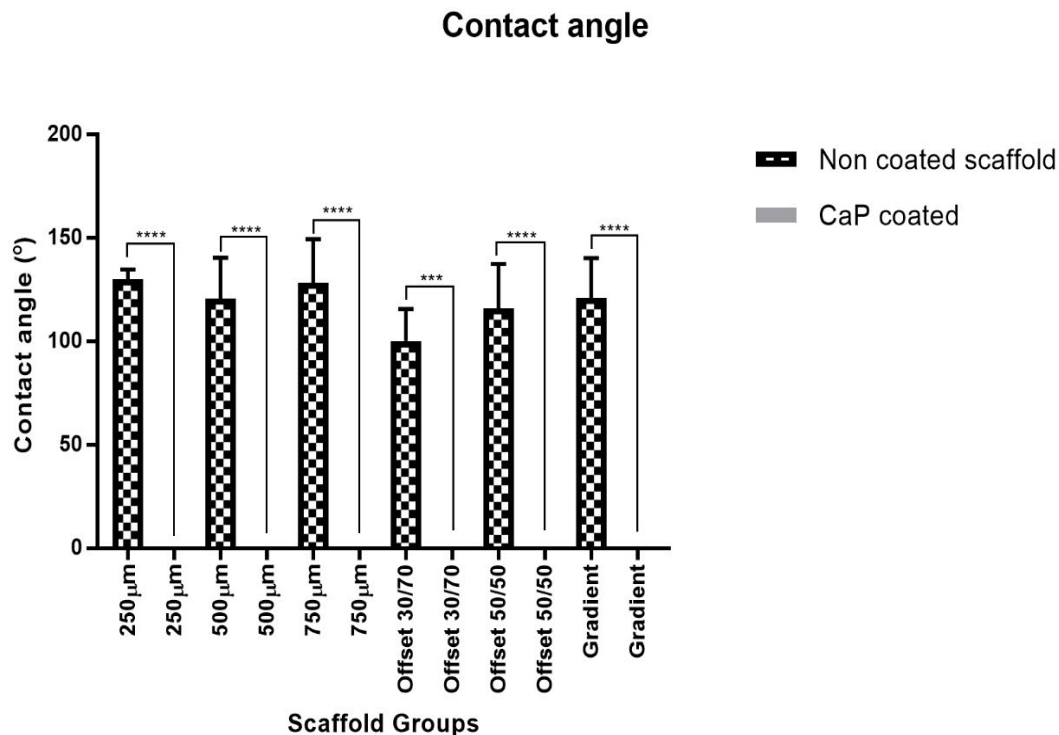


Figure 3.5. Image of contact angle assessment and graph showing CaP coating significantly reduced the hydrophobic nature of the PCL fibres. **** $p < 0.0001$, *** $p < 0.001$ CaP coated scaffolds versus non coated scaffolds.

Mechanical Properties

The compressive stress-strain curves and summarized results of compressive modulus, yield strength and maximum stress (50% strain) obtained for the samples under wet conditions (PBS) at 37 °C are shown in Fig. 3.6 and Table 3.1. The stress-strain curves of the MEW scaffolds demonstrated a typical behavior undergoing deformation. This comprises three distinct regions: a linear-elastic region followed by a plateau of roughly constant stress leading into a final region of steeply rising stress (densification stage). However, the stress-strain curves trend of each MEW scaffold exhibited differently under compression loading. As shown in Figure 3.6, there is a difference in deformation between the scaffolds up to 50% strain and the slope of stress-strain pattern for gradient scaffold that was more than that of the other scaffolds. The gradient scaffold showed the highest compression stress (38.2 ± 3.7 kPa) at 50% strain, whereas, the 500 μm homogeneous pore size induced the highest compressive modulus (137.2 ± 58.4 kPa) and yield strength (3.2 ± 0.75 kPa) compared to the other scaffolds under compression loading (Table 3.1). As the compression test was conducted in wet conditions (aqueous solution), it's likely the reduction of compressive modulus in the 750 μm scaffolds was due to their large pore size allowing more water penetration into the pores, thus influencing the stress curve performance during the compression load. However, the precise mechanism is still unknown and more detailed studies are required to clarify this phenomenon.

To further precisely estimate the mechanical properties of MEW fabricated scaffolds under axial loading with a complete fracture, tensile testing was performed (20). The tensile stress-strain curves of the fabricated PCL scaffolds are shown in Table. 2 and Fig 7A. All curves demonstrate similar trends with different offset magnitudes. The tensile (Young's) modulus (E) calculated by determining the slope of the stress-strain curve along the deformation portion, decreased from 4.34 ± 0.032 kPa in the 250 μm homogenous pore size scaffold to 1.67 ± 0.24 kPa and 0.91 ± 0.25 kPa in the 500 μm and

750 μm homogenous pore size scaffolds respectively. The tensile modulus also decreased from 3.32 ± 0.30 kPa in the gradient scaffold to 3.11 ± 0.12 kPa and 2.21 ± 0.29 kPa in the offset 50/50 and offset 30/70 scaffolds respectively (Figure 3.7-B). On the other hand, elongation at break in offset 50/50 and gradient scaffolds were higher than homogeneous architectures. This difference increased significantly in the offset 50/50 scaffold compared to the homogeneous structures (Figure 3.7-C).

The highest ultimate tensile strength (UTS, Figure 3.7-D) was observed in the homogenous 250 μm pore size PCL scaffold (640 ± 11.6 kPa) followed by the gradient (517.5 ± 6.2 kPa), offset 50/50 (510 ± 6.2 kPa) and homogenous 500 μm (482 ± 17.5 kPa) scaffolds. The lowest UTS (230 ± 14.1 kPa) was observed in the 750 μm homogenous pore size scaffold. Therefore, the homogenous 250 μm pore size scaffold had the highest capacity to resist loads tending to elongate compared to other scaffolds. Statistical analysis confirmed that the 250 μm scaffolds had significantly higher mechanical properties under tensile loading than those with a homogeneous larger pore size, offset and gradient pattern under tensile testing conditions ($p \leq 0.01$).

Table 3.1. Compressive Young's Modulus mean values for the CaP treated PCL fibrous scaffolds; a-d ($p=0.003$); e ($p=0.01$); f-h ($p < 0.0001$).

Sample	Compressive Young's Modulus (kPa)*	Compressive Yield Strength (kPa)	Maximum Stress (50% strain) (kPa)
250 μm	31.9 \pm 10.2 ^{a, c}	1.5 \pm 0.42 ^e	19.5 \pm 2.8 ^f
500 μm	137.2 \pm 58.4 ^{b, d}	3.2 \pm 0.75	28 \pm 2.6 ^g
750 μm	130.2 \pm 24.1 ^b	3.1 \pm 0.45	16.1 \pm 2.2 ^{f, h}
Offset.30.70	21.6 \pm 4.6 ^c	1.3 \pm 0.2 ^e	25.7 \pm 1.4 ^{f, g}
Offset.50.50	77 \pm 4.6	1.65 \pm 0.62 ^e	18.3 \pm 1.5 ^{f, h}
Gradient	32.1 \pm 4.2 ^c	1.4 \pm 0.41 ^e	38.2 \pm 3.7

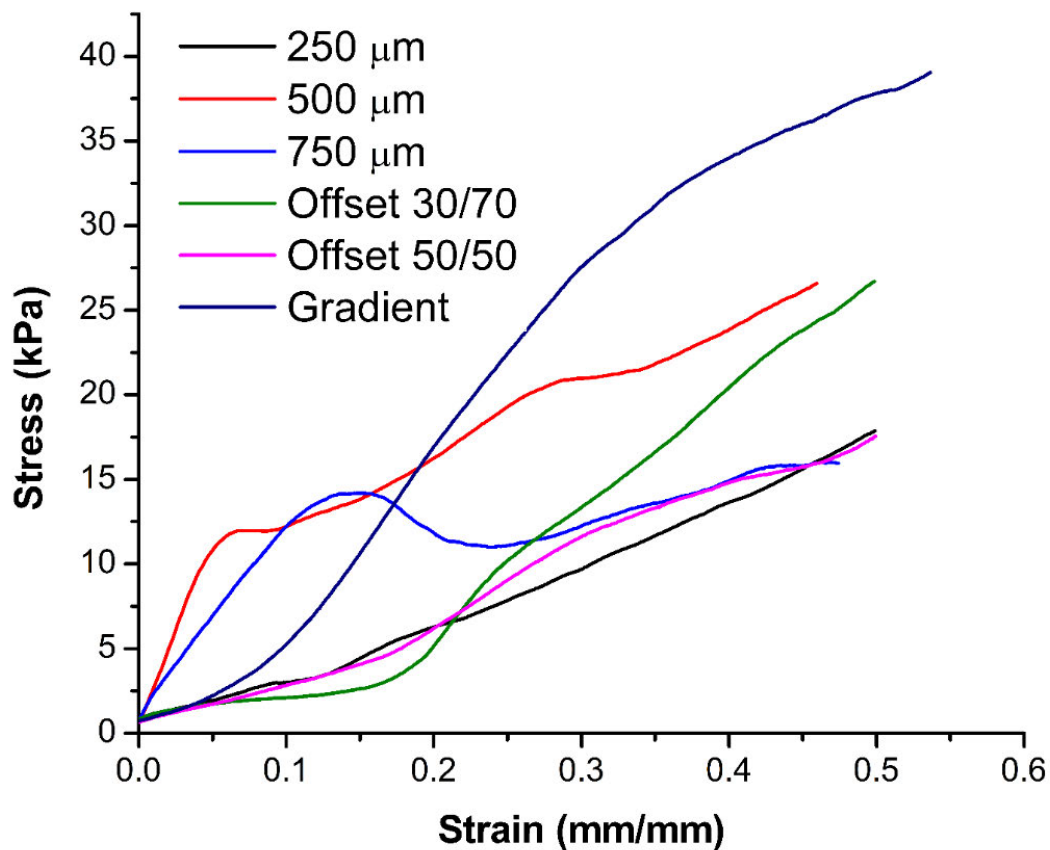


Figure 3.6. Typical Stress-strain curves under compression loading.

Table 3.2. Tensile strength for the CaP treated PCL fibrous scaffolds; a-c ($p < 0.0001$); d-f ($p < 0.0001$); g-l ($p=0.003$).

Sample	Young's Modulus (kPa)	Elongation at break (%)	Ultimate tensile strength (kPa)	Stiffness (N/m)
250 μm	4.34 \pm 0.32	832 \pm 4.21 ^a	640 \pm 11.67 ^{d, e, f}	3.28 \pm 0.23 ^g
500 μm	1.67 \pm 0.24	912 \pm 6.10 ^{a, b}	482 \pm 17.52 ^d	1.21 \pm 0.17 ^h
750 μm	0.91 \pm 0.25	1019 \pm 17.59 ^b	230 \pm 14.10 ^{d, e, f}	0.43 \pm 0.12 ⁱ
Offset.30.70	2.21 \pm 0.29	967 \pm 58.51 ^{a, b}	442.5 \pm 12.90 ^{d, e, f}	1.75 \pm 0.11 ^j
Offset.50.50	3.11 \pm 0.12	1186 \pm 101.11 ^c	510 \pm 6.24 ^e	2.40 \pm 0.05 ^k
Gradient	3.32 \pm 0.30	1120 \pm 101.42 ^c	517.5 \pm 6.21 ^f	2.92 \pm 0.21 ^l

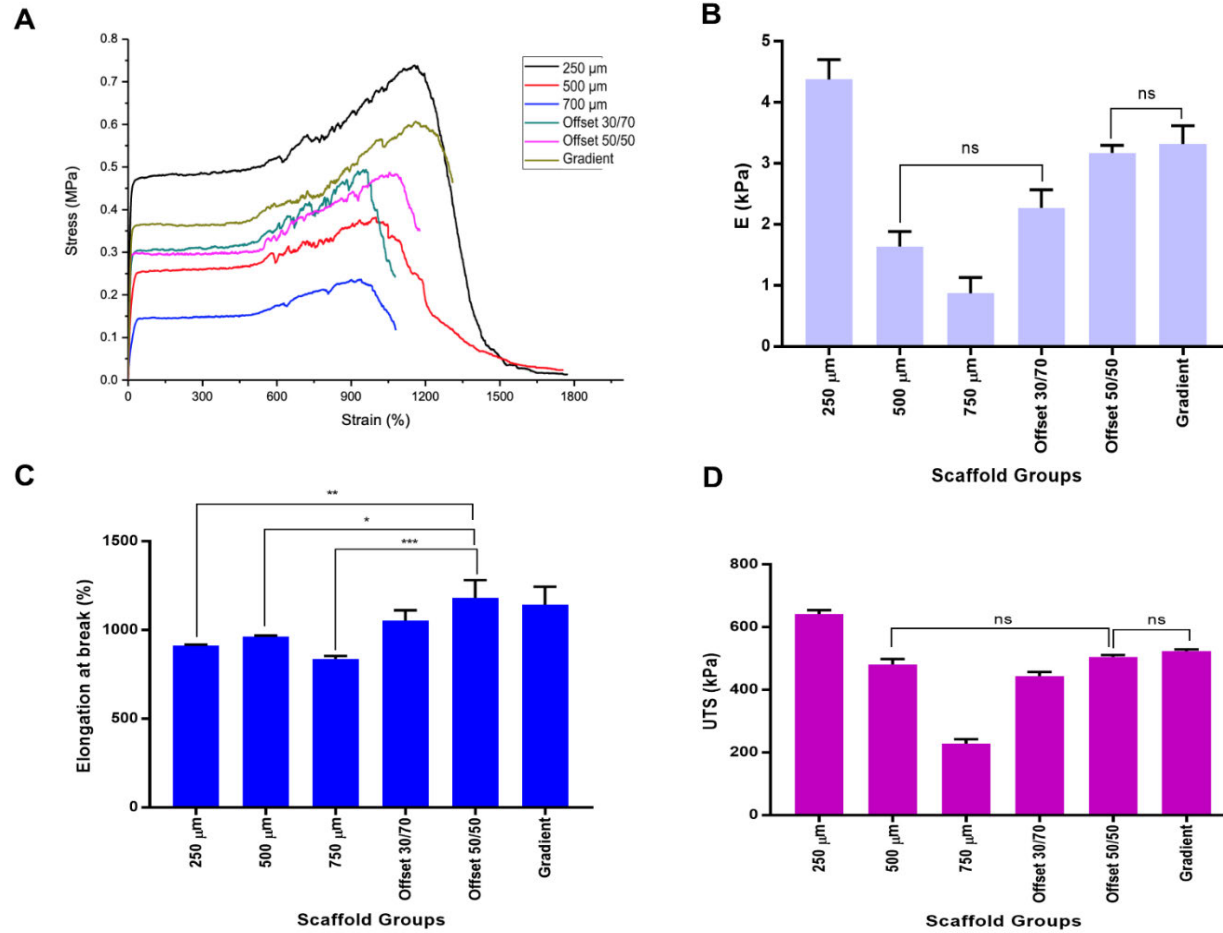


Figure 3.7. Mechanical properties of CaP coated melt electrowritten PCL scaffolds (A) stress strain curves, (B) Young's modulus, (C)

Elongation at break, (D) Ultimate tensile strength (UTS). ns: non-significant, *** $p < 0.0005$, ** $p < 0.007$, * $p < 0.04$.

Micro-Computed Tomography Image Analysis

Micro-CT (μ -CT) analysis was utilised to measure the porosity as well as the 3-D pore morphology of the PCL scaffolds. As shown in Figure 3.8-A, MEW fabrication produced a well-distributed and homogeneous pore structure throughout the scaffold. Quantification of the porosity of the scaffolds via reconstruction of three-dimensional images of the porous PCL (Figure 3.8-B) showed that larger pores lead to higher porosity than smaller pores. Porosity values were 93%, 95%, 97%, 92%, 94% and 95% for the 250 μ m, 500 μ m, 750 μ m, offset 30/70, offset 50/50 and gradient scaffolds respectively.

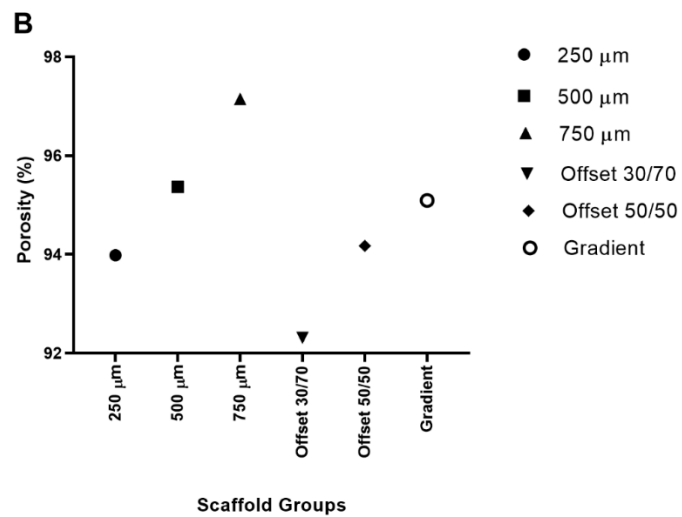
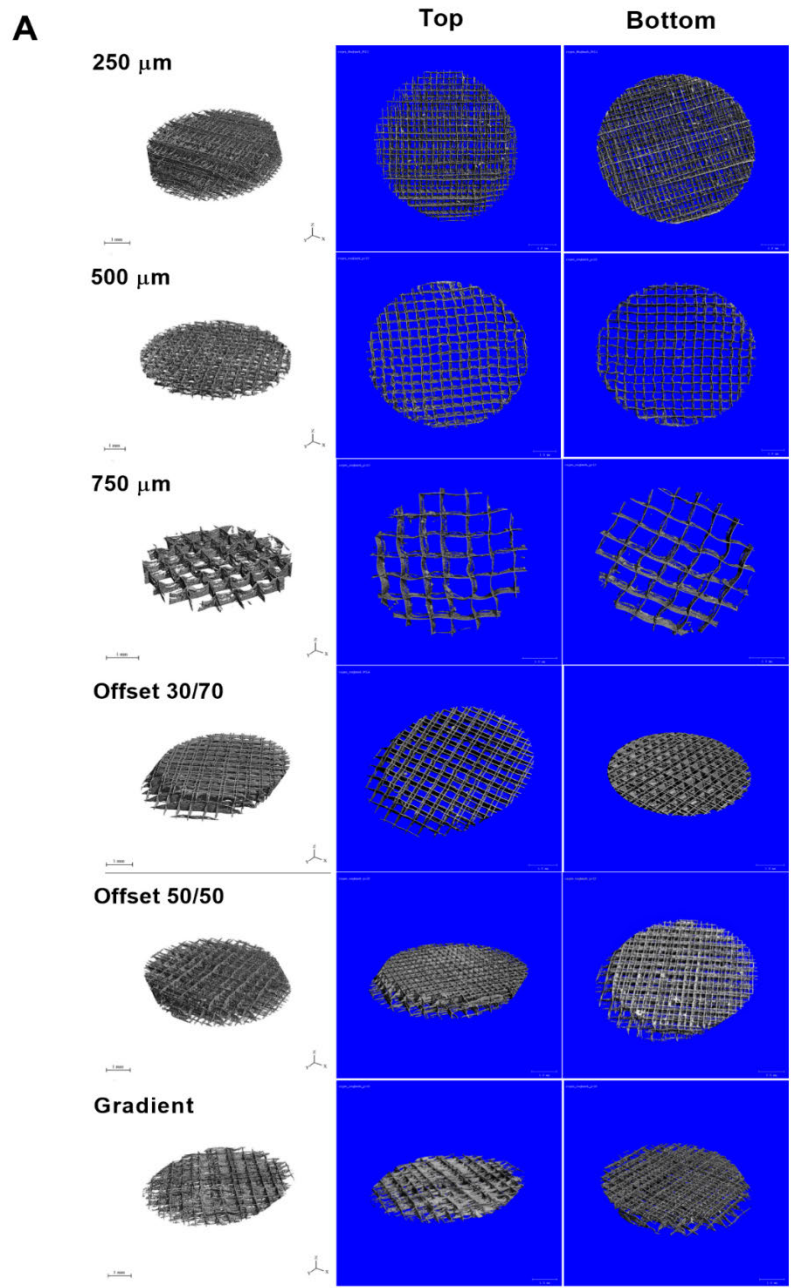


Figure 3.8. (A) Images of Micro-CT analysis of the 3D porous PCL scaffolds fabricated using MEW and (B) quantification of the porosity of the scaffolds.

Surface Area

Brunauer–Emmett–Teller (BET) analysis was used to determine the total surface area of the CaP-coated and non-coated scaffolds is summarized in Table 3.3 and Figure 3.9. Significantly, all groups showed a greater surface area following CaP coating compared to the non-coated scaffolds. The highest surface area was 5.22 m²/g for the coated offset.30.70 scaffold while the lowest surface area of 0.49 m²/g was seen with the non-coated 750 μm homogeneous scaffold (Figure 3.9).

Isotherm graphs (supplementary Figure S6) showed that there were minimum changes (hysteresis) between desorption (brown line) and adsorption (red line) of gas. This represented pore size distributions obtained from the branch of argon absorption isotherms, using BJH analysis. A relatively narrow pore size distribution was observed in all samples with pore sizes in the range of 4.1 nm to 7.9 nm, typical of open mesoporous materials (average 2-50 nm). The gradient scaffold had the widest pore diameter of 7.6 nm among the coated groups, while the largest pore diameter among the non-coated scaffolds was in the offset.30.70 (Table 3.3). BET analysis of total surface area within isotherm graphs for the NaOH treated scaffolds also have been presented as supporting information (Table S1, Figure S6).

Table 3.3. Total surface area of coated PCL scaffolds obtained by BET under IUPAC classification. *All scaffolds showed an open pore form structure.

Scaffold	Surface area (m ² /g)		Isotherm		Pore size* (nm) Mesoporous		Pore Area (m ² /g)	
	CaP coated	Non coated	CaP coated	Non coated	CaP coated	Non coated	CaP coated	Non coated
250 μm	4.61	1.70	Type II		7.1	4.1	4.04	2.24
500 μm	2.11	0.57	Type II		6.1	5.3	1.86	0.51
750 μm	1.24	0.49	Type II		4.9	5.5	1.01	0.45
Offset. 30.70	5.22	3.34	Type II		6.7	7.9	4.39	3.07
Offset. 50.50	3.62	1.14	Type II		6.9	4.3	2.93	1.74
Gradient	2.68	0.99	Type II		7.6	5.5	2.31	0.91

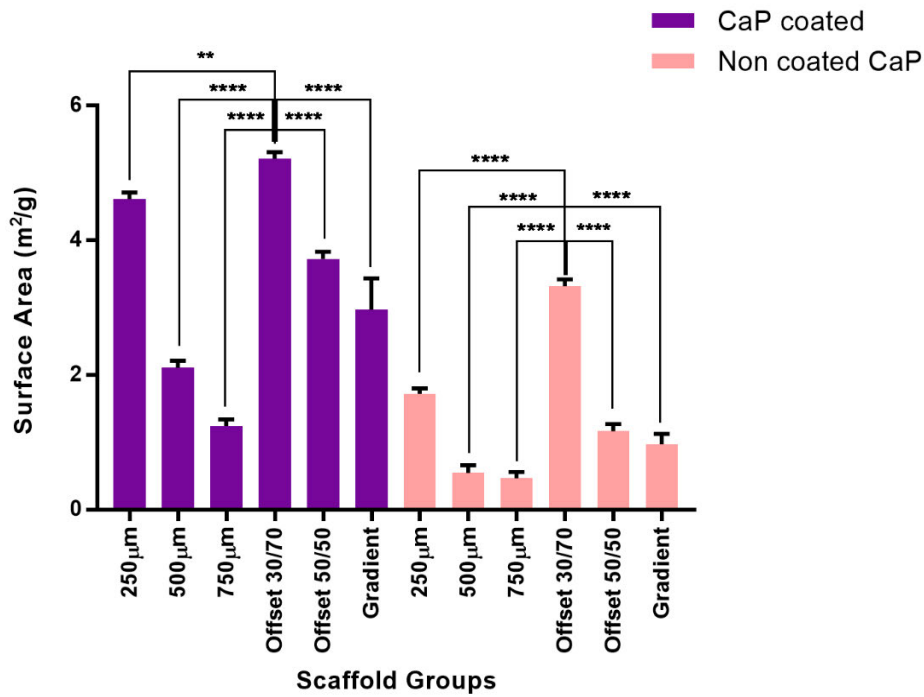
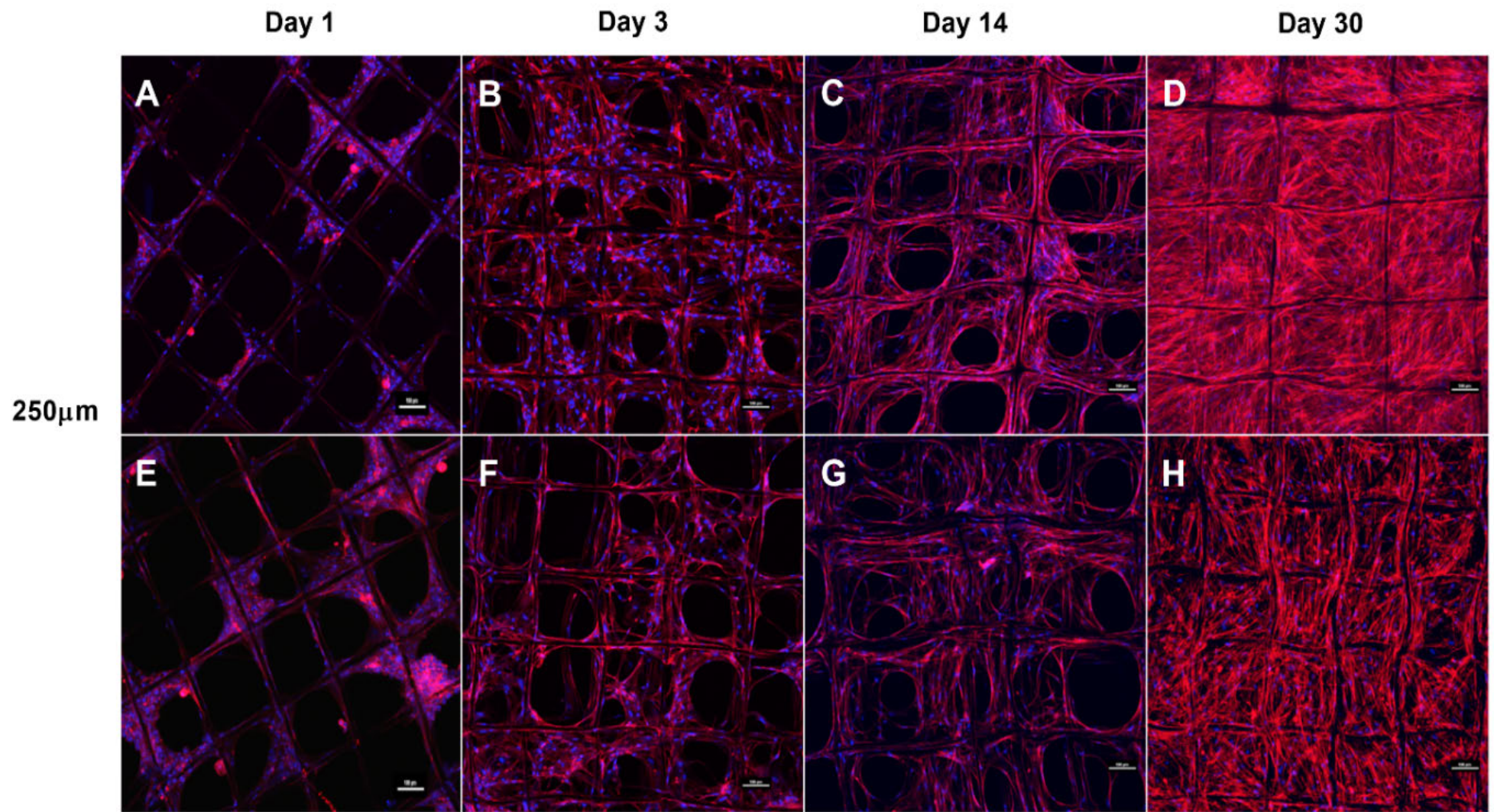


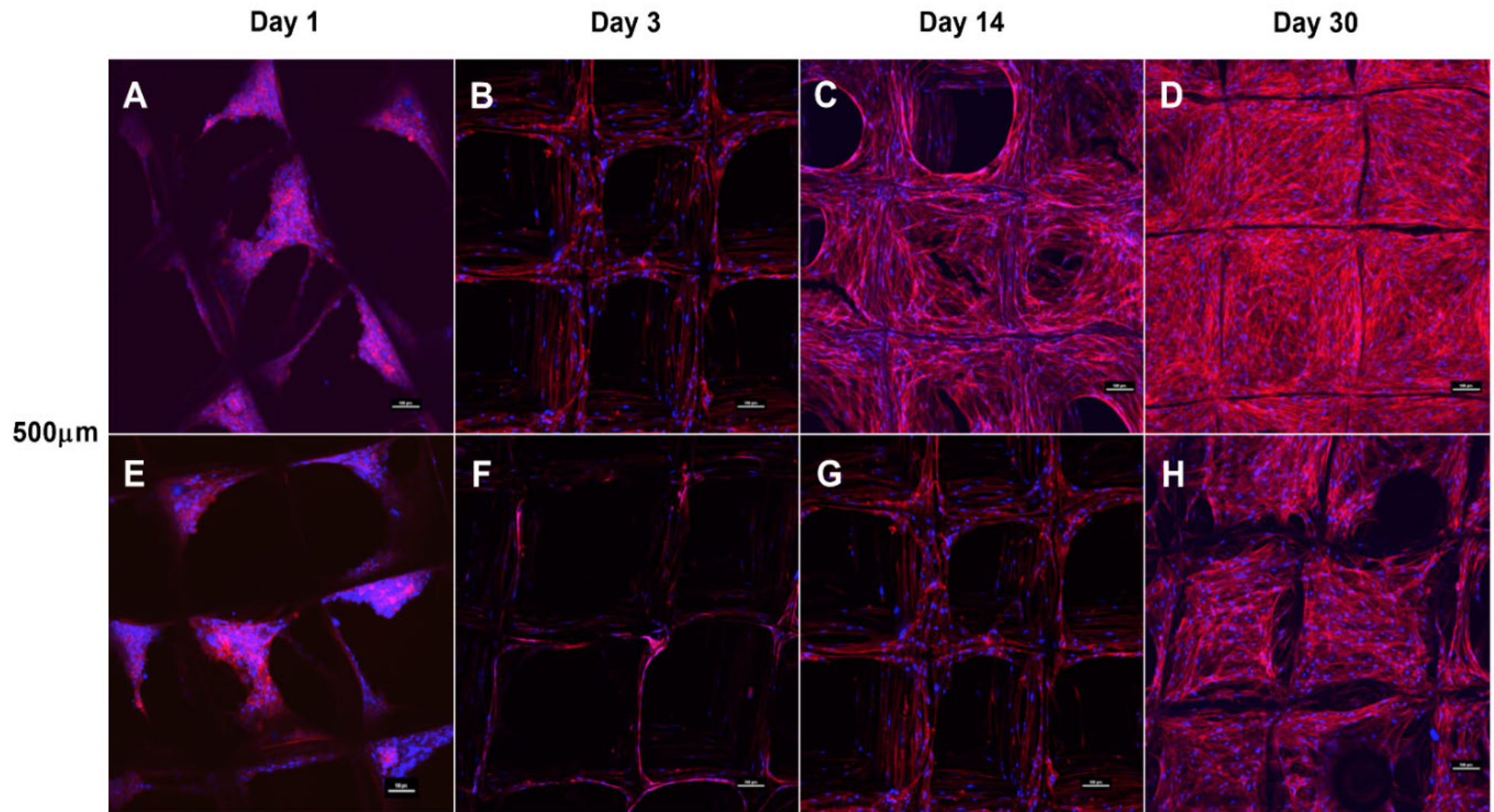
Figure 3.9. Mean specific surface area of the six different melt electrowritten CaP coated and non-coated PCL scaffold architectures. **** $p < 0.0001$, ** $p < 0.001$ versus offset.30.70 scaffold.

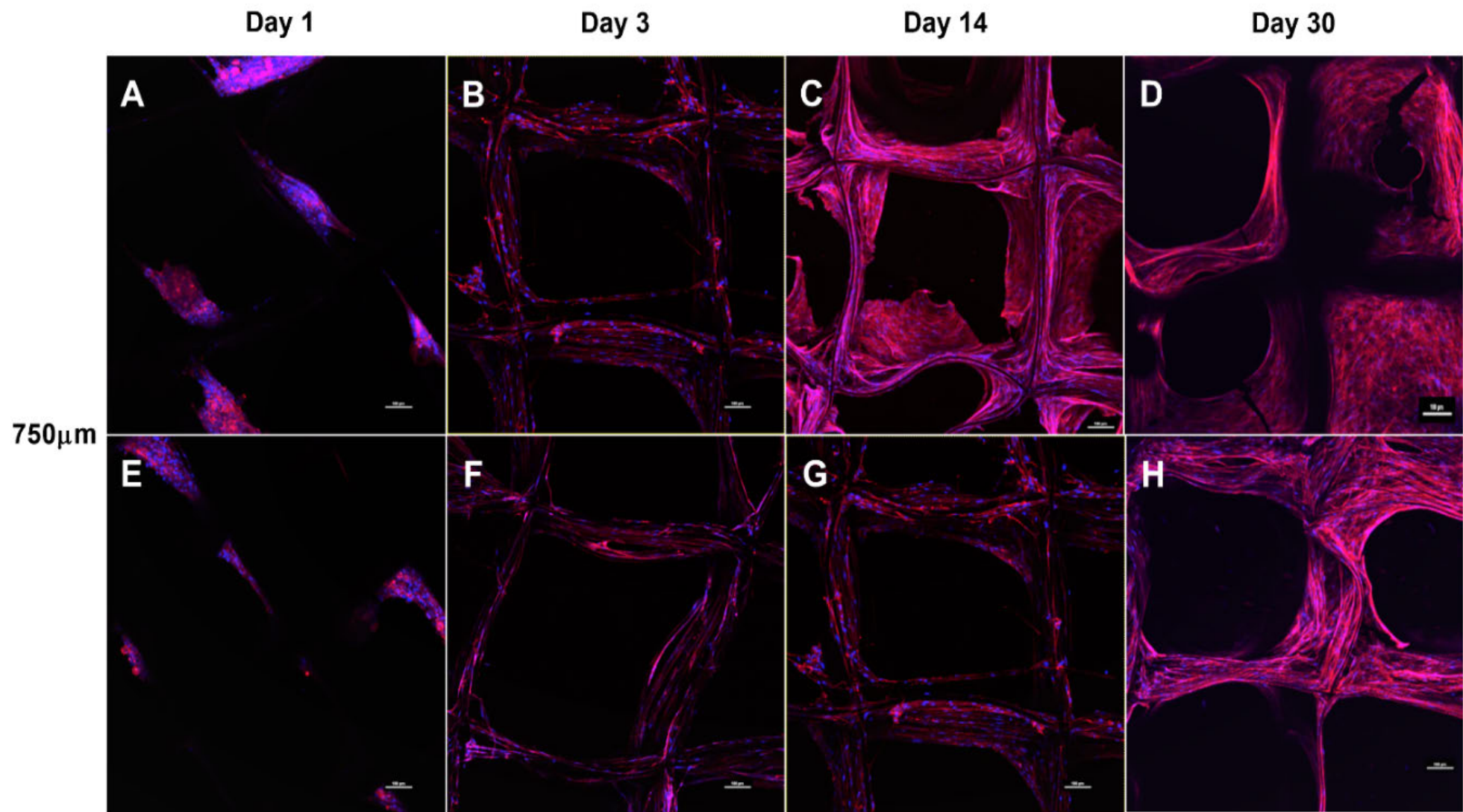
Osteoblast Activity

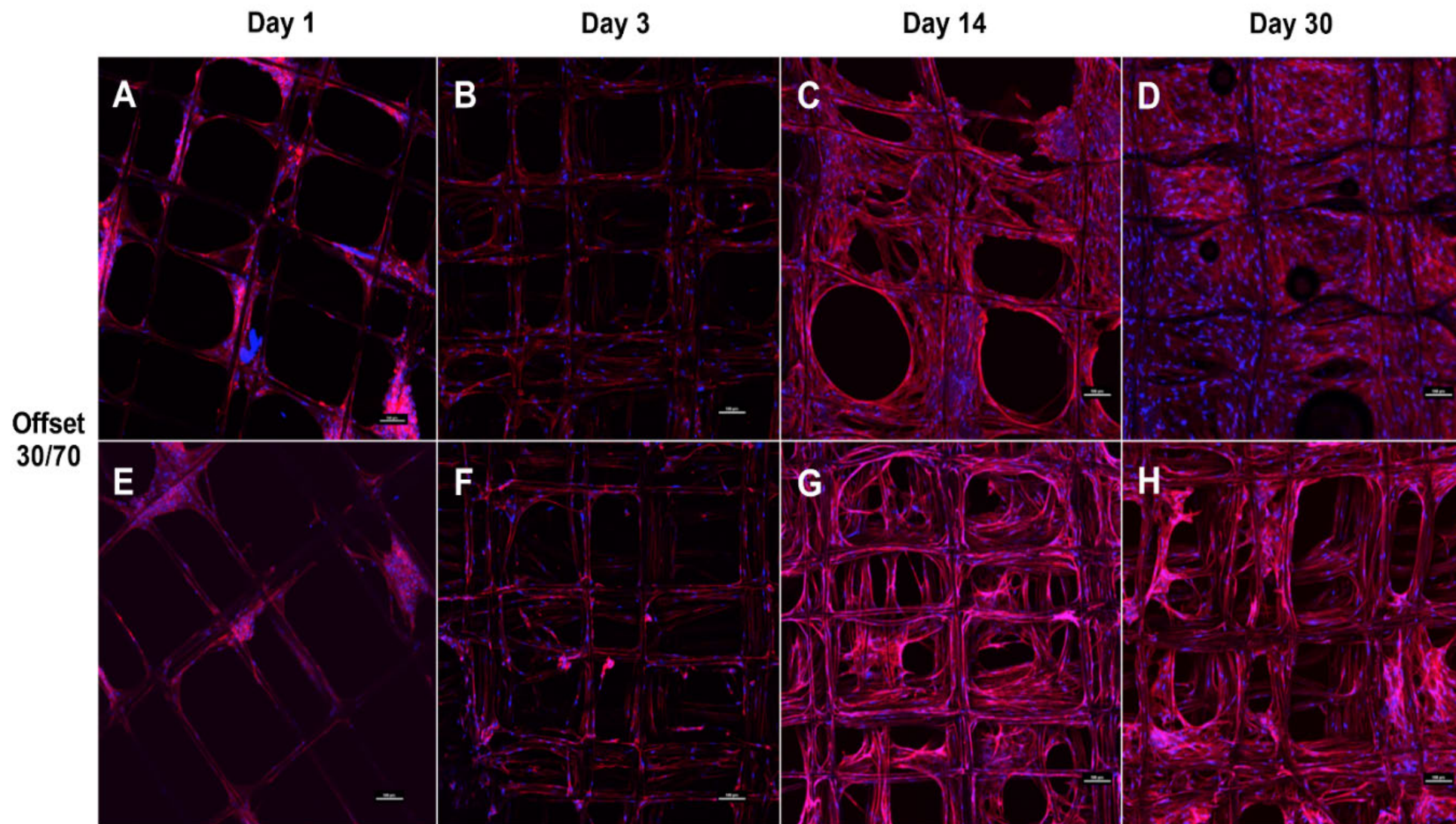
Morphological Analysis

Confocal laser scanning microscopy was used to assess the biocompatibility of the scaffolds as assessed by the attachment, proliferation and spreading of osteoblasts into the scaffold (Figure 3.10). After 24 hrs culture, DAPI/ Phalloidin staining showed cells attached to the fibres with the cell density slightly at the edge of the scaffolds. Between days 3 and 14 of culture, the cells elongated along the fibres and formed a bridge to fill the gap between intersecting fibres. After day 30 of culture the scaffold pores were covered by continuous cell sheets. This cell driven pore closure started from the walls and corners of individual pores as seen at early time points, then filled towards the pore centre. Reconstructed z-stack images of cell distribution within the gradient scaffold after 3 days showed a thick layer of cells on the bottom side of scaffold (250 μm layer) reducing in density toward the centre of the scaffold (500 μm layer) with the least number of cells on the top surface where the cells were initially seeded (750 μm layer). After 30 days cell culture, a migration of cells toward the central area of the scaffold was observed (Figure 3.10, Gradient 3D). The other scaffold groups showed similar patterns of cell infiltration and colonization (data not shown).









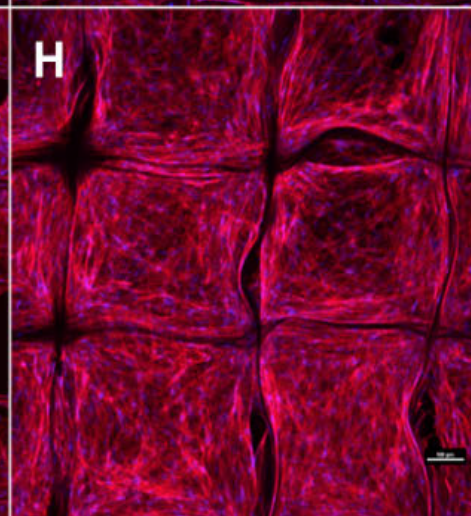
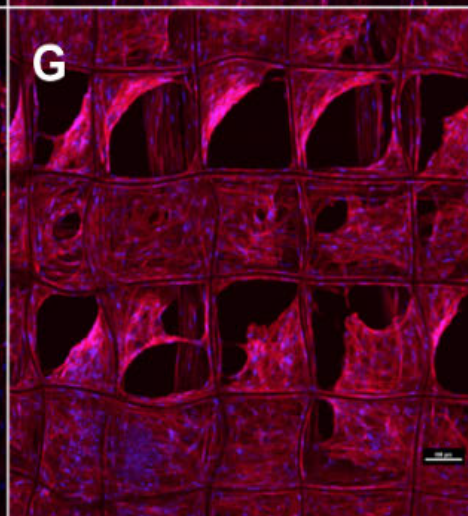
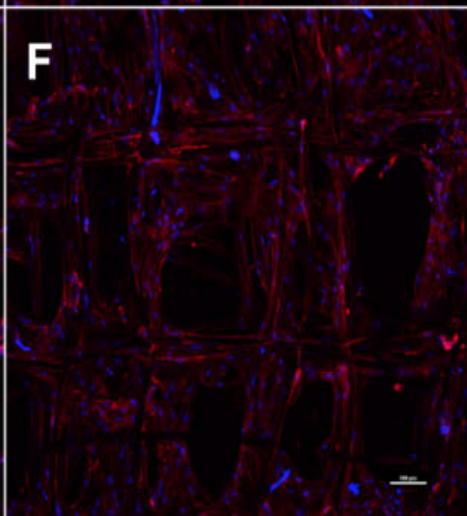
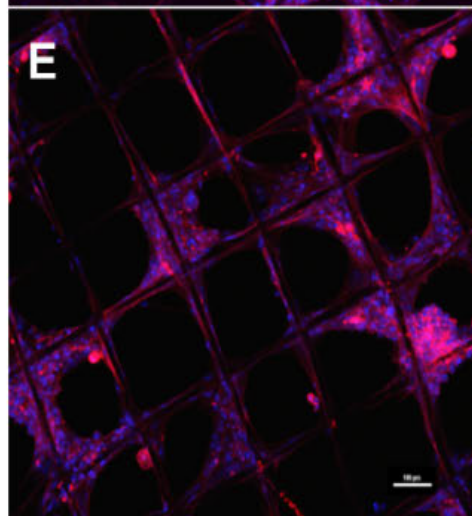
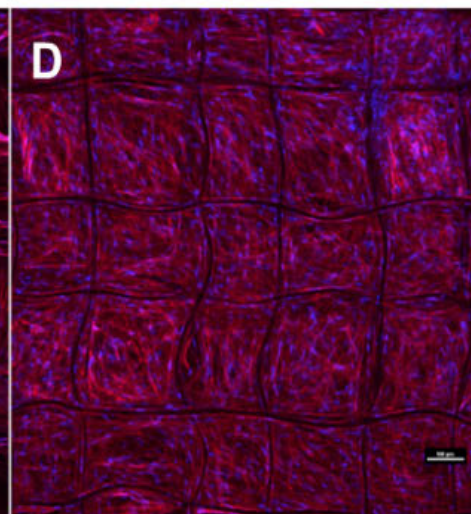
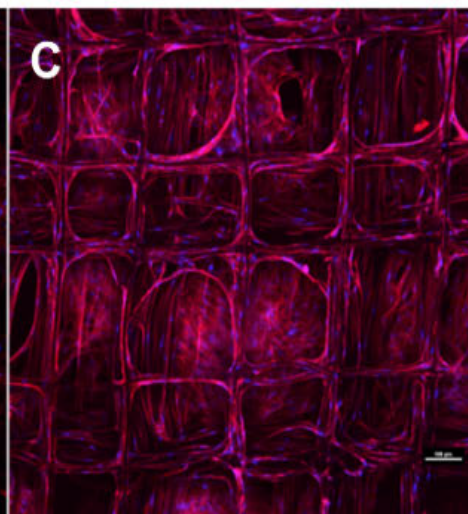
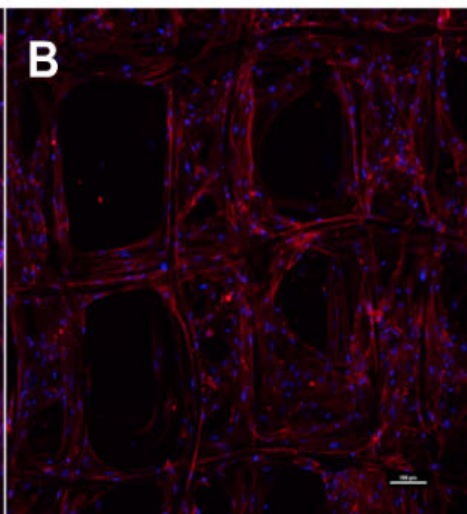
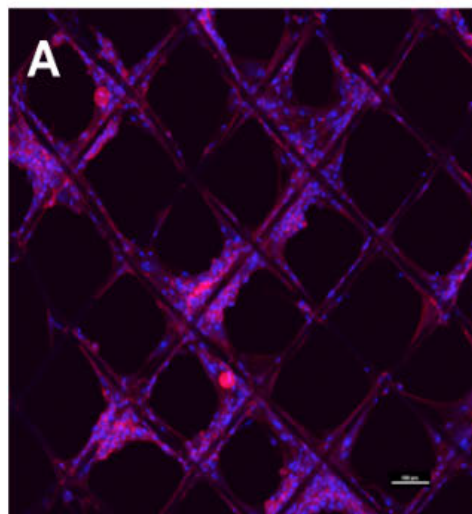
Day 1

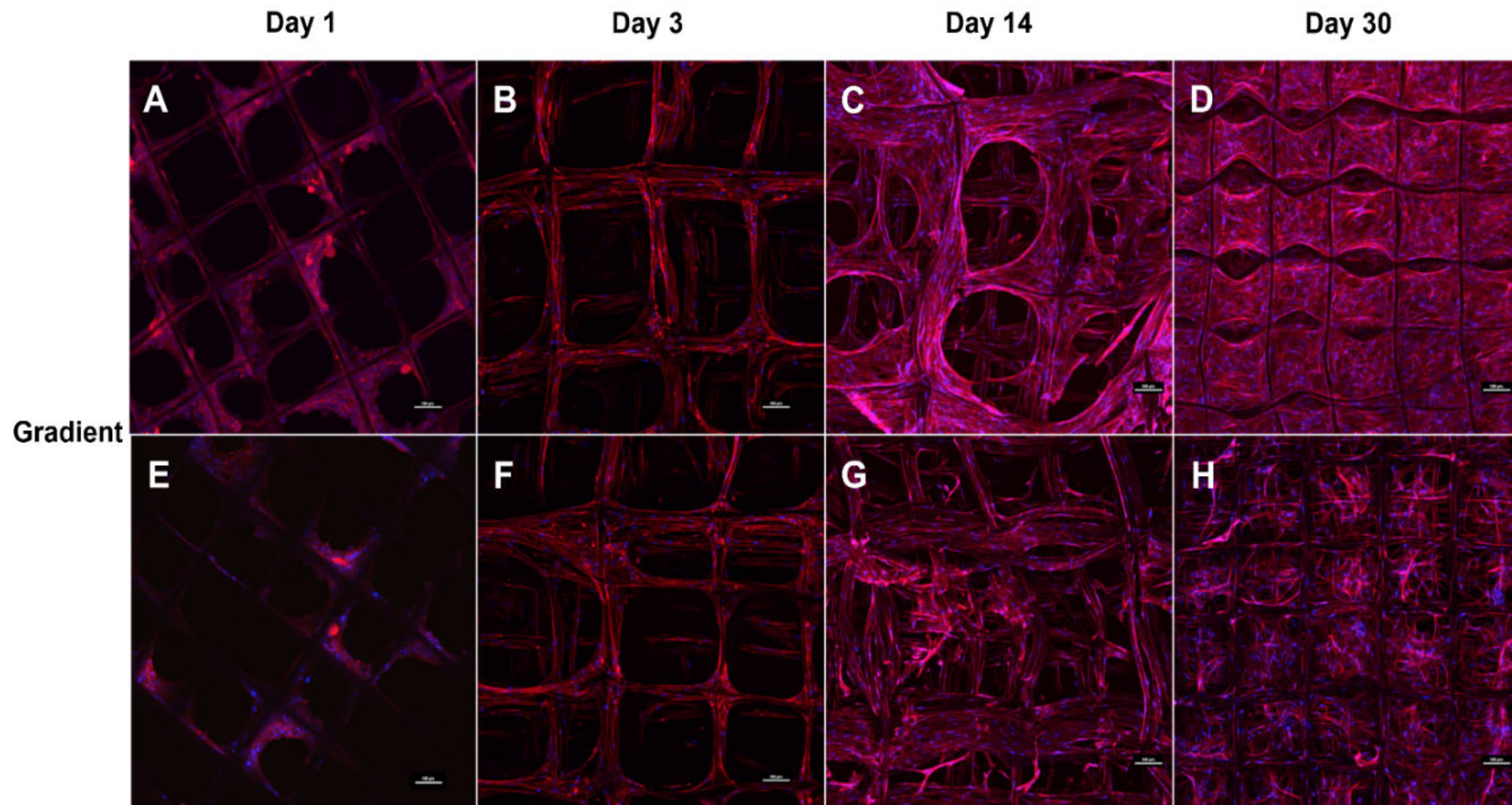
Day 3

Day 14

Day 30

Offset
50/50





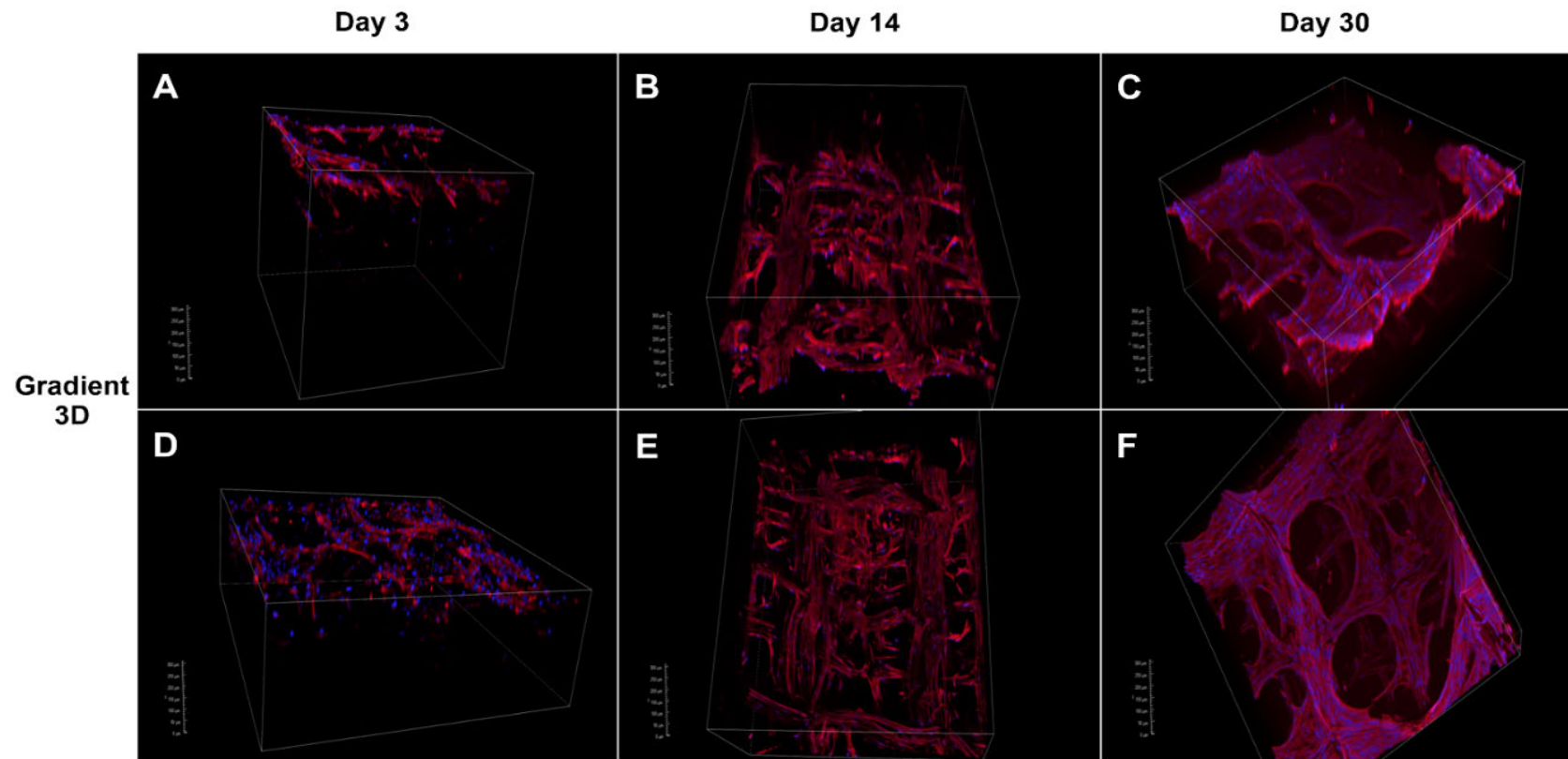


Figure 3.10. Confocal laser scanning microscopy images of osteoblast cells labelled with conjugated fluorescent phalloidin (red) for actin staining and DAPI (blue) for nuclei staining in 250 μm , 500 μm , 750 μm , offset 30/70, offset 50/50 and gradient scaffolds after 1 day, 3 days, 14 days and 30 days; (A, B, C, D) in basal medium, (E, F, G, H) in osteogenic medium; (Scale bar: 100 μm); (Gradient 3D) 3D-reconstruction of a z-stack of confocal images in gradient scaffolds.

Cell Proliferation

A DNA assay was used to quantify the number of cells in the scaffolds over the 30 day cell culture period. Differences in osteoblast cell numbers after 1 day in both the basal and osteogenic medium suggested that the different pore sized scaffolds significantly affected the seeding efficacy (Figure 3.11). The 250 μm homogeneous pore size, offset and gradient scaffolds all showed higher numbers of attached cell whereas the 500 μm and 750 μm homogeneous pore sized scaffolds had the lowest levels of cell attachment. On day 3, the offset.30.70 scaffold showed the highest cell numbers followed by the 250 μm scaffold in basal medium. Cell growth on all scaffolds increased significantly after 14 days of culture in both the basal and osteogenic medium. By this time point the highest cell numbers were seen in the gradient scaffolds. After 30 days of cell culture, the gradient scaffolds in basal medium remained as having the highest numbers of attached osteoblasts among all of the groups. Osteogenic stimulation did not appear to have any significant effect on proliferation (Figure 3.11) although no assays to quantify osteogenic differentiation was performed. The 750 μm homogeneous pore sized scaffold showed the lowest cell numbers at all the time points.

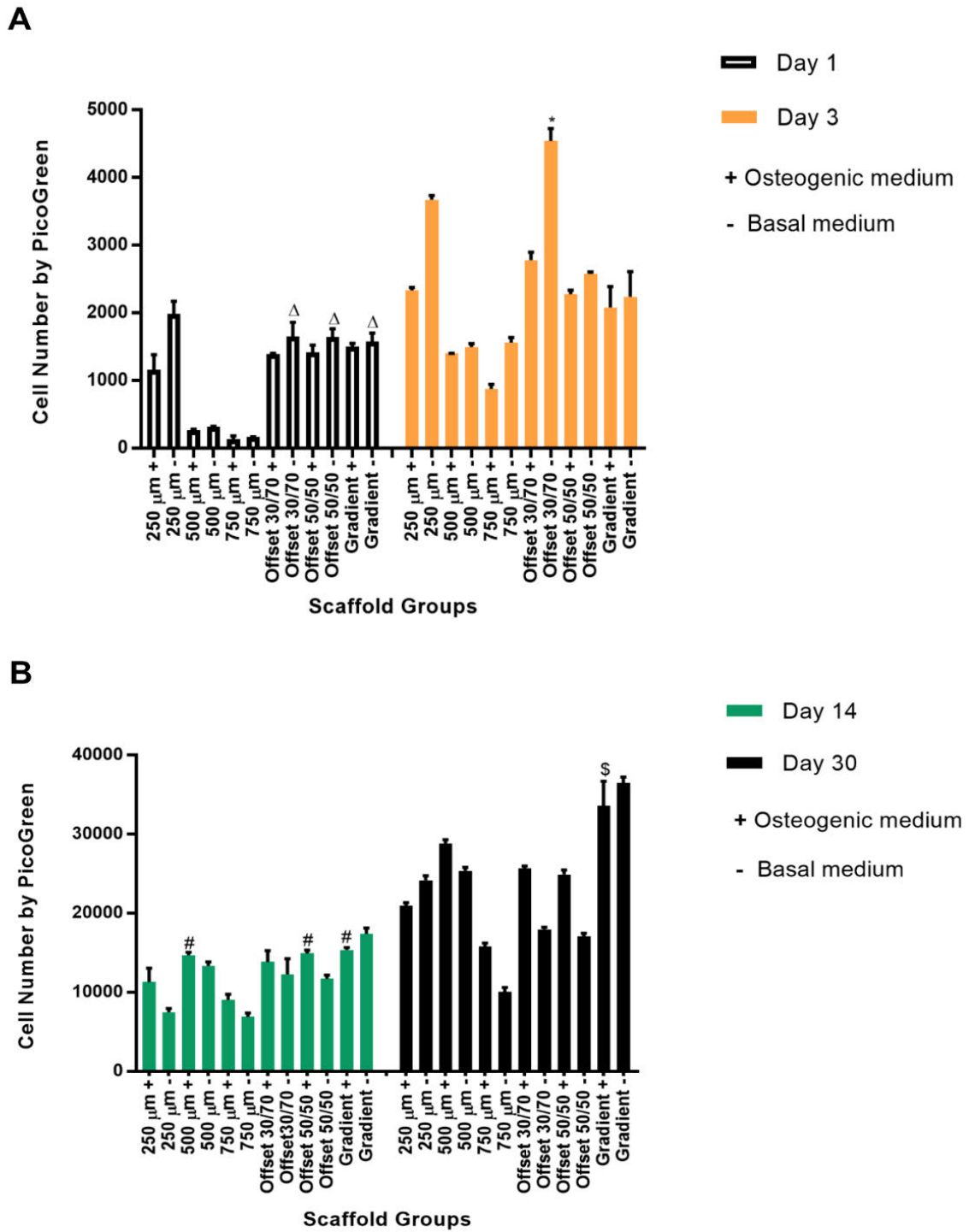


Figure 3.11. The proliferation of osteoblasts in osteogenic (+) and basal medium (-) seeded on PCL scaffolds with different porosity for 1, 3, 14 and 30 days. * significant versus other scaffolds. Δ non-significant versus 250 μ m -. # and \$ non-significant versus Gradient - ($p < 0.01$).

DISCUSSION

Previous studies have shown that the pore size and geometry of scaffolds can affect the stiffness and strength of the structure as well as cellular behaviour e.g. ECM deposition, localization, attachment, and differentiation. For example, when the elastic modulus of the scaffold is constant, the pore size of the structure will not be occluded by the external loads which leads to inappropriate ingrowth and infiltration of the cells towards the porous structure (21). In this study, different scaffold designs were reproducibly prepared from medical grade PCL using MEW. This is an appropriate approach to manufacturing scaffolds with micron diameter-sized fibres that accurately controls the distribution of pores within the scaffold. This has great potential in the construction of scaffolds with small pore sizes used in biomedical applications and overcomes shortfalls in FDM 3-D printing systems which create scaffolds with larger sized fibre dimensions and limited interconnected pore distance. Also the smaller dimensions of the MEW fibres can accelerate scaffold degradation rate and drug release, electrowritten scaffolds are considered as promising candidates for these applications. This is attributed to the enhanced solubility, permeability and porous fiber surface, due to the presence of holes on the fibre surface which increases the surface area for faster degradation (22, 23).

In our study, the melt electrowritten filaments displayed a smaller fibre diameter and greater surface area (Figures S7, S8 and S9, Table S2 supporting information) compared to FDM 3D-printed fibres. Total porosity of the scaffold increased by generating sufficient large gaps between the filaments to support cells and allowed higher resolution for printing small pore sizes (Figure S10 supporting information). This is in contrast to FDM 3-D printed scaffolds where printing small pore sizes is compromised due to the fibers (24, 25).

Although FDM fibers provide good mechanical support in load bearing e.g. bone applications, the MEW material with its greater surface area improves cell adhesion by

enhancing intracellular signalling between cells and the biomaterial surface (26). Furthermore the MEW is a low cost and efficient technique compared to FDM 3-D printing systems that allowed us to fabricate ultra-thin fibers (27).

This is clinically relevant as these highly porous and interconnected scaffolds simulate the native extracellular environment (28). In this study six homogeneous and heterogeneous (offset and gradient) geometries were compared for their mechanical properties and ability to promote cell attachment and proliferation.

The biological rationale for this approach arises from the variation in bone density (cortical to cancellous) present in the form of axial and radial structural gradients in flat and long bone tissue architectures respectively. Heterogeneous patterned scaffolds with a gradient porosity containing both small and large pore sizes can mimic the more porous layer of the light spongy cancellous bone, while more compact areas simulate the stiff cortical bone. This architecture has been shown to improve cell infiltration in the highly porous region by facilitating the availability of sufficient concentrations of nutrients, gas diffusion and waste removal, while the denser structure improved the response of biomaterials to external loads and better cell attachment due to the greater surface area²⁷⁻³⁰. Therefore, the application of a gradient or offset design for three-dimensional scaffolds simulates the native *in vivo* environment.

To achieve these geometries, MEW provides a more predictable and accurate approach for the deposition of fine (~10 µm) fibres layer by layer onto a collector without buckling. Accurate fibre deposition is influenced by the direction and the speed of the collector, practical voltage, distance from the tip of the needle to collector and the flow rate. Although the temperature, pressure, distance and the speed of collector as well as other parameters contribute to the fiber diameter, the applied voltage does not influence on the printed fibre diameter as demonstrated by Dayan et al (7). SEM micrographs of the printed PCL scaffolds in this study showed that optimisation of these parameters i.e.

regulated collector speed, specific voltage and optimised flow rate, resulted in unbroken filaments without interruption during the printing process (29) producing uniform fibre morphology and scaffolds with a high degree of accuracy of pore size in agreement with other studies applying the same optimized parameters for the production of non-woven meshes. SEM microscopy showed that the MEW process also maintained the desired square pore shape in homogeneous architectures i.e. 250, 500 and 750 μm . The porous structure was highly interconnected and thus promoted cell infiltration. Overall fibre diameter did not show any significant variation during printing by MEW and was between 6-10 μm (Figure S2), however while the fabricated pores were homogeneous in size, the fibre deposition fluctuated in scaffolds with larger space distances, i.e. in the homogeneous 750 μm scaffold and 750 μm in gradient scaffolds in order to avoid deformation of the molten polymer needed to span the larger distance to reach the next contact point.

The substitute scaffold material used *in vivo* should maintain adequate mechanical strength over critical phases of the tissue-healing process to withstand the physiological environment and be tear resistant during implantation (20). Each group of the fabricated scaffolds reacted differently in the wet environment under compression loading. Data reported in Fig. 6 showed that the structure with a gradient morphology had a higher mechanical strength at 50% strain in comparison with the other scaffolds. However, the 500 μm homogeneous pore size scaffold induced a higher young's modules and yield strength compared to the rest of the scaffolds. This is attributed to the scaffold architecture and the distribution of fibre along the scaffold which modifies the resilience and the mechanical performance (30). Thus, these differences might be related to water infiltration during the test, the porosity, structure and fibre packing density of the scaffold among other factors. In contrast to the tensile experiment results, the compression test was measured under physiological conditions and further studies are needed to investigate

the effect of different test conditions (e.g. air/wet, temperature) on the internal architecture and overall scaffold mechanical performance.

Reflecting the linear relationship between the resistance to mechanical loading and bone density due to the presence of mineral phase crystal and osteon infiltration (13), higher supported tensile properties, including ultimate tensile strength, maximum load, Young's modulus, and elongation have been achieved in scaffolds with uniform small pores. It has been suggested that the improved tensile properties of small pore size scaffolds can be attributed to the increased tear resistance of the higher fiber density packed per mm within the scaffold compared to large pore scaffolds with less densely packed fibers. The large contributions of spun interconnected fibers within the PCL scaffold results in higher tensile properties (31). Studies including ours report that the mechanical properties of an interconnected fiber matrix increase with decreasing fibre pore size (20). Thus, it is possible that the enhanced tensile properties for the MEW scaffold are due to the fiber packed density of the 250 μm pore size scaffold.

However heterogeneous porous patterns containing both small and large pore sizes may result in better tensile properties, while constructs with one large pore size have been shown to decrease the stiffness properties of scaffolds (30). Therefore larger pore dimensions have been suggested for low tensile loading environments and oriented smaller pores are considered more appropriate for higher loads (32). Our findings also showed that the strain distribution values were affected by the different porosity values with higher porosity resulting in lower mechanical strength.

The mechanical stiffness of scaffolds also provides stability against loading forces and pressure. In the present study, both the offset and gradient scaffolds had a higher elastic modulus than the homogeneous 500 μm and 750 μm pore size scaffolds. This suggests that the tensile properties of the scaffolds with identical porosities can be further modified by the underlying microstructure. The offset 50/50 scaffold for example showed that

under conditions of tensile stress, the percent elongation at break point was highest compared to the other constructs. These results agree with previous studies that showed a greater elastic modulus was achieved in 100 % offset PCL-tricalcium phosphate scaffolds compared to no-offset scaffolds with the same porosity (33).

Scaffold stiffness has been shown to influence the cytoskeletal organisation of adherent cells resulting in a cell morphology that can affect cell differentiation. Previous studies suggest softer substrates persuade the cells to adopt a round shape while stiffer substrates induce more cell spreading. These alterations in phenotypes coincide with cellular changes such as differentiation by reprogramming the cells to commit to a specific lineage (34). Scaffold stiffness also affects cell viability and growth as shown by osteoblasts which demonstrated greater proliferation and mineralisation on a stiffer substrate (35). This agrees with our cell proliferation analysis which illustrated higher proliferation rates in gradient, 250 μm and offset 50/50 scaffolds which showed more stiffness compared to the other structures.

CaP coating due to its similarity to inorganic mineral phase crystals found in bone, is well known to enhance the bioactivity of biomaterials, by releasing calcium and phosphorus ions that modulate osteoclasts and osteoblasts activity. CaP coating therefore can enhance osteogenic gene expression and ALP activity in bone cells, cell-seeding efficiency, cell proliferation and infiltration (36). Natural PCL also has a low surface wettability and poor surface bioactivity. Following surface treatment with NaOH, it readily adsorbs CaP onto the surface and the SEM analysis of the coated scaffold surface morphology showed that the fibres were covered by CaP particles with a resultant increase in topographical roughness. Previous studies have shown that the application of CaP onto the scaffold surface increases the surface area and cell adsorption and subsequent cellular behaviour (37).

A concomitant reduction in contact angle to zero following CaP coating indicated a significant increase in surface energy and therefore wettability of the scaffold. *In vivo*, this increase in hydrophilicity due to the expansion in surface area has a profound influence on the biological interactions between the surrounding environment and the biomaterial including the adhesion and adsorption of proteins, cell behavior and ultimately the process of osteointegration. CaP however exhibits poor mechanical stability and is brittle by nature due to higher solubility (38). The available surface area of scaffolds is dependent on the porosity i.e. there is an inverse relationship between the specific surface area and mean pore size (39). Micropores (<100 μm), due to their greater surface area have been shown to effect more favourable protein adhesion, more reactivity, better flow of nutrient fluids and waste products and enhanced cell attachment (40). However, some *in vivo* studies have suggested that a higher surface area does not necessarily increase cell numbers as the potential for cell proliferation due to migration improved in scaffolds with larger pores (41).

In this *in vitro* study, scaffolds with offset 30/70 architectures were shown to have surface areas higher than the smallest homogeneous (250 μm) scaffolds but similar numbers of adherent cells after one day of culture.

Although a high level of DNA was observed in the 250 μm scaffold at the first time point, the difference between 250 μm and the offset 30/70 scaffold, which had a greater surface area, was not significant as cell seeding efficiency and subsequent cell proliferation is influenced by not only surface area but also wettability (contact angle). In addition, the seeded scaffold was transferred to the new plate after 6 hr pre-incubation, therefore, the difference between 250 μm and offset 30/70 in cell attachment at the first time-point can be associated to the more hydrophilic nature of the 250 μm scaffold that created a non-significant increase in cell adherence after 24 hr.

The available surface within a pore depends on the mean pore size of the scaffold in nanometer scale which influences the ligand density within the scaffold to allow the cells to be bound. Within a porous scaffold the pores are required to be large enough to establish a maximum ligand density leading to efficient binding of cells and thus allowing them to migrate into the scaffold structure (42, 43). This agrees with the present study where the wide pore diameter was demonstrated in the gradient scaffolds which could explain the improved cell numbers during the 30 days of culture. Although the high mean pore size was observed in gradient structures, and the 250 μm also showed a very similar pore of 7 nm. This may suggest a range of pore sizes is critical for any scaffold depending on the cell type. Pore size is particularly relevant to cell attachment as the interaction between the cells and biomaterials is mediated via transmembrane proteins and as micron-scale pores can mediate protein adsorption on the scaffold surfaces (44), they can play a key role in determining cell fate. While the limited interfacial area of scaffolds with large pores can inhibit cell adhesion, they can play a crucial role in the proliferation and migration of the cells into the scaffold (9). As such, cell infiltration may be restricted by pore size reduction due to greater surface area to volume ratio. Therefore, designing a scaffold architecture that has a sufficiently high surface area to promote cell adhesion but with a pore size optimal for cell proliferation and infiltration, could favourably alter cells behaviour. For example, a study of various offset value scaffolds with similar porosity (62%) showed superior cell proliferation and viability in offset value scaffolds >50% (12). Indeed, in the present study, the highest cell numbers were observed in the gradient scaffold after 30 days despite its lower surface area in contrast to either the offset or 250 μm scaffolds. This result was in agreement with a similar study that showed that cell growth of human osteosarcoma cells in gradient (100–700–100 μm and 700–100–700 μm) pore size PCL scaffolds was enhanced by 40% compared to homogeneous scaffolds under static culture conditions (30). Studies of scaffold fluid

dynamics has also shown that infiltration diffused widely in both x and y directions in offset scaffolds resulting in longer contact times between the biomaterial and the fluid containing the cells. This suggests that offset and gradient scaffolds may provide advantages for the prevention of nutrient loss, cell-seeding and possible proliferation efficiency by providing a wider contact area (33).

High porosity matrix scaffolds have been shown to favour cell aggregation and differentiation within the scaffold, while low porosity matrices led to higher cellular proliferation (45). It appears that restricted pore size and hence a lack of space for infiltration, tends to limit cell proliferation (46, 47). Higher pore size permits cells to better communicate and there is no inhibition on cell-cell interaction and cell aggregation (48). In our study, the gradient scaffold, a combination of small and large pore sizes with similar porosity, promoted cell proliferation while the smaller pore size and offset scaffolds displayed reduced cell density. It may be hypothesized that after 30 days in the 250 μm homogeneous scaffolds the cell-cell contact and proliferation were restricted due to reduced space, which induced contact inhibition and/or promoted the cell towards a non-proliferative stage. Meanwhile, faster cell proliferation and migration occurred in the larger pores of the gradient scaffold as there was still empty space to be populated by the proliferating cells in the gradient structures after 30 days of cell seeding (49).

Cell interaction with the gradient scaffold after 30 days as assessed by cytoskeletal organization (actin staining), showed that the fibre surfaces of the scaffolds were completely covered by cells. In 3-D the cells initially concentrated at the bottom of the scaffold during the early days of culture and subsequently proliferated and migrated layer by layer through the structure to the top of the scaffolds by bridging over the fibres, aggregating at the corners, elongating along the edges and covering the open pore architecture completely. Poor cell-scaffold interaction as a result of large pore sizes can deteriorate the efficiency of cell-seeding (33) and this was consistent with observations

in the present study where the 500 and 750 μm homogeneous pore sized scaffolds had relatively low cell proliferation compare to the 250 μm , offset and gradient scaffolds.

CONCLUSION

In this study, the influence of pore size and scaffold offset and gradient architecture on human osteoblast attachment, migration and proliferation was examined *in vitro*. Using MEW, three homogeneous (250, 500 and 750 μm pore size) two offset.(30.70 and 50.50) and a gradient (250 μm bottom – 500 μm middle – 750 μm top) scaffold were assessed. The 250 μm pore size scaffold had the highest tensile properties, most likely due to the higher fibre density with the scaffold compared to the large pore scaffolds. The offset and 250 μm homogeneous scaffolds had surface characteristics that were highly efficient for cell seeding while cell proliferation was the highest on the gradient scaffold after 30 days. Taken together, gradient and offset scaffolds have advantageous properties that promote cell infiltration and growth. This is the first study to link the offset and gradient structures with the proliferation and migration of osteoblast cells on PCL scaffolds fabricated by a MEW approach.

Acknowledgments

Naghmeh Abbasi was sponsored by a scholarship from Griffith University, Australia. This study is part of her PhD research project being carried out at Griffith University. The authors would like to express their gratitude to Institute of Health and Biomedical Innovation (IHBI) and the Central Analytical Research Facility (CARF) of QUT, Australia, for providing some facilities and technical support for this study also Dr. Cedryck Vaquette for his advice and general supervision of this research. We want to acknowledge and thank Marcin Gwiazda, Derrick Maxwell and Deepak Ipe for their technical support.

Supporting Information

Table S1. Mean specific surface area of melt electrowritten NaOH treated PCL scaffold.

Scaffold	Surface area (m²/g)	Isotherm	Pore size (nm) Mesoporous	Pore Area (m²/g)
250 μm	3.35	Type II	2.0	1.86
500 μm	0.49	Type II	5.16	0.42
750 μm	6.14	Type II	1.94	3.30
Offset. 30.70	2.76	Type II	1.98	1.52
Offset. 50.50	0.47	Type II	5.58	0.34
Gradient	0.89	Type II	26.02	0.96

Table S2. Total surface area of FDM 3D-printed and melt electrowritten PCL scaffolds (pore size: 250 μm) obtained by BET under IUPAC classification. *All scaffolds showed an open pore form structure.

Scaffold Pore size (250 μm)	Surface area (m²/g)	Isotherm	Pore size (nm) Mesoporous	Pore Area (m²/g)
Melt electrowritten	1.70	Type II	4.1	2.24
3D-printed	0.03	Type II	4.77	0.03

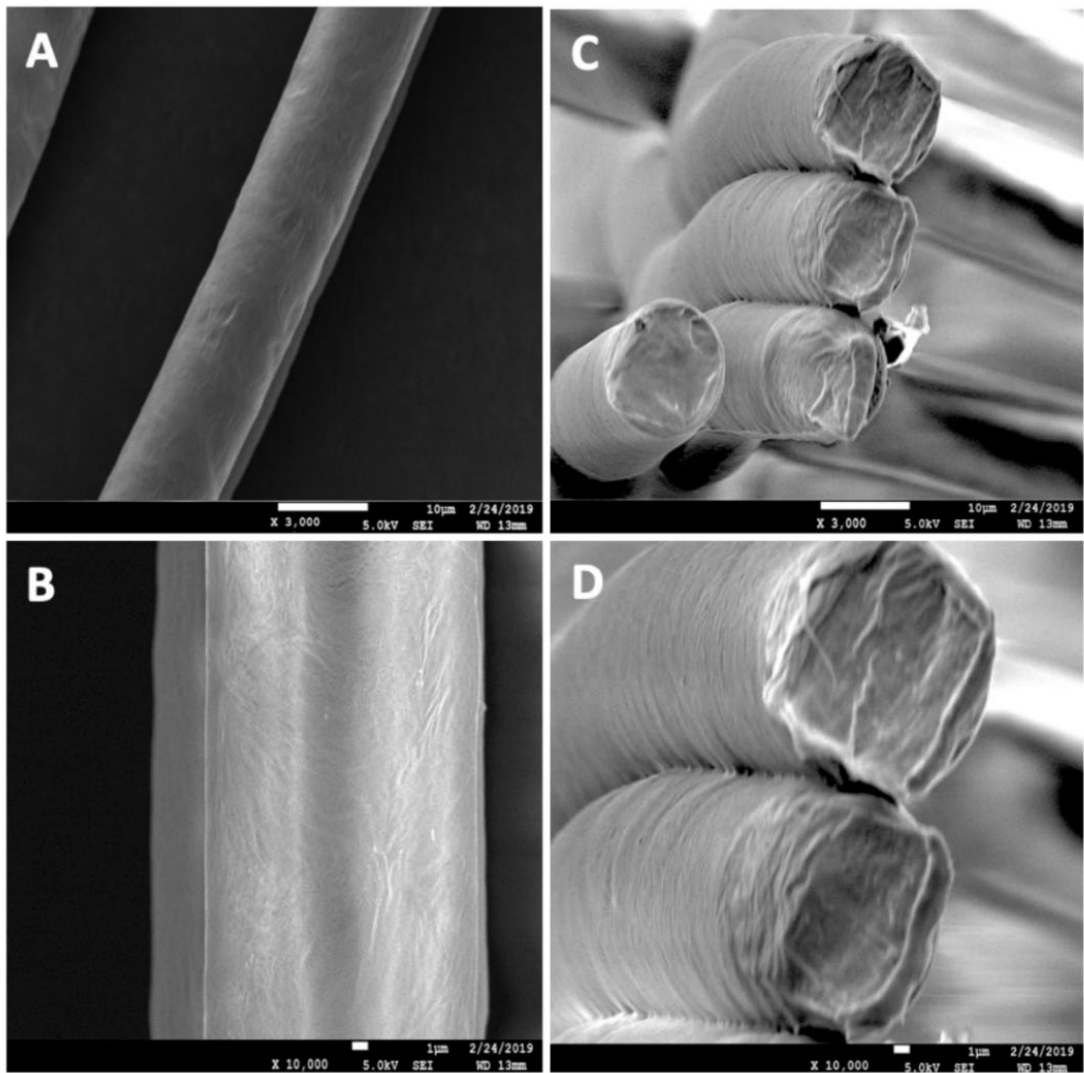


Figure S1. SEM images of PCL surfaces modified by treating with NaOH (C, D) Cross-sectional view of scaffold fibers.

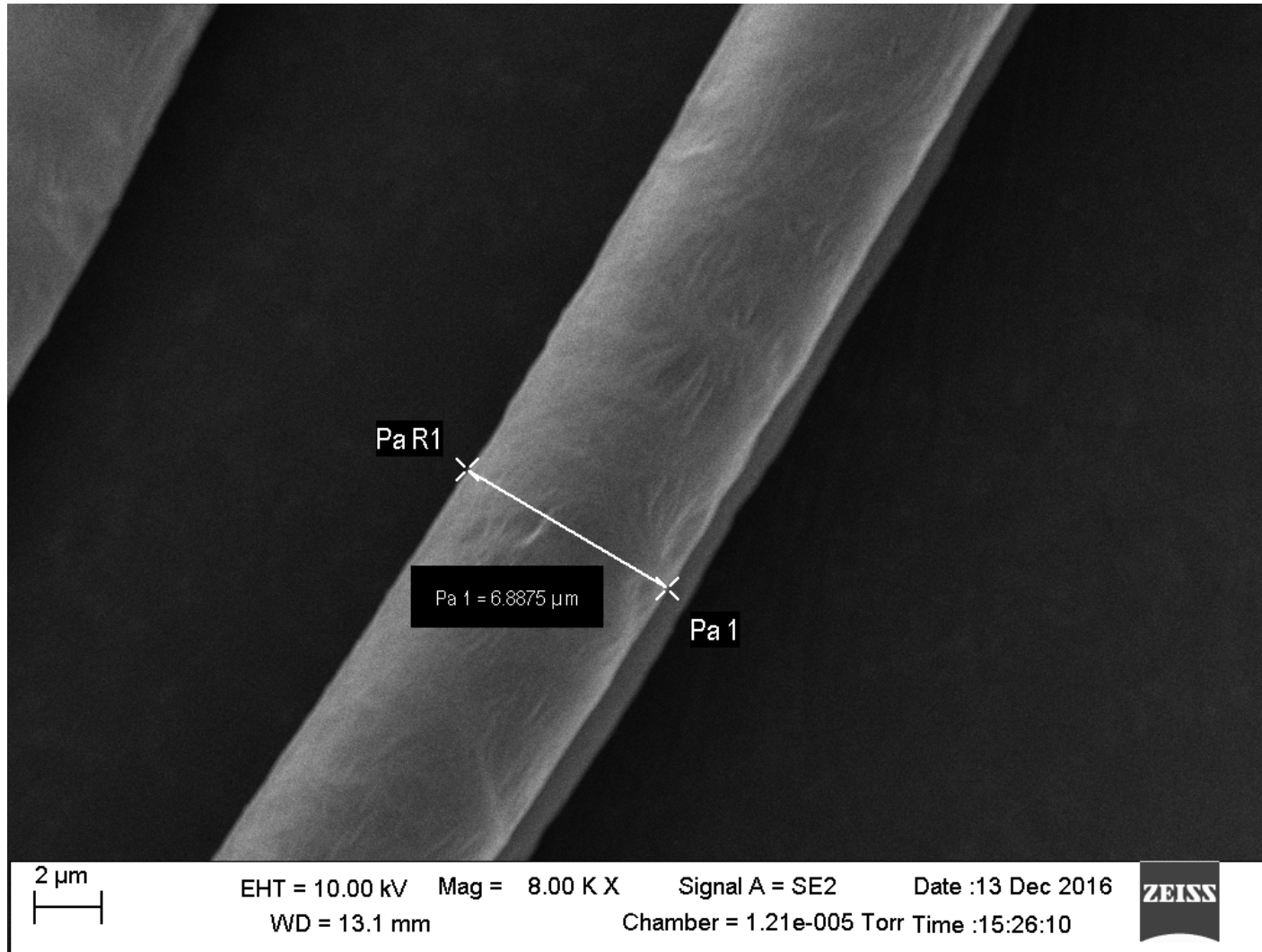
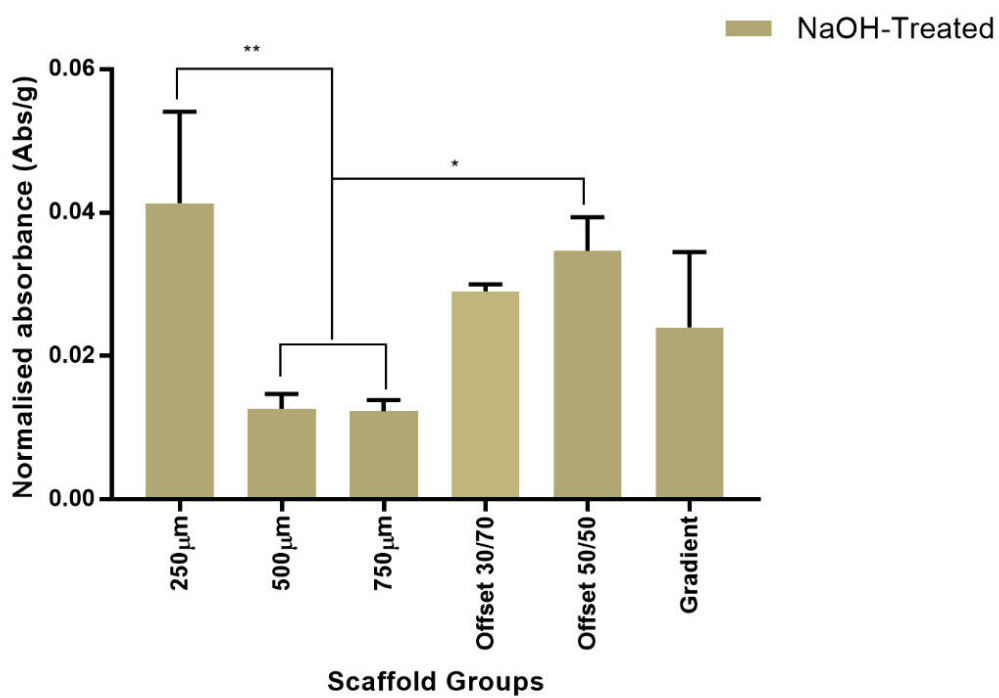


Figure S2. SEM images of mean fibre diameter of melt electrowritten PCL scaffold.

Alizarin Red S staining



NaOH-Treated



Figure S3. Qualitative and quantitative assessment of alizarin Red staining of PCL surfaces modified by treating with NaOH. * $p \leq 0.024$, ** $p \leq 0.0036$.

Contact angle

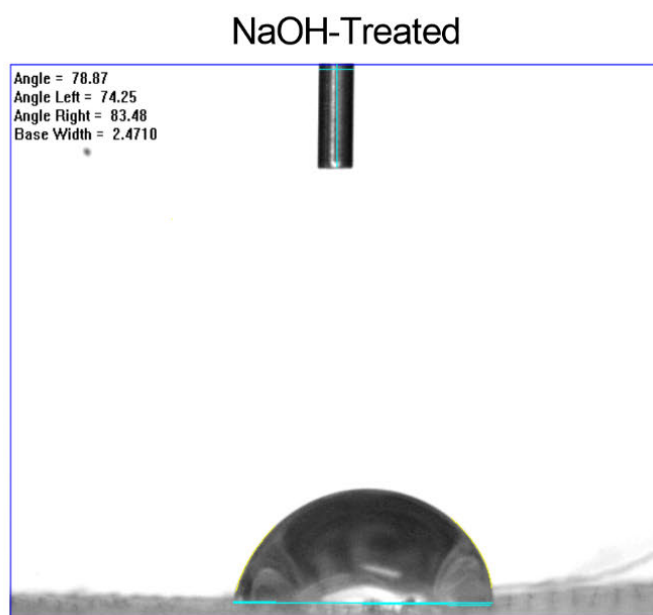
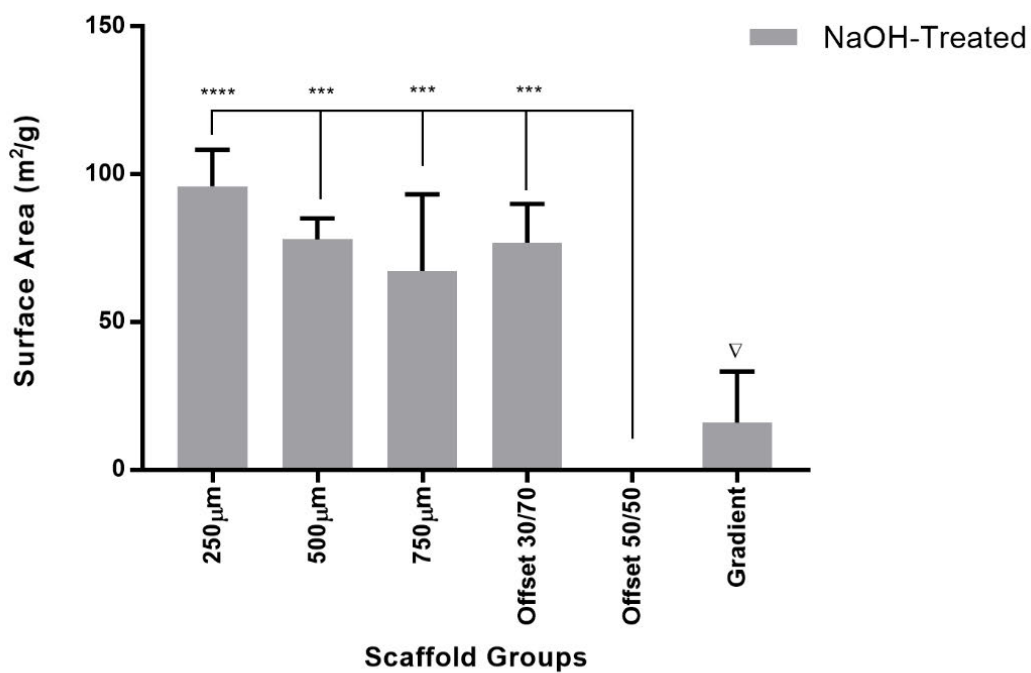


Figure S4. Contact angle measurements on pore surfaces of NaOH treated PCL scaffold.

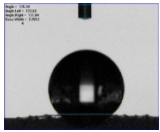
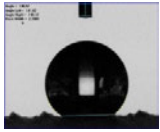
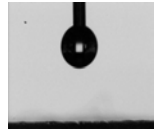
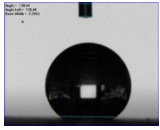
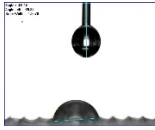
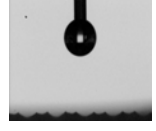
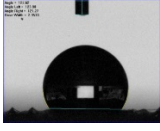
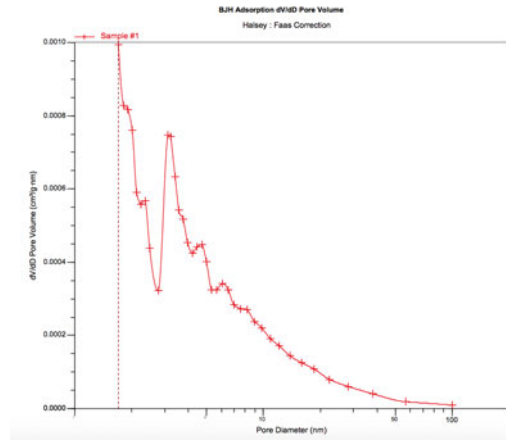
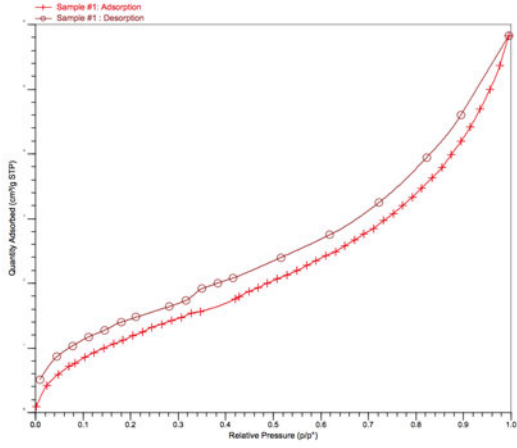
Sample scaffolds	Non-Coated	Contact Angle (°)	NaOH-Treated	Contact Angle (°)	Coated	Contact Angle (°)
250 μm		130.0175		95.988		0
500 μm		130.9675		77.898		0
750 μm		128.568		67.296		0
Offset. 30.70		100.178333		68.918		0
Offset. 50.50		116.086667		0		0
Gradient		19.408		15.92		0

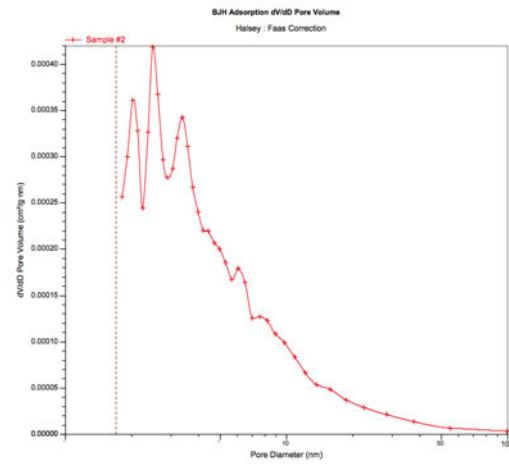
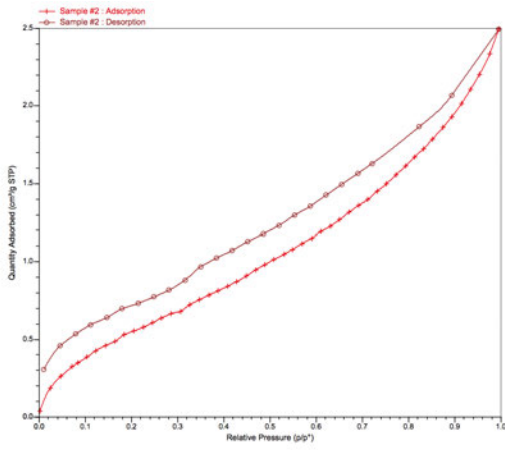
Figure S5. Various contact angle measurements on different pore surfaces of PCL scaffold.

A)

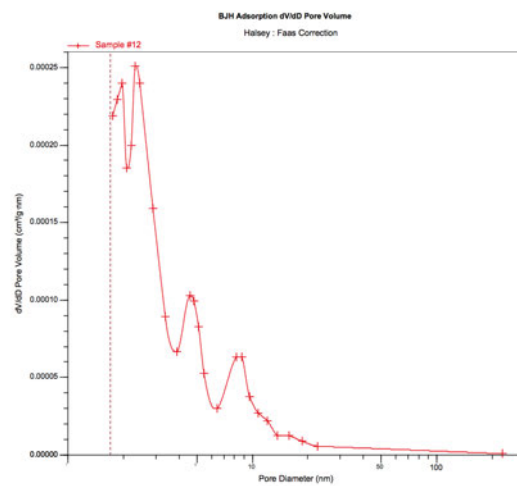
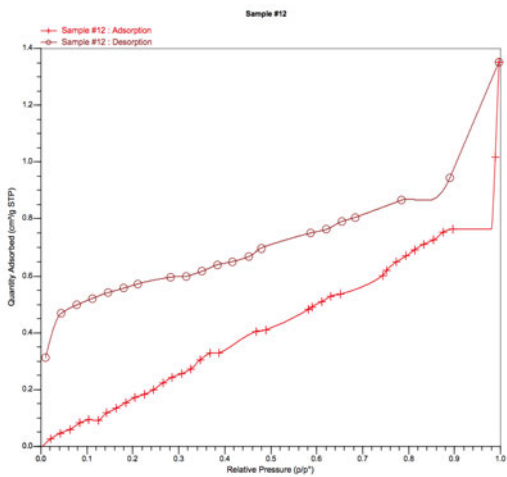
250
μm



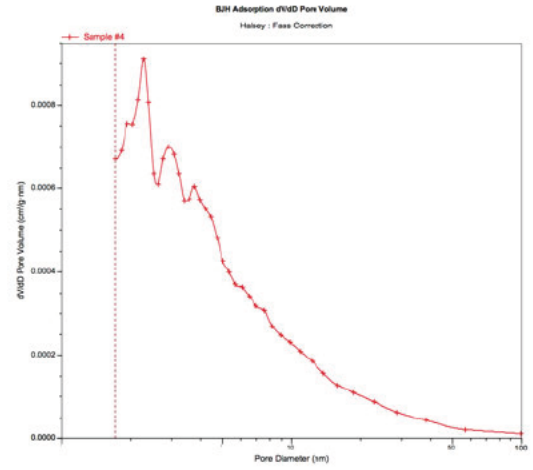
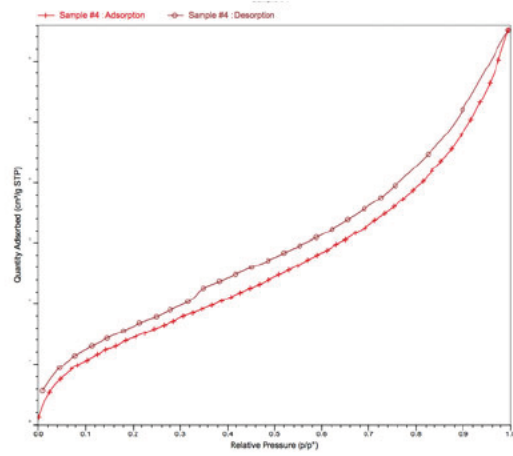
500
μm



750
μm

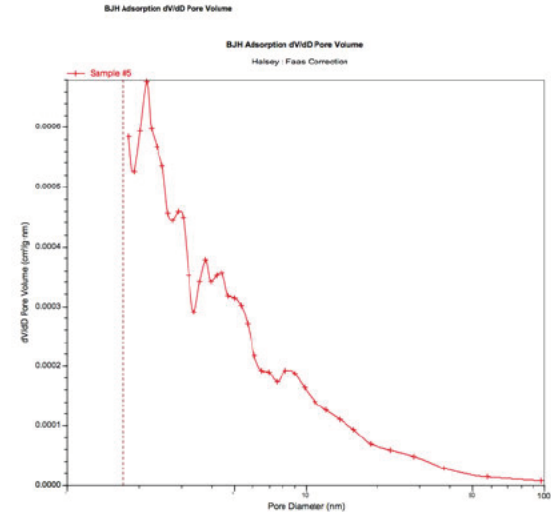
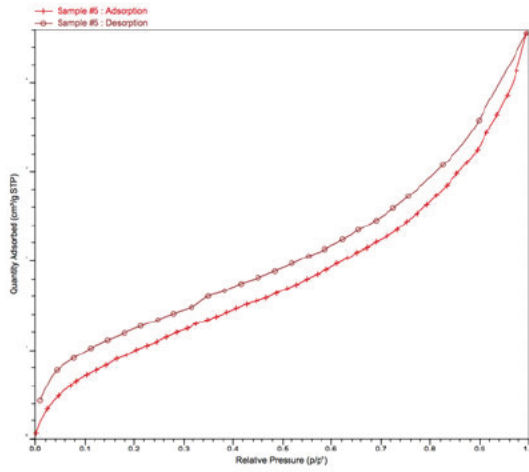


Offset.30.70

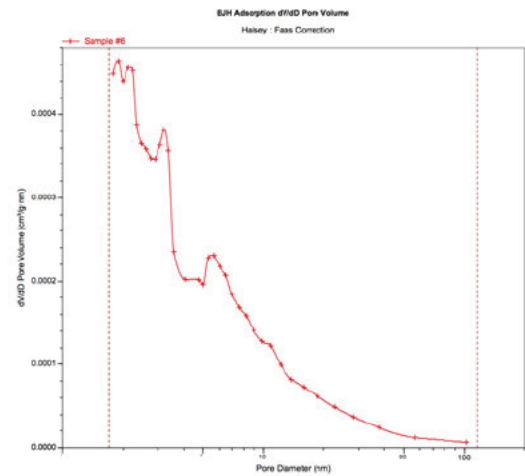
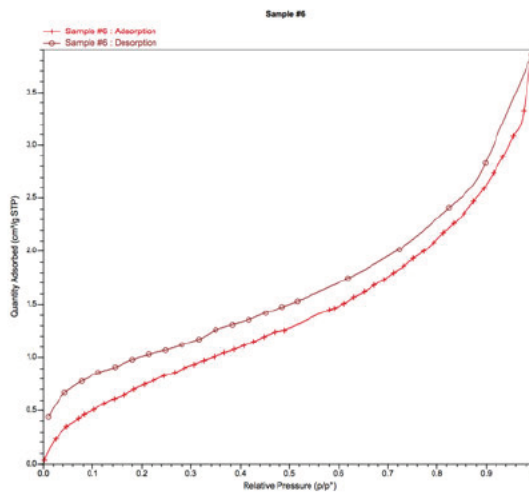


Offset.50.50

Quantity Adsorbed (cm³ STP)

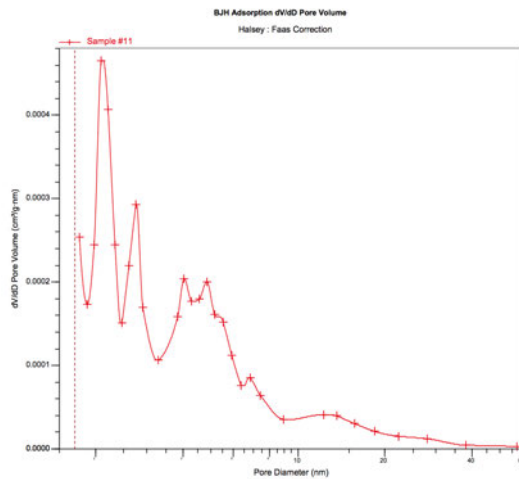
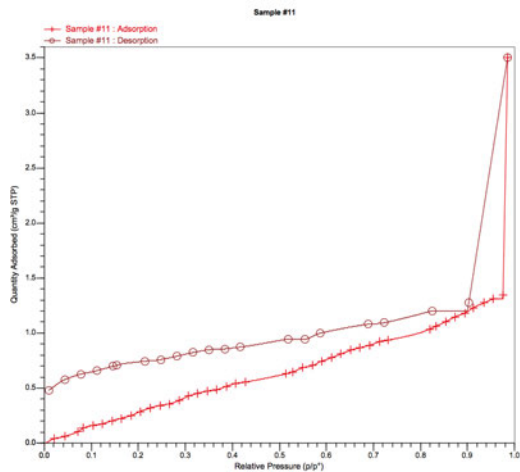


Gradient

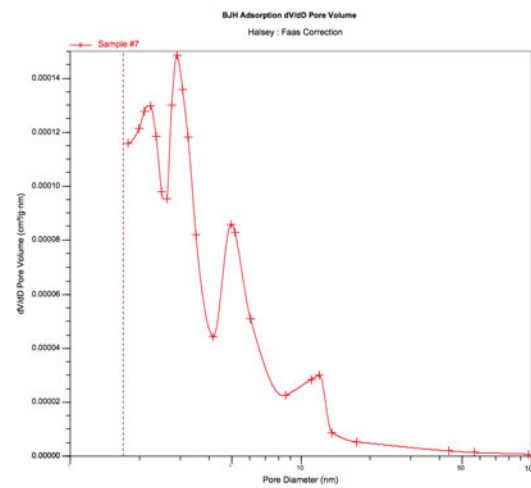
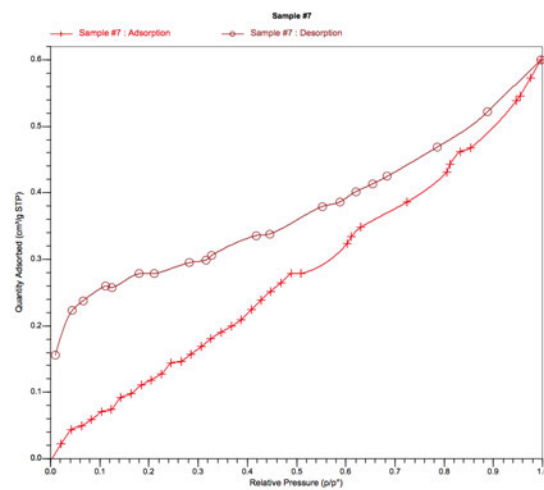


B)

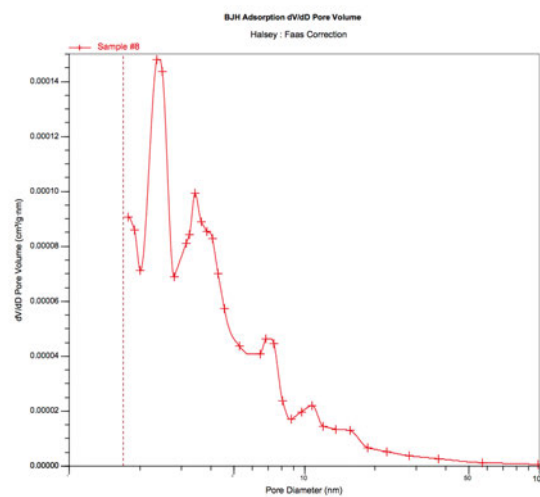
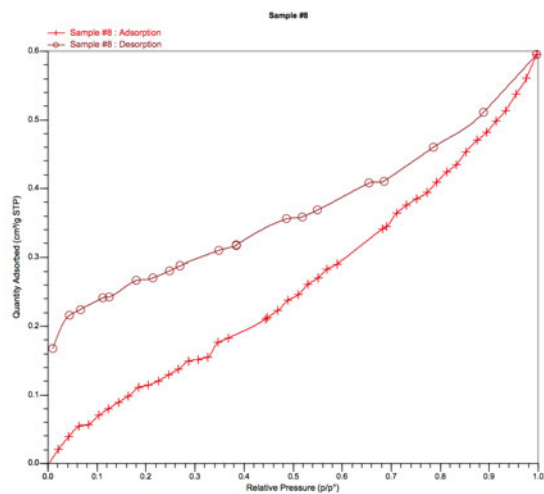
250 μm



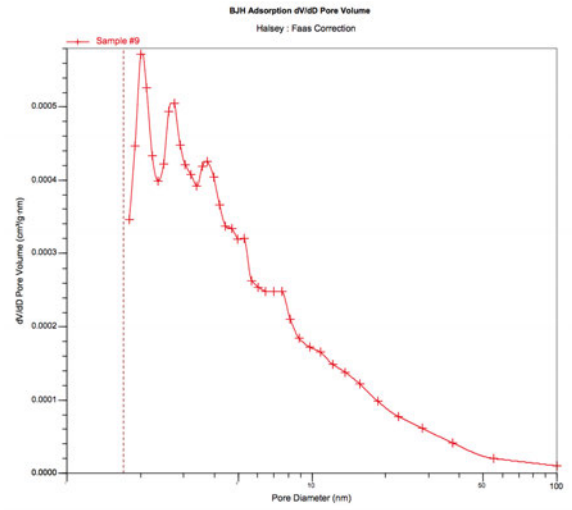
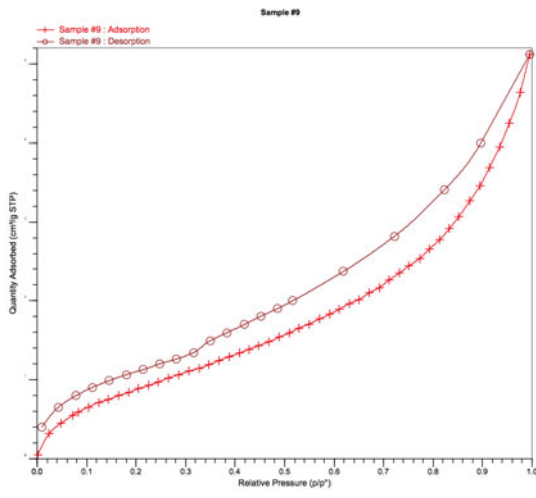
500 μm



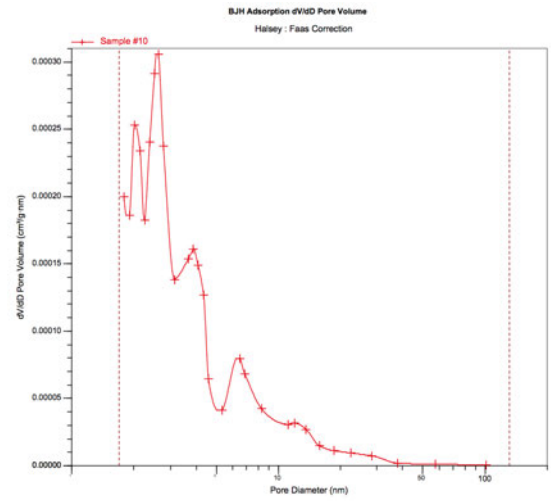
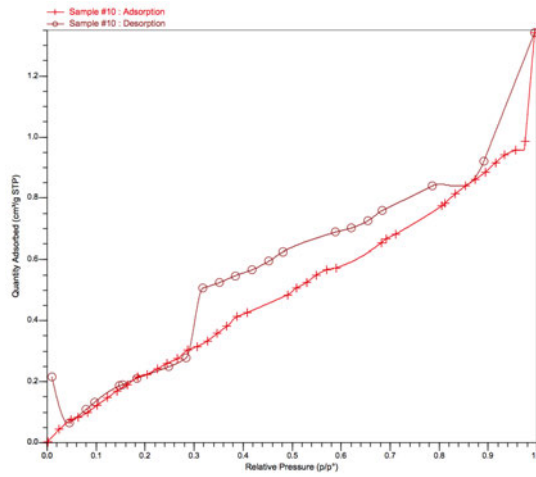
750 μm



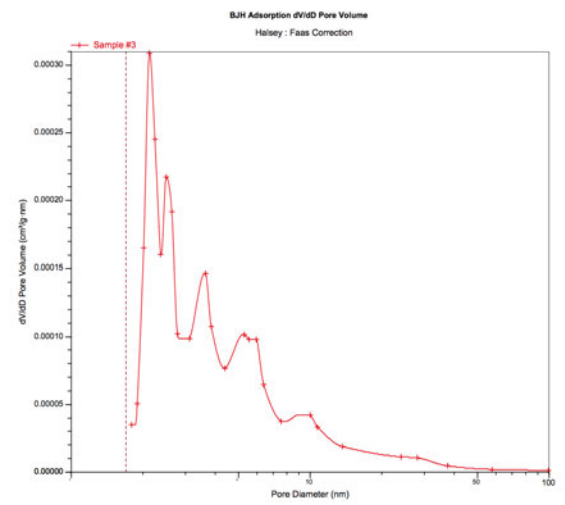
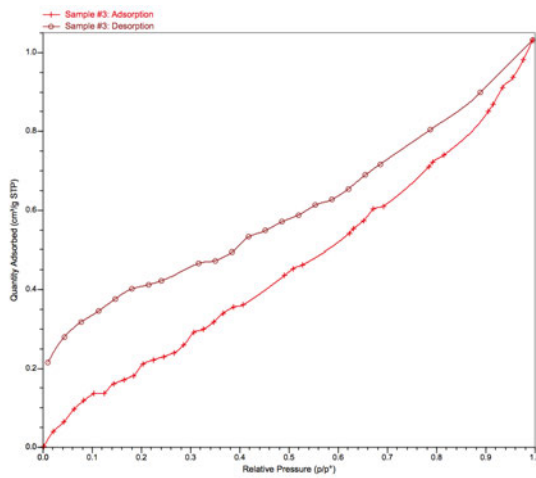
Offset.30.70



Offset.50.50

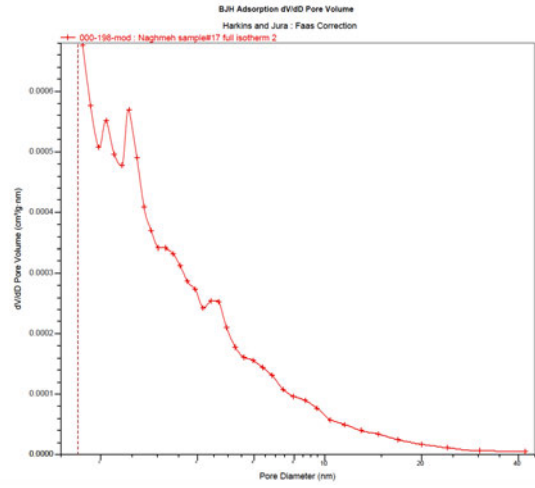
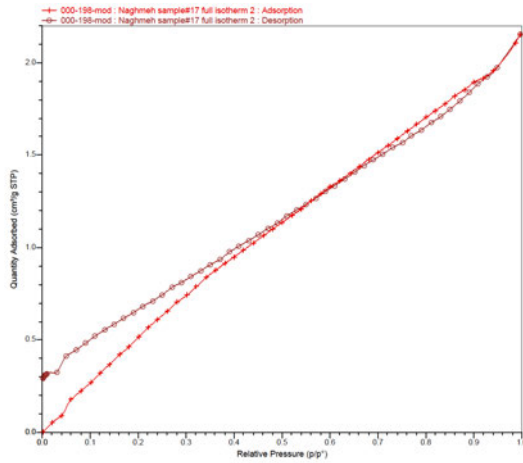


Gradient

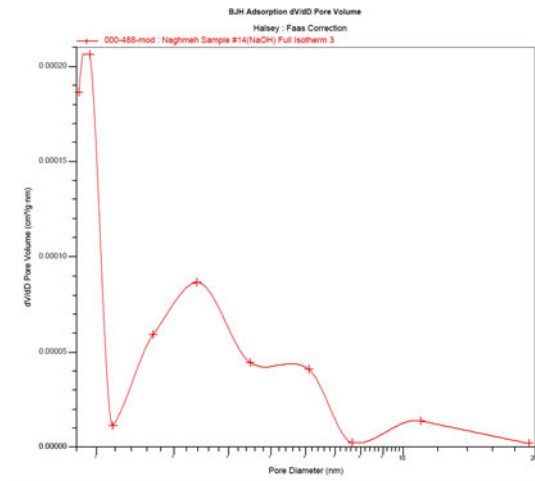
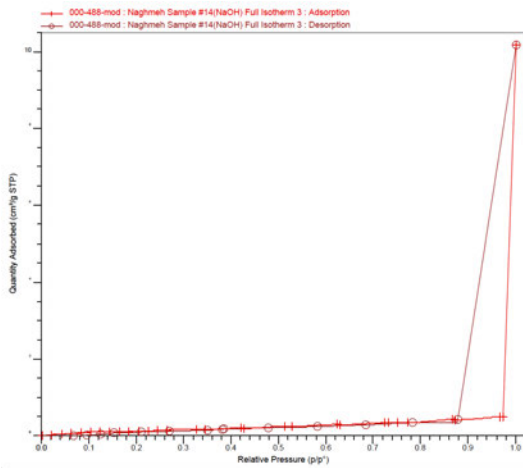


C)

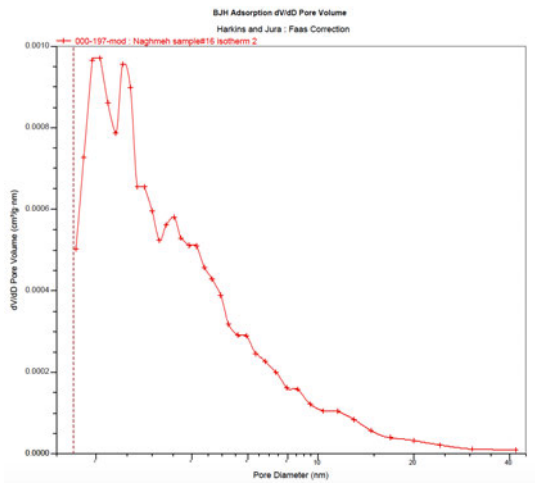
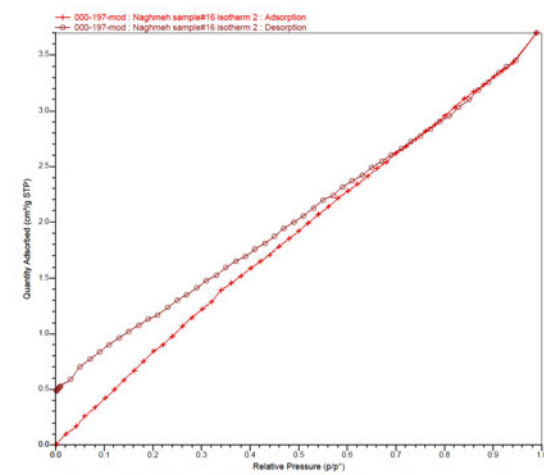
250 μm



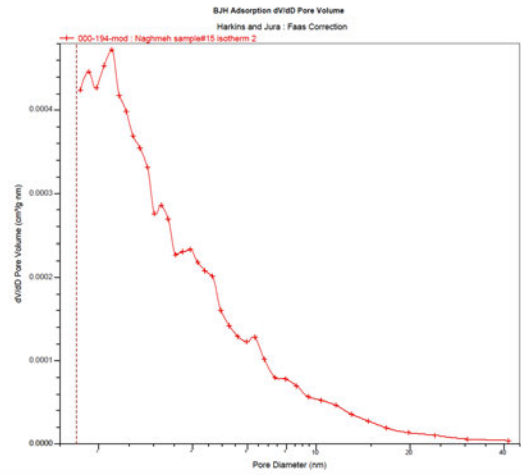
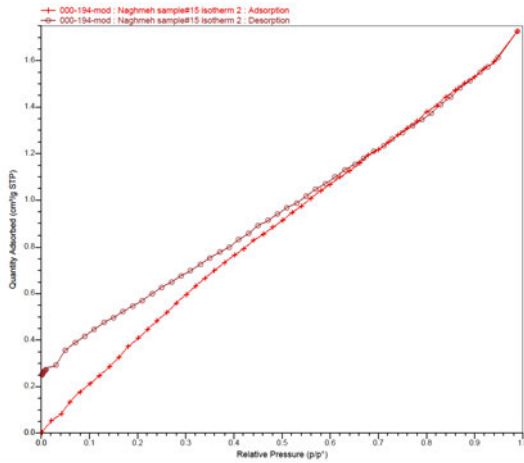
500 μm



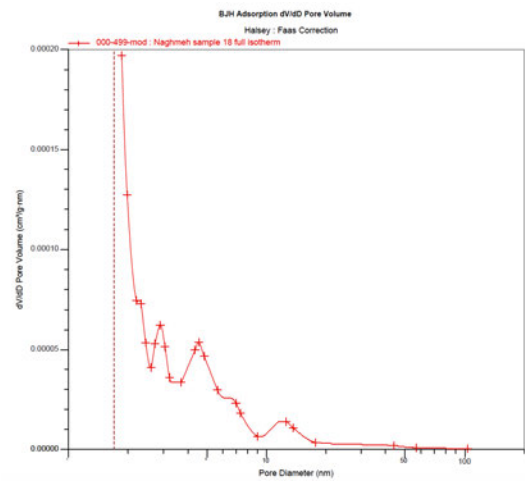
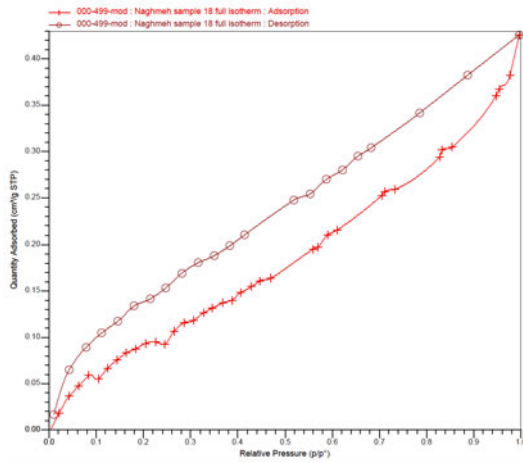
750 μm



Offset.30.70



Offset.50.50



Gradient

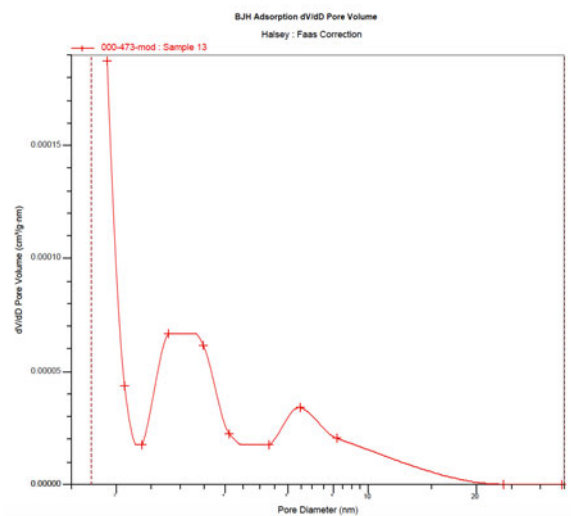
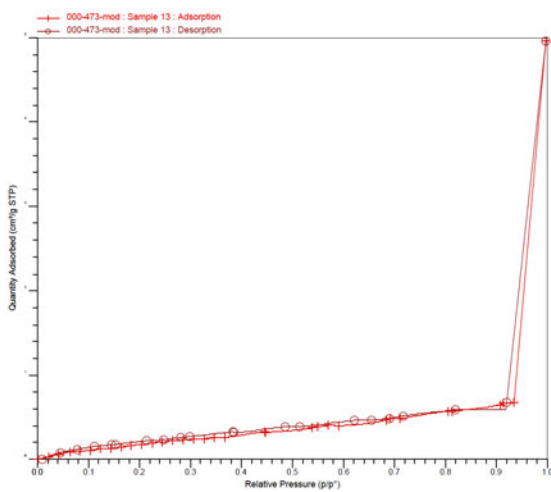


Figure S6. The BET surface area calculated from argon adsorption–desorption isotherms (A) CaP coated scaffolds, (B) Non coated scaffolds, (C) NaOH treated scaffold.

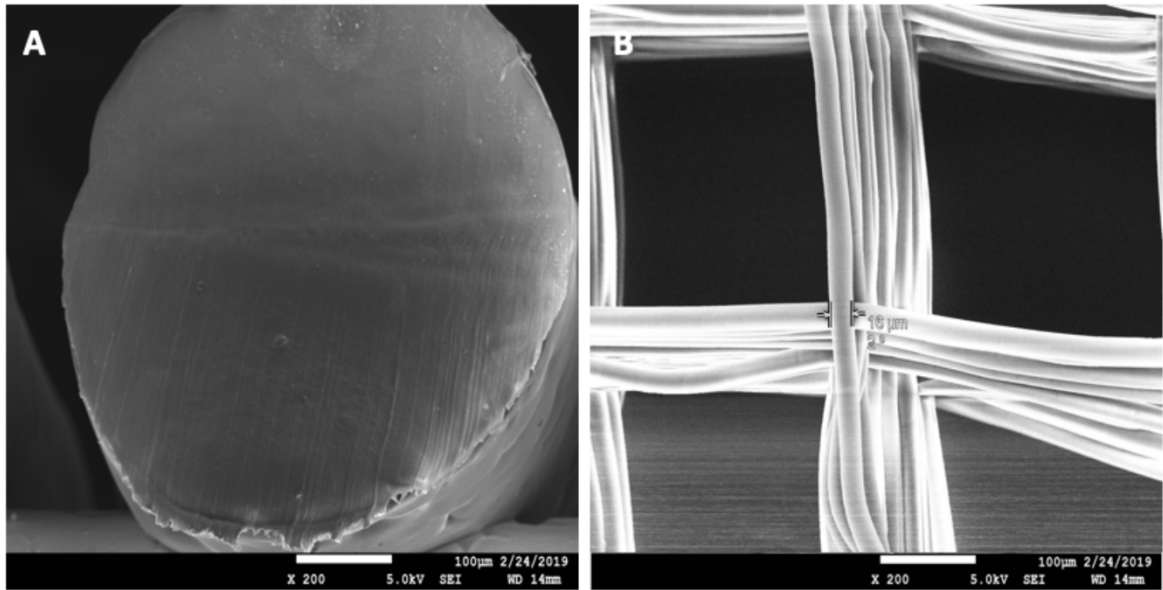


Figure S7. SEM cross section images of mean fibre diameter (A) FDM 3D printed, (B) Melt electrowritten PCL scaffold.

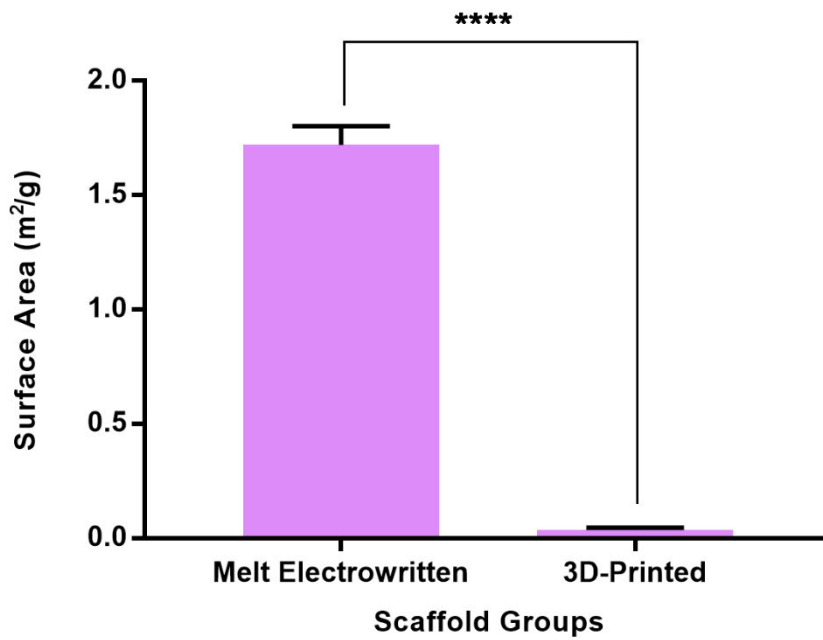
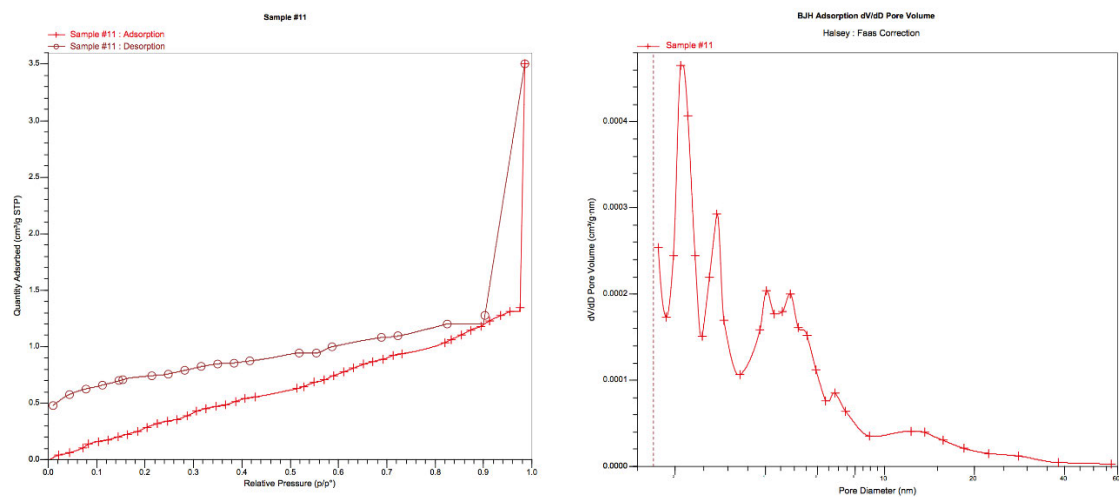


Figure S8. Mean specific surface area of the melt electrowritten and FDM 3D printed PCL scaffold.

A)



B)

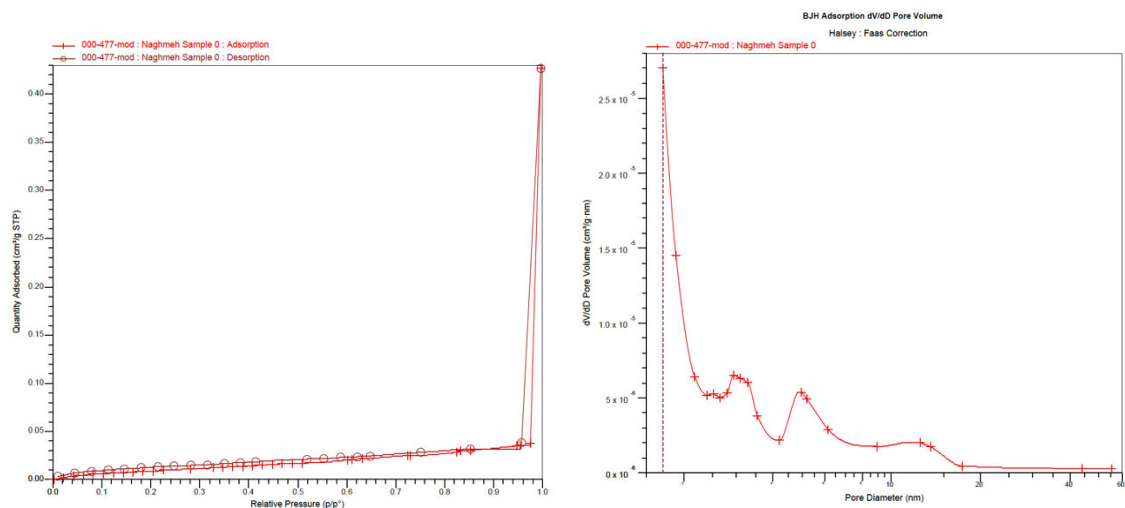


Figure S9. The BET surface area calculated from argon adsorption–desorption isotherms, (A) Melt electrowritten, (B) FDM 3D-printed PCL scaffold.

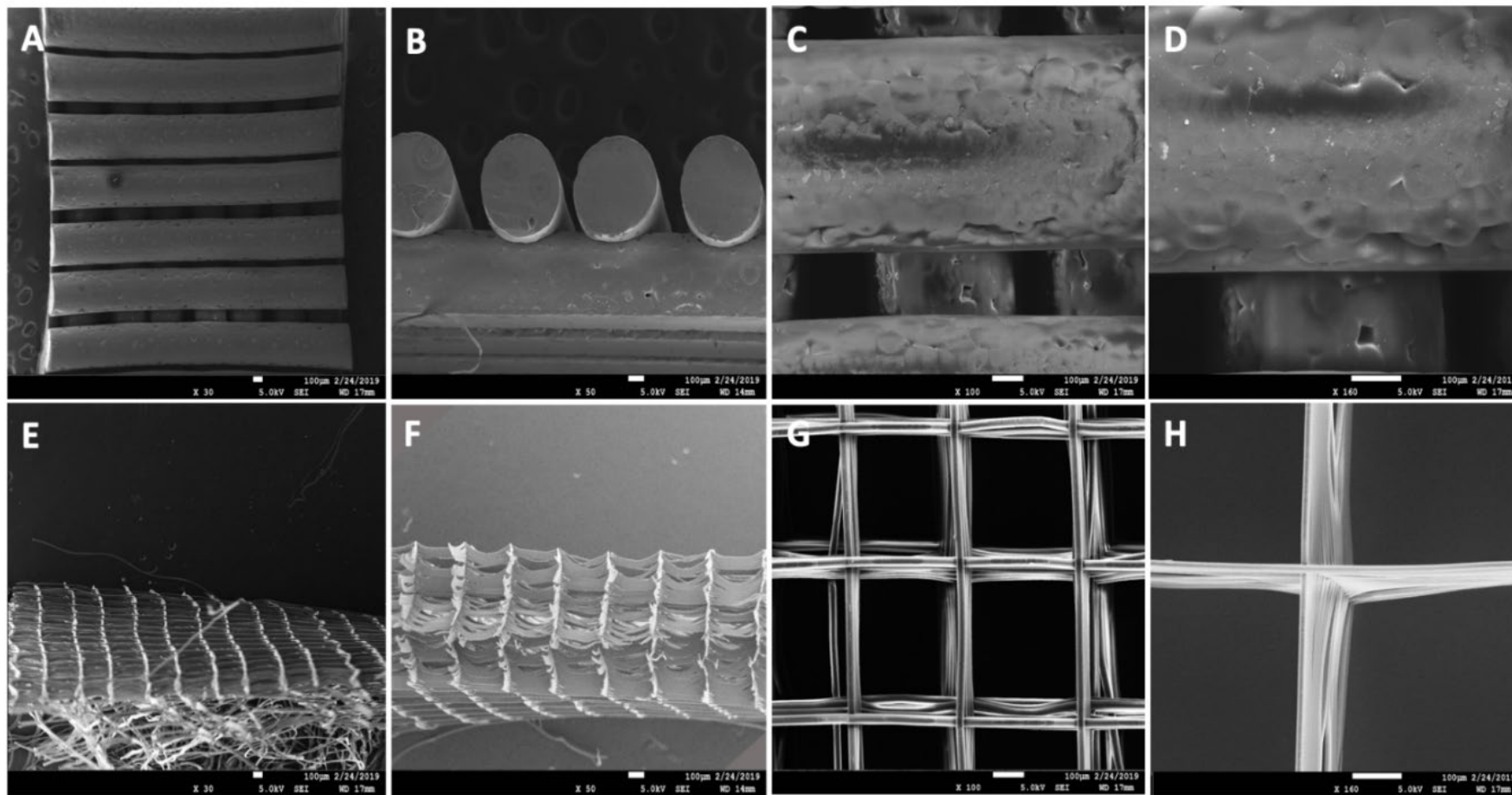


Figure S10. SEM micrographs of pore size distribution of (A-D) FDM 3D printed, (E-H) Melt electrowritten PCL scaffold, (B, F) Cross sections; (pore size: 250 μm).

References

1. Chocholata P, Kulda V, Babuska V. Fabrication of Scaffolds for Bone-Tissue Regeneration. *Materials*. 2019;12(4).
2. Wunner FM, Wille ML, Noonan TG, Bas O, Dalton PD, De-Juan-Pardo EM, et al. Melt Electrospinning Writing of Highly Ordered Large Volume Scaffold Architectures. *Adv Mater*. 2018;30(20).
3. Ashworth JC, Mehr M, Buxton PG, Best SM, Cameron RE. Optimising collagen scaffold architecture for enhanced periodontal ligament fibroblast migration. *J Mater Sci-Mater M*. 2018;29(11).
4. Ma HS, Feng C, Chang J, Wu CT. 3D-printed bioceramic scaffolds: From bone tissue engineering to tumor therapy. *Acta Biomater*. 2018;79:37-59.
5. Jun I, Han HS, Edwards JR, Jeon H. Electrospun Fibrous Scaffolds for Tissue Engineering: Viewpoints on Architecture and Fabrication. *Int J Mol Sci*. 2018;19(3).
6. Liu M, Zhang Y, Sun S, Khan AR, Ji J, Yang M, et al. Recent advances in electrospun for drug delivery purpose. *J Drug Target*. 2019;27(3):270-82.
7. Dayan CB, Afghah F, Okan BS, Yildiz M, Menciloglu Y, Culha M, et al. Modeling 3D melt electrospinning writing by response surface methodology. *Mater Design*. 2018;148:87-95.
8. Bruzauskaite I, Bironaite D, Bagdonas E, Bernotiene E. Scaffolds and cells for tissue regeneration: different scaffold pore sizes-different cell effects. *Cytotechnology*. 2016;68(3):355-69.
9. Zhang YB, Li RY, Wu WZ, Qing YA, Tang XF, Ye WL, et al. Adhesion and Proliferation of Osteoblast-Like Cells on Porous Polyetherimide Scaffolds. *Biomed Res Int*. 2018.

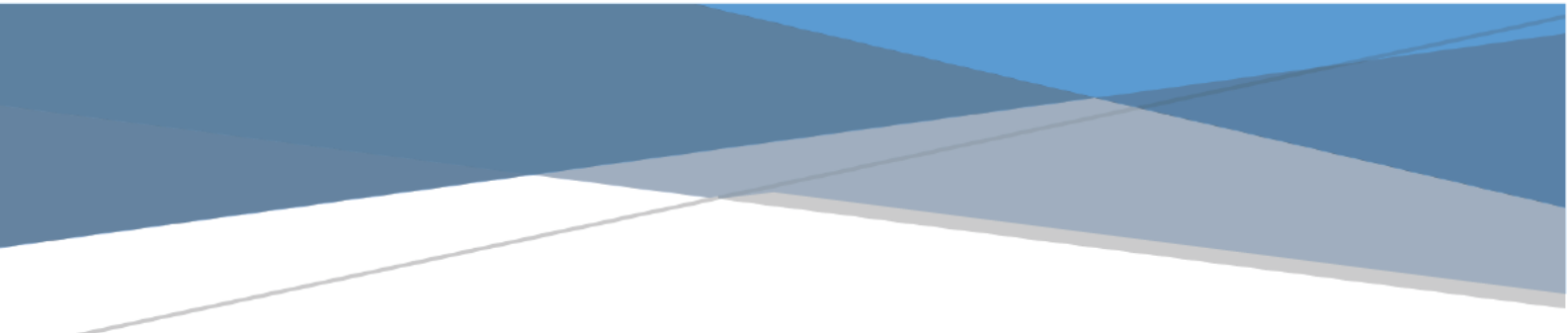
10. Lai YX, Cao HJ, Wang XL, Chen SK, Zhang M, Wang N, et al. Porous composite scaffold incorporating osteogenic phytomolecule icariin for promoting skeletal regeneration in challenging osteonecrotic bone in rabbits. *Biomaterials*. 2018;153:1-13.
11. Hoai TT, Nga NK. Effect of pore architecture on osteoblast adhesion and proliferation on hydroxyapatite/poly(D,L) lactic acid-based bone scaffolds. *J Iran Chem Soc*. 2018;15(7):1663-71.
12. Yilgor P, Sousa RA, Reis RL, Hasirci N, Hasirci V. 3D plotted PCL scaffolds for stem cell based bone tissue engineering. *Macromol Symp*. 2008;269:92-9.
13. Afshar M, Anaraki AP, Montazerian H. Compressive characteristics of radially graded porosity scaffolds architected with minimal surfaces. *Mat Sci Eng C-Mater*. 2018;92:254-67.
14. Lammi MJ, Piltti J, Prittinen J, Qu CJ. Challenges in Fabrication of Tissue-Engineered Cartilage with Correct Cellular Colonization and Extracellular Matrix Assembly. *Int J Mol Sci*. 2018;19(9).
15. Lin YH, Chiu YC, Shen YF, Wu YHA, Shie MY. Bioactive calcium silicate/poly-epsilon-caprolactone composite scaffolds 3D printed under mild conditions for bone tissue engineering. *J Mater Sci-Mater M*. 2018;29(1).
16. Pluta K, Sobczak-Kupiec A, Poltorak O, Malina D, Tyliczszak B. Bioactivity tests of calcium phosphates with variant molar ratios of main components. *J Biomed Mater Res A*. 2018;106(7):1941-50.
17. Abdal-Hay A, Abbasi N, Gwiazda M, Hamlet S, Ivanovski S. Novel polycaprolactone/hydroxyapatite nanocomposite fibrous scaffolds by direct melt-electrospinning writing. *Eur Polym J*. 2018;105:257-64.
18. Vaquette C, Ivanovski S, Hamlet SM, Hutmacher DW. Effect of culture conditions and calcium phosphate coating on ectopic bone formation. *Biomaterials*. 2013;34(22):5538-51.

19. Chakravorty N, Ivanovski S, Prasadam I, Crawford R, Oloyede A, Xiao Y. The microRNA expression signature on modified titanium implant surfaces influences genetic mechanisms leading to osteogenic differentiation. *Acta Biomater.* 2012;8(9):3516-23.
20. Abdal-hay A, Hussein KH, Casettari L, Khalil KA, Hamdy AS. Fabrication of novel high performance ductile poly(lactic acid) nanofiber scaffold coated with poly(vinyl alcohol) for tissue engineering applications. *Mat Sci Eng C-Mater.* 2016;60:143-50.
21. Wang S, Liu LL, Li K, Zhu LC, Chen J, Hao YQ. Pore functionally graded Ti6Al4V scaffolds for bone tissue engineering application. *Mater Design.* 2019;168.
22. Ding YP, Li W, Zhang F, Liu ZH, Ezazi NZ, Liu DF, et al. Electrospun Fibrous Architectures for Drug Delivery, Tissue Engineering and Cancer Therapy. *Adv Funct Mater.* 2019;29(2).
23. Bhattarai DP, Aguilar LE, Park CH, Kim CS. A Review on Properties of Natural and Synthetic Based Electrospun Fibrous Materials for Bone Tissue Engineering. *Membranes.* 2018;8(3).
24. Kabirian F, Ditkowski B, Zamanian A, Heying R, Mozafari M. An innovative approach towards 3D-printed scaffolds for the next generation of tissue-engineered vascular grafts. *Mater Today-Proc.* 2018;5(7):15586-94.
25. Gremare A, Guduric V, Bareille R, Heroguez V, Latour S, L'heureux N, et al. Characterization of printed PLA scaffolds for bone tissue engineering. *J Biomed Mater Res A.* 2018;106(4):887-94.
26. Fuchs A, Youssef A, Seher A, Hochleitner G, Dalton PD, Hartmann S, et al. Medical-grade polycaprolactone scaffolds made by melt electrospinning writing for oral bone regeneration - a pilot study in vitro. *Bmc Oral Health.* 2019;19.
27. Brown TD, Dalton PD, Hutmacher DW. Direct Writing By Way of Melt Electrospinning. *Adv Mater.* 2011;23(47):5651-+.

28. De Mori A, Fernandez MP, Blunn G, Tozzi G, Roldo M. 3D Printing and Electrospinning of Composite Hydrogels for Cartilage and Bone Tissue Engineering. *Polymers-Basel*. 2018;10(3).
29. Hrynevich A, Elci BS, Haigh JN, McMaster R, Youssef A, Blum C, et al. Dimension-Based Design of Melt Electrowritten Scaffolds. *Small*. 2018;14(22).
30. Sobral JM, Caridade SG, Sousa RA, Mano JF, Reis RL. Three-dimensional plotted scaffolds with controlled pore size gradients: Effect of scaffold geometry on mechanical performance and cell seeding efficiency. *Acta Biomater*. 2011;7(3):1009-18.
31. Vijayavenkataraman S, Zhang S, Lu WF, Fuh JYH. Electrohydrodynamic-jetting (EHD-jet) 3D-printed functionally graded scaffolds for tissue engineering applications. *J Mater Res*. 2018;33(14):1999-2011.
32. Boccaccio A, Uva AE, Fiorentino M, Lamberti L, Monno G. A Mechanobiology-based Algorithm to Optimize the Microstructure Geometry of Bone Tissue Scaffolds. *Int J Biol Sci*. 2016;12(1):1-17.
33. Yeo M, Simon CG, Kim G. Effects of offset values of solid freeform fabricated PCL-beta-TCP scaffolds on mechanical properties and cellular activities in bone tissue regeneration. *J Mater Chem*. 2012;22(40):21636-46.
34. Lv H, Li L, Sun M, Zhang Y, Chen L, Rong Y, et al. Mechanism of regulation of stem cell differentiation by matrix stiffness. *Stem Cell Res Ther*. 2015;6:103.
35. Khatiwala CB, Peyton SR, Putnam AJ. Intrinsic mechanical properties of the extracellular matrix affect the behavior of pre-osteoblastic MC3T3-E1 cells. *Am J Physiol-Cell Ph*. 2006;290(6):C1640-C50.
36. Jeong J, Kim JH, Shim JH, Hwang NS, Heo CY. Bioactive calcium phosphate materials and applications in bone regeneration. *Biomater Res*. 2019;23:4.

37. Escada ALD, Machado JPB, Claro APRA. Characterization of Calcium Phosphate Coating Produced by Biomimetic Method. *Mater Res-Ibero-Am J*. 2015;18(1):3-8.
38. Neto AS, Ferreira JMF. Synthetic and Marine-Derived Porous Scaffolds for Bone Tissue Engineering. *Materials*. 2018;11(9).
39. Lara-Padilla H, Mendoza-Buenrostro C, Cardenas D, Rodriguez-Garcia A, Rodriguez CA. Influence of Controlled Cooling in Bimodal Scaffold Fabrication Using Polymers with Different Melting Temperatures. *Materials*. 2017;10(6).
40. Rustom LE, Poellmann MJ, Wagoner Johnson AJ. Mineralization in micropores of calcium phosphate scaffolds. *Acta Biomater*. 2019;83:435-55.
41. Chen YH, Frith JE, Dehghan-Manshadi A, Kent D, Bermingham M, Dargusch M. Biocompatible porous titanium scaffolds produced using a novel space holder technique. *J Biomed Mater Res B*. 2018;106(8):2796-806.
42. O'Brien FJ, Harley BA, Yannas IV, Gibson LJ. The effect of pore size on cell adhesion in collagen-GAG scaffolds. *Biomaterials*. 2005;26(4):433-41.
43. Murphy CM, Haugh MG, O'Brien FJ. The effect of mean pore size on cell attachment, proliferation and migration in collagen-glycosaminoglycan scaffolds for bone tissue engineering. *Biomaterials*. 2010;31(3):461-6.
44. Chen SS, Gao S, Jing JG, Lu QH. Designing 3D Biological Surfaces via the Breath-Figure Method. *Adv Healthc Mater*. 2018;7(6).
45. Tamburaci S, Tihminlioglu F. Biosilica incorporated 3D porous scaffolds for bone tissue engineering applications. *Mat Sci Eng C-Mater*. 2018;91:274-91.
46. Daugela P, Pranskunas M, Juodzbaly G, Liesiene J, Baniukaitiene O, Afonso A, et al. Novel cellulose/hydroxyapatite scaffolds for bone tissue regeneration: In vitro and in vivo study. *J Tissue Eng Regen M*. 2018;12(5):1195-208.

47. Nocera AD, Comin R, Salvatierra NA, Cid MP. Development of 3D printed fibrillar collagen scaffold for tissue engineering. *Biomed Microdevices*. 2018;20(2).
48. Gupte MJ, Swanson WB, Hu J, Jin XB, Ma HY, Zhang ZP, et al. Pore size directs bone marrow stromal cell fate and tissue regeneration in nanofibrous macroporous scaffolds by mediating vascularization. *Acta Biomater*. 2018;82:1-11.
49. Conde CM, Demarco FF, Casagrande L, Alcazar JC, Nor JE, Tarquinio SB. Influence of poly-L-lactic acid scaffold's pore size on the proliferation and differentiation of dental pulp stem cells. *Braz Dent J*. 2015;26(2):93-8.



CHAPTER 4

**ROLE OF OFFSET AND GRADIENT
ARCHITECTURES OF 3-D MELT
ELECTROWRITTEN SCAFFOLD ON
DIFFERENTIATION AND MINERALIZATION OF
OSTEOBLASTS**

STATEMENT OF CONTRIBUTION TO CO-AUTHORED PUBLISHED PAPER

This chapter includes a **published** co-authored paper. The bibliographic details of the co-authored paper, including all authors, are:

Naghme **Abbasi**, *Saso Ivanovski*, *Karan Gulati*, *Robert M. Love*, *Stephen Hamlet*. *Role of Offset and Gradient Architectures of 3-D Melt electrowritten Scaffold on Differentiation and Mineralization of Osteoblasts*. *Biomaterials Research Journal*; 2020 January, <https://doi.org/10.1186/s40824-019-0180-z> (IF: 4.831)

My contribution to the paper involved:

Designing of the project, provision of the data, the preliminary analysis and categorisation of the data into a usable format and providing direction on the scope and structure of the analysis, interpretation of results and drafting of paper.



Date 10-Dec-2019

Naghme



Date 10-Dec-2019

Corresponding authors of paper: Dr. Stephen Hamlet



Date 10-Dec-2019

Supervisor: Dr. Stephen Hamlet

ABSTRACT

Cell-scaffold based therapies have the potential to offer an efficient osseous regenerative treatment and PCL has been commonly used as a scaffold, however its effectiveness is limited by poor cellular retention properties. This may be improved through a porous scaffold structure with efficient pore arrangement to increase cell entrapment. To facilitate this, MEW has been developed as a technique able to fabricate cell-supporting scaffolds with precise micro pore sizes via predictable fibre deposition. The effect of the scaffold's architecture on cellular gene expression however has not been fully elucidated.

The design and fabrication of three different uniform pore structures (250, 500 and 750 μm), as well as two offset scaffolds with different layout of fibres (30% and 50%) and one complex scaffold with three gradient pore sizes of 250 - 500 - 750 μm , was performed by using MEW. CaP modification was applied to enhance the PCL scaffold hydrophilicity and bone inductivity prior to seeding with osteoblasts which were then maintained in culture for up to 30 days. Over this time, osteoblast cell morphology, matrix mineralisation, osteogenic gene expression and collagen production were assessed.

The in vitro findings revealed that the gradient scaffold significantly increased ALP activity in the attached osteoblasts while matrix mineralization was higher in the 50% offset scaffolds. The expression of osteocalcin and osteopontin genes were also upregulated compared to other osteogenic genes following 30 days culture, particularly in offset and gradient scaffold structures. Immunostaining showed significant expression of osteocalcin in offset and gradient scaffold structures.

This study demonstrated that the heterogenous pore sizes in gradient and fibre offset PCL scaffolds prepared using MEW significantly improved the osteogenic potential of osteoblasts and hence may provide superior outcomes in bone regeneration applications.

INTRODUCTION

Bone lesions that results from fracture, infections and tumors require targeted strategies for effective clinical treatment (1). The combination of a three-dimensional scaffold combined with growth factors and/or cells has significant potential in bone tissue engineering as an ideal bone substitute option. However such scaffolds are not widely applied in clinical medicine, with the inability to seed a large enough cell population into scaffolds being one key impediment (2). A desirable porous interconnected scaffold is required to allow uniform cell diffusion and distribution throughout the entire scaffold structure (3). Many studies have attempted to solve this problem with various approaches, such as using bioreactors for enhanced cell proliferation, chemical and biological surface modification and varying the pore size of the scaffolds in a coordinated fashion to geometrically represent a cross section of a bone defect for an individual patient as a result of trauma or cancer metastasis (4-7). Notably, previous studies showed that cell differentiation is influenced by the porosity, elasticity and stability of the scaffold (8).

MEW scaffold fabrication enables precise control of the porosity, pore morphology and pore size of the printed scaffold architecture (9). This allows predictable strain and stress distribution within the scaffold, which can be further optimized to produce an environment favouring higher cell infiltration through appropriate interconnectivity within the scaffold and subsequent vascularization and angiogenesis (10).

Previous studies have shown rapid bone formation was associated with pore sizes between 290 and 310 μm . While smaller pore sizes enhance the mechanical properties of the scaffold, the optimal size for vascularization was noted to be $\sim 400 \mu\text{m}$ (11)(12). Therefore, fabrication of a 'gradient' porous scaffold, whereby the pore size gradually increases from one layer to the next, may overcome some of the individual limitations of both small and large homogeneous pore size scaffolds.

Gradient structures provide macropores suitable for vascularization, efficient gas/waste diffusion and nutrient supply at the expense of reduced mechanical stability. However, the denser structure of a heterogeneous gradient architecture improves ion signalling and protein adsorption as well as mechanical properties of the scaffolds, such as compressive strength. Additionally, they facilitate greater protein adsorption and better cell adhesion which decreases in the larger pore size of a homogeneous scaffold (13). Interestingly, the gradient scaffold architecture is similar to the natural structure of native bone tissue that represents different mineral density from cancellous bone to cortical bone (14, 15).

Furthermore, higher pore size in gradient scaffolds has been shown to enhance permeability, cell migration, as well as sufficient nutrients and oxygen tension in larger pores and up-regulate osteopontin and collagen type I expression, thus generating more bone mass, vascularization and blood vessel ingrowth while inhibiting the formation of cartilaginous tissue in the regenerating sites (16, 17). On the other hand, the smaller size of gradient pores promote cell seeding and growth by providing higher surface area (18). The complex heterogeneous and hierarchical structure of bone tissue creates significant variation in the compressive and tensile strength of different regions within bone. It's been shown that the morphology of the pores influences the mechanical properties and the structure of the scaffolds i.e. with more complex morphological architectures, the compressive strength will be increased (19), however, the scaffolds with greater Young's modulus and smaller pore size are preferred in applications required to withstand greater loads (20). According to Sobral et al, the simple architecture of homogeneous scaffolds is prone to collapse under high stress applied to the scaffolds, while the complexity of non-uniform porous scaffolds enables them to recover after deformation and maintain their elastic state which is critical for biomaterials implanted for bone applications (21). Our previous studies have shown that, when compared to simpler homogeneous structures, scaffolds with offset and gradient architectures resulted in significantly higher

cell distribution and proliferation following seeding (22). As a logical extension of this work, this study will investigate the potential effects of heterogeneous porous scaffold architectures, particularly offset and gradient structures on osteogenic gene expression by osteoblasts seeded into these scaffolds and the rate of mineralization throughout the construct.

MATERIALS AND METHODS

Preparation of Microfibrous PCL Membrane

A melt electrowriter (MEW) system was used to produce a fibrous scaffold with the fibre diameter in a range of 6-10 μm . The parameters for the components nozzle diameter, voltage, temperature and feeding rate were described in as previously reported (22). Two different scaffold structures; homogeneous pore size (250 μm , 500 μm , 750 μm) and heterogeneous architecture including a tri-layer scaffolds with different pore sizes from 250 μm on top, 500 μm in the middle, and 750 μm at the bottom of the scaffold and offset scaffolds in which layers were printed with various offset values of 30% and 50% compared to the previous layer.

Subsequent CaP coating was perform using simulated body fluid (SBF). The surface modification was achieved in three steps; 1) pre-treatment of the samples in 1M NaOH aqueous solution for surface activation for 0.5 hour 2) immersion of the samples in 10X SBF at 37 °C for 1 hour 3) soaking the samples in 0.5M NaOH for 0.5 hour to obtain an uniform coating then rinsing with distilled water and allowing to dry.

Cell Culture

Human osteoblast cells (hOB) obtaining from alveolar bone of a healthy female were seeded onto the scaffolds (2×10^4 in 15 μl) and cultured in either osteogenic or basal medium for 3, 14 and 30 days, according to previously reported protocols (22).

Scanning Electron Microscopy (SEM)

Cell morphology after 30 days culture on the electrowritten scaffolds was captured by scanning electron microscopy (SEM). The substrates from cell culture were fixed in 3% glutaraldehyde, then dehydrated by treating in 0.1M Cacodylate buffer three times, each 10min and post-fixed with 1% Osmium Tetroxide for 1 hr. After that, the specimens were washed in Milli-Q water two times, each 10 min. The samples were then rinsed in a concentration gradient of ethanol (40%-100%) 10 min for each. To visualise cell penetration into the scaffolds, cross-sections of the samples were fragmented in liquid nitrogen in the middle stages of the dehydration process. Finally, hexamethyldisilazane (HMDS, Sigma Aldrich, UK) was used to replace the critical point drying step in biological samples for two times, each 30 min. The samples were mounted on the Al stubs using adhesive carbon tapes and were Au-coated for observation by the SEM (Zeiss Sigma FESEM).

ALP Activity

The concentration of ALP in cells was measured after 3, 14 and 30 days of culture using p-nitrophenyl phosphate as a phosphatase substrate in a commercial ALP colorimetric assay Kit (Sigma Chemical, St. Louis, MO, USA) at a wavelength 405 nm according to the manufacturer's instructions. The ALP concentration was subsequently normalised to the total protein content (Quick Start Bradford protein assay, Bio-rad, Australia) of each sample.

Alizarin Red Staining (ARS)

To assess the osteogenic potential of the osteoblasts cultured in the melt electrowritten scaffolds with different pore sizes, alizarin red S staining of calcium deposited in the extracellular matrix of osteoblasts cultured on the scaffolds after 14 and 30 days was carried out. Briefly, the culture media was removed and the scaffolds washed using PBS.

The cells within the scaffolds were fixed in 4% paraformaldehyde then placed in 500 μ L of Alizarin Red S solution (40 mM) for 20 min at room temperature. After washing, the stained cells and scaffolds were imaged using an inverted phase contrast tissue culture microscope (Olympus, CKX 41, NY, USA). Quantification of these results was achieved by dissolving the samples in 1mL 10% Cetylpyridinium Chloride for 1 hr before transferring to 96 well plates and measuring the absorbance at 540 nm in a microplate reader (POLARstar Omega, BMG LABTECH, Germany). The average value of the negative controls (scaffold without cells) (22) was subtracted from the values of the corresponding experimental groups.

Micro-Computed Tomography (μ -CT) of Cell-Scaffold Construct

To further evaluate mineralisation within the cell-seeded scaffolds, μ -CT analysis of constructs cultured in osteogenic differentiation medium was compared to the control group (basal medium) after 30 days of culture. The volume of mineralisation was measured by the μ -CT software (μ CT40, SCANCO Medical AG, Brüttisellen, Switzerland). The average value of the negative controls (cell seeded scaffolds in expansion media) was subtracted from the values of the corresponding experimental groups. The sample was put inside the tube containing deionised water so that, it was located at the bottom of tube and cotton wool was used to stop moving of sample during scanning process. The tube was sealed to prevent solution evaporation. For scanning, the high-resolution mode was selected and the X-ray tube was applied at 45 kVp and 177 μ A. Integration time was set to 300 m sec and a three-fold frame averaging was applied using the same μ -CT hardware, acquisition, and reconstruction parameters as above. Three-dimensional images of the scaffolds were reconstructed by the software package.

Real-Time PCR Analysis (q-PCR)

RNA was extracted from the osteoblast cells 14 and 30 days after seeding onto the scaffolds using a TRIzol extraction kit (Ambion, USA). Following cDNA synthesis from

100 ng of total RNA (Taqman cDNA synthesis kit, Life Technologies, USA), the expression of osteopontin (*opn*), osteocalcin (*ocn*), bone morphogenetic protein 2 (*bmp-2*), alkaline phosphatase (*alp*), collagen type Ia (*col Ia*), wingless-related integration site (*wnt*) family member 3a (*wnt3a*), and wnt family member 5a (*wnt5a*) was achieved with an ABI 7900HT real-time PCR system (Life Technologies, USA) using SYBR Green Real-Time PCR Master Mix (Life Technologies, USA) and the following protocol; 3 minutes at 95 °C for polymerase activation followed by 40 cycles of 10 seconds denaturation at 95 °C, 20 seconds annealing at 58°C, and 1second extension at 72°C. β -*actin* expression was used as a house keeping gene and for normalization of the data.

Immunofluoresce Staining

For immunocytochemical analysis of the osteoblast cells cultured on different pore size PCL scaffolds (tissue culture plate acted as the control group) for 14 and 30 days, cells were fixed with 4% paraformaldehyde in PBS (Polysciences, Warrington, PA, USA) for 30 min at room temperature then gently rinsed with PBS. The cell membranes were then permeabilized and blocked with a protein blocker solution (1% BSA, 22.52mg Glycine in 0.1% Tween 20 in PBS), Sigma Aldrich) for 30 min. After washing, the cells were incubated in the following diluted primary antibodies at 4°C overnight: mouse monoclonal anti-Collagen IA (1:250, SantaCruz Biotechnology, USA), rabbit polyclonal anti-Collagen III (1:100, abcam, Australia), mouse monoclonal anti-Osteocalcin (1:200, abcam, Austrailia).

The cells were rinsed in PBS (three times, 5min per wash) and incubated in the appropriate secondary antibody i.e. Alexa Fluor 488-conjugated goat anti-rabbit (1:200, abcam, Australia) or F(ab')₂-Goat anti-Mouse IgG FITC (1:200, ThermoFisher Scientific, USA) at room temperature in the dark for 1 hour. Cell nuclei were stained using 40, 6-diamidino-2-phenylindole (DAPI, Vector Laboratories, Burlingame, CA, USA) in PBS

(1:1000) for 30 min. The samples were mounted onto glass slides for visualisation using a fluorescence microscope (Nikon, Eclipse- Ti, U.S.A).

Statistical Analysis

Statistical analysis of any differences between means was performed using a two-way ANOVA with correction for multiple comparisons. The experiments were run in triplicate. A p-value of <0.05 was considered as statistically significant.

RESULTS

Cell-Scaffold Morphology

Figure 4.1 SEM images show the morphology and pore arrangement of the MEW PCL scaffolds prior to cell seeding. Thirty days following seeding with osteoblasts, SEM images showed good attachment and growth of the osteoblasts onto the PCL scaffolds (Figure 4.2-a, b, c). Optimum cell attachment and proliferation was identified on the 250 μm pore size homogeneous scaffold and the offset architecture scaffolds where the majority of cells appeared to be entrapped in the space between two displaced fibres in the offset groups. The 500 μm and 750 μm pore sizes appeared to be too large for the cells to interact with the scaffold fibers whereas in the gradient group the cells passed through the largest pore size at the top of scaffold then settled down into the smaller pores at the bottom of the construct (Figure 4.2-c).

Under lower magnification, information on the degree of scaffold mineralization and the position of the cells within this mineralized matrix after 30 days culture can be observed (Figure 4.2-a, b). Reflecting the cell attachment results, calcified matrix production occurred predominately on the offset and 250 μm surface scaffolds. At higher magnification, globular shaped deposits could be distinguished in the vicinity of the more dense regions of cell-fibre junctions and in the smaller areas between the pores (Figure 4.2-c). In the gradient group, the cells appeared more concentrated at the bottom of

scaffold structure having passed through the large pore size at the top of scaffold and settled down into the smaller pores at the bottom of scaffold (Figure 4.2-d).

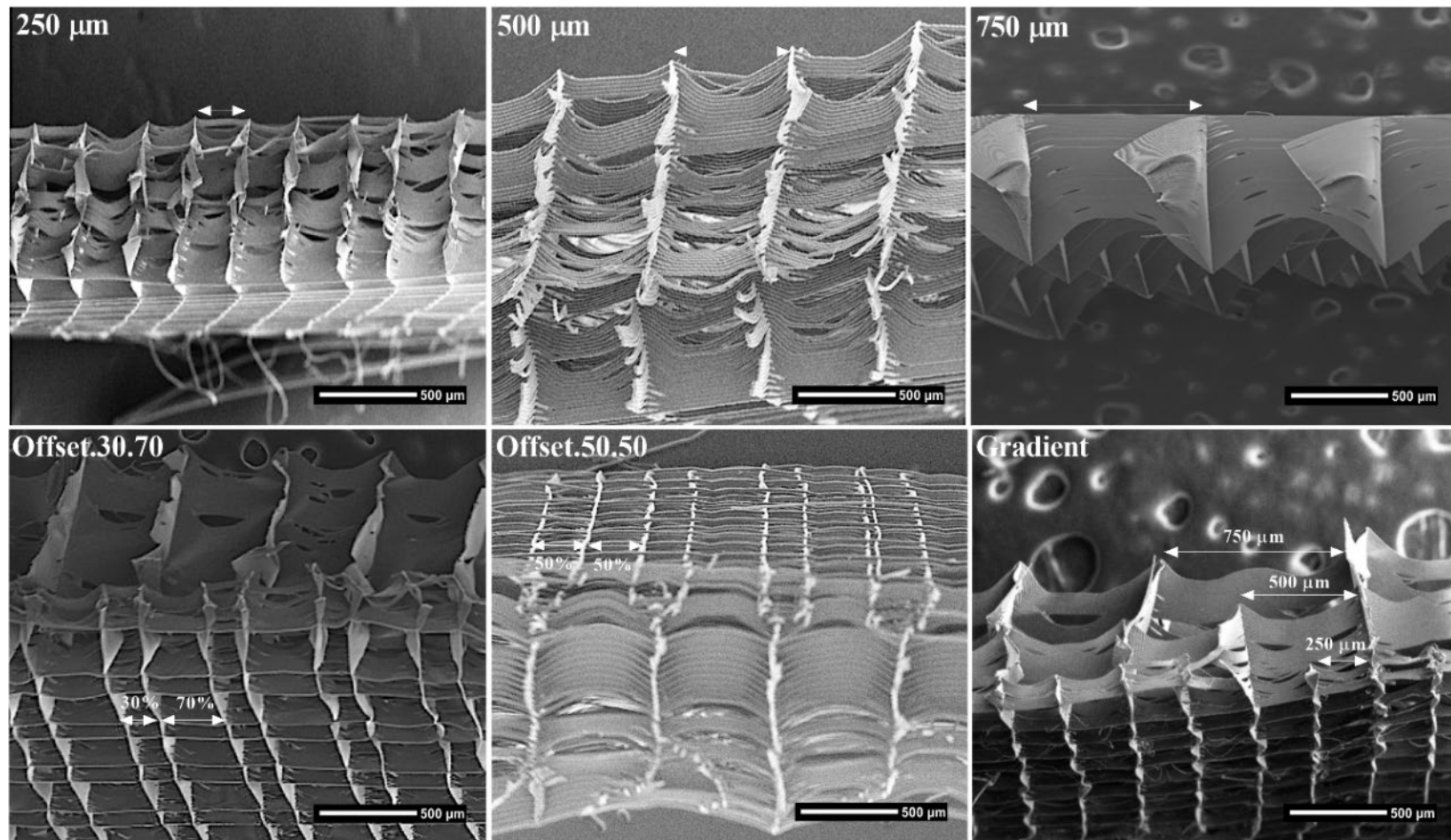
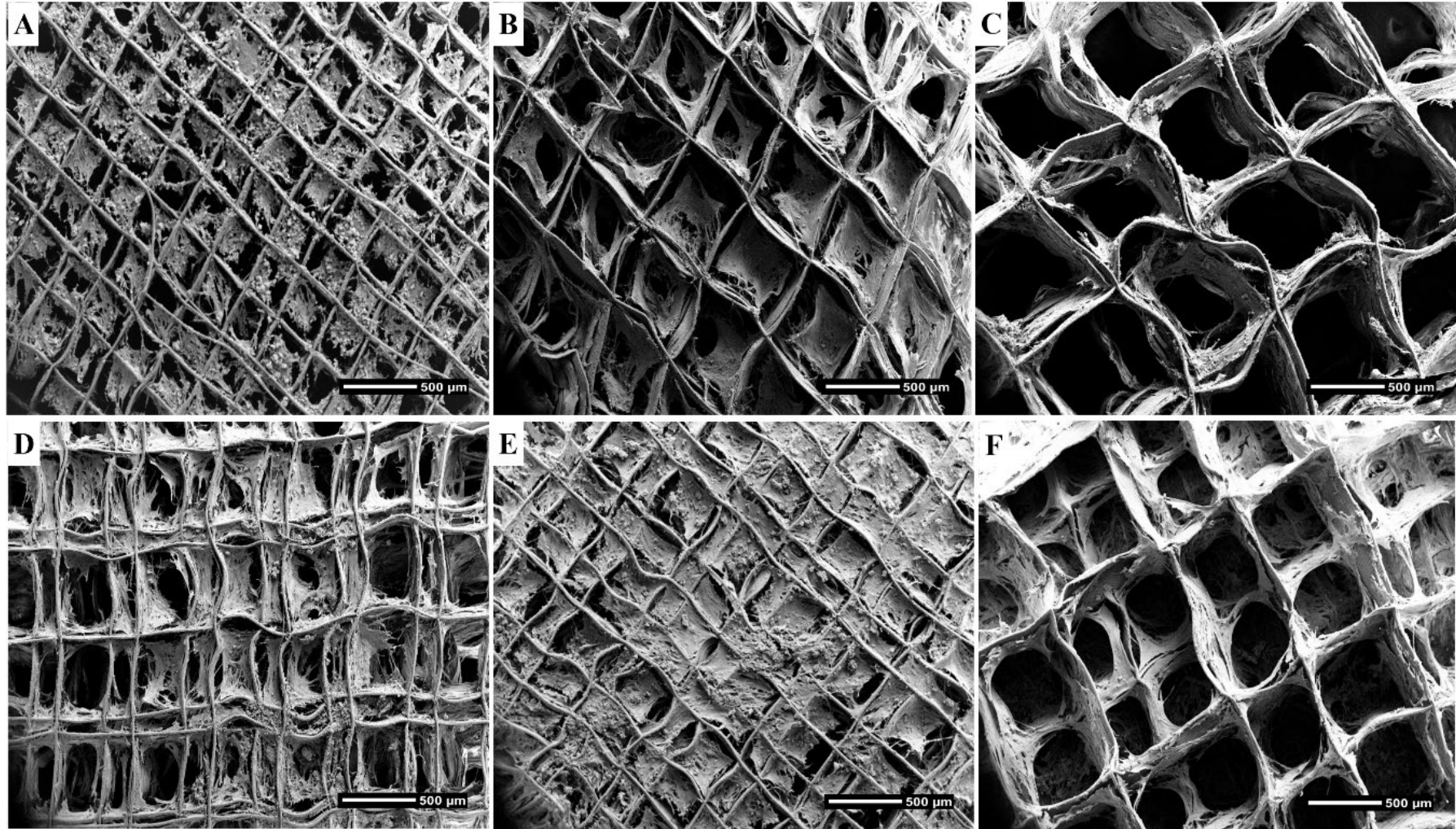
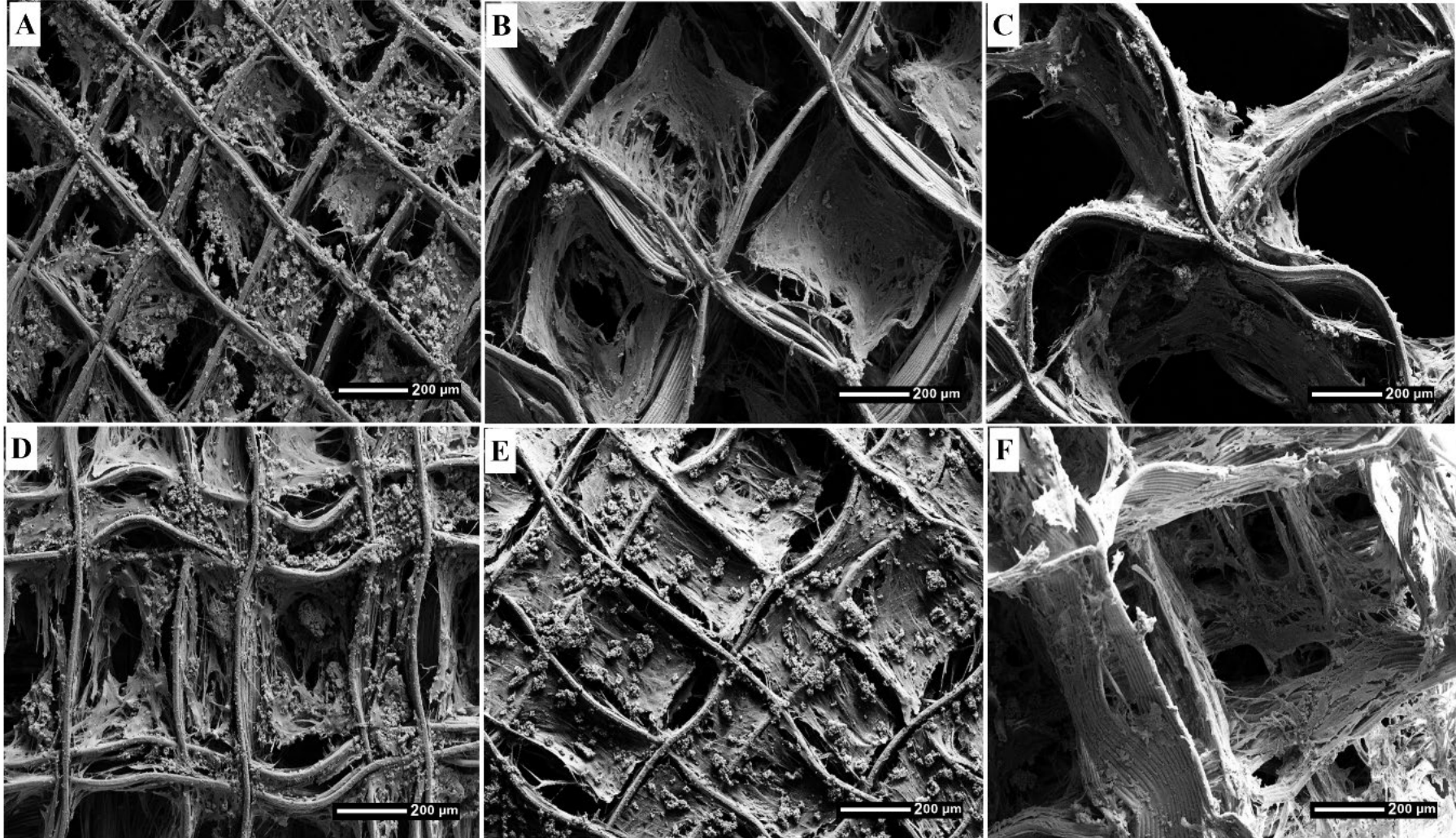


Figure 4.1. SEM image of the porous scaffold structures.

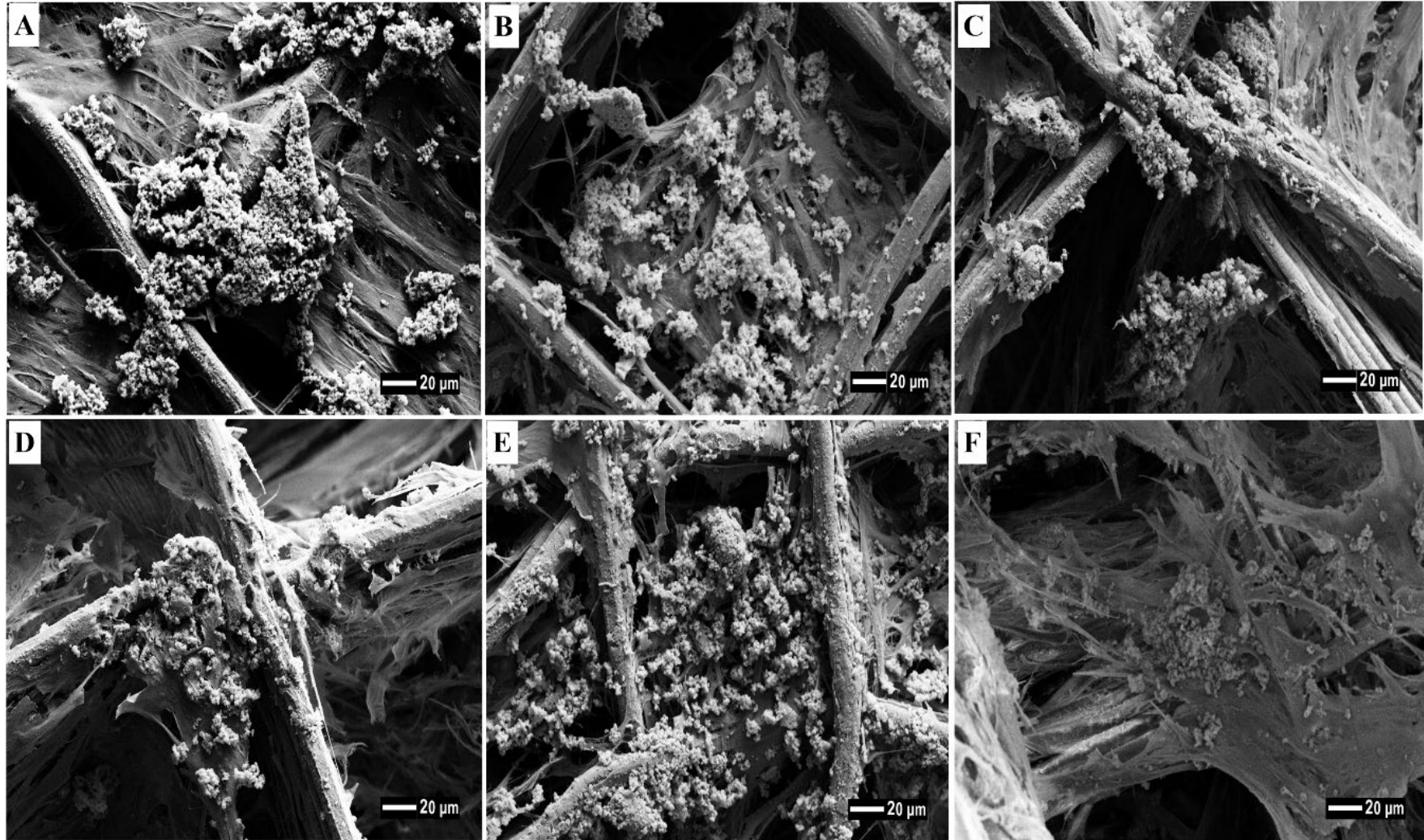
a



b



C



d

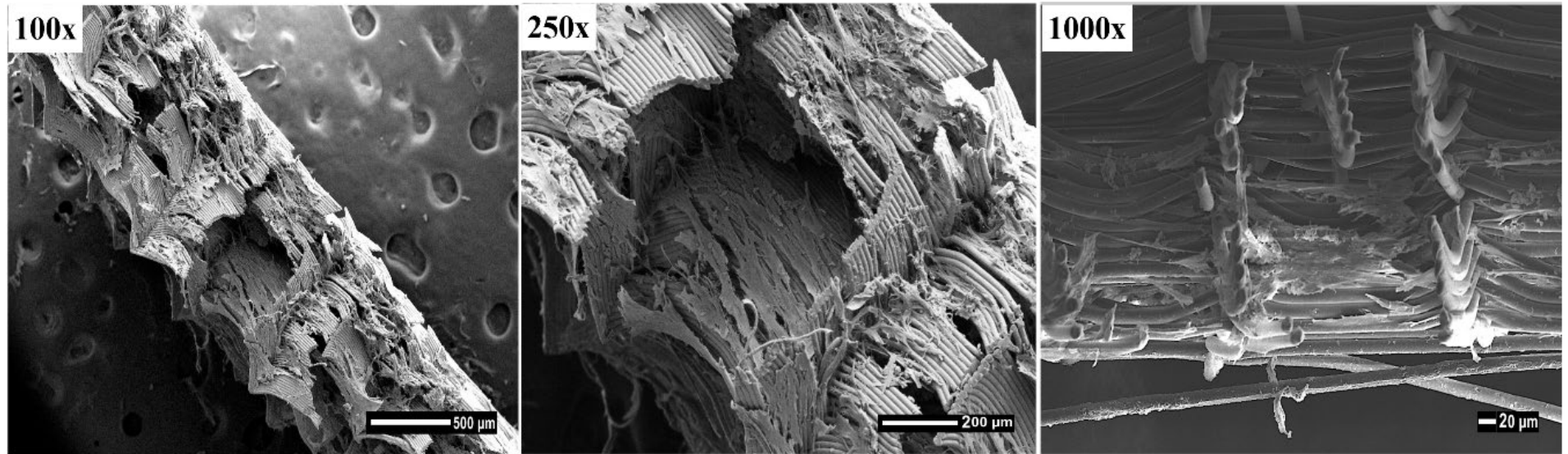
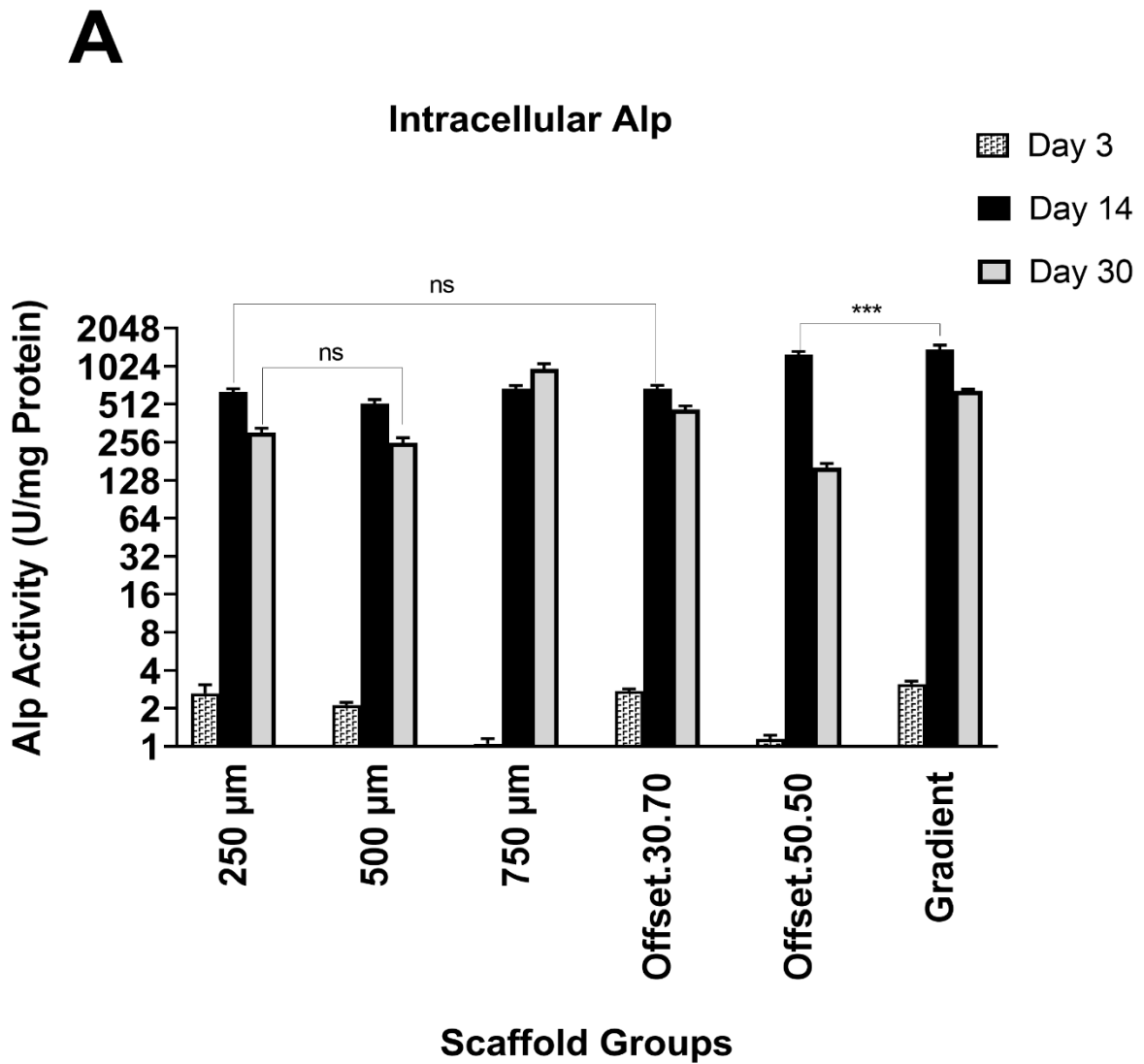


Figure 4.2. SEM micrographs showing different magnification (a) 100X, (b) 250X and (c) 1000X of the morphology and mineralization of hOB on the electrowritten PCL scaffolds after 30 days of culture A: 250 μm; B: 500 μm; C: 750 μm; D: Offset.30.70; E: Offset.50.50; F: Gradient. (d) Cross-sectional view of gradient scaffold structure.

Impact of Porous Scaffolds on ALP Activity of Osteoblast Cells

ALP activity was very low at day 3 in all groups (Figure 4.3-A, B) in the similar ranges between 0.7 to 3.1 that the maximum amount was displayed for gradient, 250 μm and offset.30.70 scaffolds respectively. By day 14 ALP activity had increased in all groups with the highest levels of activity in osteoblasts cultured on the offset.50.50 and gradient scaffolds. However, it was peaked significantly for the gradient structure culturing in osteogenic media compare to the other groups. By 30 days of culture, a reduction of ALP activity was seen for all groups except the homogeneous 750 μm pore size scaffolds.



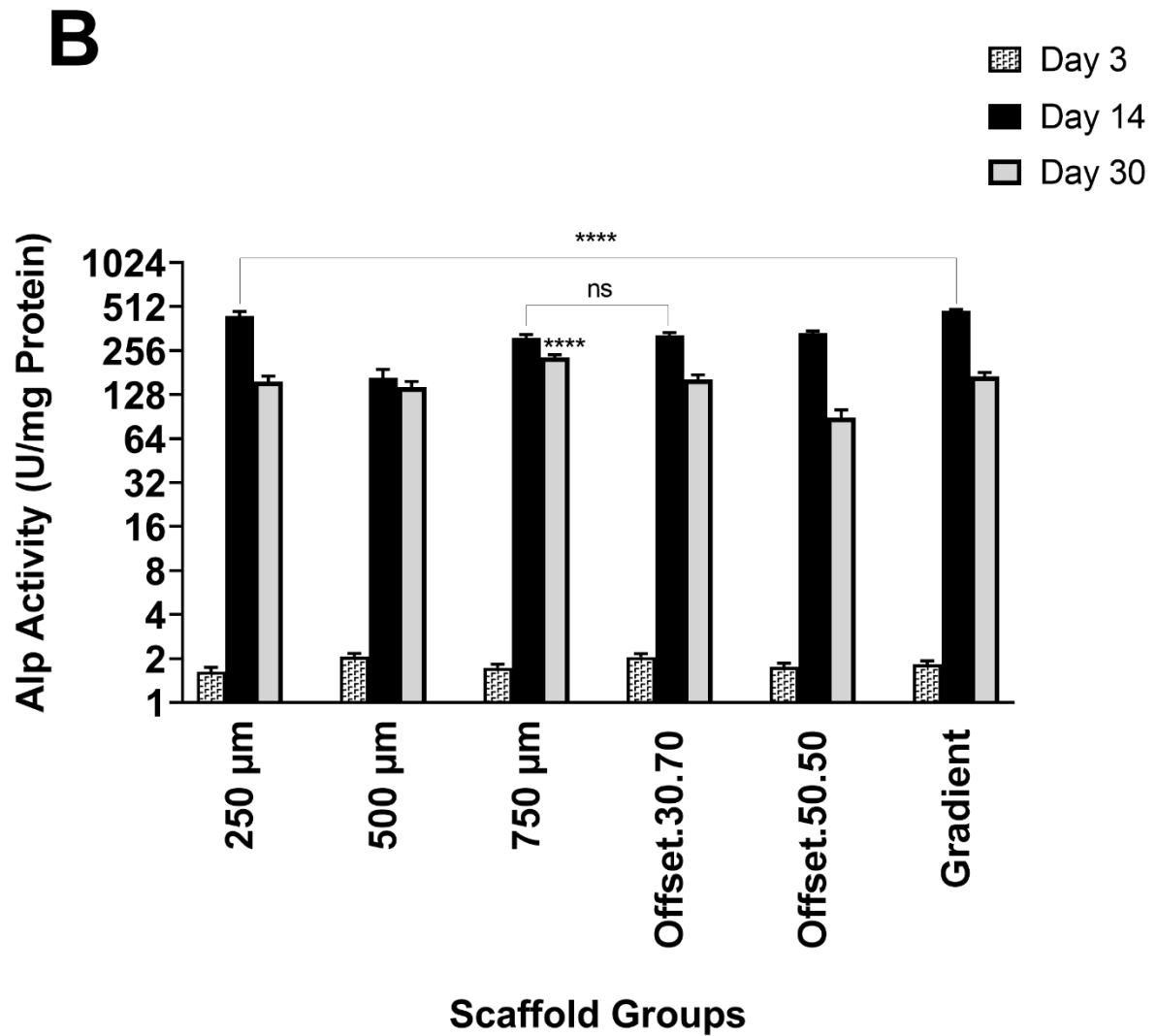
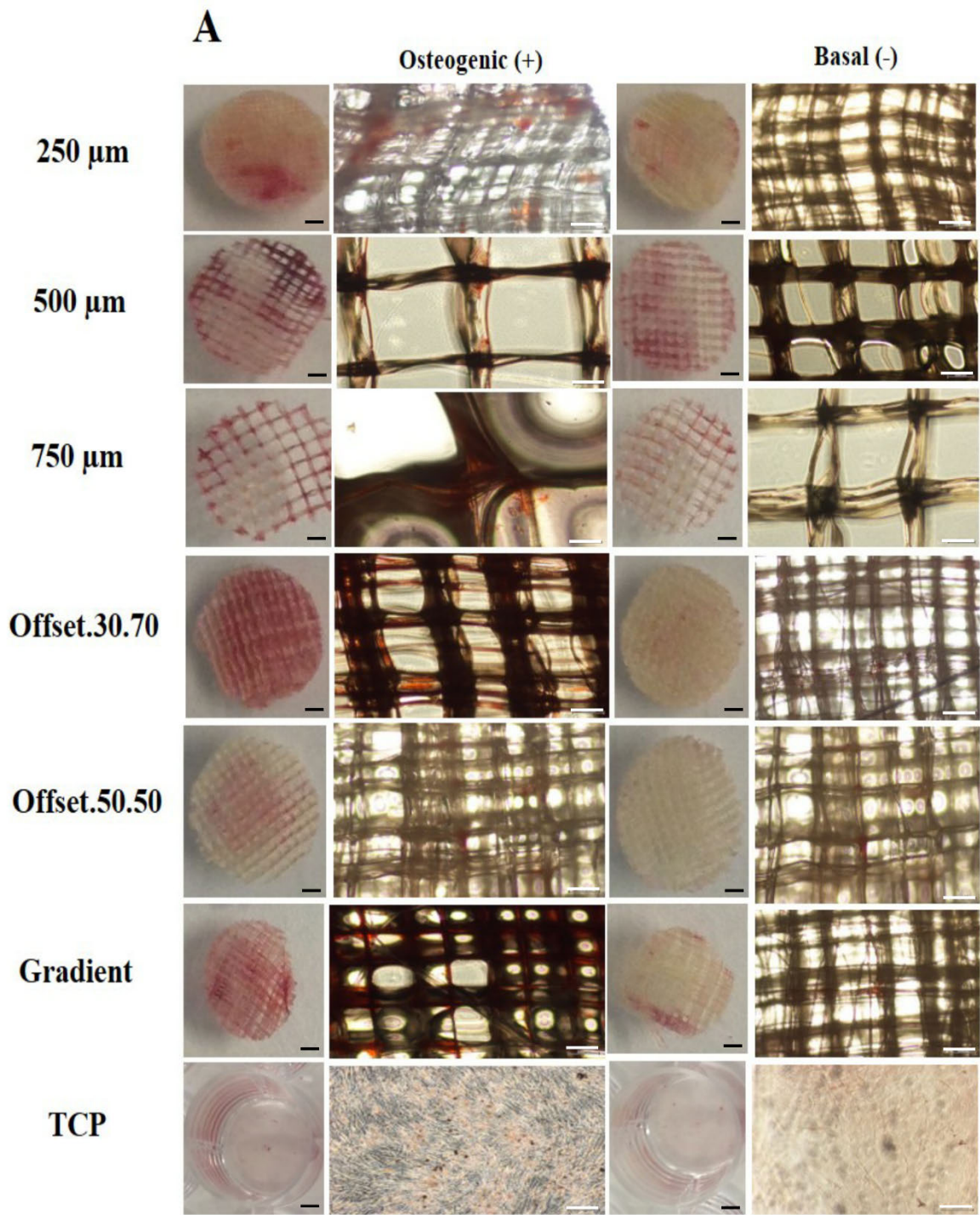


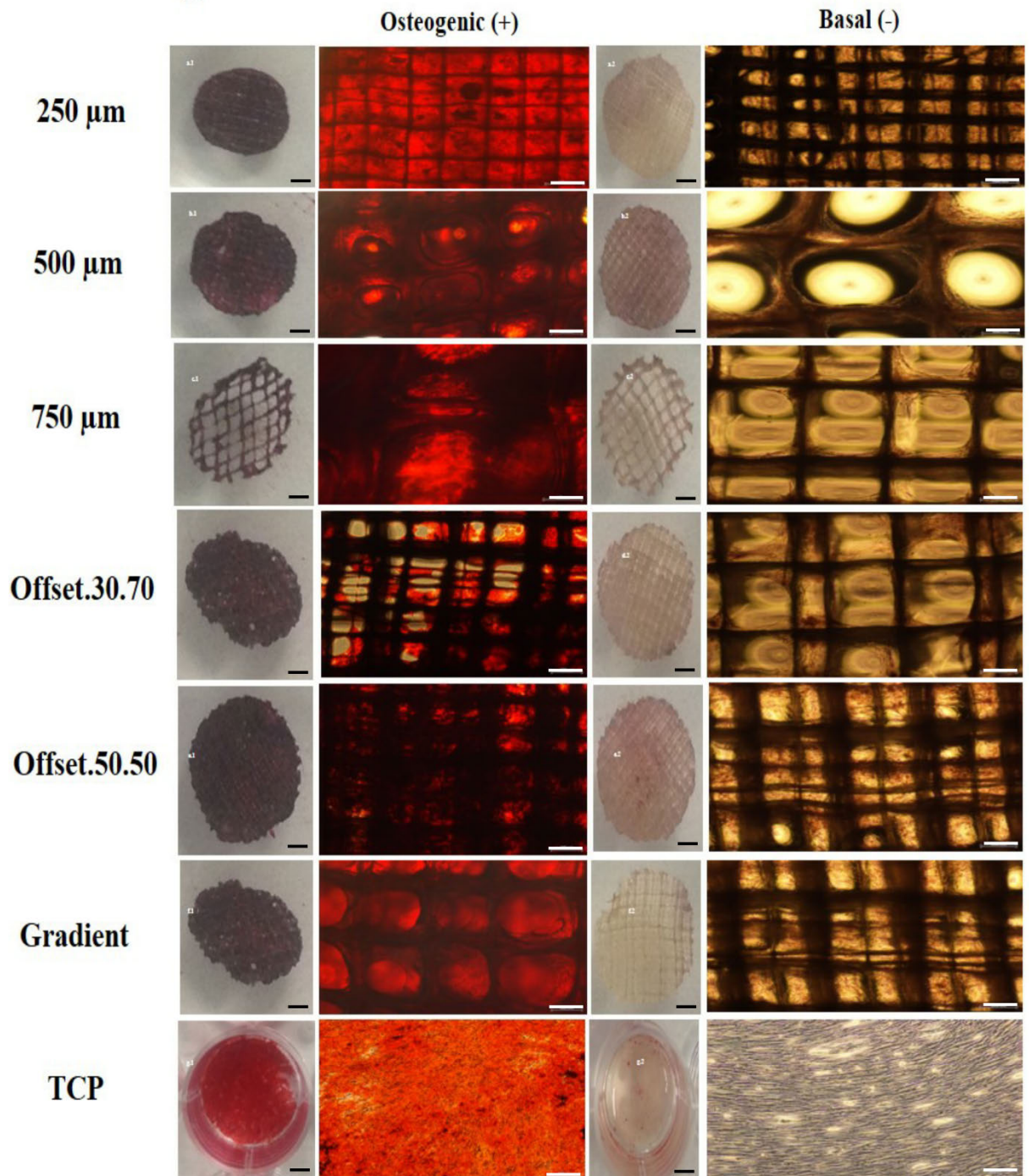
Figure 4.3. ALP activity of osteoblasts in osteogenic (A) and basal (B) medium seeded on PCL scaffolds with various porous structures for 3, 14, and 30 days; ns: non-significant; *: significant versus other scaffolds at the same time point ($p < 0.01$).

Influence of Porous Scaffolds on Calcium Deposition by Osteoblast Cells

To assess mineralized matrix formation on the scaffold, analysis of calcium deposition was performed after 14 and 30 days of culture in osteogenic and basal medium (Figure 4.4-A, B). The analysis of alizarin red staining showed a significant difference in calcium accumulation in the scaffolds cultured in osteogenic differentiation medium compared to

basal medium as the control group. The data indicated that all scaffolds were able to significantly induce osteogenic differentiation through the augmentation of calcium in the extracellular matrix. The calcium deposition started to appear after 14 days and gradually increased up to 30 days in osteogenic medium. Figures 4.4-C, D showed the quantitative analysis of mineralization in all of the groups where the average calcium deposition was higher on offset.50.50, offset.30.70 and 250 μm PCL scaffolds respectively. The 750 μm showed the lowest amount after 30 days.



B

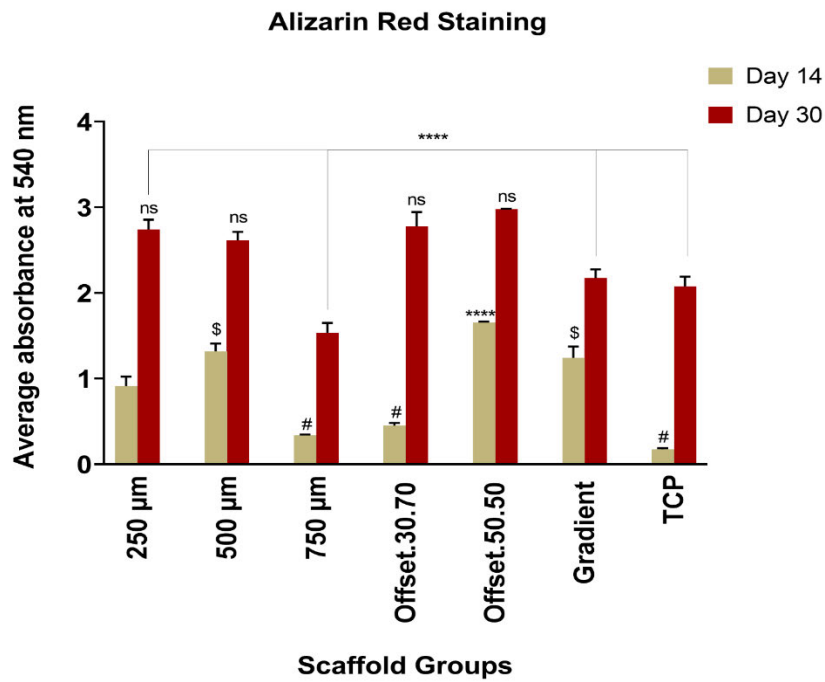
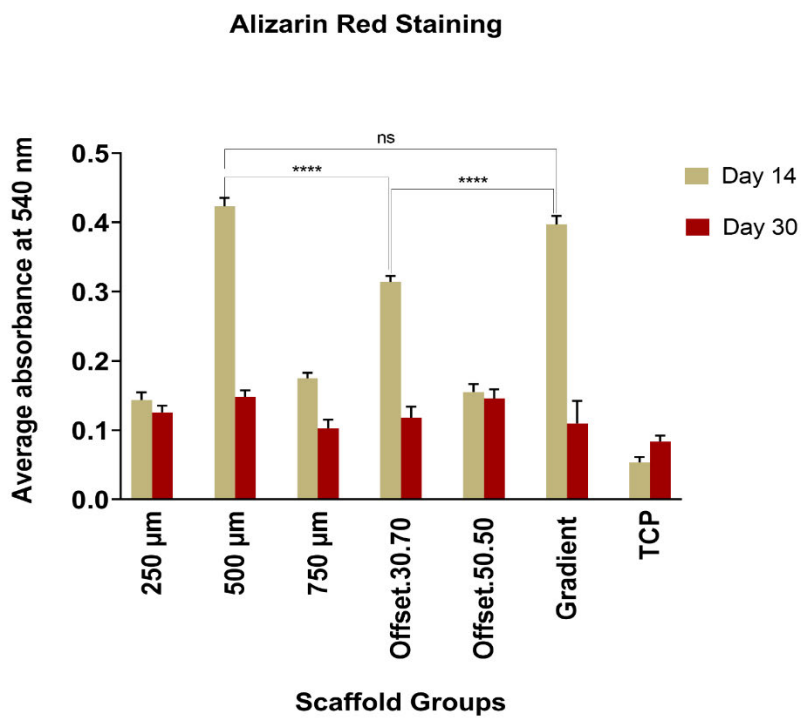
C**D**

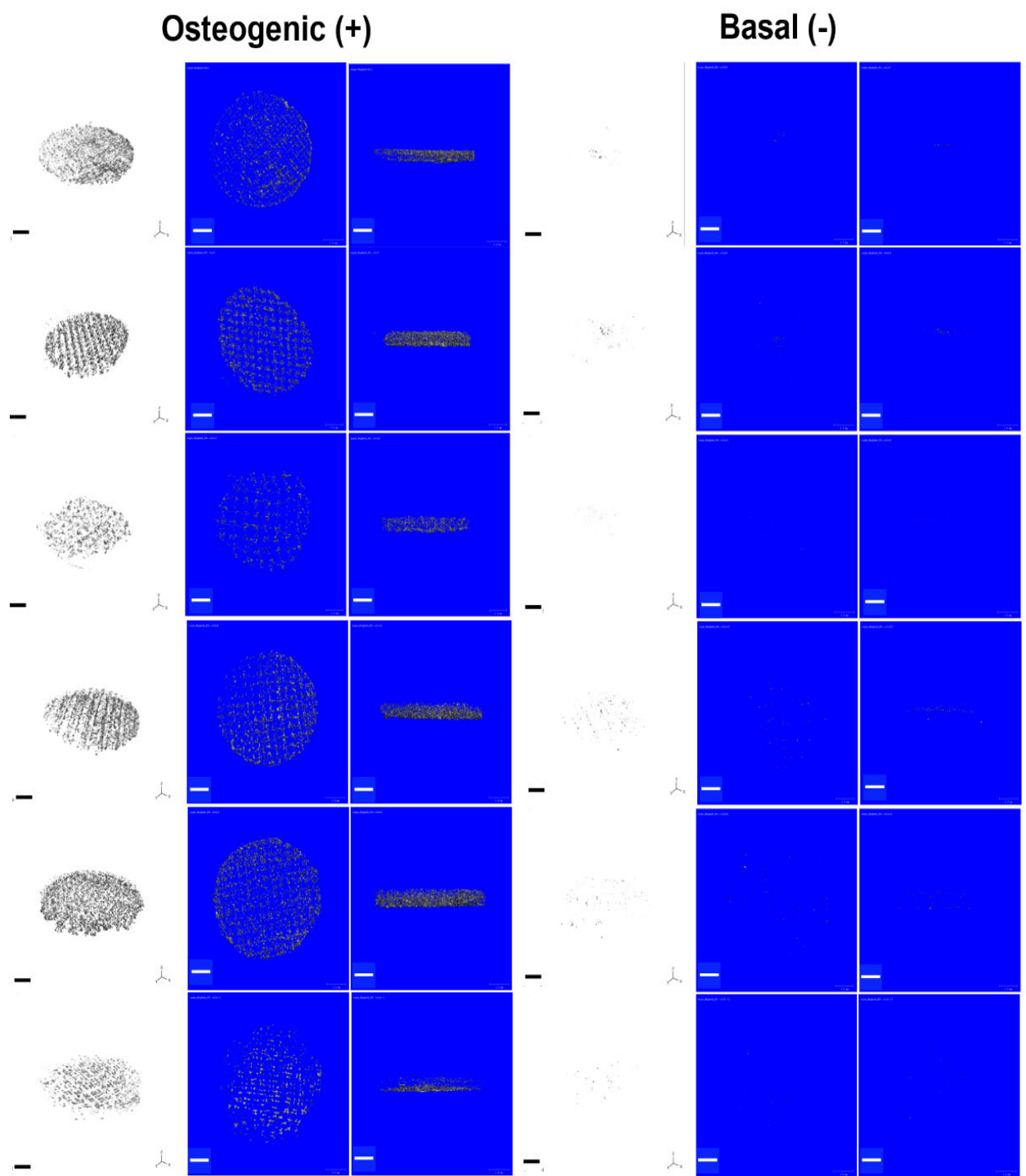
Figure 4.4. Alizarin Red staining of osteoblast cells seeded on porous PCL scaffolds maintained for (A) 14 and (B) 30 days in basal and osteogenic medium; Quantitative analysis of Alizarin Red staining in osteogenic (C) and basal (D) medium by measuring

the optical density (OD); ns, # and \$: non-significant; *: significant versus other scaffolds having the same sign ($p < 0.01$); Black scale bar = 1mm, White scale bar = 200 μm .

Impact of Porous MEW Scaffolds on Osteoblast Cells Mineralization

Figure 4.5 compares extracellular matrix mineralisation of osteoblasts seeded onto the scaffolds and cultured in osteogenic media with those cultured in basal media. As expected from the corresponding alizarin red staining data, mineralization was distributed within the pores of the scaffold (Figure 4.5-A). Consistent with the alizarin red staining, pixel quantification of the μ -CT images (Figure 4.5-B) also confirmed that the offset.50.50 scaffold had the highest amount of mineralisation while the 750 μm pore size scaffold showed the lowest level of mineralization.

A



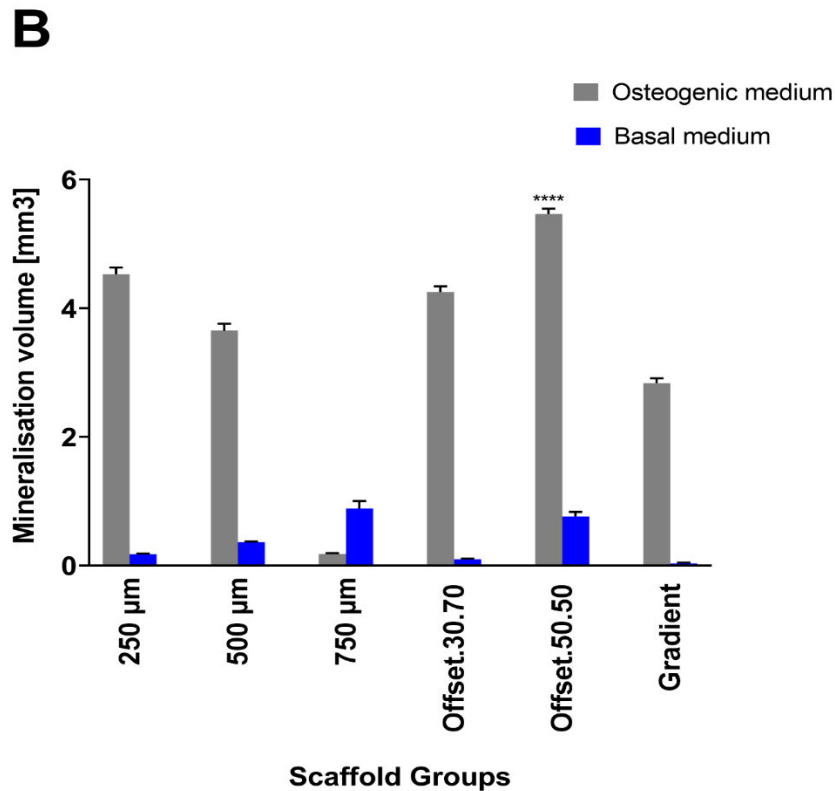
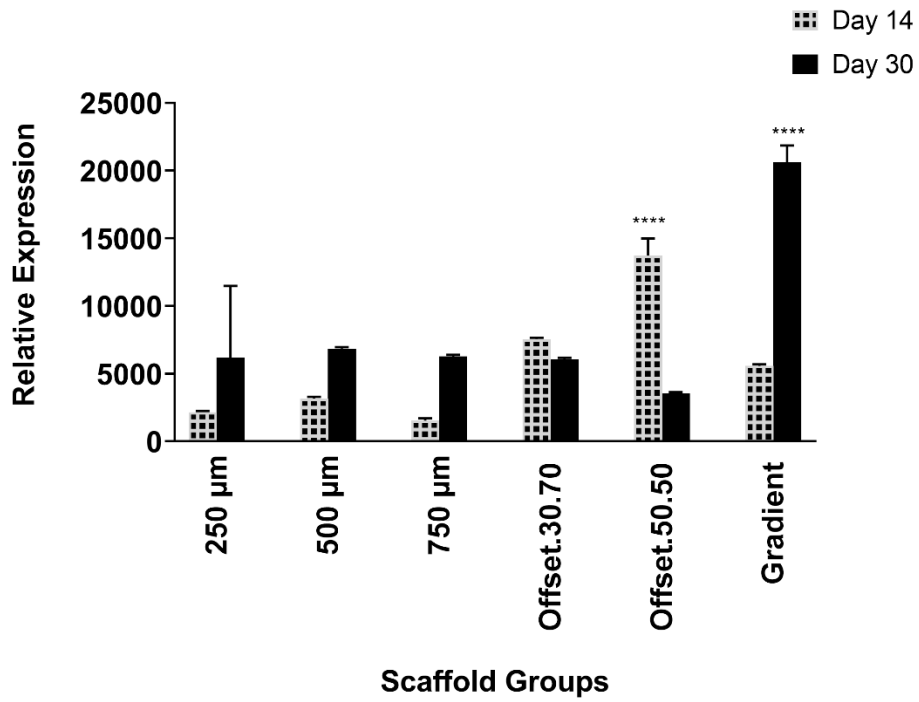
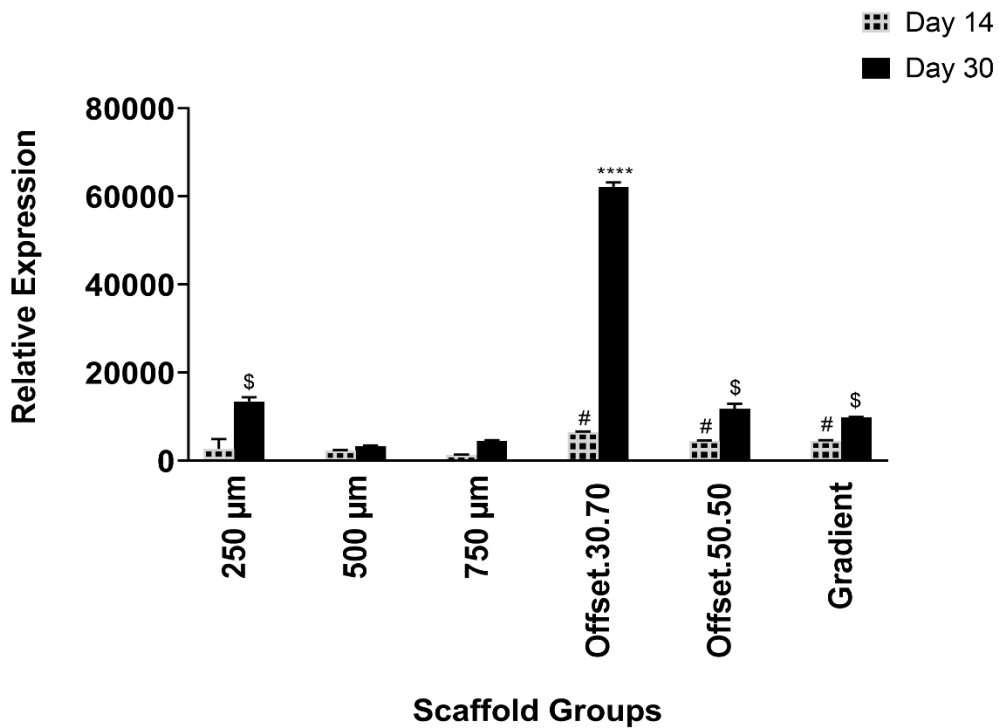


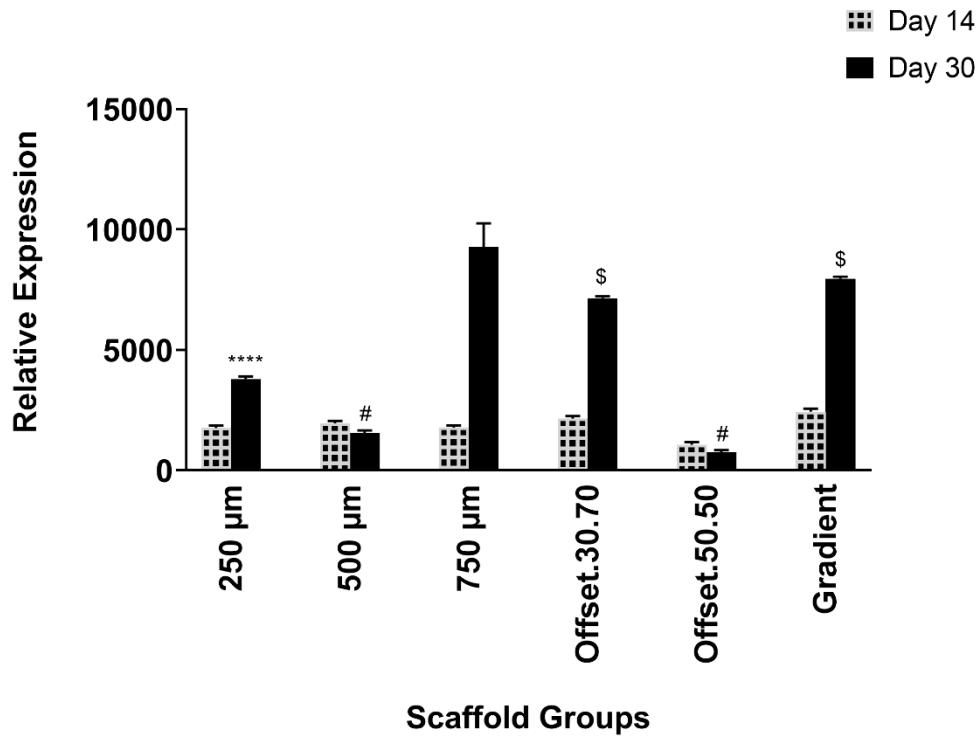
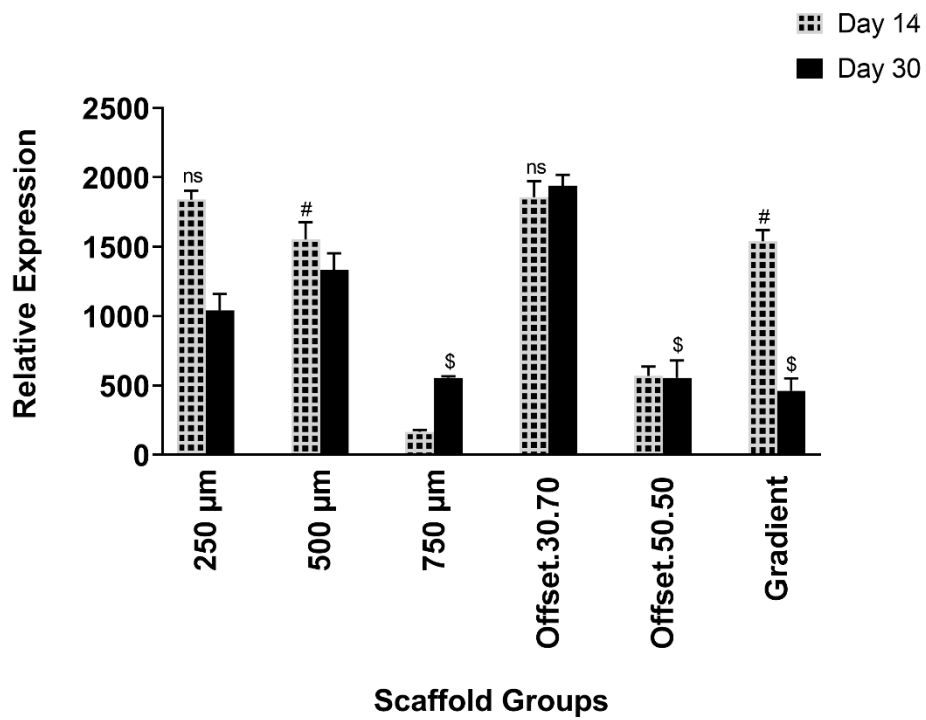
Figure 4.5. ECM mineralization indicated in grey and the micro-CT images were segmented from each other in 2D and 3D images. (A) Micro-CT analysis of the 3D cell/scaffolds mineral deposition after 30 days cultured in osteogenic and basal medium. (B) Quantitative comparison of the mineral volumes/total volume ratio within the scaffolds. *: significant compared to other groups ($p < 0.0001$); Scale bar = 1mm.

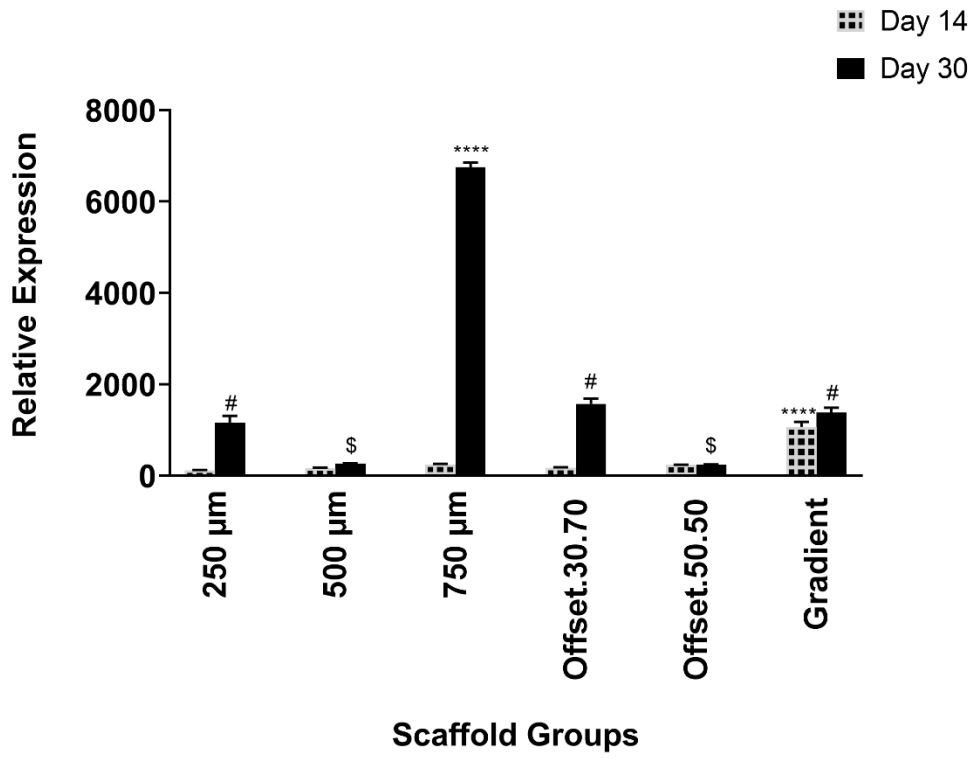
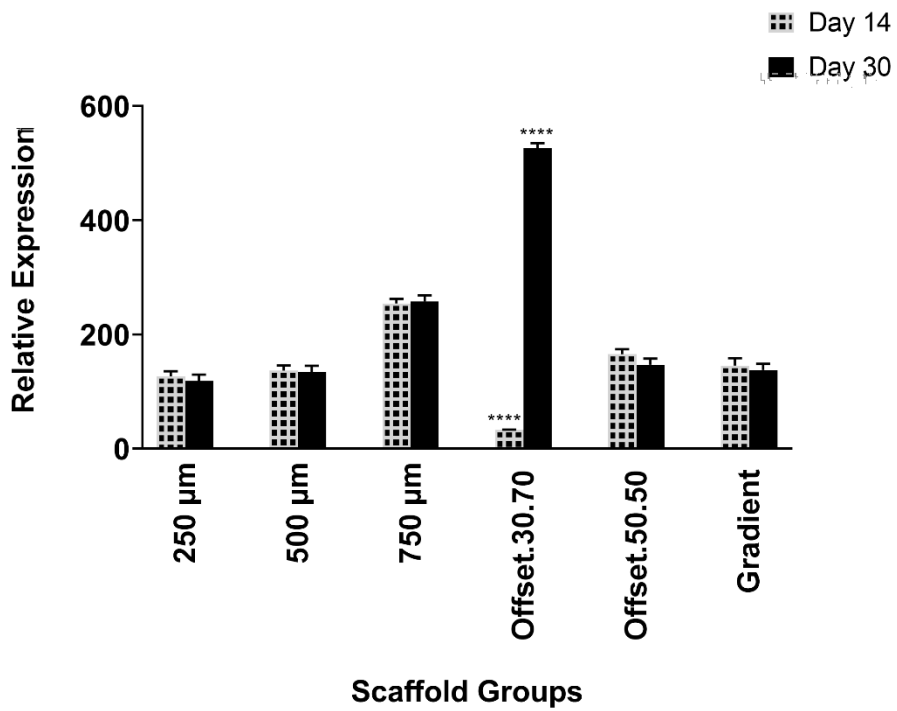
Effect of Porous Scaffolds on Osteoblast Gene Expression of Osteogenic Markers

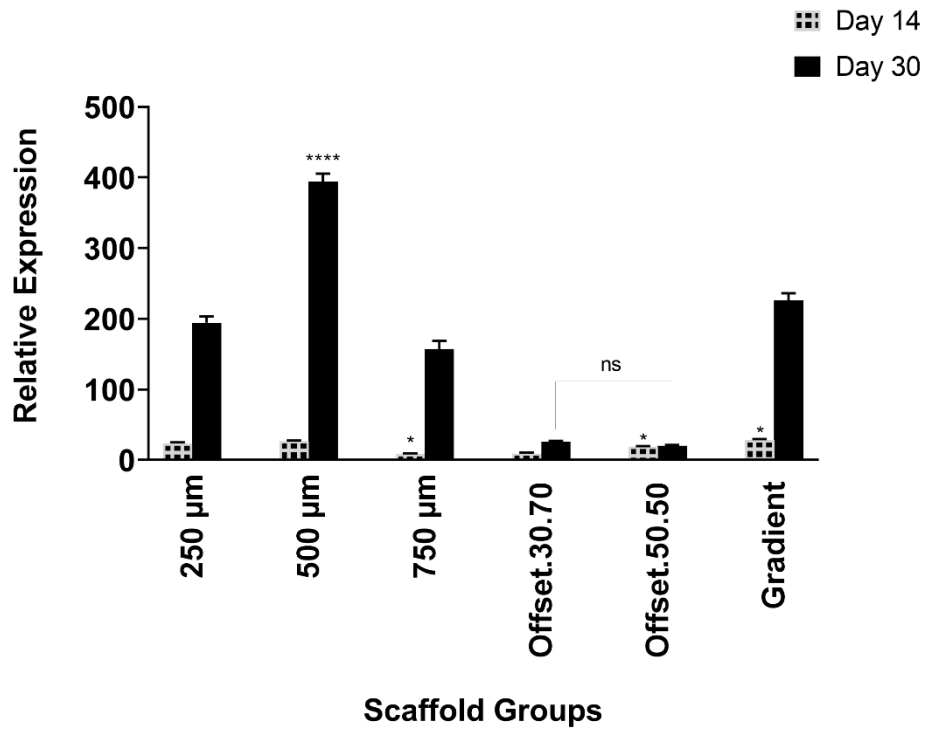
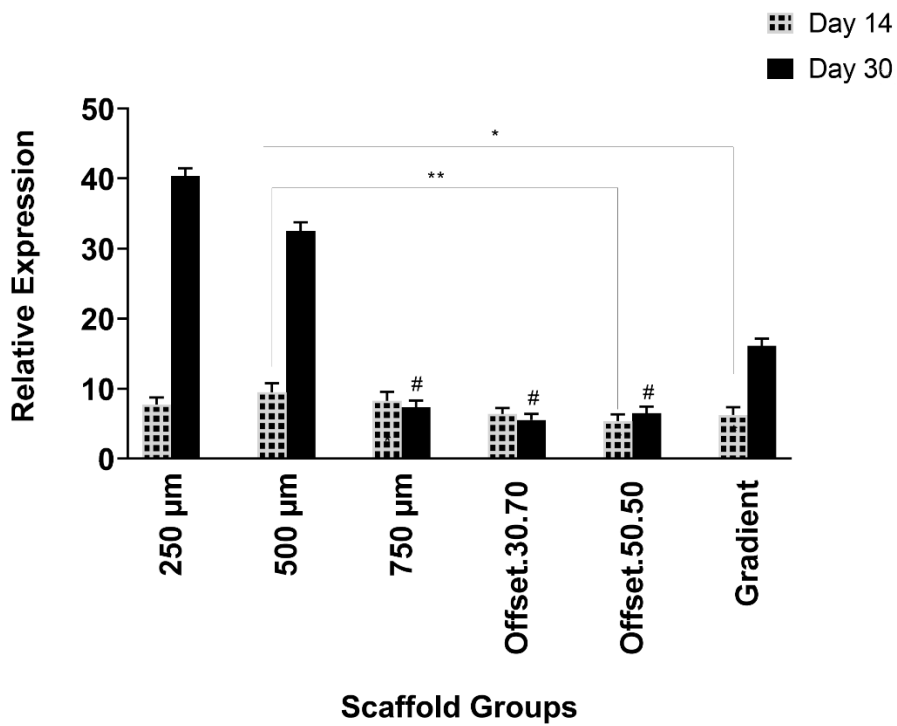
Expression of the osteogenic markers *col 1a*, *alp*, *ocn* and *opn*, as well as the osteogenesis associated signalling molecules *bmp-2*, *wnt3a* and *wnt5a*, in osteoblasts cultured on the scaffolds were analysed by quantitative real-time PCR (Figure 4.6). After 14 days of culture in osteogenic medium, *col 1a* transcript levels were significantly higher compared to the other genes. Also, the expression of *col 1a* increased in offset.30.70 and 50.50 scaffolds on day 14. Among the different pore sizes, the gradient architecture induced the highest expression level of *wnt5a* and *ocn*. The expression of *alp* was not significantly

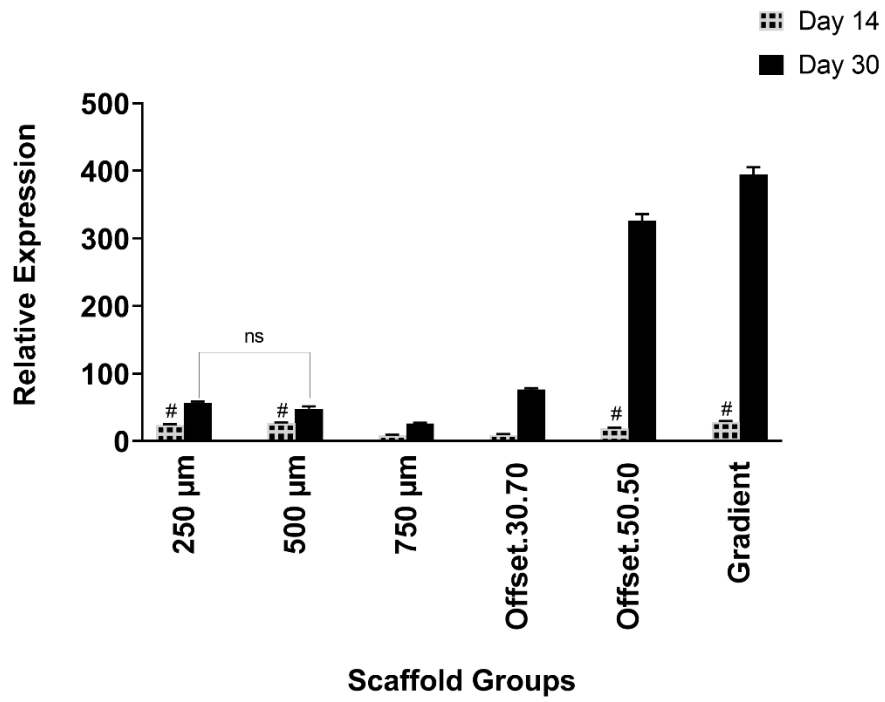
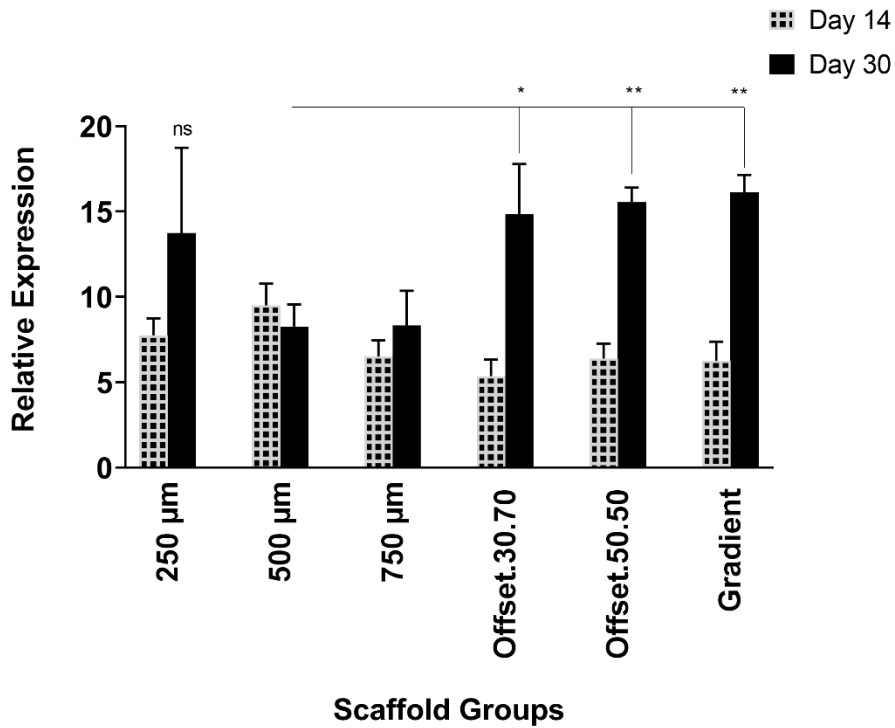
different between the groups, except for 750 μm which showed the maximum level, while the lowest expression was observed for offset.50.50. The *alp* expression was up-regulated in offset.30.70 and gradient scaffold groups, but this was not statistically significant compared to the other groups. Following 30 days of cell culture, the mineralization-related markers *ocn* and *opn* were up-regulated. In all groups, the expression of *alp* was less than *ocn* and *opn* after 30 days. Therefore, all of the scaffold groups stimulated the upregulation of *alp* and *col I* expression at early stages of osteogenic differentiation after 14 days, while, the gradient and offset.30.70 scaffolds were able to express *ocn* and *opn*. Increase of *bmp2* gene expression was observed in 250 μm , offset.30.70 and gradient scaffolds, and at the highest quantity in the 750 μm group, compared to other groups. The assessed data demonstrated the high expression of *wnt5* in the gradient and offset.50.50 scaffolds.

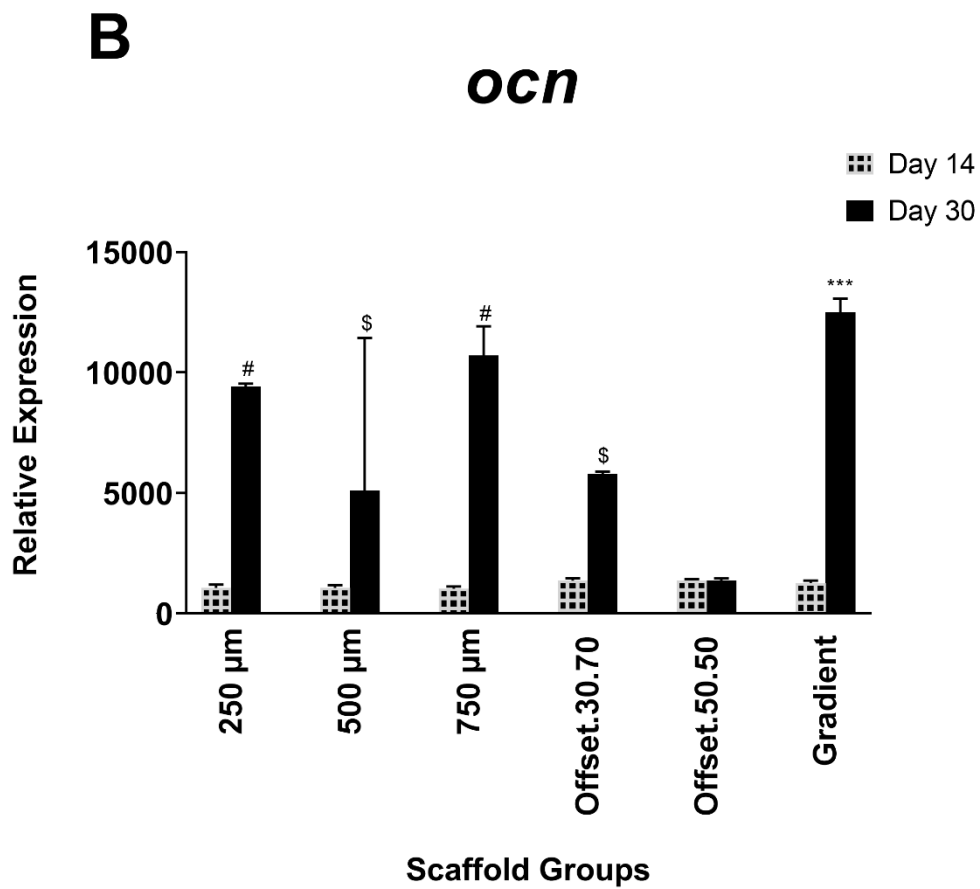
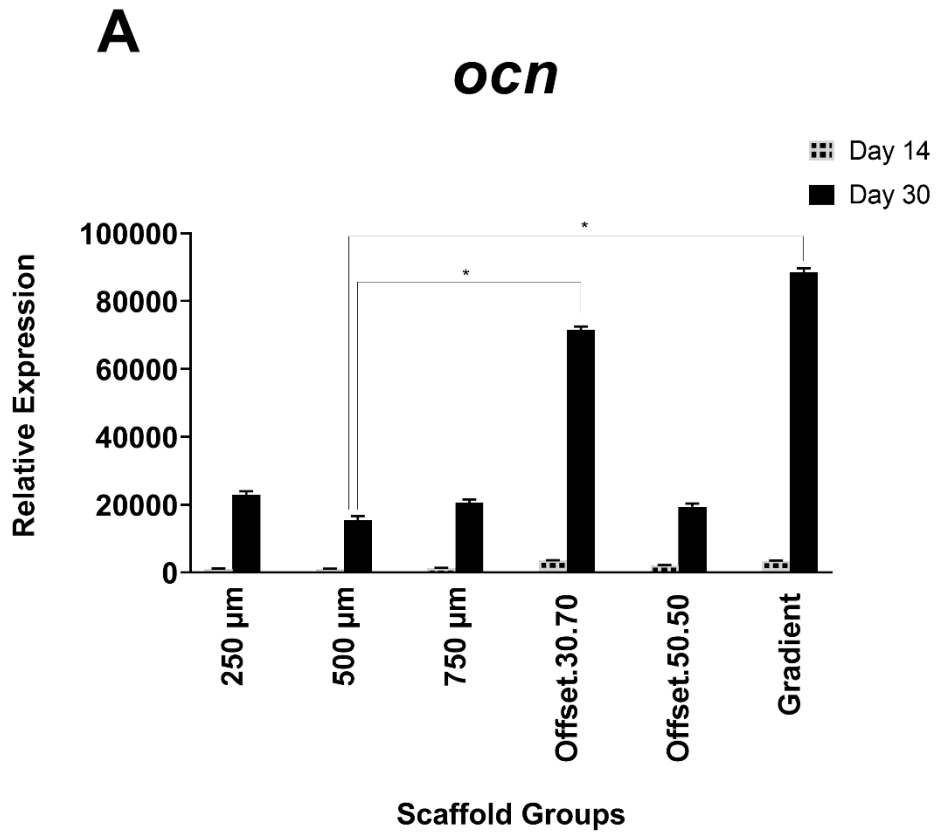
A***col la*****B*****col la***

A*alp***B***alp*

A***bmp2*****B*****bmp2***

A**wnt3a****B****wnt3a**

A**wnt5a****B****wnt5a**



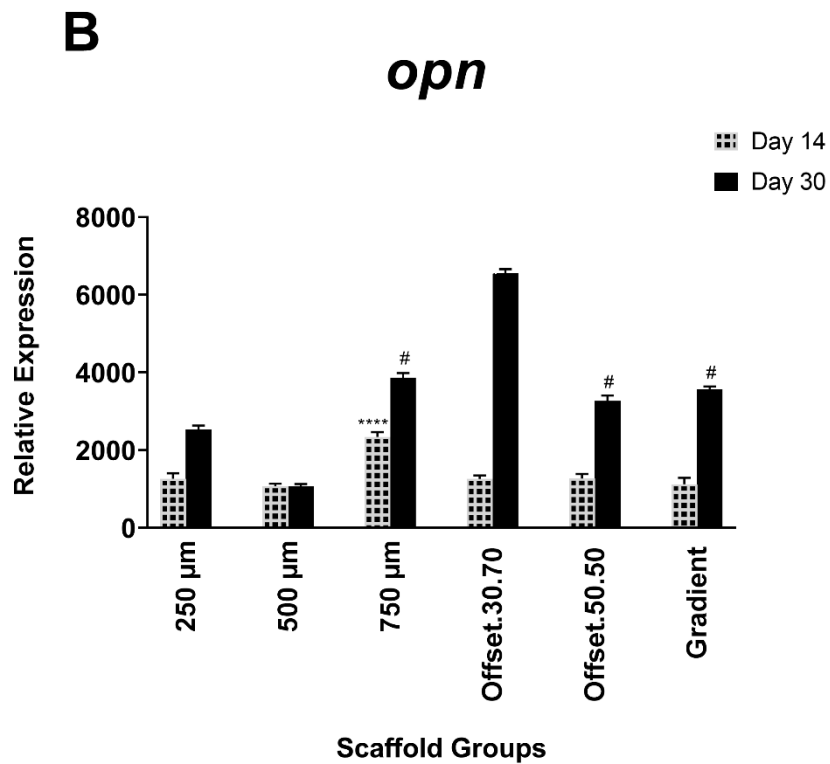
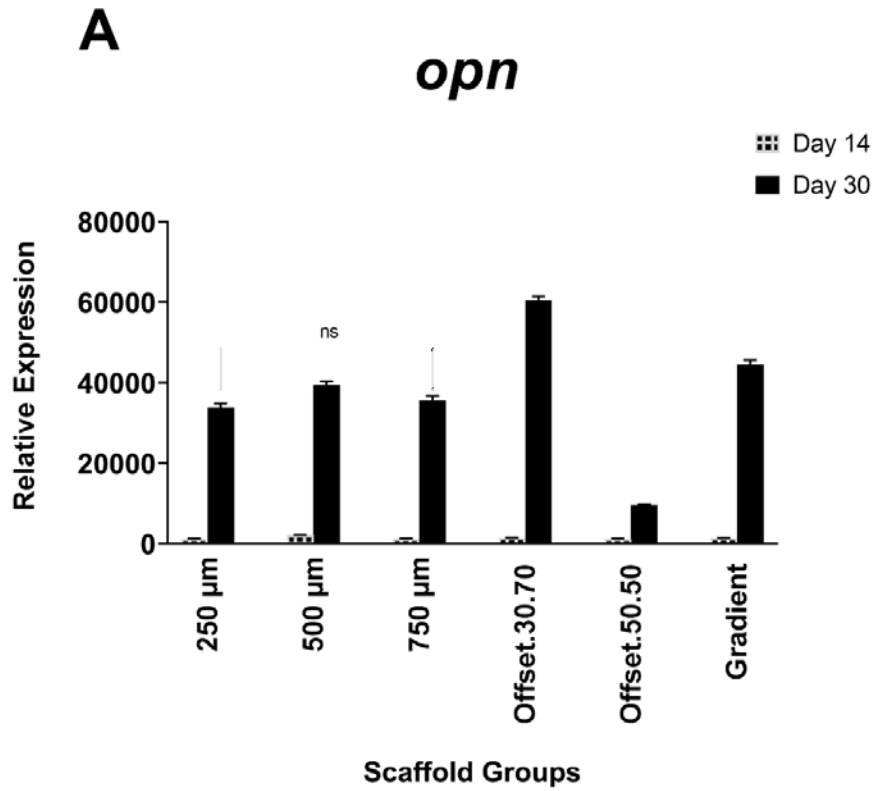


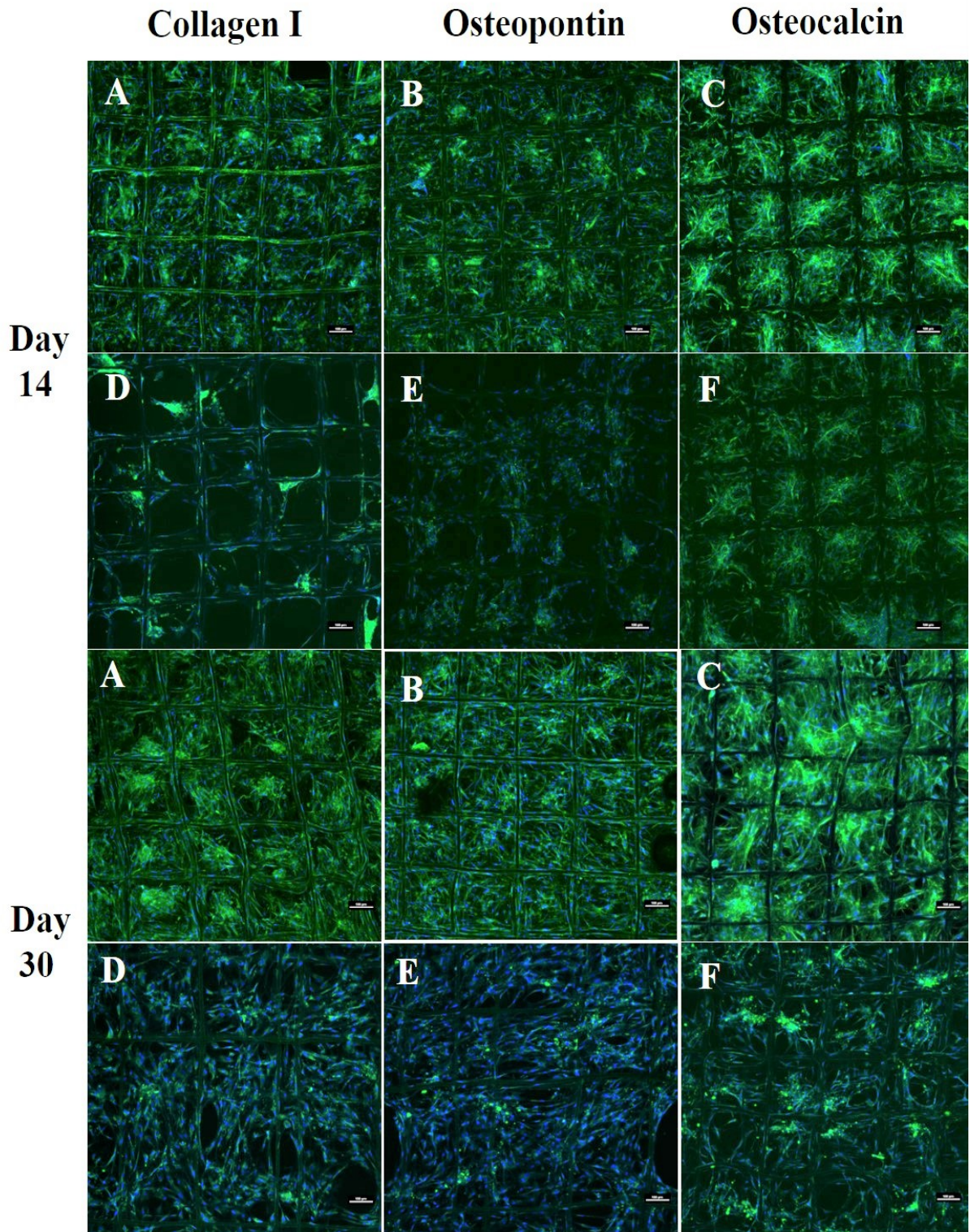
Figure 4.6. Gene expression pattern during mineralization of human osteoblast cells seeded on PCL scaffold structures in osteogenic (A) and basal (B) medium for 3, 14, and

30 days Expression of genes was analyzed by real- time PCR and normalized to the levels of β -actin. ns, # and \$: non-significant; *: significant versus other scaffolds having the same sign ($p < 0.0001$).

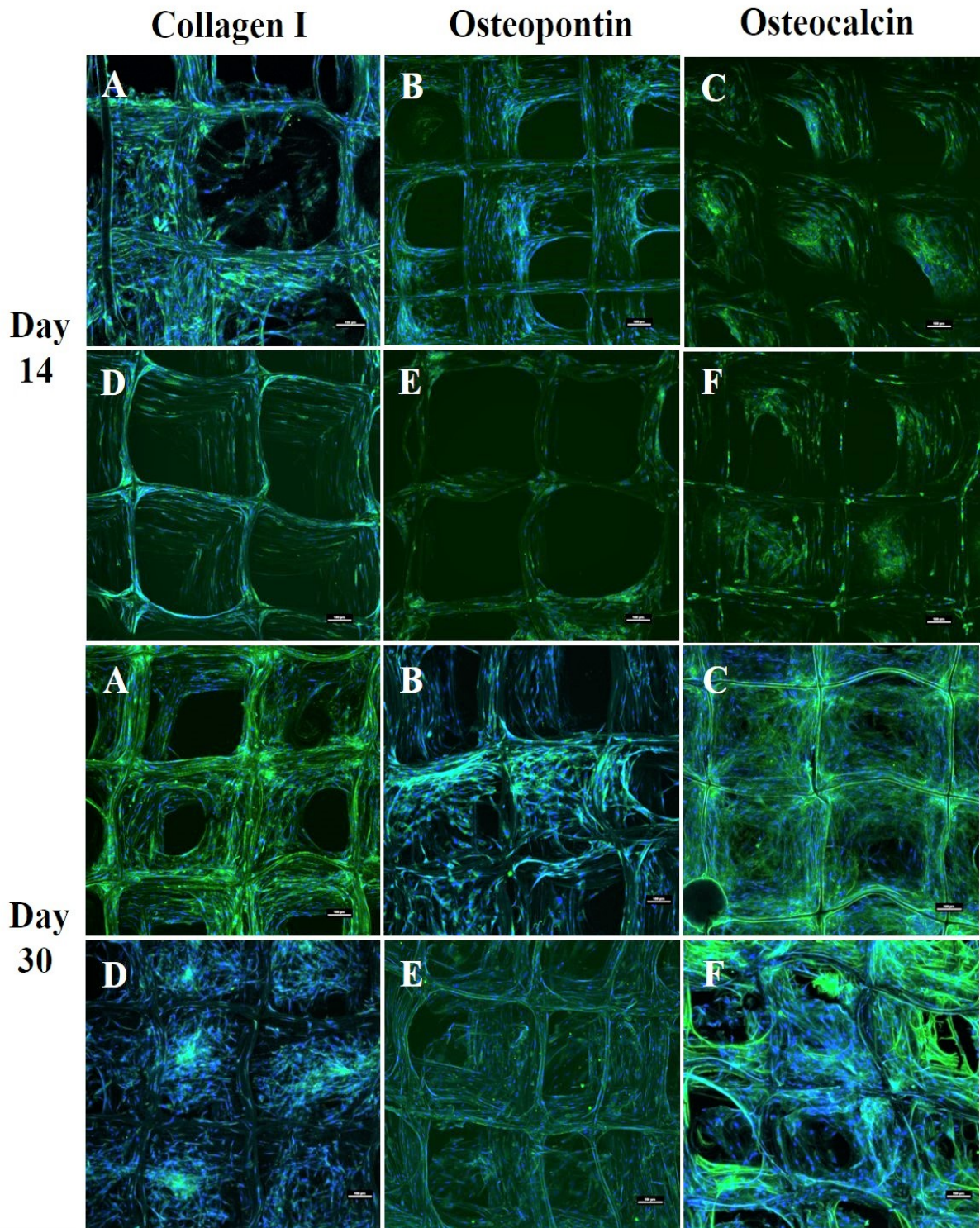
Osteoblast-Related Protein Expression

To evaluate the osteoconductivity of microporous melt electrospun PCL scaffolds, osteoblast cells were seeded on these scaffolds and cultured in osteogenic medium for 30 days *in vitro*. Immunocytochemistry was subsequently used to visualise collagen type I, collagen type III and osteocalcin deposition within the cellular matrix (Figure 4.7). Confocal microscopy demonstrated similar biocompatibility of the scaffolds as shown by the uniform spatial distribution of the cells on all six scaffold types. As expected, the images confirmed that collagen type I, collagen type III and osteocalcin were all expressed on all the scaffolds cultured in osteogenic media for 14 days and 30 days (Figure 4.7). These data indicated that all of the scaffolds showed markedly better expression of osteocalcin compare to the other two proteins. It was obvious that the number of differentiated cells on the scaffolds increased with time. The pore spaces were filled and covered completely by the cells after 30 days, particularly in gradient and offset scaffolds. However, the expressions of collagen type I, collagen type III and osteocalcin on the scaffolds cultured in osteogenic media were much higher than those on the scaffolds cultured in basal medium (Figure 4.7).

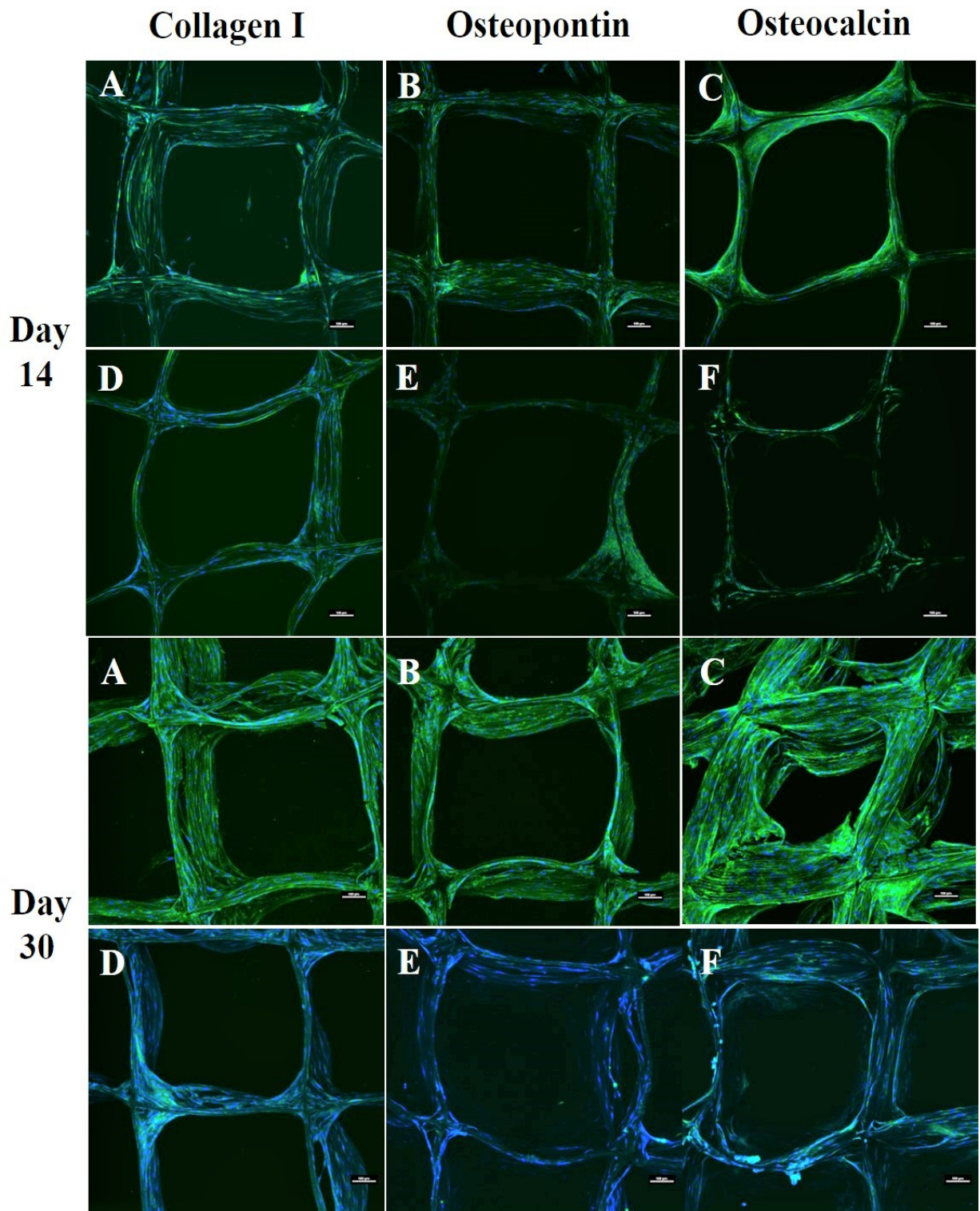
a



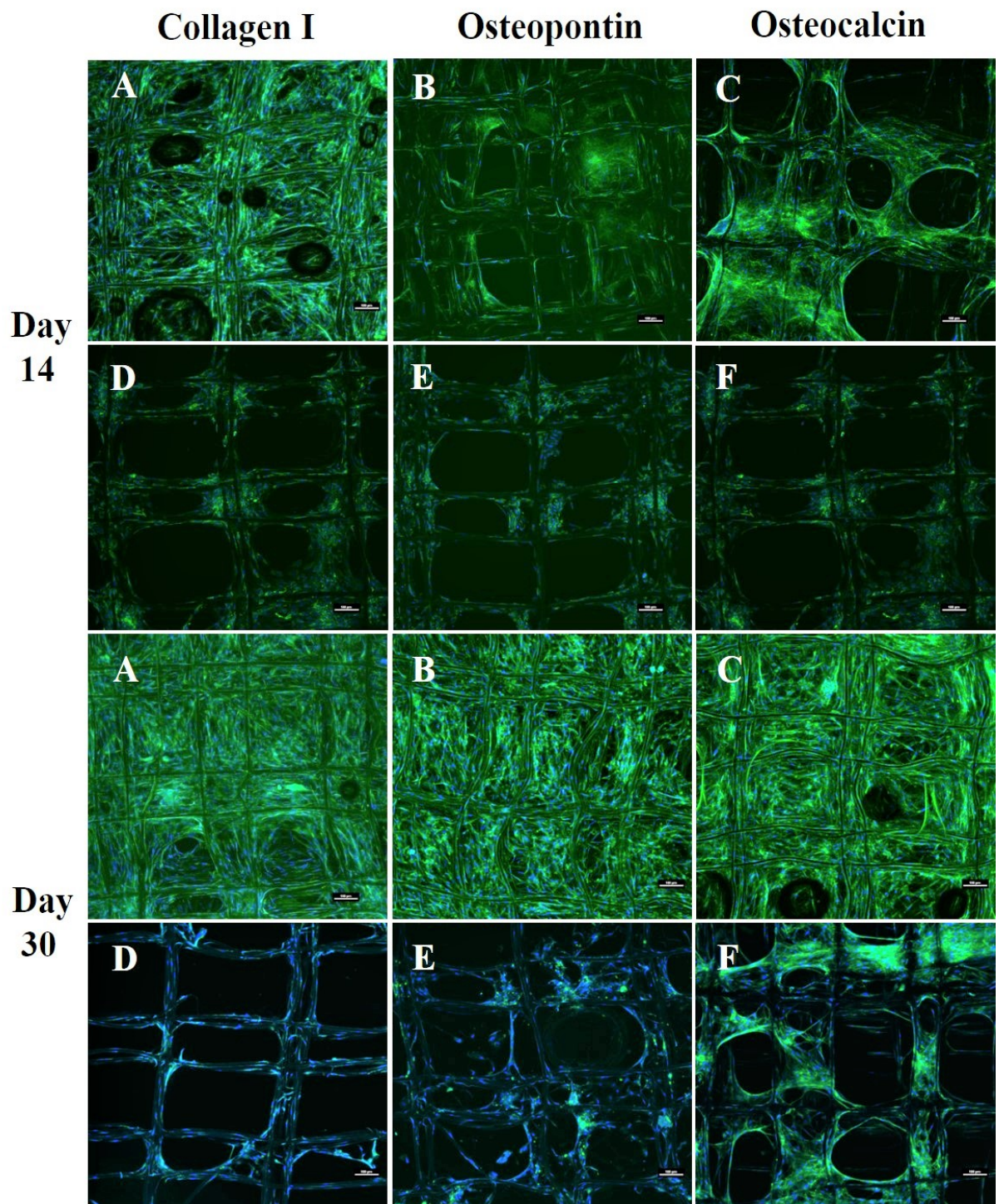
b



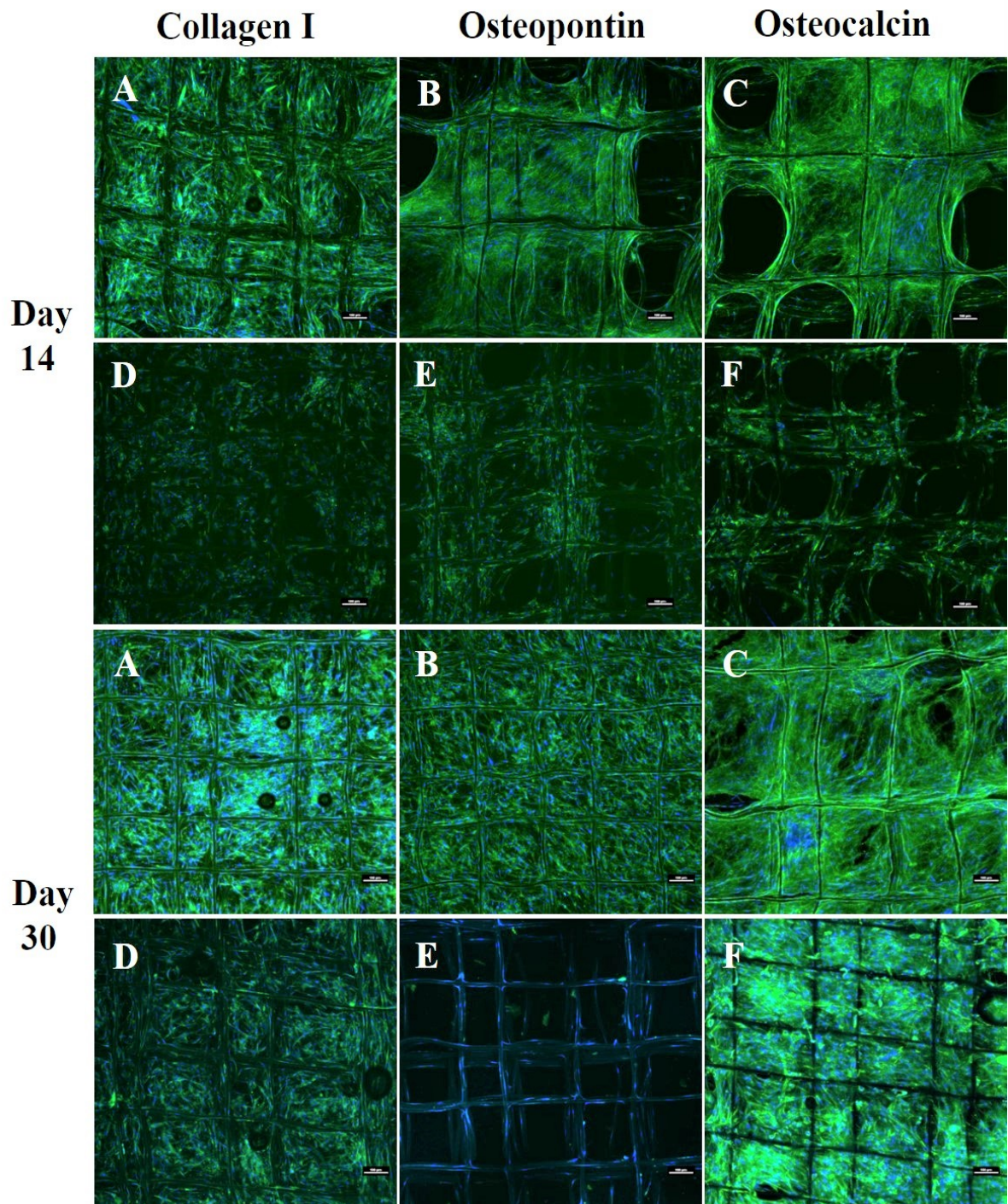
C



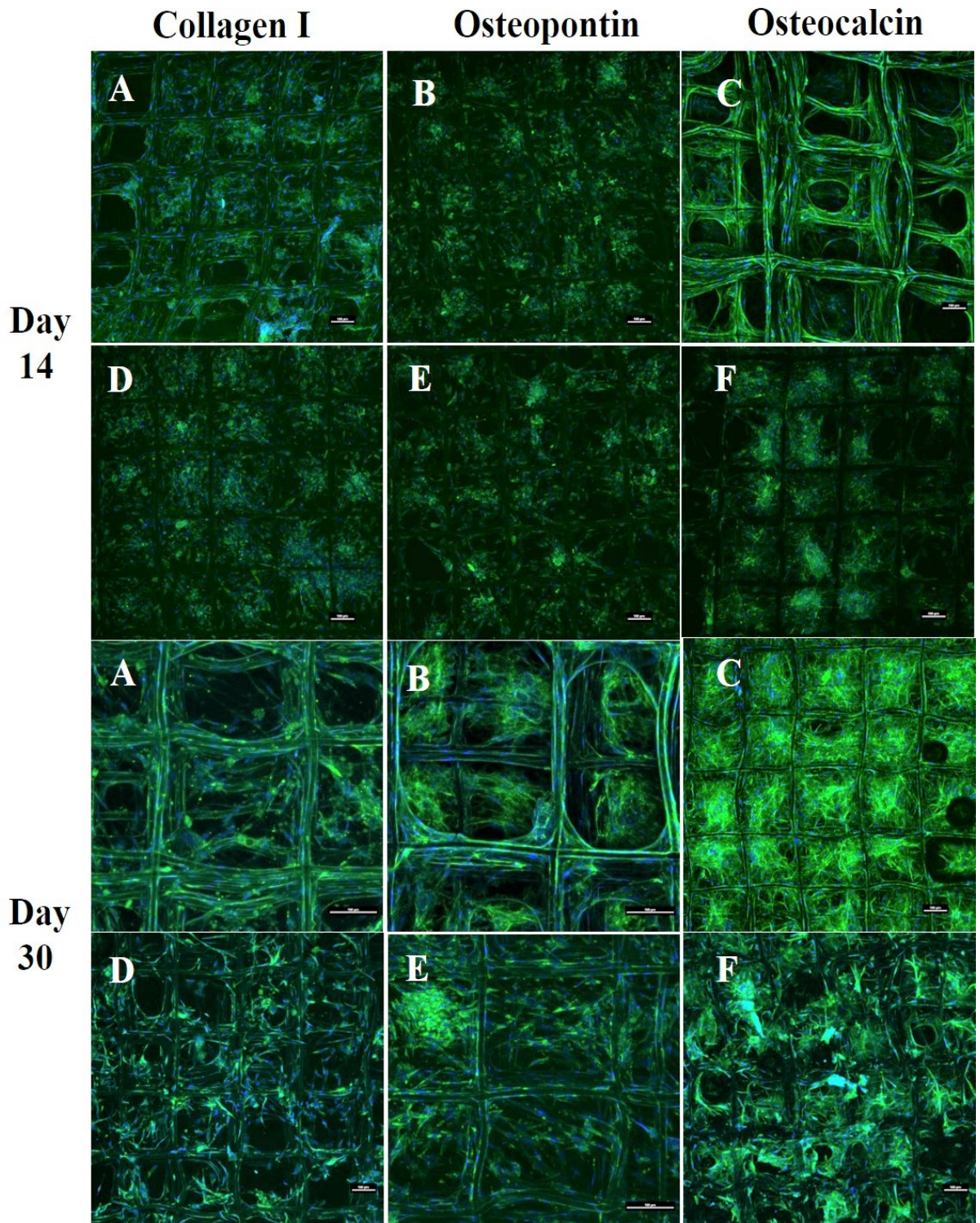
d



e



f



g

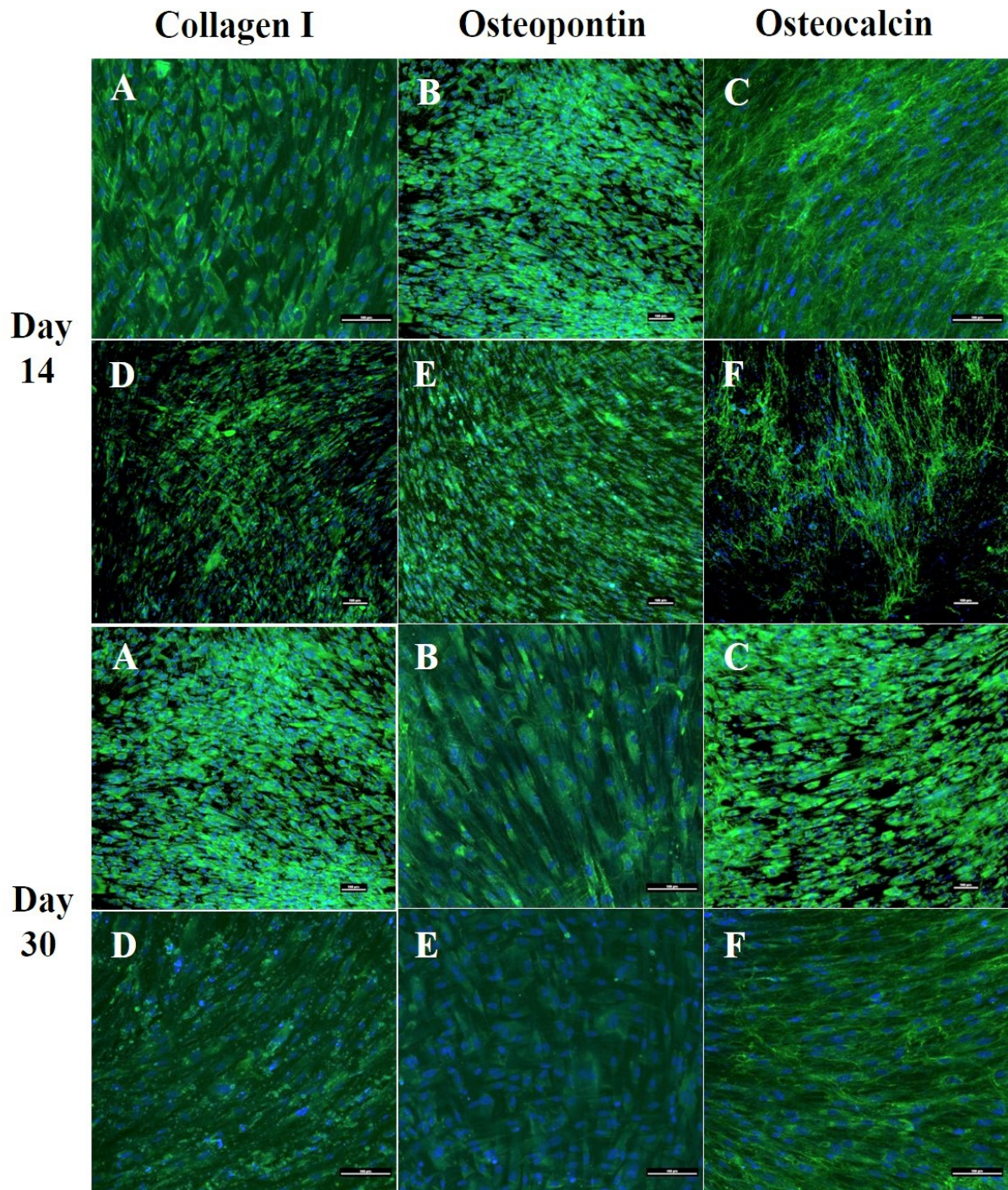


Figure 4.7. Immunocytochemistry analysis of osteogenic markers (collagen I, osteopontin and osteocalcin) for human osteoblast cells cultured in: (A, B, C) Osteogenic medium (D, E, F) Basal medium after 14 and 30 days; a: 250 μm ; b: 500 μm ; c: 750 μm ; d: Offset.30.70; e: Offset.50.50; f: Gradient; g: Tissue culture plate (TCP). Merge:

Hoechst staining of the nucleus (blue), staining of the antibodies (green fluorescence); (Scale bar=100 μm).

DISCUSSION

Several strategies can be utilized to attain porous scaffolds. As melt-electrowriting fabrication delivers a stable electrostatically drawn jet without whipping or random fibre deposition (as in solution electrospinning) it can be used for the formation of gradient structures mimicking native bone by precisely controlling fiber placement (23). The proliferation and differentiation of cells within 3D scaffolds are affected by both the size and geometry of the scaffold's pores (24) but it's not clear however whether scaffolds with a uniform pore distribution of homogenous size, or constructs with a varying pore size distribution, are more suitable for bone regeneration applications. Therefore, the present study evaluated the effect of complex offset and graded porous structures on bone differentiation in contrast to the simpler homogeneous MEW PCL scaffolds.

According to the SEM observations, the presence of more anchorage points in offset and 250 μm structures allowed more cells to populate and grow compared to the other scaffolds, suggesting that the smaller pore volume induced more cell aggregation. Porous scaffolds with an offset designs creates a higher surface area that could result in more cell distribution and proliferation. Since the fibres positioning affected the flow path of the media during cell seeding, the cell attachment efficiency increased. This is due to the presence of the 'obstacles' in the heterogeneous (offset/gradient) pore design, which provides cells with additional anchorage points during the seeding process (25). The enhanced cell growth in the smaller pore size scaffolds may also be attributed to the higher concave surfaces and curvature of the small pore size than the large pore size which results in minimizing the surface area and surface tension (26, 27).

Surface tension or surface energy comes from the tendency of cells to approach each other to achieve a balanced energy i.e. neighboring cells have the least energy and the most

stable state. This is the natural tendency of molecules to minimize their energy (28), therefore, to reduce their surface energy, the cells will select the corners of the pore space to enhance contact with the other cells. Because of the lower angle between the fibers of small pore sizes, it can provide a more suitable environment for the cells to interact with each other, thus minimizing their residual energy and becoming more stable. (29, 30). This could be the reason for higher cell proliferation and faster growth in the smaller pores of 250 μm and offset.50.50 scaffolds with the higher curvature, compared to larger pore sizes of 750 μm .

While there are no experimental findings to support the hypothesis that minimal surface areas advance bone regeneration, concave surfaces compared to convex and planar surfaces have been shown to promote bone tissue regeneration, a process that increases with higher curvature (31-33). This agrees with our study, which showed more mineralization in offset.50.50 and 250 μm scaffolds compared to the higher pore size of scaffolds.

Cells at the centre of the pores have the highest energy levels, and larger pore sizes generate more perimeter and thus less curvature (34). This may be the reason for low cell density with larger pore sizes despite more penetration of the cells into the 500 μm and 750 μm pore size scaffolds after 24 hours, compared to the 250 μm pore size scaffold. The restriction on infiltration though promotes differentiation over proliferation since the inner space is filled faster due to more interactions between cells in the smaller area, while larger pore sizes have more empty spaces promoting proliferation instead.

Our results are in agreement with the study of Di Luca et al, that also showed an increase in cell number and mineralization by reducing the pore size to 500 μm as well as in the area with the smallest pores (500 μm) of a complex four zone gradient (500/700/900/1100 μm zones) using PEOT/PBT (poly (ethylene oxide terephthalate)/poly (butylene terephthalate) and PCL scaffolds fabricated by rapid prototyping (35). They also showed

that the variety in cell density in the different regions of gradient scaffolds could be attributed to the increase of hypoxia inducible factor (HIF) in the higher hypoxic regions of small pore size where the oxygen levels could drop (36). Previous studies already suggested that rising hypoxia leads to osteochondrogenic differentiation, mediated via HIF-1 and triggered through the elevation of ALP and OCN levels and mineralization (37-40). Interestingly, we also found more calcium mineralization in smaller pore sizes of 250 μm and offset.50.50 structures.

Other models have shown that the behavior of cells can be affected by pore size. For example, chondrocytes produce large amounts of glycosaminoglycan (GAG) and collagen II in 400 μm sized pores, while they proliferate in 200 μm sized pores (41). On the other hand, human mesenchymal stromal cells (hMSCs) seeded within PEOT/PBT scaffolds had significantly higher amounts of GAG in 500 μm pore size (non-gradient) and gradient (500-1100 μm) scaffolds, compared to largest pore sizes (42).

In the present study ALP activity, an early indicator of matrix mineralization, increased significantly after 14 days in the gradient and offset.50.50 scaffolds. After 30 days ALP activity decreased (compared to day 14) in all scaffolds, except for the 750 μm pore size scaffold. This suggests that the structures with the greater porosity of 750 μm and gradient architecture stimulate ALP expression. This finding is also in accordance with the *in vitro* study by Di Luca et.al (2016) which demonstrated that an increase in pore size of poly(ethylene oxide terephthalate)/poly(butylene terephthalate) (PEOT/PBT) and PCL scaffolds enhances ALP levels during human mesenchymal stromal cell differentiation (35).

Our study also showed that ALP levels were greater in 750 μm scaffold after 30 days compared to the other scaffolds. This finding was in accordance with the study of Hutmacher et.al (2000) that indicated the structures with greater porosity could stimulate ALP expression, since countering hypoxic conditions in the smaller pore size and

unavailability of O₂ and nutrient supply for the cells (43). Kasten et.al (2008) demonstrated that the higher porosity of 65% and 75% β-tricalcium phosphate (TCP) ceramic scaffolds also enhanced ALP activity when compared to lower porosity (25%) scaffolds due to better nutrient and O₂ transportation (44). However, it also needs to be acknowledged that the higher levels of ALP activity after 30 days in the present study might also be the consequence of less cells initially attaching to the larger pore structure of the 750 μm scaffold.

Although higher porosity increased ALP activity, our results showed the offset scaffolds demonstrated superior matrix mineralization. This may be related to the surface wettability which increases surface free energy resulting in better cell attachment due to greater protein adsorption of ECM-products (45), and the rougher surface of the offset structures after CaP coating modification, which was shown in our previous study by alizarin-red staining and surface area (BET) analysis (22). It has been displayed the CaP coating on the surface of the fibres within the cells, that the higher level of mineralization was identified on the offset and then 250 μm scaffold structures through alizarin-red staining and micro-CT analysis. This is in agreement with the study of Hammerl et al (2019) that showed that CaP/PCL scaffolds formed a mineralized matrix regardless of the cell type cultured on these scaffolds (46), suggesting that released ions and wide contact area between the cells and fluids can evoke higher mineralization in short term cell culture, although evidence for this phenomenon is not yet provided. The study of Yeo et al (2012) also confirmed increased mineralization in 50% and 100% offset PCL and β-tricalcium phosphate (β-TCP) scaffolds compared to no-offset structures (25). Furthermore, higher hydrophilicity creates more surface free energy that results in better cell attachment due to the greater protein adsorption as more ECM-products are achieved by higher cell number (45). Our results indicated a high level of *col 1a* gene expression in offset scaffolds over 14 days, which were expressed at the middle stage of differentiation. *Type*

I Collagen gene expression, an early marker of osteoblast differentiation which results in increased bone mass in combination with OCN and β -catenin functions (47), as well as increased up-regulation of *ocn* gene expression was indeed seen in offset.30.70 scaffolds after 30 days. Increased *bmp-2* gene expression was also observed in 250 μ m, offset.30.70 and gradient scaffolds with the highest expression in 750 μ m scaffolds. Activation of *bmp* signalling leads to osteocalcin and ALP expression (48) and after 30 days culture the activity of ALP increased in the 750 μ m scaffolds compared to the other groups, while *bmp* expression was not upregulated.

The gradient scaffolds also had a high level of *wnt5* gene expression. The *wnt* family of secreted glycoproteins plays a critical role in bone formation, mediated through the expression of osteoblast-specific genes. Activation of this pathway also results in the expression of alkaline phosphatase, an early osteoblast marker associated with the Wnt pathway (49). The gradient scaffold was associated with the highest expression levels of *wnt5* which correlated with increased *alp* expression in gradient scaffolds after 30 days of culture.

A previous study showed that up-regulation of *bmp-2* suppressed *wnt3a* signalling in MSCs and induced osteoblast differentiation (50). Similarly, our results also showed higher expression of *wnt3a* in homogeneous 500 μ m scaffold compared to *bmp2*, which may mean that the cells in this scaffold were stimulated towards proliferation instead of differentiation, in contrast to gradient and offset scaffolds which had lower *wnt3a* expression.

High expression of *ocn* and *opn* is associated with the late stages of differentiation and mineralization (51, 52). Offset and gradient scaffolds had greater expression of *ocn* and *opn*, suggesting that these architectures enhanced osteoblast differentiation to exhibit the mature markers following 30 days. Sicchieri et al. (2012) also evaluated the effect of pore size on the osteogenic gene expression and showed that larger pore size of PLA-CaP

scaffolds increased the expression of *alp*, *type I col* and *ocn*, similar to the higher expression of these markers in the gradient structure of this study, which may be influenced by the large pore size section in the gradient scaffold (53). In the present study the increase in OCN expression especially in offset scaffolds suggests that this architecture could promote osteogenesis as osteocalcin modulates the matrix mineralization which is a later phase of osteogenic differentiation (54). The findings of this *in vitro* study need to be confirmed in an appropriate *in vivo* model, to fully elucidate the effect of heterogeneous and homogeneous pore size of melt electrospun (MEW) scaffolds on bone regeneration.

CONCLUSION

This study has shown that heterogeneous offset and gradient porous scaffolds are favourable structures for bone differentiation compared with uniform pore size scaffolds. The gradient architecture with three different pore sizes (250-500-750 μm) favoured ALP activity, while offset.50.50 scaffolds allowed more matrix mineralization and the expression of late osteogenic markers, such as osteocalcin, which promoted maturation of differentiated osteoblasts. Also, both the gradient and offset scaffolds appeared to support ECM deposition in contrast to the homogeneous porous scaffolds. Taken together, the finding of this research demonstrated the gradient pore size and the offset architecture of MEW scaffolds are able to overcome the limitation of small and large uniform pore sizes associating with cell adhesion and mineralization during the *in vitro* bone differentiation process.

Acknowledgments

The authors acknowledge the assistance of the Institute of Health and Biomedical Innovation and the Central Analytical Research Facility at the Queensland University of Technology, Australia, for providing facilities and technical support used in this study.

References

1. Kargozar S, Mozafari M, Hamzehlou S, Milan PB, Kim HW, Baino F. Bone Tissue Engineering Using Human Cells: A Comprehensive Review on Recent Trends, Current Prospects, and Recommendations. *Appl Sci-Basel*. 2019;9(1).
2. Kneser U, Schaefer DJ, Polykandriotis E, Horch RE. Tissue engineering of bone: the reconstructive surgeon's point of view. *J Cell Mol Med*. 2006;10(1):7-19.
3. Abdal-Hay A, Khalil KA, Hamdy AS, Al-Jassir FF. Fabrication of highly porous biodegradable biomimetic nanocomposite as advanced bone tissue scaffold. *Arab J Chem*. 2017;10(2):240-52.
4. Zhang ZY, Teoh SH, Chong WS, Foo TT, Chng YC, Choolani M, et al. A biaxial rotating bioreactor for the culture of fetal mesenchymal stem cells for bone tissue engineering. *Biomaterials*. 2009;30(14):2694-704.
5. Tallawi M, Rosellini E, Barbani N, Cascone MG, Rai R, Saint-Pierre G, et al. Strategies for the chemical and biological functionalization of scaffolds for cardiac tissue engineering: a review. *J R Soc Interface*. 2015;12(108).
6. Wu D, Wang Z, Wang J, Geng Y, Zhang Z, Li Y, et al. Development of a micro-tissue-mediated injectable bone tissue engineering strategy for large segmental bone defect treatment. *Stem Cell Res Ther*. 2018;9(1):331.
7. Tovar N, Witek L, Atria P, Sobieraj M, Bowers M, Lopez CD, et al. Form and functional repair of long bone using 3D-printed bioactive scaffolds. *J Tissue Eng Regen M*. 2018;12(9):1986-99.
8. Chocholata P, Kulda V, Babuska V. Fabrication of Scaffolds for Bone-Tissue Regeneration. *Materials*. 2019;12(4).
9. Ameer JM, Pr AK, Kasoju N. Strategies to Tune Electrospun Scaffold Porosity for Effective Cell Response in Tissue Engineering. *J Funct Biomater*. 2019;10(3).

10. Hrynevich A, Elci BS, Haigh JN, McMaster R, Youssef A, Blum C, et al. Dimension-Based Design of Melt Electrowritten Scaffolds. *Small*. 2018;14(22).
11. Oh SH, Park IK, Kim JM, Lee JH. In vitro and in vivo characteristics of PCL scaffolds with pore size gradient fabricated by a centrifugation method. *Biomaterials*. 2007;28(9):1664-71.
12. Lo Re G, Lopresti F, Petrucci G, Scaffaro R. A facile method to determine pore size distribution in porous scaffold by using image processing. *Micron*. 2015;76:37-45.
13. Cheng MQ, Wahafu TEHJ, Jiang GF, Liu W, Qiao YQ, Peng XC, et al. A novel open-porous magnesium scaffold with controllable microstructures and properties for bone regeneration. *Sci Rep-Uk*. 2016;6.
14. Chirchir H. Limited Trabecular Bone Density Heterogeneity in the Human Skeleton. *Anat Res Int*. 2016;2016:9295383.
15. Shi DJ, Shen JL, Zhang ZY, Shi C, Chen MQ, Gu YL, et al. Preparation and properties of dopamine-modified alginate/chitosan-hydroxyapatite scaffolds with gradient structure for bone tissue engineering. *J Biomed Mater Res A*. 2019;107(8):1615-27.
16. Gupte MJ, Swanson WB, Hu J, Jin XB, Ma HY, Zhang ZP, et al. Pore size directs bone marrow stromal cell fate and tissue regeneration in nanofibrous macroporous scaffolds by mediating vascularization. *Acta Biomater*. 2018;82:1-11.
17. Murphy CM, Duffy GP, Schindeler A, O'brien FJ. Effect of collagen-glycosaminoglycan scaffold pore size on matrix mineralization and cellular behavior in different cell types. *J Biomed Mater Res A*. 2016;104(1):291-304.
18. Wang S, Liu LL, Li K, Zhu LC, Chen J, Hao YQ. Pore functionally graded Ti6Al4V scaffolds for bone tissue engineering application. *Mater Design*. 2019;168.

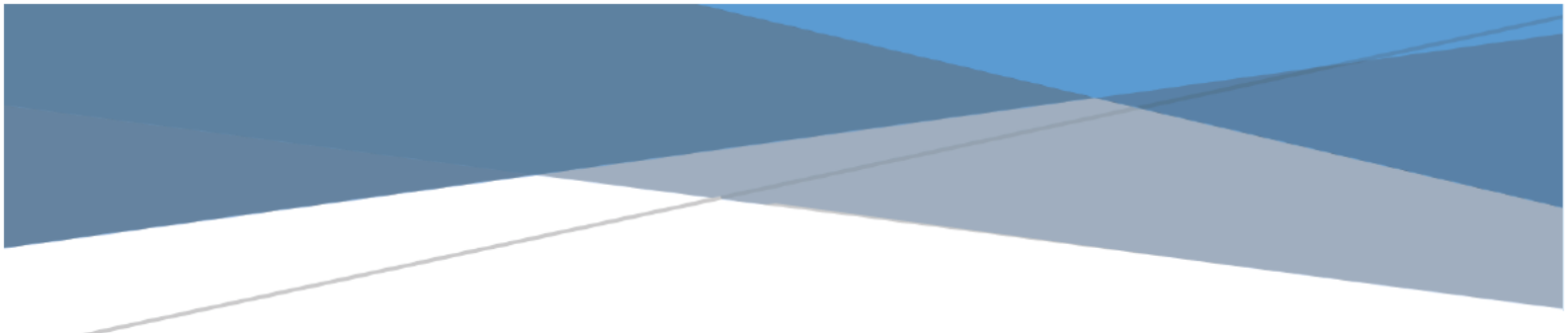
19. Cetinel O, Esen Z, Yildirim B. Fabrication, Morphology Analysis, and Mechanical Properties of Ti Foams Manufactured Using the Space Holder Method for Bone Substitute Materials. *Metals-Basel*. 2019;9(3).
20. Boccaccio A, Uva AE, Fiorentino M, Lamberti L, Monno G. A Mechanobiology-based Algorithm to Optimize the Microstructure Geometry of Bone Tissue Scaffolds. *Int J Biol Sci*. 2016;12(1):1-17.
21. Sobral JM, Caridade SG, Sousa RA, Mano JF, Reis RL. Three-dimensional plotted scaffolds with controlled pore size gradients: Effect of scaffold geometry on mechanical performance and cell seeding efficiency. *Acta Biomater*. 2011;7(3):1009-18.
22. Abbasi N, Abdal-hay A, Hamlet S, Graham E, Ivanovski S. Effects of Gradient and Offset Architectures on the Mechanical and Biological Properties of 3-D Melt Electrowritten (MEW) Scaffolds. *Acs Biomater Sci Eng*. 2019;5(7):3448-61.
23. Tournalomousis F, Ding H, Kalyon DM, Chang RC. Melt Electrospinning Writing Process Guided by a "Printability Number". *J Manuf Sci E-T Asme*. 2017;139(8).
24. Gregor A, Filova E, Novak M, Kronek J, Chlup H, Buzgo M, et al. Designing of PLA scaffolds for bone tissue replacement fabricated by ordinary commercial 3D printer. *J Biol Eng*. 2017;11.
25. Yeo M, Simon CG, Kim G. Effects of offset values of solid freeform fabricated PCL-beta-TCP scaffolds on mechanical properties and cellular activities in bone tissue regeneration. *J Mater Chem*. 2012;22(40):21636-46.
26. Rivelino D, Zamir E, Balaban NQ, Schwarz US, Ishizaki T, Narumiya S, et al. Focal contacts as mechanosensors: Externally applied local mechanical force induces growth of focal contacts by an mDia1-dependent and ROCK-independent mechanism. *J Cell Biol*. 2001;153(6):1175-85.
27. Zadpoor AA. Bone tissue regeneration: the role of scaffold geometry. *Biomater Sci-Uk*. 2015;3(2):231-45.

28. Jakab K, Damon B, Marga F, Doaga O, Mironov V, Kosztin I, et al. Relating cell and tissue mechanics: Implications and applications. *Dev Dynam.* 2008;237(9):2438-49.
29. Dierkes U, Hildebrandt S, Sauvigny F, Kuster A, Jakob R. *Minimal Surfaces*, 2nd Edition. *Grundlehr Math Wiss.* 2010;339:Xi-+.
30. He HM, He Q, Xu FY, Zhou Y, Ye ZY, Tan WS. Dynamic formation of cellular aggregates of chondrocytes and mesenchymal stem cells in spinner flask. *Cell Proliferat.* 2019;52(4).
31. Ambrosi D, Guana F. Stress-modulated growth. *Math Mech Solids.* 2007;12(3):319-42.
32. Ambrosi D, Guillou A. Growth and dissipation in biological tissues. *Continuum Mech Therm.* 2007;19(5):245-51.
33. Boccaccio A, Uva AE, Fiorentino M, Lamberti L, Monno G. A Mechanobiology-based Algorithm to Optimize the Microstructure Geometry of Bone Tissue Scaffolds. *Int J Biol Sci.* 2016;12(1):1-17.
34. Fenchel W. Curvature and twisting of enclosed space curves. *Math Ann.* 1929;101:238-52.
35. Di Luca A, Ostrowska B, Lorenzo-Moldero I, Lepedda A, Swieszkowski W, Van Blitterswijk C, et al. Gradients in pore size enhance the osteogenic differentiation of human mesenchymal stromal cells in three-dimensional scaffolds. *Sci Rep-Uk.* 2016;6.
36. Hsu SH, Chen CT, Wei YH. Inhibitory Effects of Hypoxia on Metabolic Switch and Osteogenic Differentiation of Human Mesenchymal Stem Cells. *Stem Cells.* 2013;31(12):2779-88.
37. Balogh E, Toth A, Mehes G, Trencsenyi G, Paragh G, Jeney V. Hypoxia Triggers Osteochondrogenic Differentiation of Vascular Smooth Muscle Cells in an HIF-1 (Hypoxia-Inducible Factor 1)-Dependent and Reactive Oxygen Species-Dependent Manner. *Arterioscl Throm Vas.* 2019;39(6):1088-99.

38. Mokas S, Lariviere R, Lamalice L, Gobeil S, Cornfield DN, Agharazii M, et al. Hypoxia-inducible factor-1 plays a role in phosphate-induced vascular smooth muscle cell calcification. *Kidney Int.* 2016;90(3):598-609.
39. Wagegg M, Gaber T, Lohanatha FL, Hahne M, Strehl C, Fangradt M, et al. Hypoxia Promotes Osteogenesis but Suppresses Adipogenesis of Human Mesenchymal Stromal Cells in a Hypoxia-Inducible Factor-1 Dependent Manner. *Plos One.* 2012;7(9).
40. Ichijima T, Matsuzaka K, Tonogi M, Yamane GY, Inoue T. Osteogenic differences in cultured rat periosteal cells under hypoxic and normal conditions. *Exp Ther Med.* 2012;3(2):165-70.
41. Lin TH, Wang HC, Cheng WH, Hsu HC, Yeh ML. Osteochondral Tissue Regeneration Using a Tyramine-Modified Bilayered PLGA Scaffold Combined with Articular Chondrocytes in a Porcine Model. *Int J Mol Sci.* 2019;20(2).
42. Di Luca A, Szlajak K, Lorenzo-Moldero I, Ghebes CA, Lepedda A, Swieszkowski W, et al. Influencing chondrogenic differentiation of human mesenchymal stromal cells in scaffolds displaying a structural gradient in pore size. *Acta Biomater.* 2016;36:210-9.
43. Hutmacher DW. Scaffolds in tissue engineering bone and cartilage. *Biomaterials.* 2000;21(24):2529-43.
44. Kasten P, Beyen I, Niemeyer P, Luginbuhl R, Böhner M, Richter W. Porosity and pore size of beta-tricalcium phosphate scaffold can influence protein production and osteogenic differentiation of human mesenchymal stem cells: An in vitro and in vivo study. *Acta Biomater.* 2008;4(6):1904-15.
45. Paterlini TT, Nogueira LFB, Tovani CB, Cruz MAE, Derradi R, Ramos AP. The role played by modified bioinspired surfaces in interfacial properties of biomaterials. *Biophys Rev.* 2017;9(5):683-98.

46. Hammerl A, Cano CED, De-Juan-Pardo EM, van Griensven M, Poh PSP. A Growth Factor-Free Co-Culture System of Osteoblasts and Peripheral Blood Mononuclear Cells for the Evaluation of the Osteogenesis Potential of Melt-Electrowritten Polycaprolactone Scaffolds. *Int J Mol Sci.* 2019;20(5).
47. Pflug T, Uyen HD, Rudloff S. Reduced beta-catenin expression affects patterning of bone primordia, but not bone maturation. *Biol Open.* 2017;6(5):582-8.
48. Wei XF, Chen QL, Fu Y, Zhang QK. Wnt and BMP signaling pathways cooperatively induce the differentiation of multiple myeloma mesenchymal stem cells into osteoblasts by upregulating EMX2. *J Cell Biochem.* 2019;120(4):6515-27.
49. Sebastian A, Hum NR, Muruges DK, Hatsell S, Economides AN, Loots GG. Wnt co-receptors Lrp5 and Lrp6 differentially mediate Wnt3a signaling in osteoblasts. *Plos One.* 2017;12(11).
50. Boyan BD, Olivares-Navarrete R, Berger MB, Hyzy SL, Schwartz Z. Role of Wnt11 during Osteogenic Differentiation of Human Mesenchymal Stem Cells on Microstructured Titanium Surfaces. *Sci Rep-Uk.* 2018;8.
51. Yodthong T, Kedjarune-Leggat U, Smythe C, Wititsuwannakul R, Pitakpornpreecha T. 1-Quebrachitol Promotes the Proliferation, Differentiation, and Mineralization of MC3T3-E1 Cells: Involvement of the BMP-2/Runx2/MAPK/Wnt/-Catenin Signaling Pathway. *Molecules.* 2018;23(12).
52. Liu BY, Lu YQ, Wang Y, Ge LN, Zhai NX, Han JX. A protocol for isolation and identification and comparative characterization of primary osteoblasts from mouse and rat calvaria. *Cell Tissue Bank.* 2019;20(2):173-82.
53. Sicchieri LG, Crippa GE, de Oliveira PT, Beloti MM, Rosa AL. Pore size regulates cell and tissue interactions with PLGA-CaP scaffolds used for bone engineering. *J Tissue Eng Regen M.* 2012;6(2):155-62.

54. Carvalho MS, Poundarik AA, Cabral JMS, da Silva CL, Vashishth D. Biomimetic matrices for rapidly forming mineralized bone tissue based on stem cell-mediated osteogenesis. *Sci Rep-Uk*. 2018;8.



CHAPTER 5

IN VIVO BONE REGENERATION STUDIES USING OFFSET AND GRADIENT MELT ELECTROWRITTEN (MEW) PCL SCAFFOLD

ABSTRACT

Tooth loss resulting in bone resorption in the jaw and can cause serious complications when the remaining bone level is low which hinder subsequent dental reconstruction treatment using prosthetic implants. Biomaterial-based bone tissue engineering however is a promising method to increase bone volume. In our previous in vitro studies, we demonstrated that the gradient and offset architectures of three-dimensional MEW polycaprolactone scaffolds could successfully direct cells toward an osteogenic lineage with resulting mineralization. The objective of this study therefore was to evaluate the osteoinductive capacity of these same scaffolds during bone healing in vivo.

Full thickness calvarial defects were created in female Wistar rats and subsequently filled with either a 250 μm , 500 μm , offset.50.50, gradient.250top (layer order 250-500-750 μm) or gradient.750top (layer order 750-500-250 μm) CaP coated scaffold. Empty defects acted as a control. After 4 and 8 weeks of healing, the rats were sacrificed and the calvaria containing the implant were recovered. Newly formed bone was assessed via micro computed tomography (μCT) as well as histological and immunohistochemical analysis.

The new bone volume to total volume (BV/TV) ratio was significantly enhanced in the grad.250top scaffold 8 weeks post-implantation. Histological investigations showed completed new bone tissue coverage for grad.250top following 500 μm scaffolds. However, the degree of soft tissue was replaced by new formed bone in the scaffolds with smaller pore sizes, the less evidence and incomplete of bone healing were observed in 250 μm , offset.50.50 scaffolds and the blank calvaria defect following 8 weeks.

Immunohistochemical analysis showed the expression of markers of osteogenesis i.e. OCN, OPN, ALP, Col I and BMP-2 were present in all scaffold groups at both time points. In particular, the mineralization marker osteocalcin was detected with the highest

intensity in the grad.250top and offset.50.50 scaffolds. Moreover, the expression of vascular endothelial markers of CD34, CD105, VEGF and vWF suggested angiogenesis was involved in stimulating the remodeling phase of the repair process. These results suggest that the gradient pore size structure provides the better mimicking natural bone by acceleration of osteogenesis-angiogenesis coupling.

INTRODUCTION

Defects of craniofacial bones associated with tooth loss or fracture, can lead to significant implications in the appearance and oral function of patients (1). Significant advances in tissue engineering resulting in the reconstruction of bone defects have been due to the design of optimal bone construct. However, the challenges of bone regeneration are multifactorial. While ideal porous scaffold materials mimic the extracellular matrix of the native tissue to ensure adequate nutrient and oxygen diffusion, waste product removal as well as cellular infiltration and vascularization, the scaffold(s) must also have adequate mechanical integrity to cope with its environment, be sufficiently biodegradable and minimise any host inflammatory response during the completion of the remodeling process (2-4).

PCL is a biodegradable polyester with a low degradation rate which is resorbed slowly making it a good candidate for regenerative medicine applications. In this respect, PCL has been shown to have significant potential for bone and cartilage repair (5). PCL also has sufficient mechanical properties to tolerate stress loads after implantation (6). The porosity of the scaffold is the most important factor regulating these mechanical properties, the penetration of regenerated tissue and subsequent vascularization. Reducing the elastic modulus by increasing the size of pores on the other hand, has also been shown to enhance cell and blood vessels infiltration (7).

According to our previous studies and other reported research, the offset and gradient pore size structured scaffolds provided dense structures that have the advantages of

mechanical integrity and high porosity for better cell infiltration in bone tissue engineering (8-11). Sobral et al. showed that gradient structured FDM poly (ϵ -caprolactone) scaffolds had better recovery after mechanical deformation as well as, better osteosarcoma cell distribution compared to homogeneous porous scaffolds (9). Serra et al. (12) however showed staggered filaments of 3-D printed polylactic acid and a bioactive CaP glass scaffold decreased the elastic modulus up to 75% in comparison with aligned fibers. Luca et al. and Oh et al. (13, 14) both showed an increase in ALP activity, calcium mineralization and faster new bone formation in compartments with the largest pores of gradient architecture PCL scaffolds. Both groups suggested the reason for improvement was due to a better supply of oxygen and nutrients in the larger pores of the gradient structure.

Melt electrowritten scaffolds are stable and solvent-free and therefore don't have the limitations of solution electrospinning which may have some toxicity to cells due to incomplete evaporation of solvents as well as undirected fiber orientation resulting in insufficient porosity due to a potentially firmly compressed nonwoven mesh structure which inhibits cell infiltration (15-17). This means blood vessels ingrowth and the vascularization process can't be developed properly after graft implantation. Therefore, the cells do not survive or integrate with the host tissue (18). Melt electrowritten scaffolds provide predictable filament deposition which creates uniform pore size distribution, orientation and pore interconnectivity (19) resulting in an improvement of angiogenesis, vascularized tissue and cell penetration / ingrowth leading to faster repair of bone defects. This chapter aims to address the lack of *in vivo* data assessing the effect of melt electrowritten PCL scaffolds with offset and gradient structures on bone regeneration.. In this study, medical grade PCL was utilized to fabricate membranes according to our published protocol via the technique of MEW (10). The scaffolds were coated with CaP to improve the hydrophilicity and bioactivity before being implanted into a critical sized

osseous defect created in the calvarium of rats. We expect significant bone regeneration because of the highly porosity of the gradient melt electrospun PCL scaffolds including large pore sizes (250-500-750 μ m).

MATERIALS AND METHODS

Animals

All animal experimentation was performed as authorized by the Griffith University Animal Ethics Committee (approval # DOH/01/17/AEC). Thirty skeletally mature female Wistar rats (150 \pm 20 g) were sourced from the Animal Resource Centre (ARC, Western Australia) and housed in pairs in a temperature controlled animal facility with 12/12 hour light/dark cycles. Both food and water was provided ad libitum.

Surgical Procedures

The initial body weight of each animal was recorded before the surgical procedures. General anaesthesia was administered using a Mediquip vaporiser which enabled precise control of the level of anaesthesia. A dosage of up to 5% of Isoflurane (ProVet, Australia) was used for induction followed by 1-3% to maintain anaesthesia. The rats were kept on a heating pad during surgery and immediately postoperatively in order to maintain body temperature. Any unconscious or sedated animals were held in separate cages without the presence of any other alert and active rats.

To assist with post-operative pain management, buprenorphine (0.05 mg/kg) was given by subcutaneous injection at least 15 minutes prior to surgery. The dorsal part of cranium was then shaved and the skin of the operation site disinfected with 50 mg/mL Povidone-Iodine (Betadine, Mundipharma BV, Netherland). A sagittal incision was made through the skin over the parietal bone and the periosteum of the calvarium and the cranial vertex was uncovered. After raising the full thickness periosteal flap, 2 circular cranial 5 mm defects were created in each animal using a trephine bur (external diameter of 5.0 mm)

(Komet Dental, Germany) under copious isotonic solution (0.9% saline) irrigation. An occlusive PTFE membrane (Cytoplast, GBR-200 Barrier Membranes, Osteogenics Biomedical, USA) was then placed on top of the exposed *dura mater* in order to prevent the infiltration of any soft tissue into the defect and away from the newly created osseous defects (Figure 5.1).

Each defect received one of the following treatments as shown in Figure 5.2: a) Blank (no scaffold), b) 250 μm pore size, c) 500 μm pore size, d) offset.50.50, e) grad.250top and f) grad.750top. The skin was then closed in layers using resorbable coated vicryl sutures (Vicryl 5.0, Ethicon, Germany). Animal revival was assisted using pure oxygen, and conscious animals were transferred into a cage until complete recovery. Postoperative analgesia (Buprenorphine 0.01 - 0.05mg/kg SC) and prophylactic antibiotic cover (Enrofloxacin, Baytril, Bayer UK) was administered subcutaneously at a dose of 2.5 mg/kg. During the postoperative period, the antibiotic delivery continued per os at a dose of 2.5 mg/kg per day for 7 days. All drug delivery was performed using a 23-gauge needle via an intraperitoneal route. Recovery was considered complete when the rats were able to move purposefully in their cage.

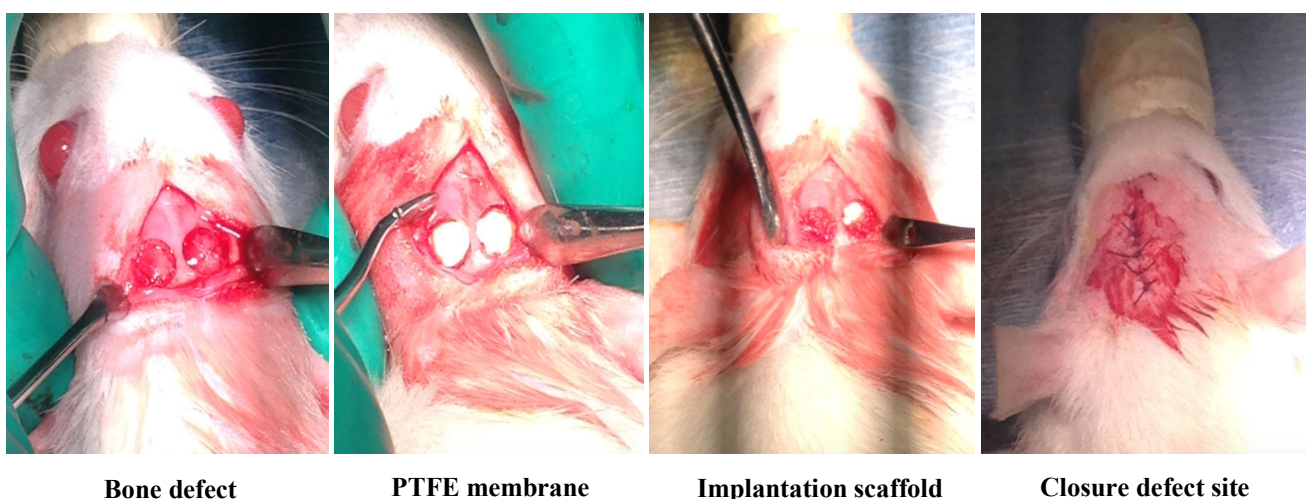


Figure 5.1: Photographs of the surgical procedures whereby two circular calvarial defects were created in the rat and subsequently filled with PTFE membrane to prevent soft tissue

infiltration. Then melt electrospun scaffolds were implanted into the defect site and the defect was closed in layers using sutures. The defects were subsequently left to heal for 4 and 8 weeks.

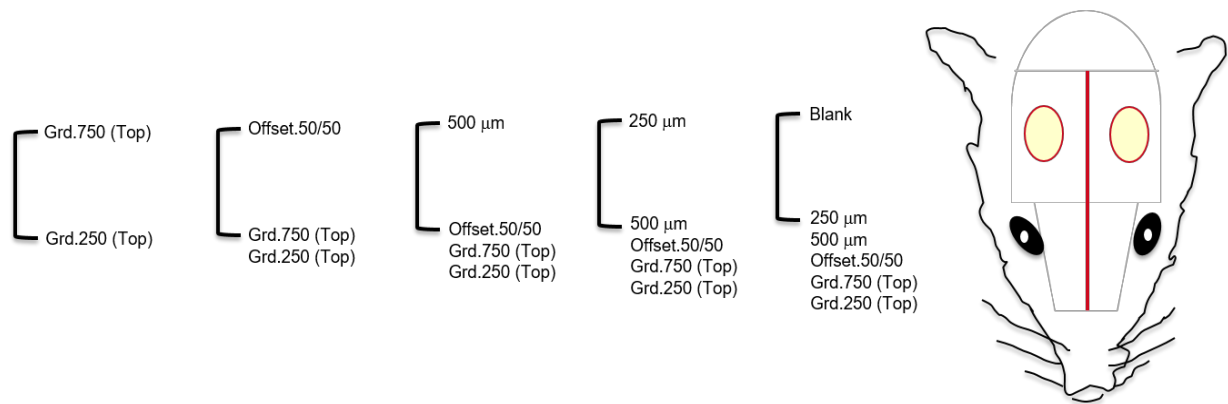


Figure 5.2. Schematic of the calvarial defects and the combination of melt electrospun scaffolds subsequently placed *in vivo*. To ensure sufficient material for subsequent analysis, five replicates of each scaffold for both healing time points (4 and 8 weeks) were placed.

The animal's surgical wound, condition, activity, food intake and any clinical signs of infection during recovery were monitored daily. Following healing periods of 4 and 8 weeks, the animals were euthanized by isoflurane overdose when the scaffolds were retrieved and fixed in 4% paraformaldehyde (PFA) in PBS for 24 h, at 4 °C for further analysis including Micro-CT, histology and immunohistochemistry.

Micro-CT Images Acquisition

Micro-CT scans of the recovered calvaria with the scaffold *in situ* was performed in a micro-computed tomography (micro-CT) scanner (μ CT40, SCANCO Medical AG, Bruttisellen, Switzerland) at a resolution of 15 μ m, a voltage of 55 kV and a current of 150 μ A at a greyscale threshold of 150. Three-dimensional images were constructed (frame averaging = 1) and the average density of mineralisation determined using the micro-CT software. New bone volume in the test scaffolds measured in the defect region

were determined by subtracting the mean bone volume of the 'blank' (without scaffold) negative control.

Histomorphometric Preparation & Analysis

Samples of the original surgical defect and 2mm of surrounding tissue were recovered from the surgical site for histologic investigation. Following fixation of the specimens in 4% PFA, they were subsequently decalcified in 14% neutral ethylenediaminetetracetic acid (EDTA) at PH 10.0 at 4 °C for 4 weeks and then dehydrated in ascending concentrations of ethanol followed by xylene. After that they were embedded in paraffin. The paraffin blocks were trimmed and 6 µm thick sections were prepared and mounted on charged slides to examine the morphology, integration of neighboring tissue into the scaffold, cell type and tissue inflammation by using haematoxylin and eosin (H&E) staining according to manufacturer's protocol.

Immunohistochemistry (IHC)

Serial paraffin sections were de-waxed in xylene and rehydrated in an ethanol gradient and then water. Antigen retrieval was performed by applying a heat-induced epitope incubation in 10 mM citrate buffer (PH = 6) at 95 °C for 5 minutes. Endogenous peroxidase activity was quenched with 3% hydrogen peroxide for 5 minutes at RT to reduce endogenous peroxidase activity, and any other potential non-specific binding sites were blocked with Background SNIPER (Biocare Medical, cat.BS966L) for 10 minutes at RT. The sections were subsequently incubated with the following primary antibodies at 4 °C overnight: anti-collagen I antibody (Col I; Abcam, ab34710, diluted 1:400), alkaline phosphatase (ALP; Abcam, ab108337, diluted 1:250), anti-bone morphogenic protein-2 antibody (BMP-2; Abcam, ab14933, diluted 1:400), anti-osteocalcin antibody (OCN; Abcam, ab13420, diluted 1:250), anti-osteopontin antibody (OPN; Abcam, ab8448, diluted 1:200), anti-CD34 antibody (Abcam, ab81289, diluted 1:200), anti-CD105 antibody (Abcam, ab231673, diluted 10 µg/ml), anti-vascular endothelial growth factor

antibody (VEGF; Abcam, ab2349, diluted 1/100), anti- Von Willbrand factor antibody (vWF; Abcam, ab6994, diluted 1/800).

After rinsing with PBS, the sections were labelled with the corresponding HRP secondary antibodies at RT. The sections were visualised with 3,3-diaminobenzidine (DAB solution; DAKO liquid DAB, ref: K3468). Mayer's hematoxylin (Thermo Scientific) was used for nuclei staining at RT. The slides were dehydrated, and the coverslips were mounted onto the slides. All the slides for each antibody were stained at the same time. The soft tissue that did not express the target antigen was considered as negative control and the calvarial bone sample as positive control. The sections were visualised by an Aperio digital pathology slide scanner (Leica Biosystems Inc, USA).

Statistical Analysis

All data were expressed as mean \pm standard deviation. Comparison between groups were analysed by analysis of variance (ANOVA, post hoc test: Tukey). The statistical software Prism 8 for windows was used for calculations and a p value <0.05 was considered statistically significant.

RESULTS

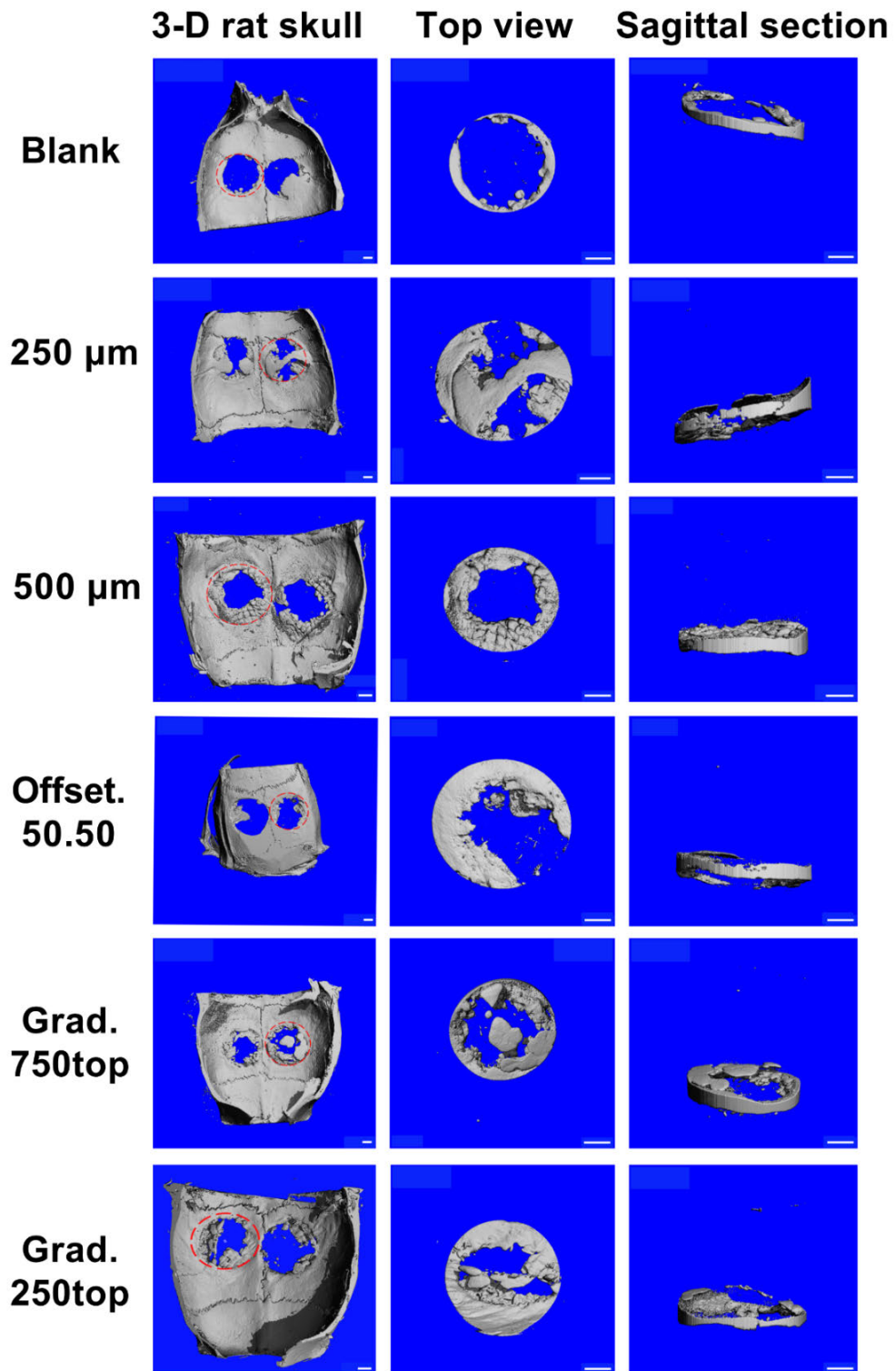
Micro-CT Evaluation of Newly Formed Bone

Figure 5.3 shows the topographic features of the newly formed bone in the scaffold-implanted calvarial defects. Images were acquired via reconstruction of the μ -CT scans using the scanner software. In the control defect, the 5mm diameter defect was shown to be a critical-sized defect as a very limited amount of new bone was regenerated after 4 and 8 weeks of healing. Any new bone was found to circle the primary bone defect. Defects filled with scaffolds with a pore size of 500 μm and the offset.50.50 structures revealed that the new bone was mainly distributed on the periphery of the implanted scaffolds rather than the central region of the porous constructs. Whilst, in 250 μm and

both gradient (250top, 750top) scaffolds, the new bone formation was not limited surrounding the defect area and the regeneration increased towards the cavity centre after 4 weeks (Figure 5.3-A). The bone images indicated that the residual material scaffold was diminished by gradual new bone growth in scaffold groups following 4-8 weeks post-implantation. At 8 weeks post-implantation, the grad.250top indicated a high degree of new bone formation compared to the other scaffold groups (figure 5.3-B). In contrast, other groups showed incomplete bone repair following 8 weeks implantation with more empty space.

The new bone volume was also measured by quantitative analysis (Figure 5.4). The BV/TV ratio showed a time-dependent increase in all the groups, however this was only significant for grad.250top scaffolds at the two different time points compared to other groups ($p \leq 0.034$). The highest BV/TV ratio was found in the grad.250top scaffold following 8 weeks post-implantation which was significant compared to 250 μm scaffold and the blank ($p \leq 0.025$) (Figure 5.4).

A



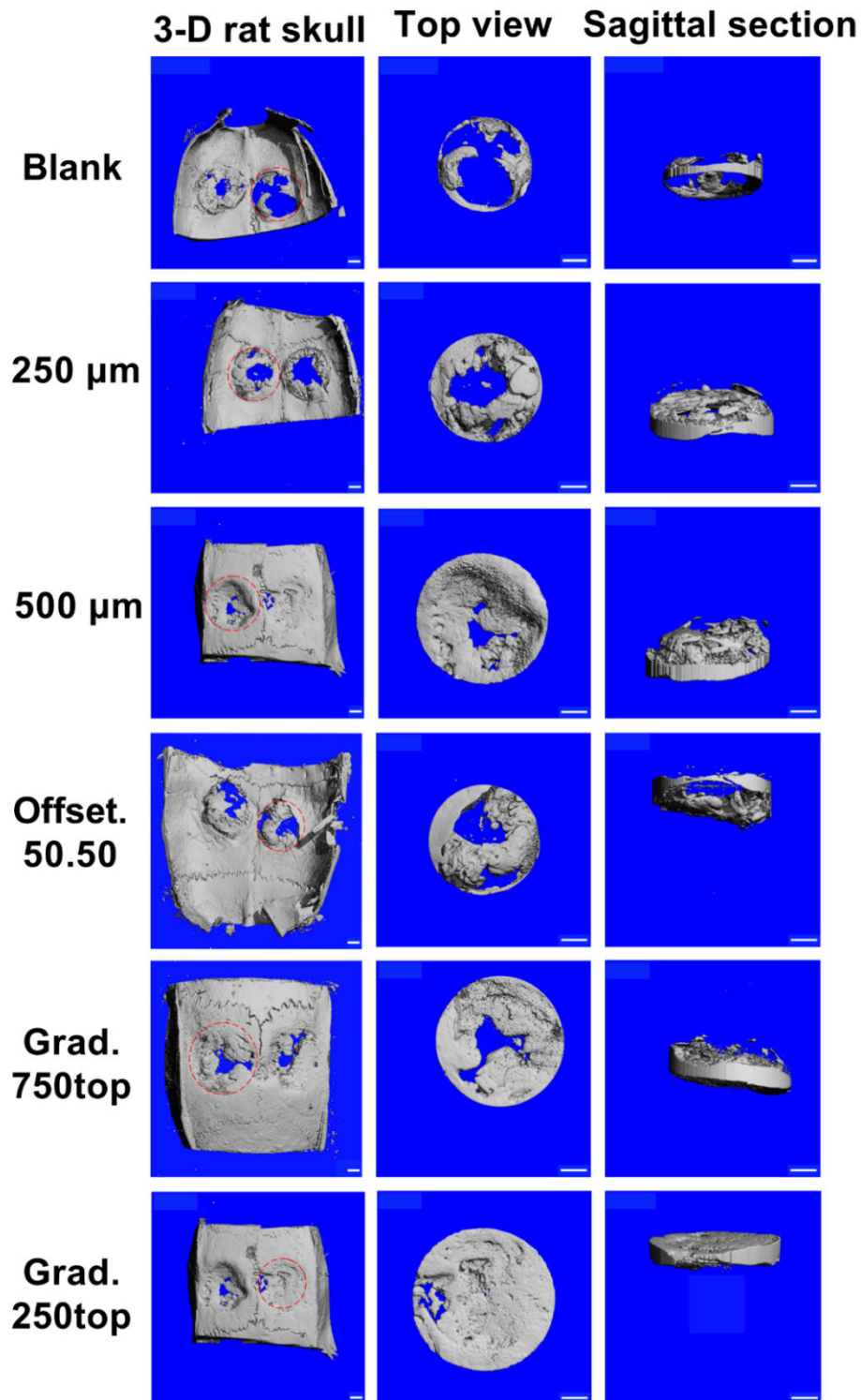
B

Figure 5.3. 3-D reconstructed Micro-CT image analysis showing the degree of bone repair in the different melt electrowritten PCL scaffolds implanted into the rat calvaria. (A) 4 weeks post implantation and (B) 8 weeks post-surgery. Top and sagittal defect views are of the area indicated by the dashed red line; Scale bar =1 mm.

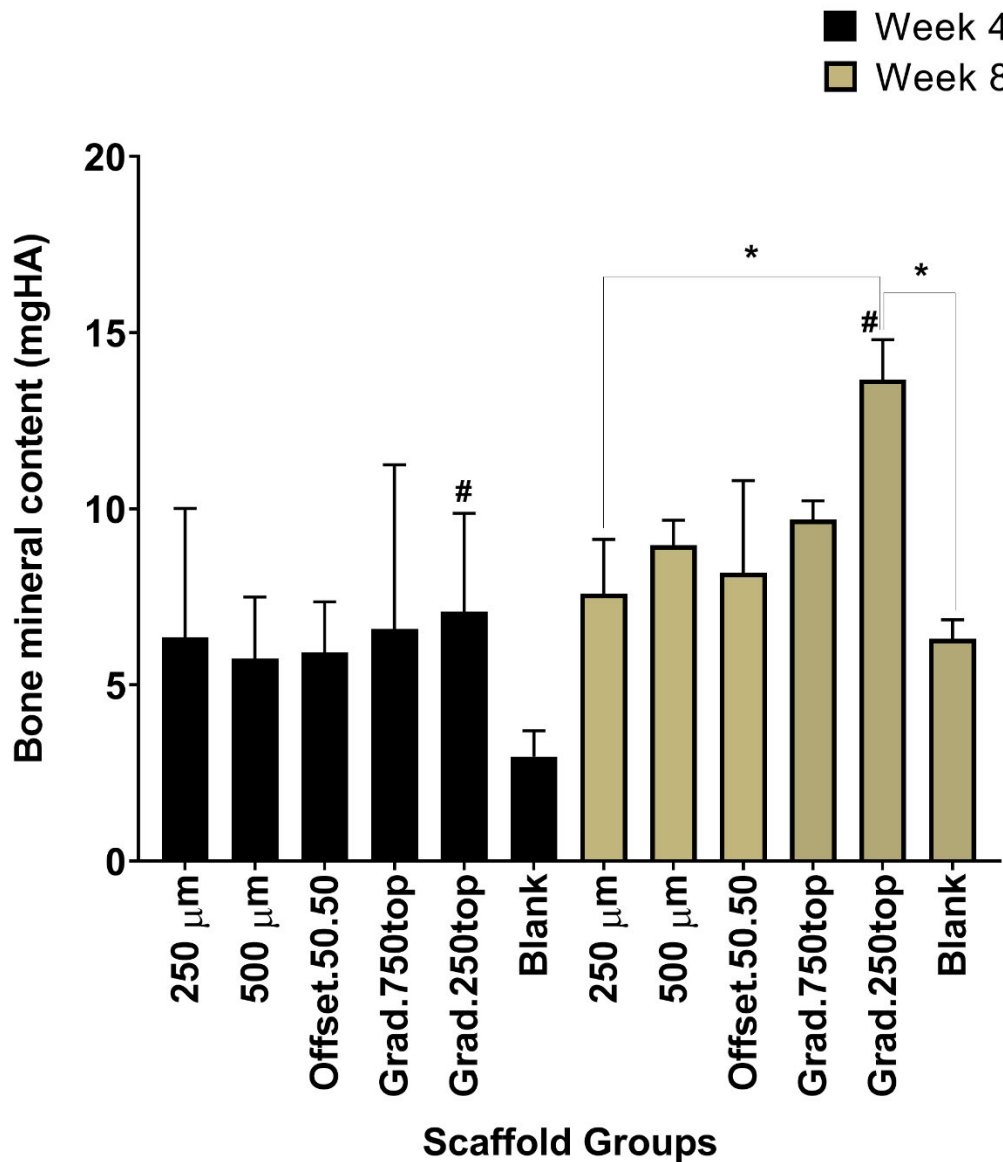


Figure 5.4. Quantitative micro-CT data analysis of bone volume to total volume ratio (BV/TV). A significant difference in the BV/TV ratio was seen between grad.250top and the 250 μ m scaffolds and the control after 8 weeks post-implantation, (number of samples/ group = 5) ($p \leq 0.025$). (#) indicates a significant difference between grad250top scaffold groups at the different time points of 4 and 8 weeks ($p \leq 0.034$).

Histological Assessment (H&E Staining)

Figure 5.5 shows representative histological images of the retrieved samples after 4 and 8 weeks of healing. At 4 weeks, new bone tissue observed in the offset.50.50 and gradient grafts was denser at the edges towards the centre of the defect area. In 250top gradient

constructs, the new bone was formed around the PCL scaffolds and generated 'osteocytes in lacuna' like structures. On the other hand, towards the centre of the scaffold more newly formed bone matrix accompanied with osteoblasts that were located close to the pores of substitute (Figure 5.5-B). Little mature bone tissue was observed within the 250 and 500 μm scaffolds, rather immature osteoid like tissue containing prominent the newly formed bone matrix tissue containing osteoblasts (Figure 5.5-A). In the control group (without scaffold) only either bone matrix or soft tissue were observed with a few less osteoblast cells (Figure 5.5-A).

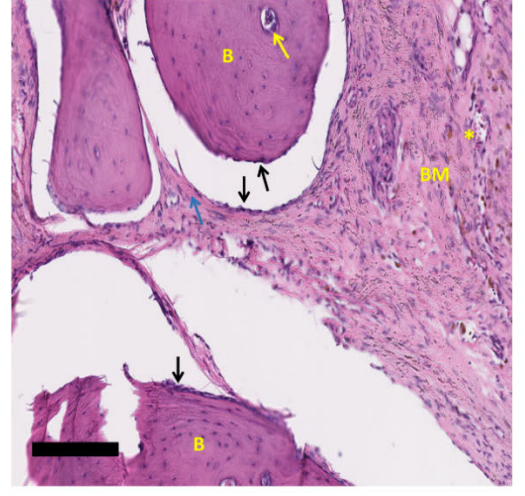
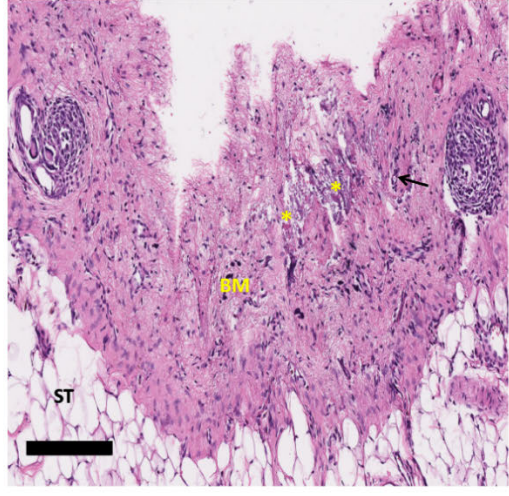
After 8 weeks healing, H&E staining demonstrated newly formed bone tissue was produced and distributed throughout the scaffolds, especially the gradient and 500 μm scaffolds. The grad.250top scaffold showed high bone content and the pores of the scaffold were completely filled with compact bone (Figure 5.5-B). The pores were observed in the images were created by xylene dissolving the PCL scaffold fibres as the pores were infiltrated with the new bone. The bone matrix was reduced in the 250 μm , offset.50.50 scaffolds and the blank in contrast to that at 4 weeks (Figure 5.5-A, B). While the 500 μm scaffold showed bone regeneration after 8 weeks, there were still more empty pores that needed to be fully covered compared to the gradient scaffolds (Figure 5.5-A) indicating that gradient scaffolds produced - more new bone tissue compared to the other groups (Figure 5.5-B).

A

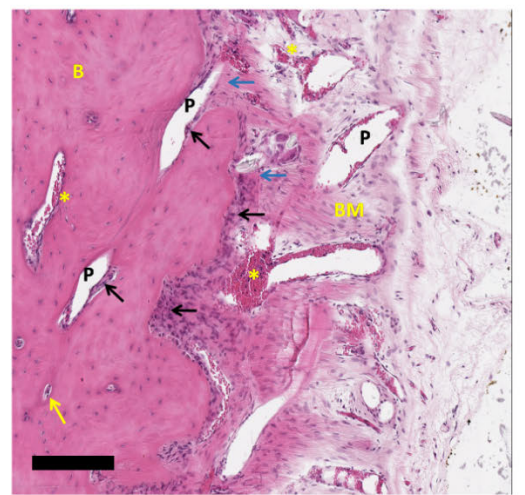
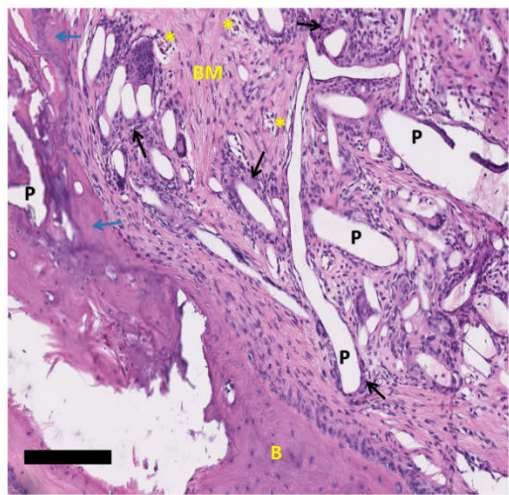
Week 4

Week 8

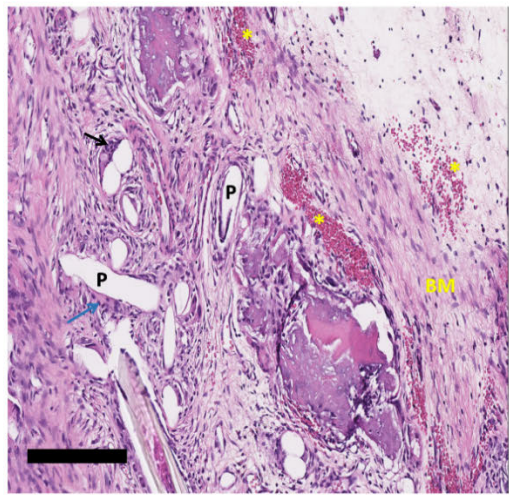
Blank



250 μ m



500 μ m



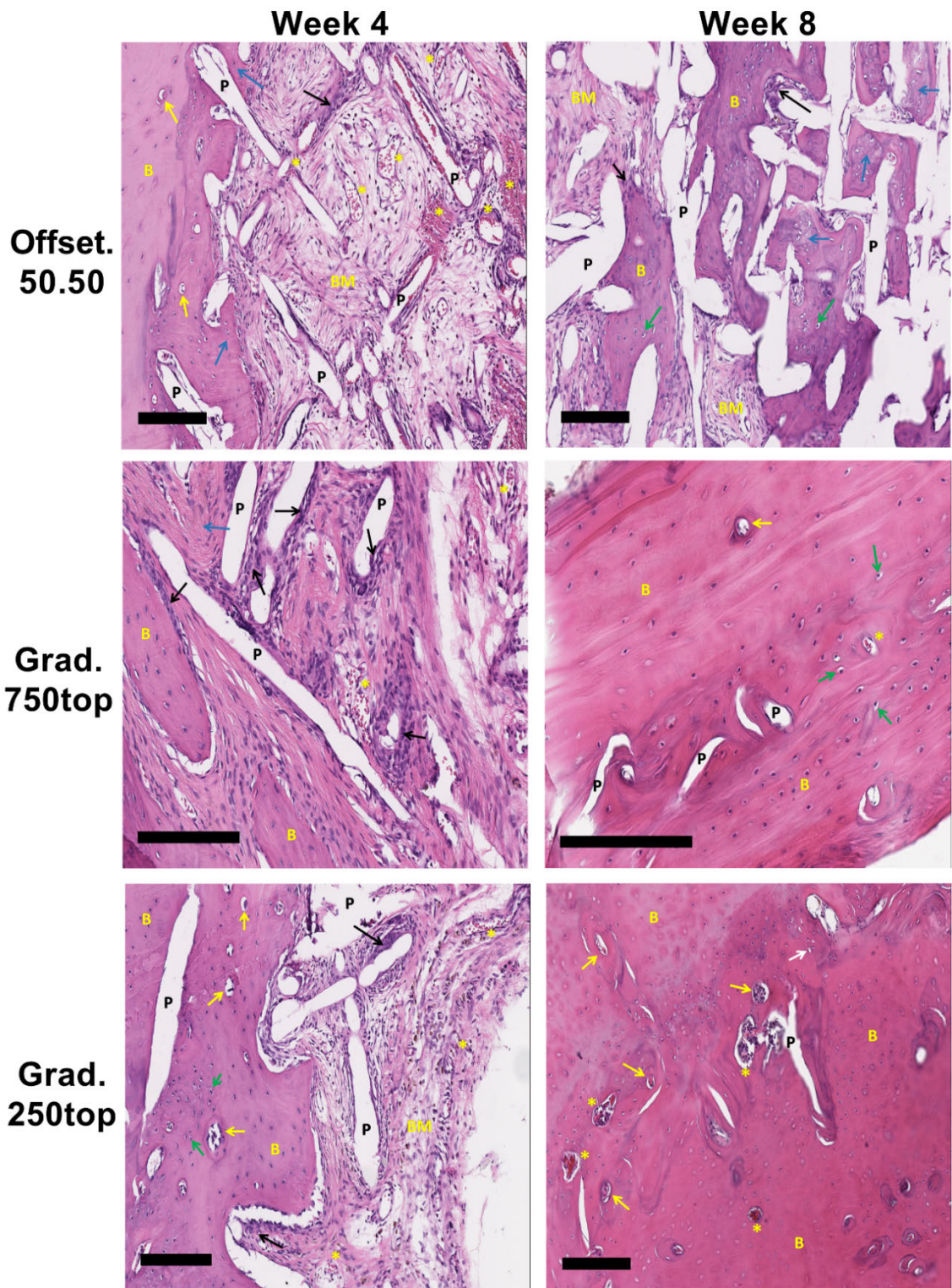
B

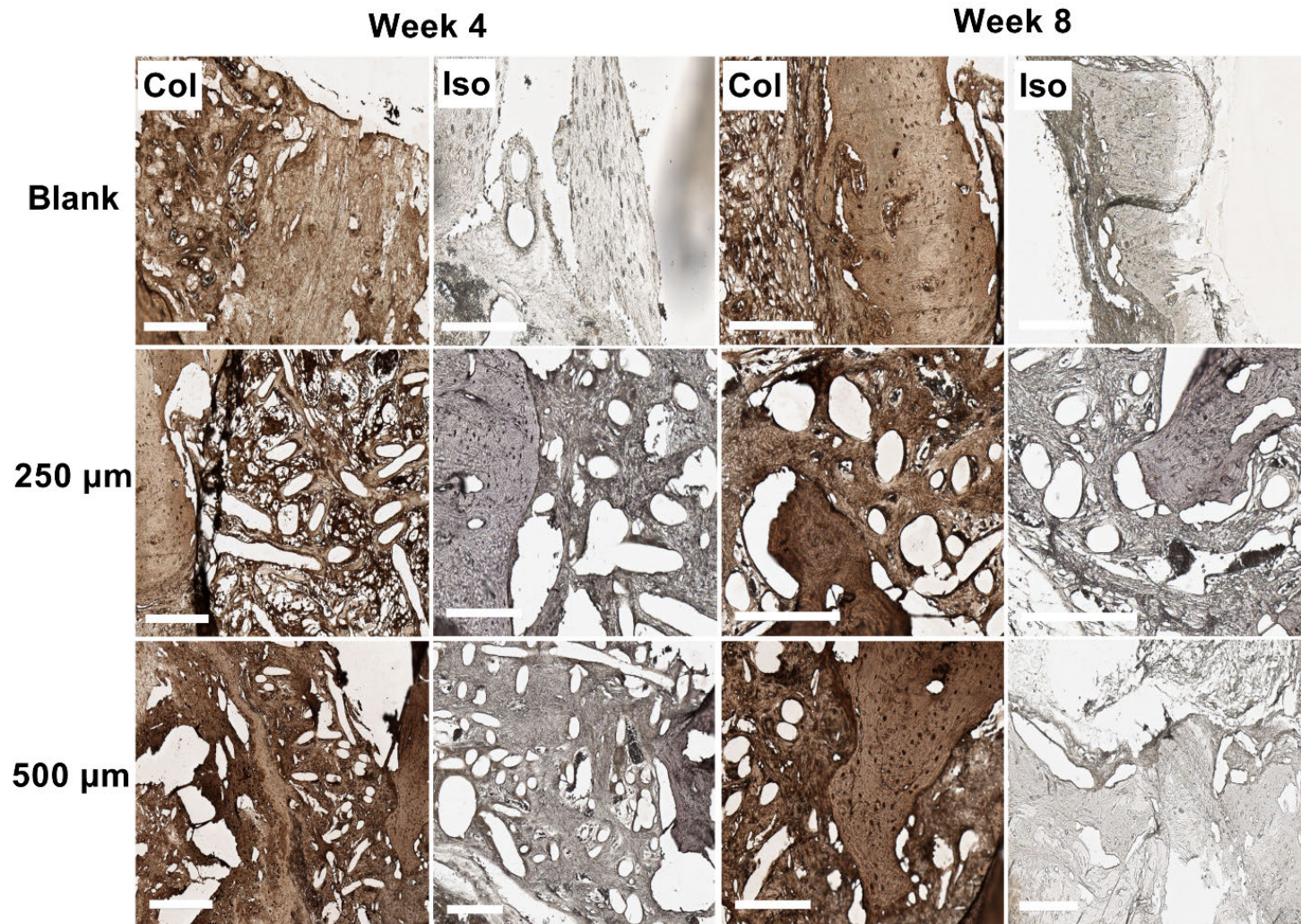
Figure 5.5. Microscope images of H&E stained tissue sections of melt electrospun PCL scaffolds implanted in rat calvarial defects 4 and 8 weeks (top and bottom panels respectively) after surgery. B: new bone; Black arrow: osteoblasts; BM: newly formed bone matrix; ST: Soft tissue; P: pore remaining implanted scaffold material; Blue arrow:

new bone forming; Green arrow: osteocytes; Yellow arrow: osteocytes in lacuna; Asterisk: blood vessel; Scale bar = 200 μm .

Collagen Type I (Col I) Immunostaining

Immunohistochemical analysis displayed markedly strong staining of Col I throughout the constructs in all groups 8 weeks after implantation. Staining was less intense for scaffolds 4 weeks post-surgery suggesting the expression of collagen I increased with healing time. No positive stained tissues were seen in the negative control group (Figure 5.6-A) however significantly more Col I production was observed in the 250 μm and offset.50.50 scaffolds after 8 weeks compared to the other groups (Figure 5.6).

A



B

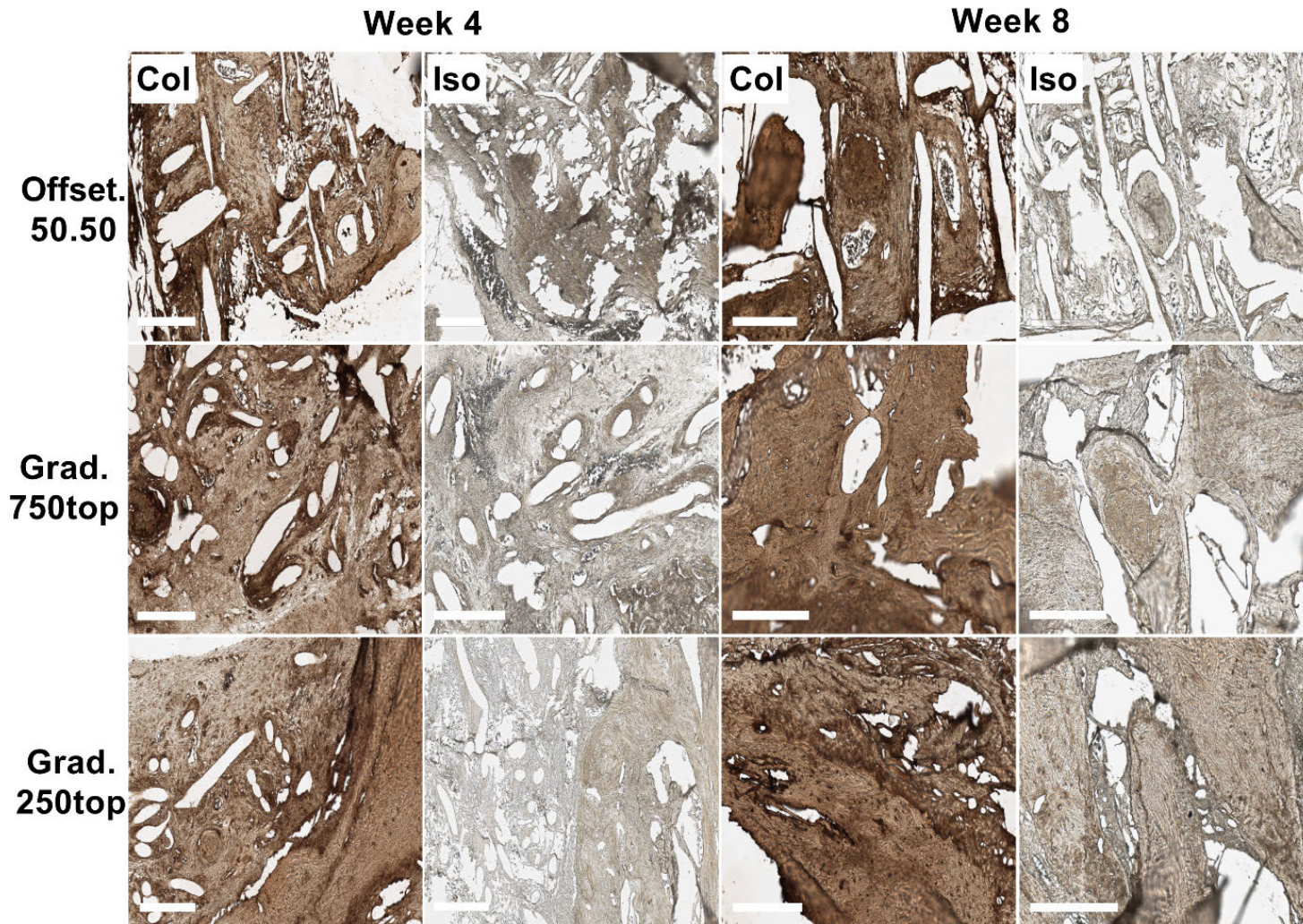
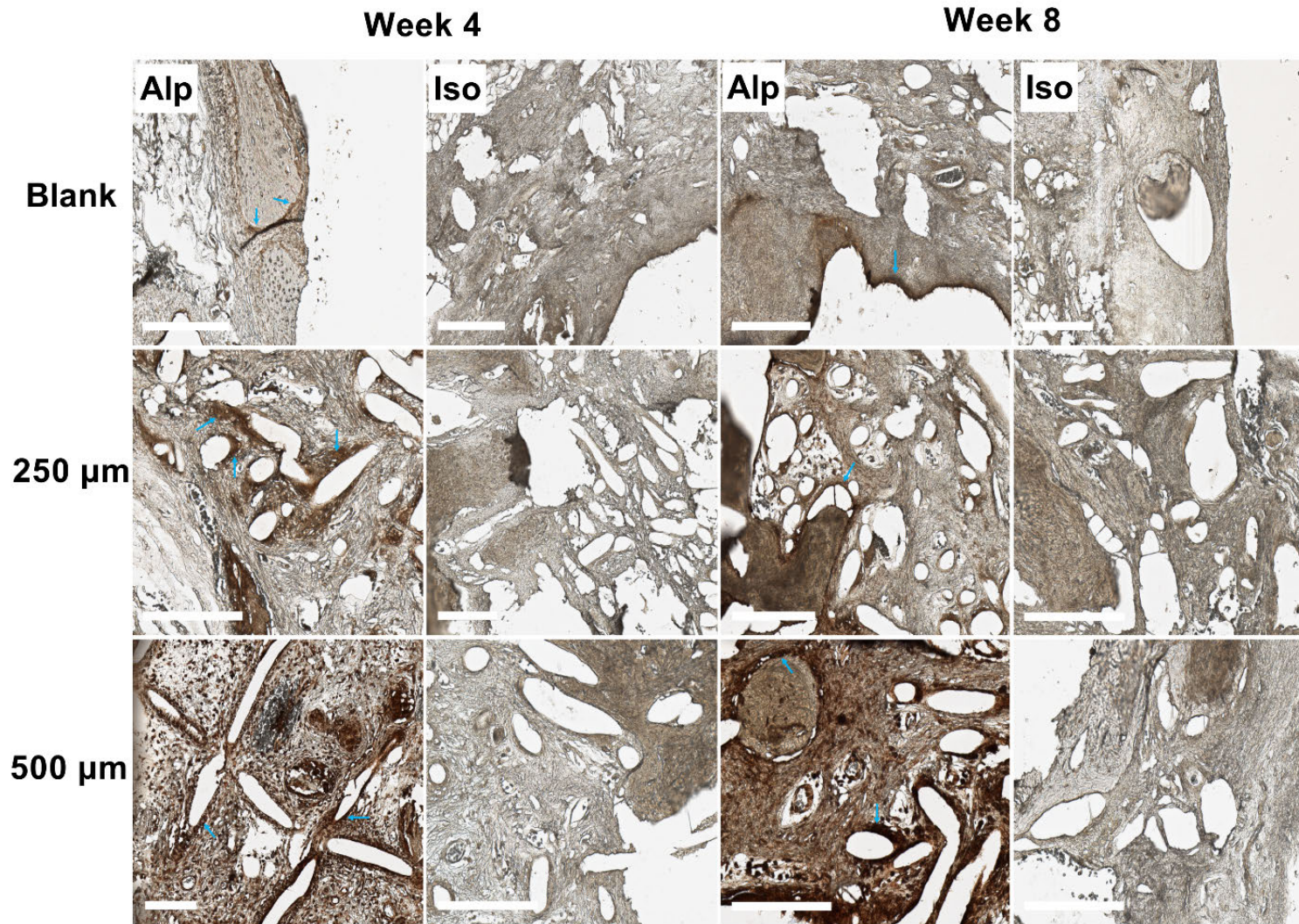


Figure 5.6. IHC analysis of Col I in calvarial defects from rats 4 and 8 weeks post-implantation of melt electrospun PCL scaffolds. (A) Blank (defect control without implanted scaffold), 250 μm , 500 μm . (B) Offset.50.50, Grad.750top, Grad.250top. Col: Collagen staining, Iso: Isotype control; Scale bar = 200 μm .

Alkaline Phosphatase (Alp) Immunostaining

IHC analysis of the stained sections showed the overall trend for all groups apart from the blank was for the ALP expression level to increase from Weeks 4 to 8 and this was most pronounced in the 500 μm scaffold group (Figure 5.7). The positive staining areas were mostly localized at the pore margins or the borderline of newly formed bone tissue as have been shown (blue arrow) in all the scaffold groups as an intense staining at the edge of pores (Figure 5.7).

A



B

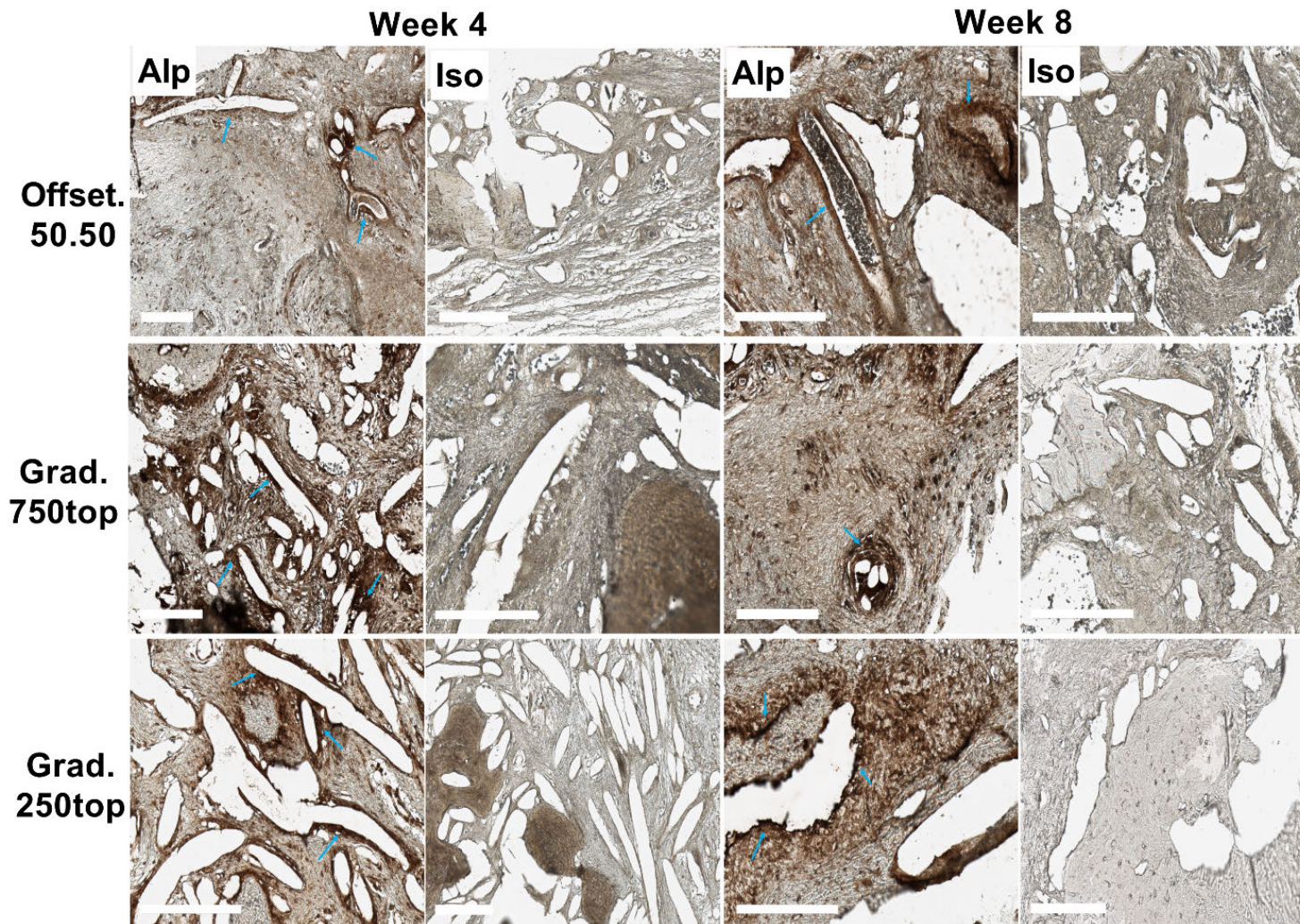
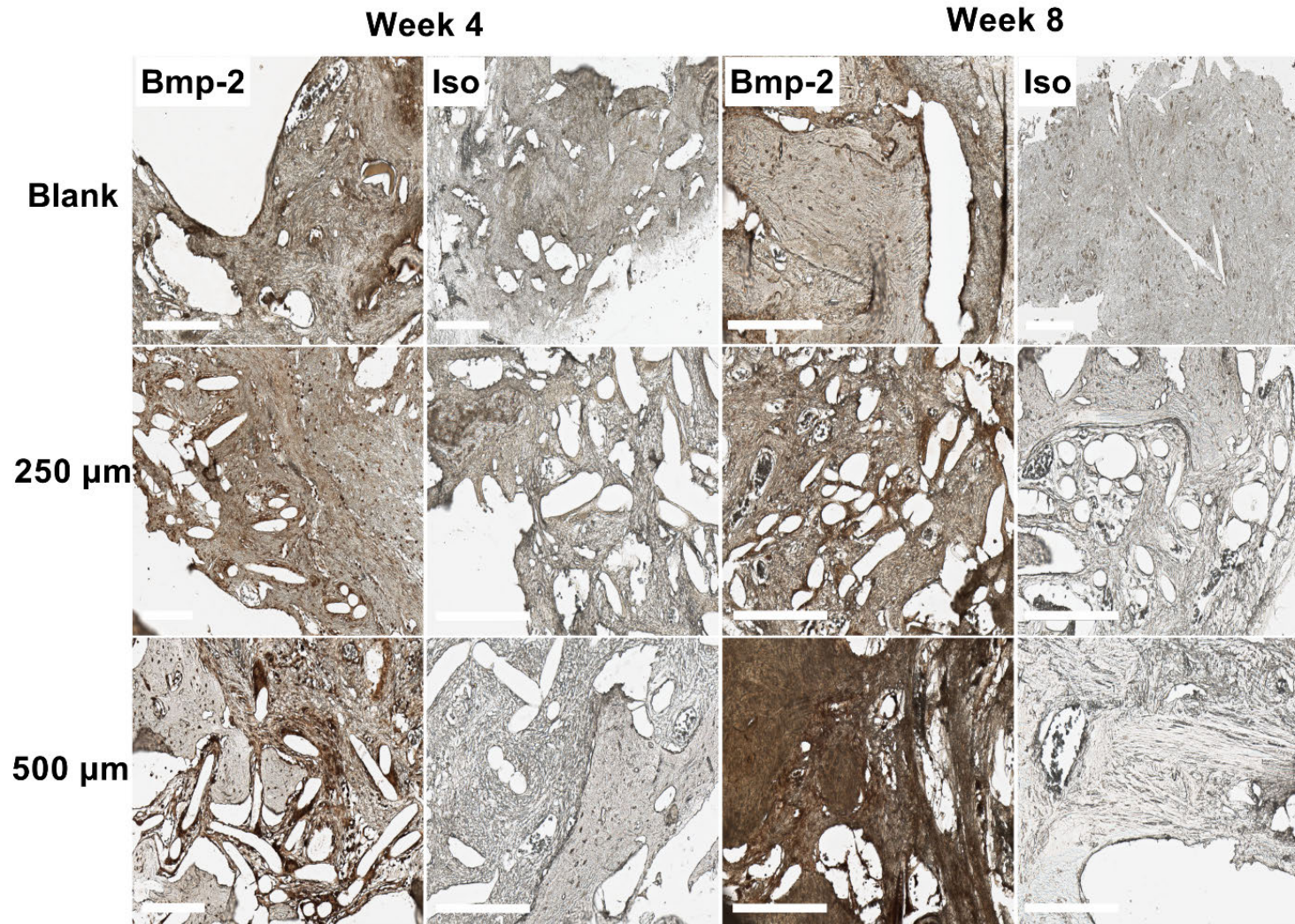


Figure 5.7. IHC analysis of Alp in calvarial defects from rats 4 and 8 weeks post-implantation of melt electrospun PCL scaffolds. (A) Blank (defect control without implanted scaffold), 250 μm , 500 μm . (B)) Offset.50.50, Grad.750top, Grad.250top. Alp: Alp staining, Iso: Isotype control; Scale bar = 200 μm .

Bone Morphogenetic Protein - 2 (Bmp-2) Immunostaining

IHC analysis showed a significant difference between the two time points of 4 and 8 weeks for the 500 μm scaffold. Also, It appears that 500 μm scaffold at 8 weeks of treatment has the highest BMP2 expression compared to the other groups (Figure 5.8-A). However, there was also strong staining observed between weeks 4 to 8 for the offset.50.50, grad.750top and grad.250top samples (Figure 5.8-B).

A



B

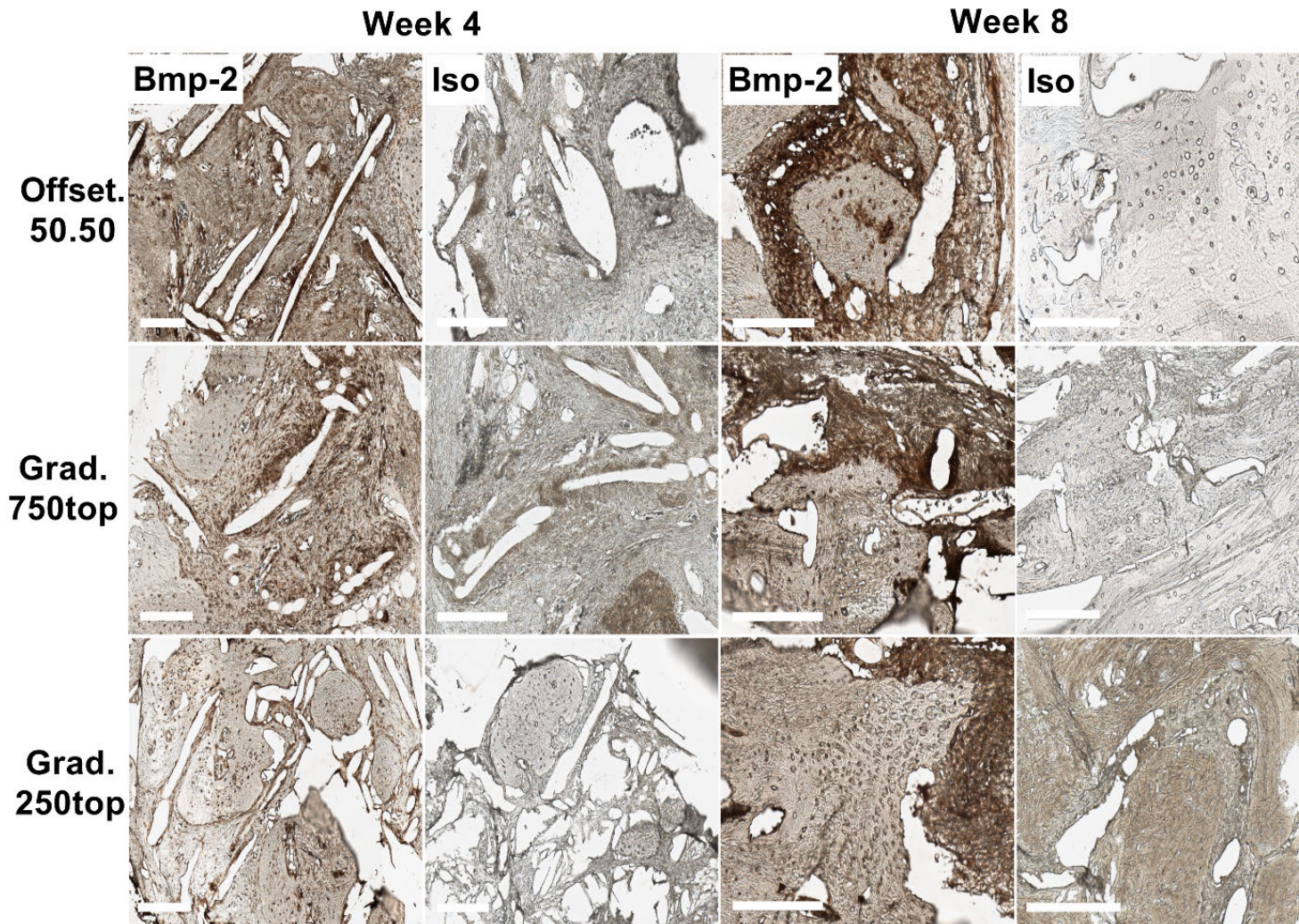
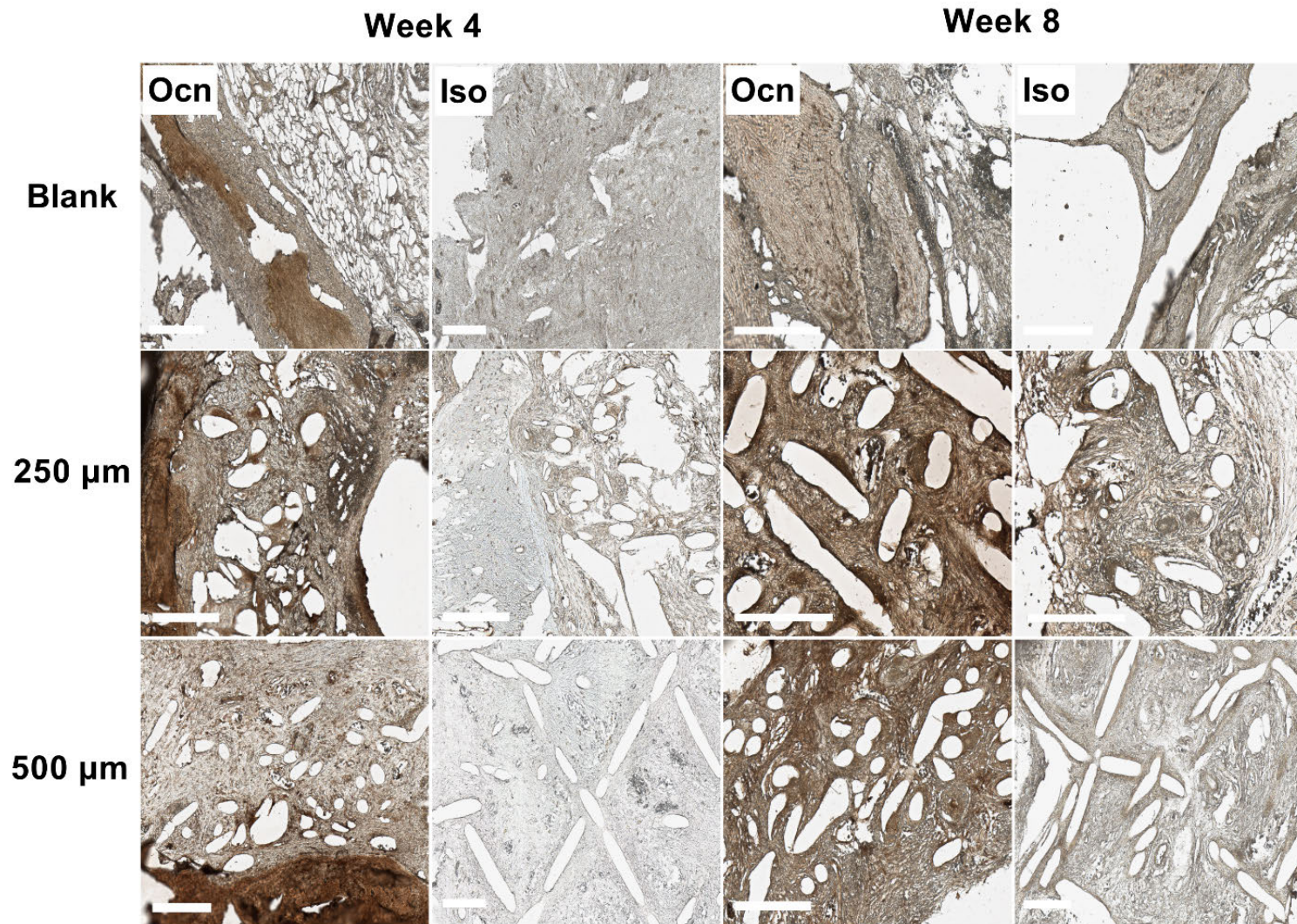


Figure 5.8. IHC analysis of Bmp-2 in calvarial defects from rats 4 and 8 weeks post-implantation of melt electrospun PCL scaffolds. (A) Blank (defect control without implanted scaffold), 250 μm , 500 μm . (B) Offset.50.50, Grad.750top, Grad.250top. Bmp-2: Bmp-2 staining, Iso: Isotype control; Scale bar = 200 μm .

Osteocalcin (Ocn) Immunostaining

The IHC results showed the specific expression of Ocn in positive groups compare to the negative ones which showed just background staining (Figure 5.9). The intensity of ocn staining increased in grad.250top in comparison with the other scaffold groups following 4 weeks of healing (Figure 5.9-B). However, the similar expression levels of Ocn for 250 and 500 μm attributed to the original old bone not the new formed bone at 4 weeks. Immunohistochemistry for Ocn revealed the staining intensity was greater in grad.250top, offset.50.50 and 250 μm scaffolds compared to the others after 8 weeks, although there was more newly formed bone tissue in the grad.250top group than those two groups which indicated the greater osteogenic activity in the gradient structure (Figure 5.9-B).

A



B

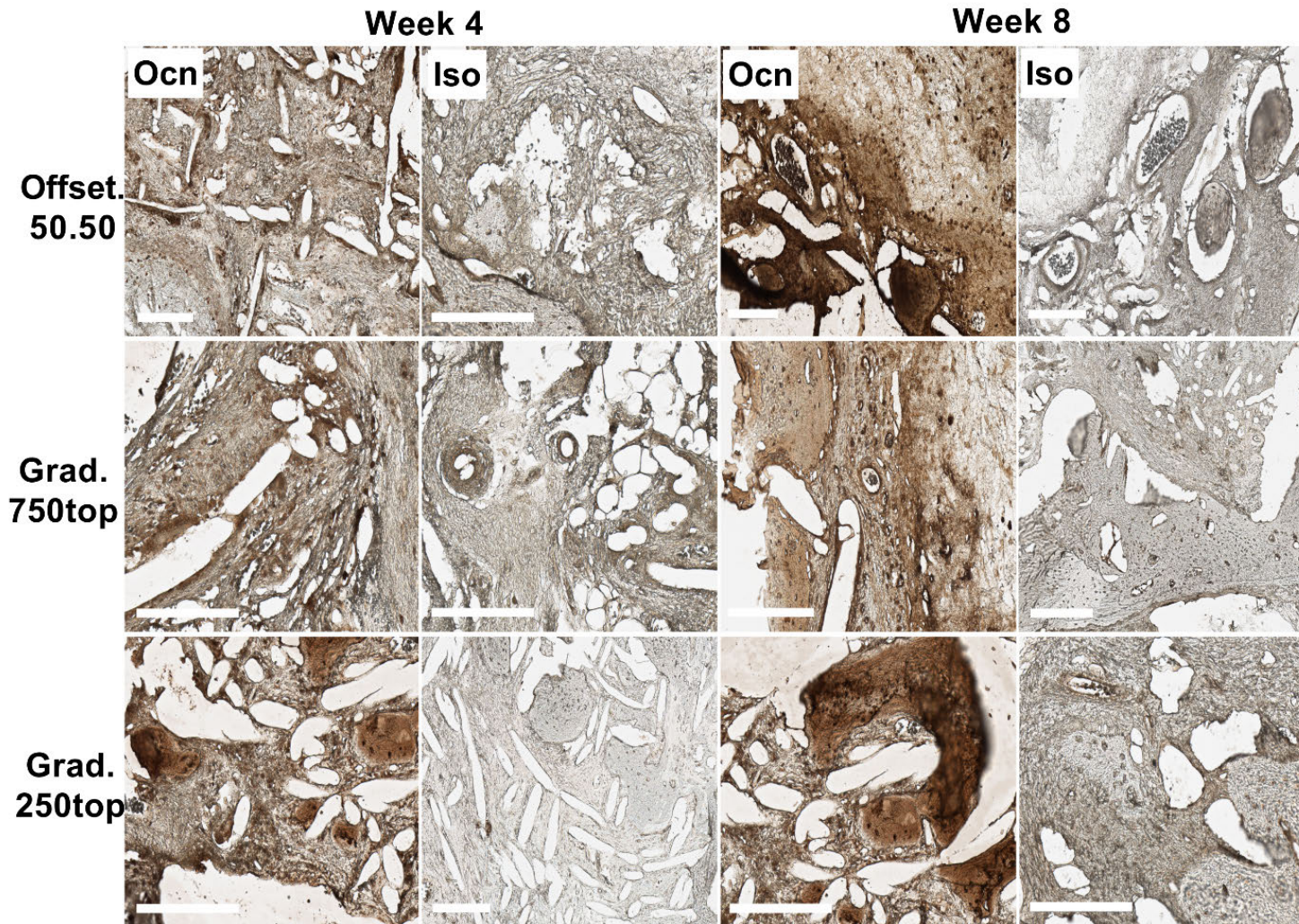
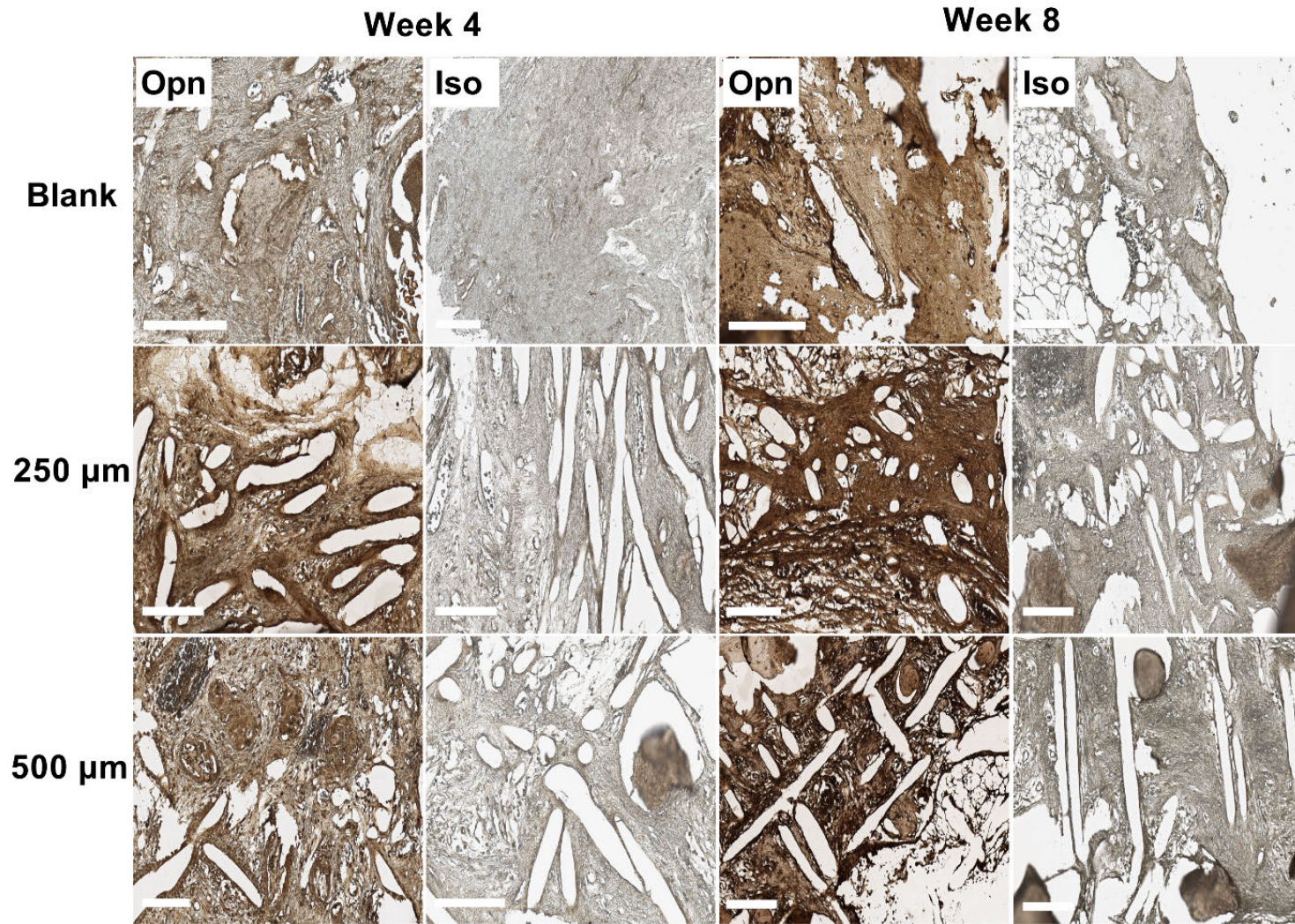


Figure 5.9. IHC analysis of Ocn in calvarial defect of rat 4 and 8 weeks of post-implantation of the melt electrospun PCL scaffolds. (A) Blank (defect control without implanted scaffold), 250 μm , 500 μm . (B) Offset.50.50, Grad.750top, Grad.250top. Ocn: Osteocalcin staining, Iso: Isotype control; Scale bar = 200 μm .

Osteopontin (Opn) Immunostaining

Immunohistochemistry for Opn showed that osteopontin was strongly detected for all groups after 8 weeks of implantation compared with the groups at week 4 (Figure 5.10). Higher expression was localized in more mineralized areas of the new bone tissue in 500 μm and the gradient scaffold structures in comparison to the other tissues (Figure 5.10-A, B). However, more intense staining was also found at the margins of the pores where there are active osteoblasts.

A



B

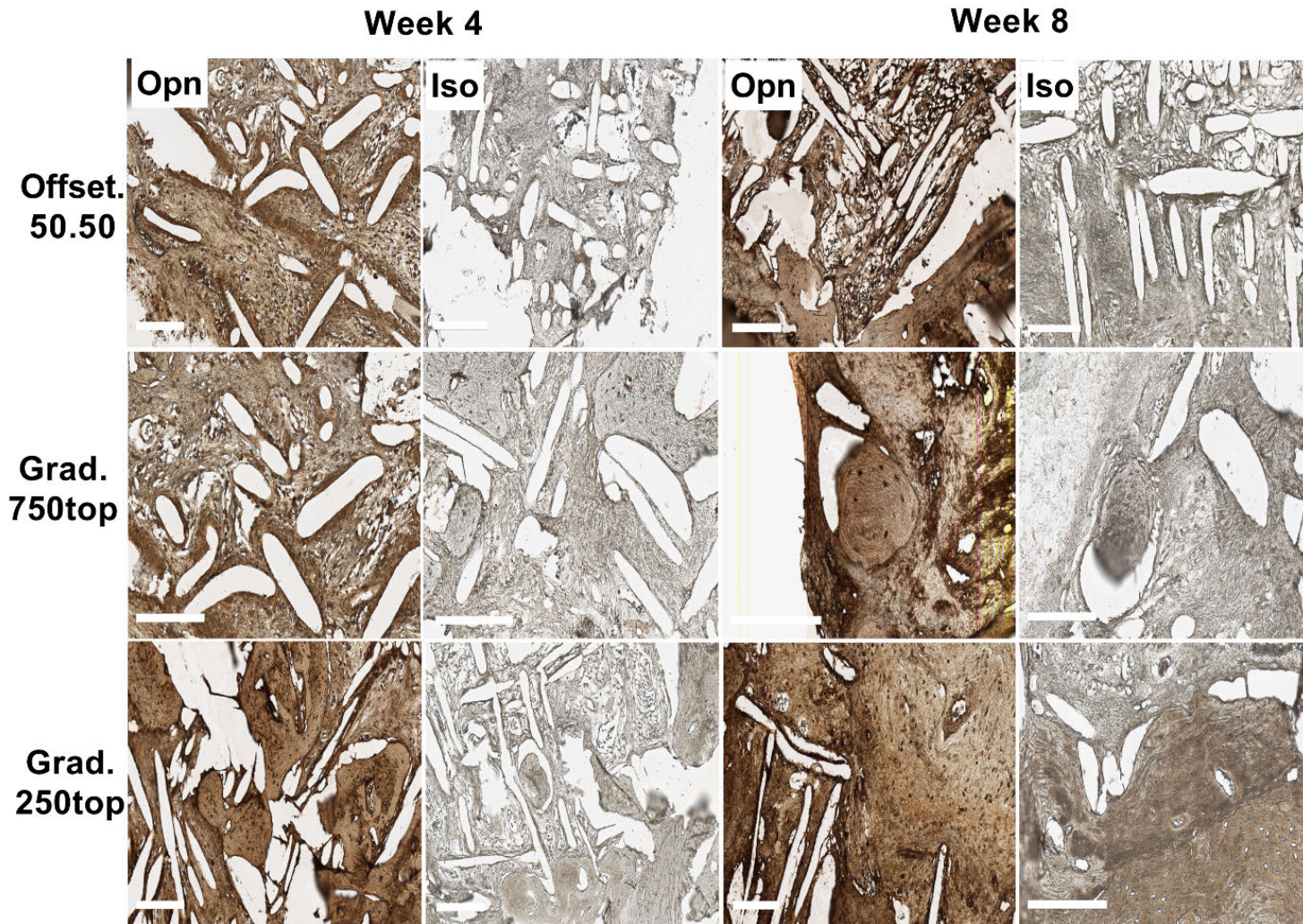
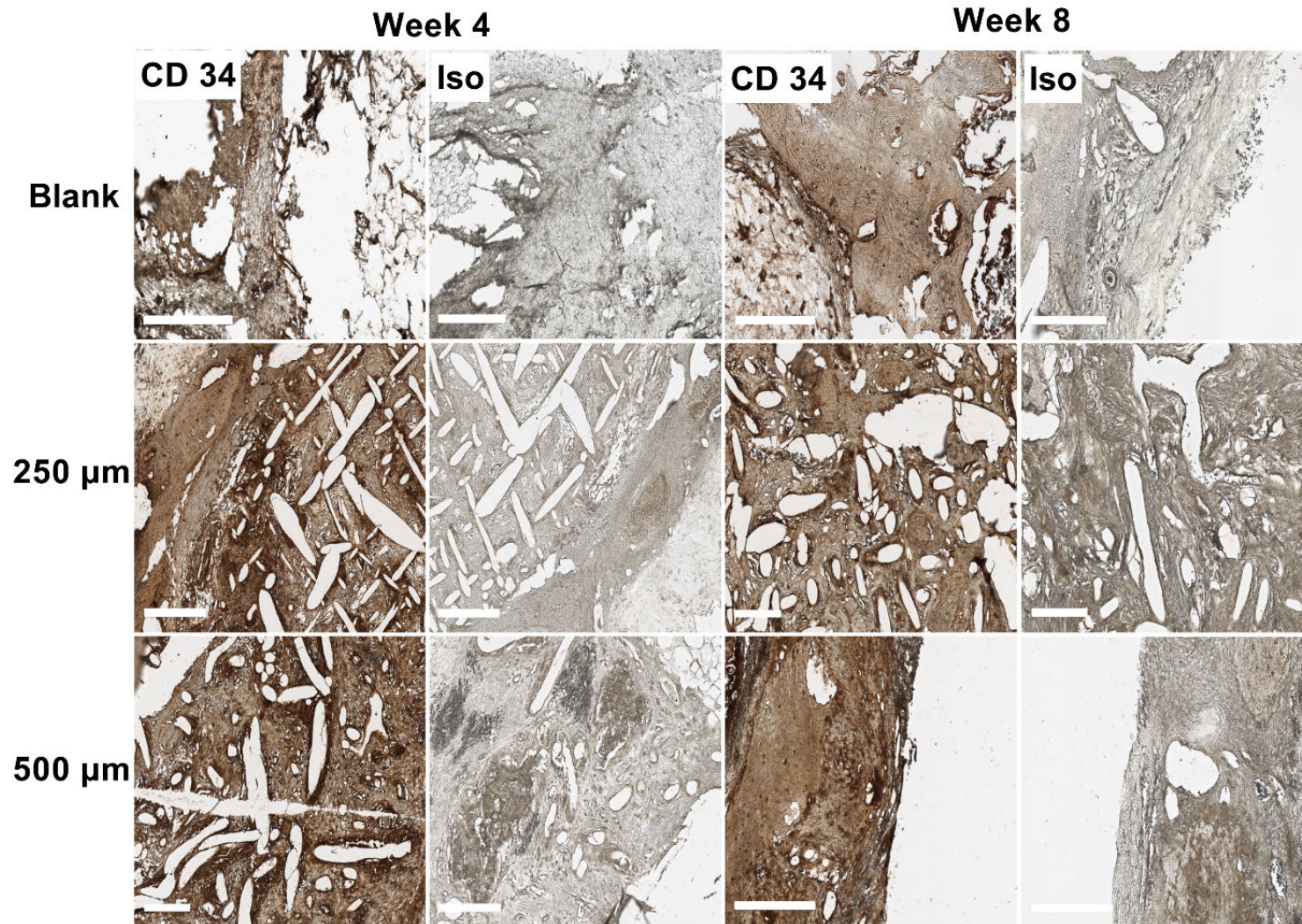


Figure 5.10. IHC analysis of Opn in calvarial defect of rat 4 and 8 weeks of post-implantation of the melt electrospun PCL scaffolds. (A) Blank (defect control without implanted scaffold), 250 μm , 500 μm . (B) Offset.50.50, Grad.750top, Grad.250top. Opn: Osteopontin staining, Iso: Isotype control; Scale bar = 200 μm .

CD34 Immunostaining

CD34 is a transmembrane glycoprotein which is expressed on early endothelial cells. Our results showed it was detected in all the positive groups compared to isotype control groups (Figure 5.11). The intensity of staining was almost the same in all the groups between 4 and 8 weeks after surgery. CD34 positive cells were more localized either around the pores in 250, 500 μm and both gradient scaffolds (Figure 5.11), or close to the primary host bone tissue and bone-soft tissue interface in 250 μm scaffolds after 4 weeks or in soft tissue surrounded the new bone or pores of 500 μm , offset.50.50 and the gradient scaffolds 8 weeks after implantation (Figure 5.11-A)

A



B

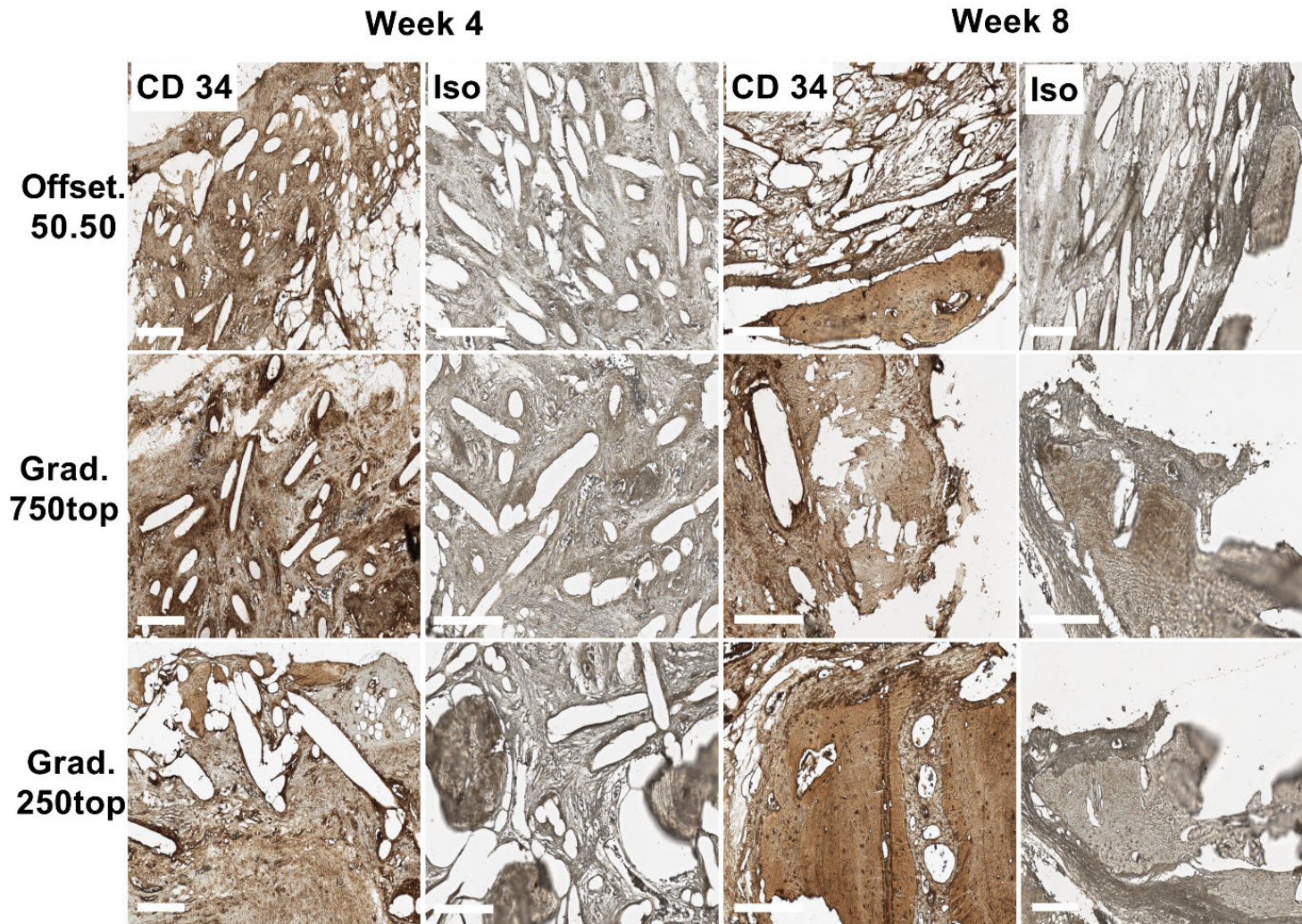
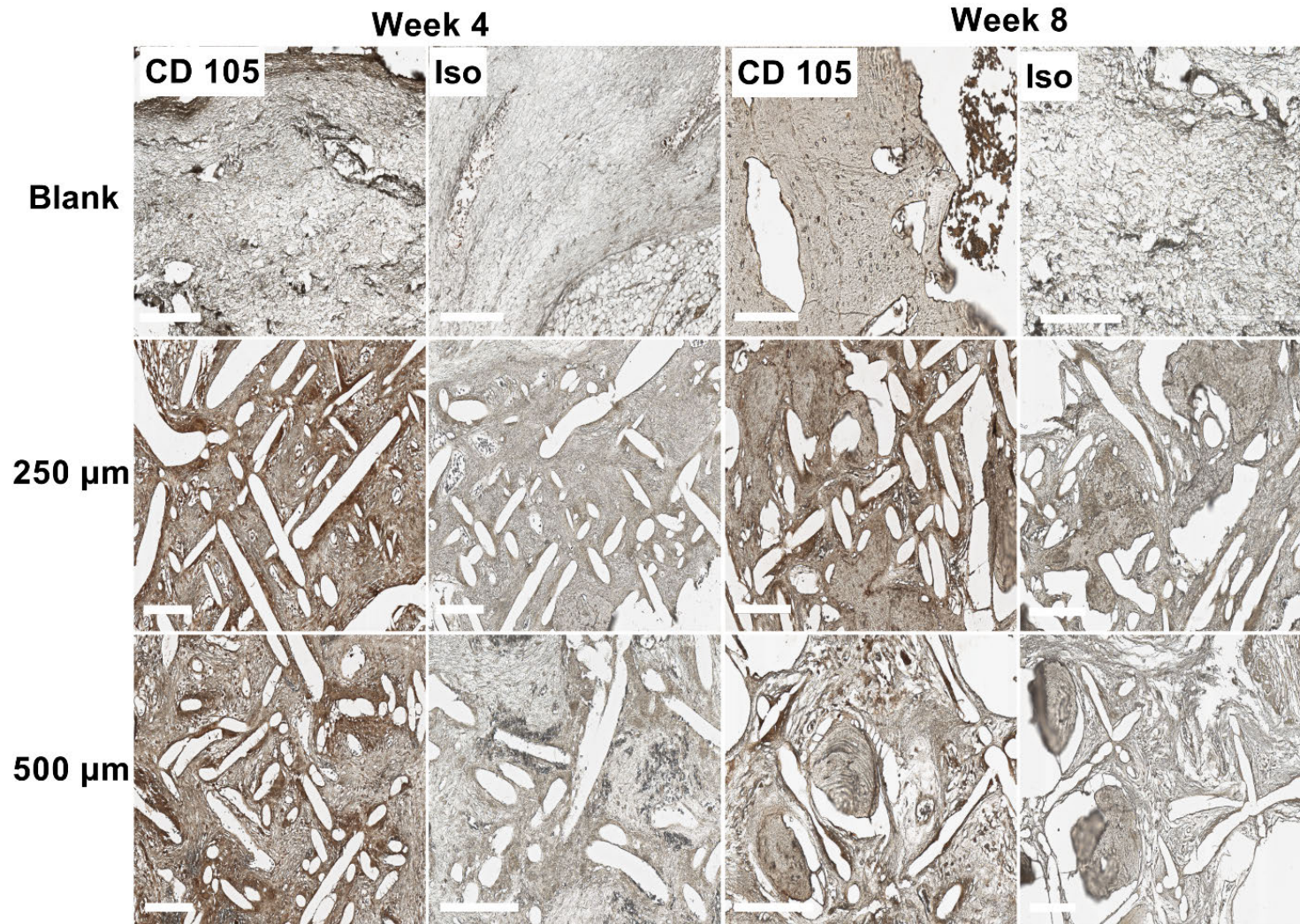


Figure 5.11. IHC analysis of CD34 in calvarial defect of rat 4 and 8 weeks of post-implantation of the melt electrospun PCL scaffolds. (A) Blank (defect control without implanted scaffold), 250 μm , 500 μm . (B) Offset.50.50, Grad.750top, Grad.250top. CD34: CD34 staining, Iso: Isotype control; Scale bar = 200 μm .

CD105 Immunostaining

CD 105 or Endoglin (ENG) is the type I membrane glycoprotein located on cells surfaces and will express in endothelial cells once neoangiogenesis begins. A similar tendency of CD105 expression as for CD34 expression above was observed regarding localization of the positive cells surrounding the scaffold pores. The difference for CD105 is the positive cells were accumulated more in the new compact bone regions in all the scaffold groups after 8 weeks instead of bone matrix tissue as seen for CD34 (Figure 5.12). In addition, strong staining was observed close to the pores in grad.250top scaffold after 4 weeks of treatment (Figure 5.12-B). In comparison to CD34, more intense staining of CD105 was detected for offset50.50 and both gradient scaffolds following 8 weeks of implantation (Figure 5.12-B).

A



B

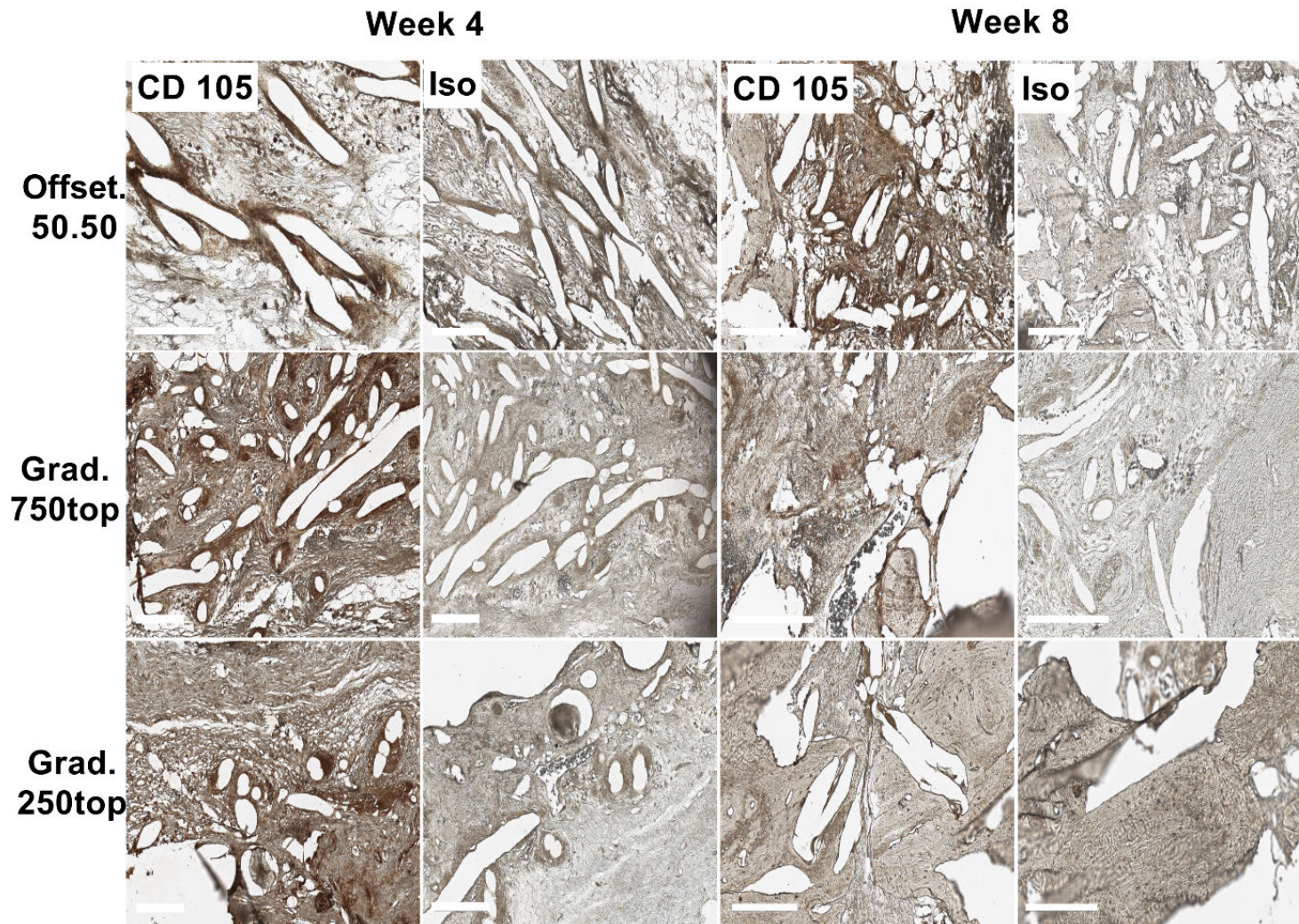
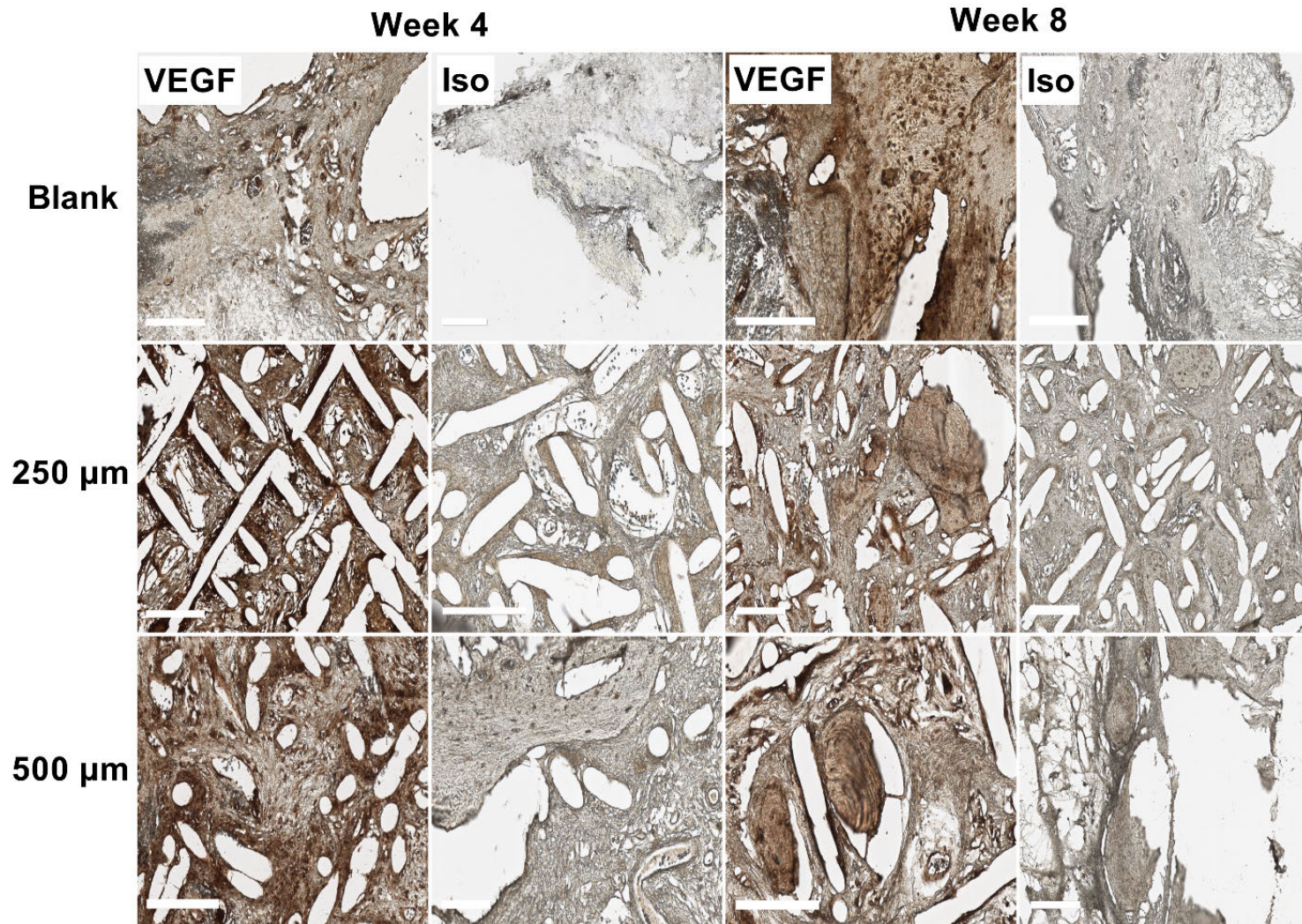


Figure 5.12. IHC analysis of endoglin (CD105) in calvarial defect of rat 4 and 8 weeks of post-implantation of the melt electrospun PCL scaffolds. (A) Blank (defect control without implanted scaffold), 250 μm , 500 μm . (B) Offset.50.50, Grad.750top, Grad.250top. CD105: CD105 staining, Iso: Isotype control; Scale bar = 200 μm .

Vascular Endothelial Growth Factor (VEGF) Immunostaining

The expression of VEGF in PCL implants showed that VEGF expression was intense compared to the negative control group except in blank defect (Figure 5.13). Intense staining was observed in grad.250top after 4 weeks compared to other scaffold groups (Figure 5.13-B). However, 8 weeks following implantation, strong staining was indicated for offset.50.50 which was localized around the pores and the bone matrix tissue (Figure 5.13-B), followed by 500 μm and grad.250top scaffolds that indicated newly formed bone tissue (Figure 5.13).

A



B

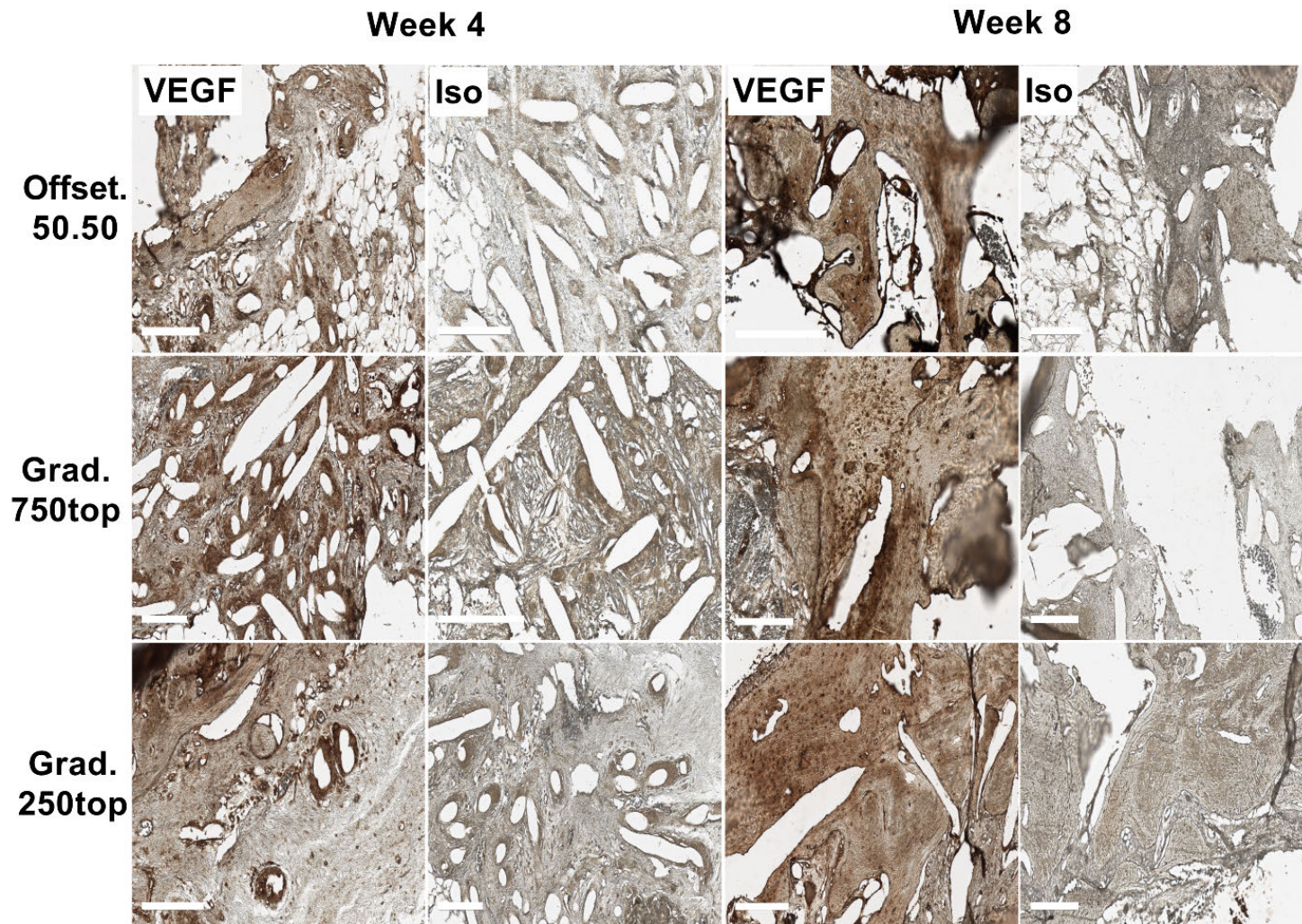
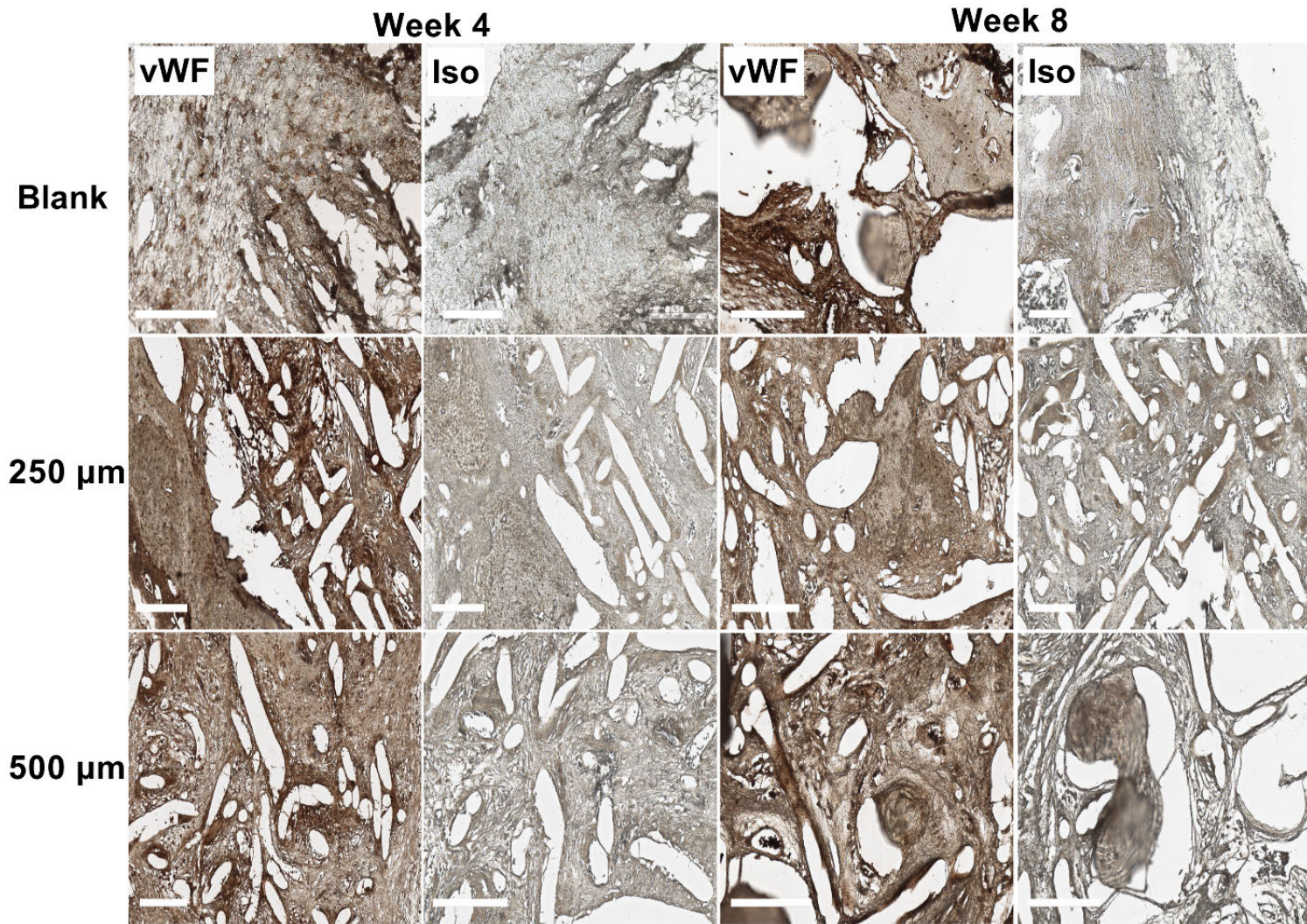


Figure 5.13. IHC analysis of VEGF, in calvarial defect of rat 4 and 8 weeks of post-implantation of the melt electrospun PCL scaffolds. (A) Blank (defect control without implanted scaffold), 250 μm , 500 μm . (B) Offset.50.50, Grad.750top, Grad.250top. VEGF: VEGF staining, Iso: Isotype control; Scale bar = 200 μm .

Von Willebrand Factor (vWf) Immunostaining

The IHC analysis for vWf demonstrated that all the positive groups had greater immunoreactivity for vWf compared to VEGF protein (Figure 5.14). IHC images confirmed the homogeneous presence of vWF in all the groups at both time points (4 and 8 weeks post-implantation, Figure 14). vWF IHC showed the new distinct vessels with encapsulated cells in the 500 μm scaffold 8 weeks following treatment (Figure 5.14-A).

A



B

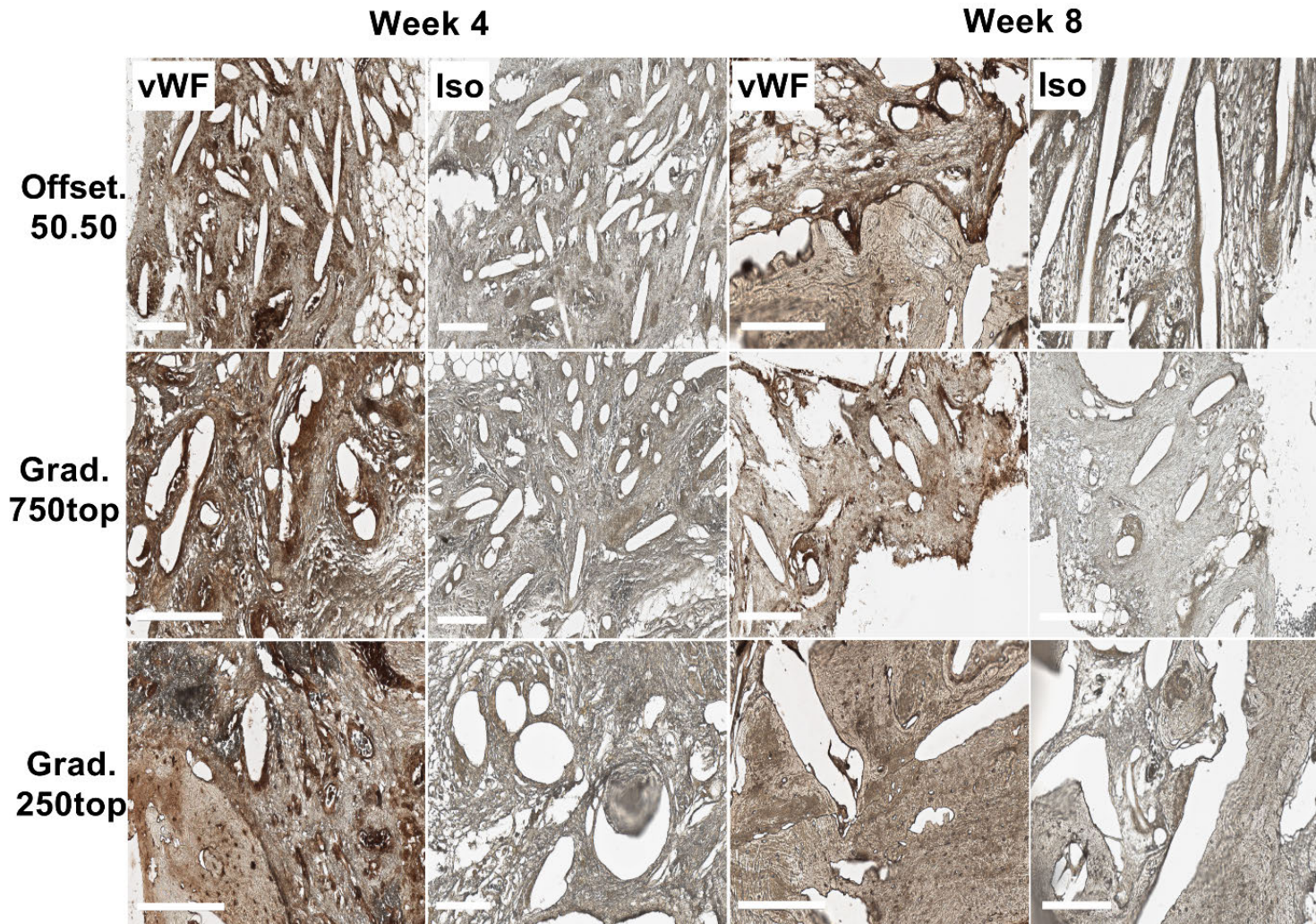


Figure 5.14. IHC analysis of vWF in calvarial defect of rat 4 and 8 weeks of post-implantation of the melt electrospun PCL scaffolds. (A) Blank (defect control without implanted scaffold), 250 μm , 500 μm . (B) Offset.50.50, Grad.750top, Grad.250top. vWF: vWF staining, Iso: Isotype control; Scale bar = 200 μm .

DISCUSSION

Bone as a supportive and protective organ, consists of 20% high-porosity cancellous bone and 80% high-stiffness compact bone with 10% porosity (20). The overall aim of this study was to investigate *in vivo*, an appropriate design structure of porous MEW scaffolds that could stimulate osteogenesis.

The response of bone to implanted scaffolds and its integration are influenced by the scaffold surface composition (21). Indeed studies have shown some bone regeneration could be obtained in the absence of seeded cells (22). In this study, CaP coated scaffolds in the form of HAP were implanted *in vivo* to regenerate bone defects. This followed from previous *in vitro* studies which demonstrated that the incorporation of HAP particles into the scaffolds improved their mechanical properties and had a beneficial effect on cell-mediated mineralization and bone formation (23, 24). In addition, materials without bioactive surfaces have been shown to lead to longer recovery time for bone repair due to a lack of recognition sites for bone-bonding ability in non-coated surface scaffolds (25). Li et al. also demonstrated scaffolds with more roughness on the surface enhanced the surface area of the scaffolds which facilitated bone formation (26).

A balance between architecture and mechanical properties of the scaffolds is essential for effective bone regeneration. Scaffolds need to maintain sufficient porosity to allow vascularization, cell penetration and surrounding tissue ingrowth, as well as have adequate mechanical strength similar to that of natural bone, to prevent premature failure of the implants (27, 28). One of the most promising methods to control scaffold pore size

and the level of porosity is MEW (10). Although open-cell pores might be more applicable to promote osteogenesis due to better access of oxygen and new bone development into the porosities as well as better vascularization through the channels created by pores connections (29), the type of pores obtaining by MEW technique are the closed-cells pores without interconnectivity with each other and enclosed by the pore walls (30).

In this study we applied standard trephine surgery, not the surgical elevator that might keep the dura intact from damaging. A 5mm calvarial defect was used in our study to evaluate new bone formation. Although some studies have suggested a > 6mm defect to be 'critical-sized' i.e. defects smaller than this size can regenerate spontaneously, previous studies by our group have shown 5mm to be critical (31). Moreover a number of studies have chosen a 5 mm defect as a standard bilateral skull defect in the rat to minimize the animal numbers used and meet the 3R criteria (Reduction, Replacement, Refinement) (20, 32). Also, a defect of the cranium is a commonly used model to evaluate bone reconstruction due to the absent blood supply, lack of muscle tissue and poor bone repair (20). Bone healing is influenced not only by the defect size, but also depends on the age and strain of the patient and vascularization. In addition, surgical techniques that might destroy the dura mater which is a source of osteoinductive factors and the osteogenic cells is another factor which influence the process of bone reconstruction (32). Our results on bone regeneration in the control group was similar to the study of Cooper et al. that showed incomplete healing for 2.3 mm bone defects in Sprague-Dawley rats 6 weeks following operation. Also, they demonstrated that the treatment did not improve bone healing after 8 weeks as the defects were filled by soft fibrous tissue suggesting the critical period of restoring bone in this defect is between 4 and 8 weeks in rodents (33). This is in agreement to our H&E staining observations which also showed the soft tissue

in the defect of the control groups (without scaffold) after 4 weeks with a few new bone areas 8 weeks following surgery.

The bone defect was obvious in blank control groups after 4 weeks. This was similar to the study of Ruan et al. that the bone recovery was limited in repair of bone defects in rabbits (34). However, the bone regeneration *increased* following 8 weeks of implantation, there was no bridges of bone to create the unified bone joint to be recognized by passing the time. This was in accordance to the study of Liu et al. that implanted composite of adipose-derived stem cells (ADSCs) seeded with heterogeneous deproteinized bone (HDB) to repair the bone defects and lead to nonunion bone healing following 8 weeks post-surgery (35).

Previous studies reported that the optimum scaffold pore size for hard tissue regeneration is between 200 – 500 μm (36). Some proposed a pore size in the range of 75 – 250 μm (37) or the range from 100 – 500 μm for bone ingrowth (38, 39). Our results indicated that a pore size of 500 μm showed the highest amount of newly formed bone compared to 250 μm scaffolds. Among the other structures, the heterogeneous grad.250top showed significantly greater new bone formation. However, it has been suggested that an increase in the pore size from 500 μm to a millimeter promoted a loss of mechanical strength of the scaffold, although inducing larger amounts of bone formation due to the flow transport of oxygen and nutrients in the larger pore size (40).

Although, the weak mechanical properties of the larger pore sizes of 500 and 750 μm scaffolds were similar to our previous findings and might not be suitable in terms of mimicking the mechanical strength of bone tissue, the tensile properties of the gradient porous scaffolds including both small and large pore sizes (250, 500 and 750 μm) increased. The smaller pore of 250 μm in the gradient architecture could compensate for the poor mechanical properties of the larger pore sizes of 500 and 750 μm (10). Also, in our current study we realized that a gradient porosity promoted the highest bone volume

compared to other structures. This was in accordance to the study of Wang et al. who implanted a porosity-graded calcium polyphosphate (PGCPP) scaffold and showed higher osteoblast colonization in the macropores in contrast to the micropores of the gradient scaffold (41).

In the micro-CT and histologic evaluations, more bone growth and penetration into the pores was attributed to the higher permeability of the gradient and 500 μm scaffolds which is able to increase the delivery of nutrients and O_2 as well as removing waste products from the larger pores of the construct (42). But the offset and 250 μm scaffolds with narrower pore sizes were more prone to blockage with soft tissue as the limitation of oxygen and nutrients diffusion that leading to inhibition of bone cell migration and bone growth (43). In grad.250top scaffolds that has the smaller pore size (250 μm) on the outside region of scaffold, i.e. near the scalp and the larger pores (750 μm) on inside towards the dura mater, more pronounced newly formed bone was observed in contrast to the grad.750top where the direction of the gradient pores are reversed. This was probably associated with the dura mater which can provide further blood supply and nutrients into the larger pore (750 μm) of grad.250top scaffolds. However, in the bottom regions of grad.750top scaffold which contains small pores of 250 μm , few neo-bone formations were founded due to insufficient blood and nutrient circulation in the narrow pores of the scaffold which is adjacent to the dura mater (44).

The expression of major markers of bone differentiation i.e. OPN, COL-I and OCN are linked with the maturation of osteoblasts and bone development (45). The degree of OCN expression was significantly more in grad.250top scaffolds which promoted more bone formation and mineralization in this scaffold structure. This is consistent with previous studies which reported more mineral accumulation to recover bone defect through OCN expression (46). Similar results were found by Tera et al. who observed intense staining of OCN on the newly formed bone 45-60 days after polytetrafluoroethylene (PTFE)

membrane implantation in the mandible of rats (47). The intense staining of OPN in all scaffolds after 8 weeks showed that normal mineralization of new bone was regulated by OPN as has been previously demonstrated.

Bone remodeling increases the activity of mature osteoclastic resorption via the modulation of Ca^{2+} and Mg^{2+} ion homeostasis releasing high levels of collagen into the mineralized matrix bone (48). This is in accordance with our findings where intense staining of Collagen was seen in all the scaffolds 8 weeks post-implantation. Two studies have stated the expression of Collagen Type I was enhanced in bone ECM mineralization which is a valuable biomarker of bone remodeling/ mineralization starting approximately two weeks after implantation, only after the morphology transition of new bone to the native tissue occurred (49, 50).

Rapid new bone formation is influenced by the mutual promotion of osteogenesis and angiogenesis (51). Additionally, other findings demonstrated that endothelial cells might stimulate osteogenesis via raising the level of BMP-2 (52). The present data also showed a high level of BMP-2 expression 8 weeks following implantation which promoted bone formation particularly in the 500 μm scaffold. Furthermore, the high level of Alp expression as well as BMP-2 was observed for this group after 8 weeks. This finding was similar to the study of Nguyen et al. who reported Alp activity was influenced by BMP-2 release (53).

The interactions between endothelial cells and the osteoblasts that promote bone healing also leads to vascular growth initiated through VEGF (54). VEGF is a common angiogenic growth factor that induces the development of tubular structures through the growth, proliferation and migration of endothelial cells (55). VEGF is involved in the entire bone healing process, from hematoma formed at a bone crack to the bone remodeling phase. The synergistic role of VEGF and BMP has been illustrated in bone healing and vascularization (56). Our immunostaining results also detected up-regulation

of VEGF and intense staining of Bmp-2 in all the scaffolds 4 and 8 weeks following implantation. The highest staining of VEGF was observed in offset.50.50 scaffolds after 8 weeks compared to other groups. This might be related to hypoxic conditions in the smaller pores of these two scaffold structures and the expression of hypoxia inducible factor-1 α (HIF-1 α) which activates in anaerobic situations to promote the upregulation of VEGF as a proangiogenic factor expanding blood vessel ingrowth and consequently increased oxygen tension in these structures that resulted in limited bone formation (57). This agrees with the study of Wu et al. that demonstrated the stimulation of angiogenesis in hypoxia-mimicking mesoporous bioactive glass (MBG) scaffolds with osteogenic properties (58). The intense staining of VEGF in 500 μ m and gradient scaffolds was lower than offset.50.50 scaffolds due to adequate large pore size in these constructs enabling sufficient oxygen, facilitating capillary sprouting and revascularization in the defect site, and successfully promoting the union of bone formation in these implanted scaffolds. As OCN is involved exclusively in bone mineralization, the protein expression of VEGF and OCN in the grad.250top scaffolds showed the highest degree of osteogenesis and angiogenesis.

The upregulation of CD34 in all the scaffold groups at 4 weeks was an indication of primitive endothelial tube formation and early angiogenic differentiation in all the structures (59) that promotes bone formation. The study of Hertweck et al. also demonstrated that the positive CD34 cells enhanced the bone volume in a co-culture system with human osteoblast cells (60). In comparison to the other protein markers, the low level of CD105 expression (a mesenchymal stem cell marker) in our scaffold groups corresponded to previous reports (61, 62). However, the higher expression of CD105 in offset.50.50 and 250 μ m scaffolds could be linked with the inhibition of osteogenesis (63). Although recent studies reported endoglin (CD 105) lead to mature and stable vessel formation by adhesion between mesenchymal stem cells (MSCs) and endothelial colony

forming cells (ECFCs) which enhances neovascularization (64-66). The presence of vWF confirmed angiogenesis in all treatment groups. These results showed strong expression of vWF in the larger pore size of 500 μm scaffolds had great potential of bone formation which was promoted by increasing vascular functions and blood vessel formation. This was in agreement with other works that observed more and faster osteogenesis, angiogenesis and uniform new formed bone distribution in larger pore sizes than those with the smaller pores (67). The grad.250top scaffold also exhibited more new bone tissue growth throughout the scaffold. This may be due to the bigger pores providing more tissue ingrowth and blood vessels that result in increased speed of new bone regeneration through the nutrient and oxygen flow improvement (68) in comparison to smaller pore sizes.

CONCLUSION

The aim of this study was to assess *in vivo*, the capacity of MEW fabricated scaffolds with similar structure to native bone tissue in terms of porosity and porous structure, to facilitate the production of new osseous tissue. In this study, we successfully implanted the porous MEW PCL scaffolds into a rat calvarial defect and evaluated the effect of gradient architecture on bone formation. Although the expression of angiogenesis and osteogenesis markers contributed to bone repair in all the scaffold groups, the constructs with a larger pore size such as 500 μm and the gradient structures, showed faster repair of critically-sized bone defects with newly formed bone coverage. However, the gradient porous architecture (grad.250top) with the larger pore size exposed to the dura mater resulted in significant enhancement of bone regeneration compare to other pore size scaffolds i.e. 500 μm and grad.750top. In summary, the MEW PCL scaffold with porosity gradient appears to be a suitable candidate to enhance the bone regeneration.

Acknowledgments

Naghmeh Abbasi was sponsored by a scholarship from Griffith University, Australia. This study is part of her PhD research project being carried out at Griffith University. The authors would like to express their gratitude to Institute of Health and Biomedical Innovation (IHBI) of QUT, Australia, for providing some facilities and technical support for this study. We want to acknowledge and thank Stephen Hamlet for general supervision of this research along with Chris Philippa and Eugen Petco for their technical support.

References

1. Tao O, Kort-Mascort J, Lin Y, Pham HM, Charbonneau AM, ElKashty OA, et al. The Applications of 3D Printing for Craniofacial Tissue Engineering. *Micromachines-Basel*. 2019;10(7).
2. Rohman G, Languet C, Ramtani S, Lataillade JJ, Lutomski D, Senni K, et al. The Use of Platelet-Rich Plasma to Promote Cell Recruitment into Low-Molecular-Weight Fucoidan-Functionalized Poly(Ester-Urea-Urethane) Scaffolds for Soft-Tissue Engineering. *Polymers-Basel*. 2019;11(6).
3. Barati D, Karaman O, Moeinzadeh S, Kader S, Jabbari E. Material and regenerative properties of an osteon-mimetic cortical bone-like scaffold. *Regen Biomater*. 2019;6(2):89-98.
4. Chocholata P, Kulda V, Babuska V. Fabrication of Scaffolds for Bone-Tissue Regeneration. *Materials*. 2019;12(4).
5. Woodruff MA, Hutmacher DW. The return of a forgotten polymer-Polycaprolactone in the 21st century. *Prog Polym Sci*. 2010;35(10):1217-56.
6. Eftekhari H, Jahandideh A, Asghari A, Akbarzadeh A, Hesarakhi S. Histopathological evaluation of polycaprolactone nanocomposite compared with tricalcium phosphate in bone healing. *J Vet Res*. 2018;62(3):385-94.
7. Qu FN, Guilak F, Mauck RL. Cell migration: implications for repair and regeneration in joint disease. *Nat Rev Rheumatol*. 2019;15(3):167-79.
8. Vasireddi R, Basu B. Conceptual design of three-dimensional scaffolds of powder-based materials for bone tissue engineering applications. *Rapid Prototyping J*. 2015;21(6):716-24.
9. Sobral JM, Caridade SG, Sousa RA, Mano JF, Reis RL. Three-dimensional plotted scaffolds with controlled pore size gradients: Effect of scaffold geometry on mechanical performance and cell seeding efficiency. *Acta Biomater*. 2011;7(3):1009-18.

10. Abbasi N, Abdal-hay A, Hamlet S, Graham E, Ivanovski S. Effects of Gradient and Offset Architectures on the Mechanical and Biological Properties of 3-D Melt Electrowritten (MEW) Scaffolds. *Acs Biomater Sci Eng*. 2019;5(7):3448-61.
11. Yeo M, Simon CG, Kim G. Effects of offset values of solid freeform fabricated PCL-beta-TCP scaffolds on mechanical properties and cellular activities in bone tissue regeneration. *J Mater Chem*. 2012;22(40):21636-46.
12. Serra T, Planell JA, Navarro M. High-resolution PLA-based composite scaffolds via 3-D printing technology. *Acta Biomater*. 2013;9(3):5521-30.
13. Di Luca A, Ostrowska B, Lorenzo-Moldero I, Lepedda A, Swieszkowski W, Van Blitterswijk C, et al. Gradients in pore size enhance the osteogenic differentiation of human mesenchymal stromal cells in three-dimensional scaffolds. *Sci Rep-Uk*. 2016;6.
14. Oh SH, Park IK, Kim JM, Lee JH. In vitro and in vivo characteristics of PCL scaffolds with pore size gradient fabricated by a centrifugation method. *Biomaterials*. 2007;28(9):1664-71.
15. Muerza-Cascante ML, Haylock D, Hutmacher DW, Dalton PD. Melt Electrospinning and Its Technologization in Tissue Engineering. *Tissue Eng Part B-Re*. 2015;21(2):187-202.
16. Guimaraes A, Martins A, Pinho ED, Faria S, Reis RL, Neves NM. Solving cell infiltration limitations of electrospun nanofiber meshes for tissue engineering applications. *Nanomedicine-Uk*. 2010;5(4):539-54.
17. Ameer JM, Pr AK, Kasoju N. Strategies to Tune Electrospun Scaffold Porosity for Effective Cell Response in Tissue Engineering. *J Funct Biomater*. 2019;10(3).
18. Dikici BA, Dikici S, Reilly GC, MacNeil S, Claeysens F. A Novel Bilayer Polycaprolactone Membrane for Guided Bone Regeneration: Combining Electrospinning and Emulsion Templating. *Materials*. 2019;12(16).

19. Robinson TM, Hutmacher DW, Dalton PD. The Next Frontier in Melt Electrospinning: Taming the Jet. *Adv Funct Mater.* 2019.
20. Liu MY, Lv YG. Reconstructing Bone with Natural Bone Graft: A Review of In Vivo Studies in Bone Defect Animal Model. *Nanomaterials-Basel.* 2018;8(12).
21. Ghassemi T, Shahroodi A, Ebrahimzadeh MH, Mousavian A, Movaffagh J, Moradi A. Current Concepts in Scaffolding for Bone Tissue Engineering. *Arch Bone Jt Surg-Ab.* 2018;6(2):90-9.
22. Xue ZZ, Sheng TL, Wang YL, Hu SM, Wen YH, Wang Y, et al. A series of d(10) coordination polymers constructed with a rigid tripodal imidazole ligand and varied polycarboxylates: syntheses, structures and luminescence properties. *Crystengcomm.* 2015;17(9):2004-12.
23. Ryan AJ, Gleeson JP, Matsiko A, Thompson EM, O'Brien FJ. Effect of different hydroxyapatite incorporation methods on the structural and biological properties of porous collagen scaffolds for bone repair. *J Anat.* 2015;227(6):732-45.
24. Jeong J, Kim JH, Shim JH, Hwang NS, Heo CY. Bioactive calcium phosphate materials and applications in bone regeneration. *Biomater Res.* 2019;23:4.
25. Przekora A. Current Trends in Fabrication of Biomaterials for Bone and Cartilage Regeneration: Materials Modifications and Biophysical Stimulations. *Int J Mol Sci.* 2019;20(2).
26. Li XW, Zhang R, Tang XX, Li B, Liu Y, Wang XK. Synthesis and Evaluation of BMMSC-seeded BMP-6/nHAG/GMS Scaffolds for Bone Regeneration. *Int J Med Sci.* 2019;16(7):1007-17.
27. Castro APG, Pires T, Santos JE, Gouveia BP, Fernandes PR. Permeability versus Design in TPMS Scaffolds. *Materials.* 2019;12(8).
28. Egan PF. Integrated Design Approaches for 3D Printed Tissue Scaffolds: Review and Outlook. *Materials.* 2019;12(15).

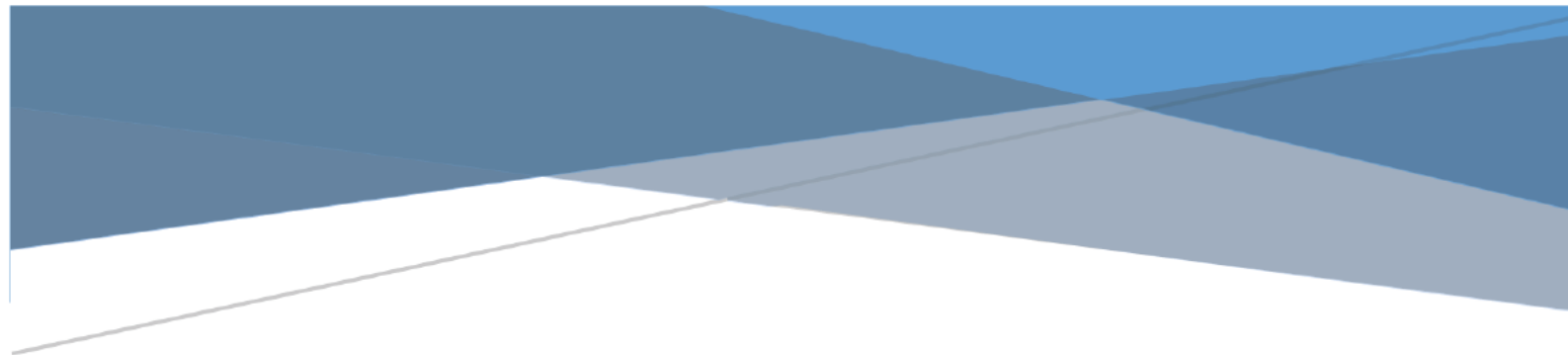
29. Liew AWL, Zhang YL. In vitro pre-vascularization strategies for tissue engineered constructs-Bioprinting and others. *Int J Bioprinting*. 2017;3(1):3-17.
30. Hrynevich A, Elci BS, Haigh JN, McMaster R, Youssef A, Blum C, et al. Dimension-Based Design of Melt Electrowritten Scaffolds. *Small*. 2018;14(22).
31. Lee RSB, Hamlet SM, Ivanovski S. The influence of titanium surface characteristics on macrophage phenotype polarization during osseous healing in type I diabetic rats: a pilot study. *Clin Oral Implan Res*. 2017;28(10):E159-E68.
32. Fragogeorgi EA, Rouchota M, Georgiou M, Velez M, Bouziotis P, Loudos G. In vivo imaging techniques for bone tissue engineering. *J Tissue Eng*. 2019;10.
33. Cooper GM, Mooney MP, Gosain AK, Campbell PG, Losee JE, Huard J. Testing the Critical Size in Calvarial Bone Defects: Revisiting the Concept of a Critical-Size Defect. *Plast Reconstr Surg*. 2010;125(6):1685-92.
34. Ruan SQ, Deng J, Yan L, Huang WL. Composite scaffolds loaded with bone mesenchymal stem cells promote the repair of radial bone defects in rabbit model. *Biomed Pharmacother*. 2018;97:600-6.
35. Liu J, Zhou P, Long Y, Huang CX, Chen DN. Repair of bone defects in rat radii with a composite of allogeneic adipose-derived stem cells and heterogeneous deproteinized bone. *Stem Cell Research & Therapy*. 2018;9.
36. Bahrami N, Bayat M, Ai A, Khanmohammadi M, Ai J, Ahmadi A, et al. Differentiation of Periodontal Ligament Stem Cells Into Osteoblasts on Hybrid Alginate/Polyvinyl Alcohol/Hydroxyapatite Nanofibrous Scaffolds. *Arch Neurosci*. 2018;5(4).
37. Pilliar RM. Porous-surfaced metallic implants for orthopedic applications. *J Biomed Mater Res*. 1987;21(A1 Suppl):1-33.
38. Bucholz RW. Nonallograft osteoconductive bone graft substitutes. *Clin Orthop Relat R*. 2002(395):44-52.

39. Laptev A, Bram M, Buchkremer HP, Stover D. Study of production route for titanium parts combining very high porosity and complex shape. *Powder Metall.* 2004;47(1):85-92.
40. Lu X, Wang YJ, Jin FC. Influence of a non-biodegradable porous structure on bone repair. *Rsc Adv.* 2016;6(84):80522-8.
41. Wang QB, Wang QG, Wan CX. Preparation and evaluation of a biomimetic scaffold with porosity gradients in vitro. *An Acad Bras Cienc.* 2012;84(1):9-16.
42. O'Brien FJ, Harley BA, Waller MA, Yannas IV, Gibson LJ, Prendergast PJ. The effect of pore size on permeability and cell attachment in collagen scaffolds for tissue engineering. *Technol Health Care.* 2007;15(1):3-17.
43. Wang S, Liu LL, Li K, Zhu LC, Chen J, Hao YQ. Pore functionally graded Ti6Al4V scaffolds for bone tissue engineering application. *Mater Design.* 2019;168.
44. Kwon DY, Kwon JS, Park SH, Park JH, Jang SH, Yin XY, et al. A computer-designed scaffold for bone regeneration within cranial defect using human dental pulp stem cells. *Sci Rep-Uk.* 2015;5.
45. Wu L, Zhao X, He B, Jiang J, Xie XJ, Liu L. The Possible Roles of Biological Bone Constructed with Peripheral Blood Derived EPCs and BMSCs in Osteogenesis and Angiogenesis. *Biomed Res Int.* 2016.
46. Shi JJ, Sun J, Zhang W, Liang H, Shi Q, Li XR, et al. Demineralized Bone Matrix Scaffolds Modified by CBD-SDF-1 alpha Promote Bone Regeneration via Recruiting Endogenous Stem Cells. *Acs Appl Mater Inter.* 2016;8(41):27511-22.
47. Tera TD, Nascimento RD, do Prado RF, Santamaria MP, Jardini MAN. Immunolocalization of markers for bone formation during guided bone regeneration in osteopenic rats. *J Appl Oral Sci.* 2014;22(6):541-53.
48. Singh A, Gill G, Kaur H, Amhmed M, Jakhu H. Role of osteopontin in bone remodeling and orthodontic tooth movement: a review. *Prog Orthod.* 2018;19.

49. Albeshri S, Alblaiheh A, Niazy AA, Ramalingam S, Sundar C, Alghamdi HS. Biomarkers as Independent Predictors of Bone Regeneration around Biomaterials: A Systematic Review of Literature. *J Contemp Dent Pract*. 2018;19(5):605-18.
50. Osugi M, Katagiri W, Yoshimi R, Inukai T, Kawai T, Hibi H, et al. Conditioned media from bone marrow derived mesenchymal stem cells and adipose derived stem cells enhanced bone regeneration in rat calvarial bone defects. *J Tissue Eng Regen M*. 2012;6:283-.
51. Li LM, Li JD, Zou Q, Zuo Y, Cai B, Li YB. Enhanced bone tissue regeneration of a biomimetic cellular scaffold with co-cultured MSCs-derived osteogenic and angiogenic cells. *Cell Proliferat*. 2019.
52. He XN, Dziak R, Yuan X, Mao KY, Genco R, Swihart M, et al. BMP2 Genetically Engineered MSCs and EPCs Promote Vascularized Bone Regeneration in Rat Critical-Sized Calvarial Bone Defects. *Plos One*. 2013;8(4).
53. Nguyen LH, Annabi N, Nikkhah M, Bae H, Binan L, Park S, et al. Vascularized Bone Tissue Engineering: Approaches for Potential Improvement. *Tissue Eng Part B-Re*. 2012;18(5):363-82.
54. Raines AL, Berger MB, Patel N, Hyzy SL, Boyan BD, Schwartz Z. VEGF-A regulates angiogenesis during osseointegration of Ti implants via paracrine/autocrine regulation of osteoblast response to hierarchical microstructure of the surface. *J Biomed Mater Res A*. 2019;107(2):423-33.
55. Ballmer-Hofer K. Vascular Endothelial Growth Factor, from Basic Research to Clinical Applications. *Int J Mol Sci*. 2018;19(12).
56. Bao XG, Shi MC, Hou CL, Xu GH. Recent Progress in the Construction of Functional Artificial Bone by Cytokine-Controlled Strategies. *Chinese Med J-Peking*. 2018;131(21):2599-604.

57. Beamer B, Hettrich C, Lane J. Vascular endothelial growth factor: an essential component of angiogenesis and fracture healing. *HSS J.* 2010;6(1):85-94.
58. Wu CT, Zhou YH, Fan W, Han PP, Chang J, Yuen J, et al. Hypoxia-mimicking mesoporous bioactive glass scaffolds with controllable cobalt ion release for bone tissue engineering. *Biomaterials.* 2012;33(7):2076-85.
59. El-Gendy R, Kirkham J, Newby PJ, Mohanram Y, Boccaccini AR, Yang XBB. Investigating the Vascularization of Tissue-Engineered Bone Constructs Using Dental Pulp Cells and 45S5 Bioglass (R) Scaffolds. *Tissue Eng Pt A.* 2015;21(13-14):2034-43.
60. Hertweck J, Ritz U, Gotz H, Schottel PC, Rommens PM, Hofmann A. CD34(+) cells seeded in collagen scaffolds promote bone formation in a mouse calvarial defect model. *J Biomed Mater Res B.* 2018;106(4):1505-16.
61. Rocha MAC, Silva LMC, Oliveira WA, Bezerra DO, Silva GCD, Silva LDS, et al. Allogeneic mesenchymal stem cells and xenogenic platelet rich plasma, associated or not, in the repair of bone failures in rabbits with secondary osteoporosis. *Acta Cir Bras.* 2017;32(9):767-80.
62. Noda S, Kawashima N, Yamamoto M, Hashimoto K, Nara K, Sekiya I, et al. Effect of cell culture density on dental pulp-derived mesenchymal stem cells with reference to osteogenic differentiation. *Sci Rep-Uk.* 2019;9.
63. Yang YJ, Wang XL, Wang YT, Hu XH, Kawazoe N, Yang YN, et al. Influence of Cell Spreading Area on the Osteogenic Commitment and Phenotype Maintenance of Mesenchymal Stem Cells. *Sci Rep-Uk.* 2019;9.
64. Rossi E, Bernabeu C, Smadja DM. Endoglin as an Adhesion Molecule in Mature and Progenitor Endothelial Cells: A Function Beyond TGF-beta. *Front Med-Lausanne.* 2019;6.

65. Rossi E, Smadja DM, Boscolo E, Langa C, Arevalo MA, Pericacho M, et al. Endoglin regulates mural cell adhesion in the circulatory system. *Cell Mol Life Sci.* 2016;73(8):1715-39.
66. Rossi E, Smadja D, Goyard C, Cras A, Dizier B, Bacha N, et al. Co-injection of mesenchymal stem cells with endothelial progenitor cells accelerates muscle recovery in hind limb ischemia through an endoglin-dependent mechanism. *Thromb Haemost.* 2017;117(10):1908-18.
67. Li JY, Zhi W, Xu TT, Shi F, Duan K, Wang JX, et al. Ectopic osteogenesis and angiogenesis regulated by porous architecture of hydroxyapatite scaffolds with similar interconnecting structure in vivo. *Regen Biomater.* 2016;3(5):285-97.
68. Wang MO, Vorwald CE, Dreher ML, Mott EJ, Cheng MH, Cinar A, et al. Evaluating 3D-Printed Biomaterials as Scaffolds for Vascularized Bone Tissue Engineering. *Adv Mater.* 2015;27(1):138-44.



CHAPTER 6

DISCUSSION AND FUTURE DIRECTIONS

The ultimate goals of reconstructive medicine are to regenerate the original architecture of a defect and to also facilitate the return of tissue's natural function. The repair of craniofacial bone defects caused by congenital disease, trauma or tumour resection often involves consolidation of multiple tissue types including bone, cartilage, neural and soft tissues, and blood vessels (1). Currently, the clinical application of bone autografts and allografts represents the 'gold standard' for the treatment of bone defects (2). However, there are many drawbacks to these treatment options including donor site morbidity, large size of the skeletal defect, limited availability of donor tissue and costly surgical methods and materials required. All of these create significant challenges to the restoration of craniofacial bone (3, 4).

Among the various approaches for the reconstruction of craniofacial bone, tissue engineering strategies using biomaterial scaffolds are potential alternatives to current treatment strategies (5). However, despite the contribution of material science technology to improvements in the field of bone regeneration, no single scaffold material fulfils all of the requirements for an effective bone substitute. Dealing with large bone defects or injuries still represents a major clinical challenge.

Different bioresorbable and biodegradable polymer scaffolds are used for bone engineering. Organic or natural polymer materials are derived from polysaccharides (cellulose, chitosan, alginate and hyaluronate) and proteins (gelatine, collagen and albumin). These have some limitations such as the need for special processing for preparation, high cost, rapid degradation, low mechanical stability and insufficient bone formation (6). The fundamental target in bone development is to imitate the mechanical and structural characteristics of the cancellous bone (7). The main advantages of synthetic polymer materials such as polyesters including polyvinyl alcohol (PVA), polylactic acid (PLA), PCL, polyethylene oxide (PEO) and polyglycolic acid (PGA) are their cost-effectiveness, appropriate mechanical integrity and great spinnability. These

characteristics are essential for 3D printing using the rapid prototyping technique, the newest approach in tissue engineering, which imposes some restrictions on the materials selected for the process of manufacturing (8, 9).

The maxilla and mandible jaw bones must have sufficient integrity to withstand the significant strain and stresses caused by jaw mastication-related muscle movements. One key concern about tissue-engineered applications is whether the biomaterial scaffold to be used has the appropriate stiffness for subsequent dense tissue regeneration (10). PCL is often used as a bone scaffold because of its high mechanical stability and sufficient compressive strength (11). Its low degradation rate and osteoconductive properties make it suitable for use as the polymeric composite in bone repair. (12) The surface bioactivity of naturally hydrophobic PCL can be improved by coating with CaP to enhance the bioactivity of the PCL scaffold (13).

In contrast to FDM 3D-printed PCL scaffolds, the MEW technique offers significant advantages because of its highly accurate control over filament deposition, which provides more precise pore diameters compared with other methodologies. That is, the higher resolution enables the 3D printing of smaller pores, which creates a greater surface area to support cell attachment. The MEW technique is also ultimately more cost-effective than FDM 3D-printed scaffolds (14). Our research study therefore concentrated on the fabrication of an ideal porous scaffold model that would be useful for bone regeneration applications using MEW.

Interestingly, no previous study has compared the effect of O₂-argon plasma treatment and NaOH solution pre-treatment on CaP deposition and stability on melt electrowritten PCL scaffolds. Our results showed that the O₂-argon plasma modification facilitated an even and uniform CaP layer on the surface of the scaffold and improved the mechanical strength compared with the plasma and NaOH pre-treatment processes alone. Although the surface modifications do not alter the mechanical properties of the biomaterials

because of ineffective underlying material, bulk modification hydrolyses aliphatic polyesters and results in chemical degradation, which affects the mechanical properties of the treated scaffold (15, 16).

Our study indicated that both plasma exposure and immersion of scaffolds in NaOH showed corrosion–erosion behaviour on the filaments, which led to poor mechanical stability of the scaffolds and a rough surface caused by deterioration of the layer components and hydrolytic degradation. Similarly, Al-Borno et al. and Pho et al. showed that immersion of materials into NaOH for a few hours decreased the original mass of the PCL scaffolds (17, 18). Yan et al (2013) found that the combined $\text{NH}_3 + \text{O}_2$ plasma treatment reduced the ultimate tensile strength of electrospun PCL nanofibrous scaffolds (19). However, compared with plasma-modified PCL scaffolds, samples containing a CaP-coated layer increased the mechanical properties. This finding was consistent with the findings of Liu et al (2011) who also showed enhancement of stiffness and mechanical properties for scaffolds with the highest mineral content and smaller grain size of mineral coatings compared with uncoated electrospun poly(lactic-*co*-glycolic acid) (PLGA) nanofibrous scaffolds (20).

CaP coating greatly increases the bioactivity of the scaffold surface. The greatest cell mineralisation was observed in the scaffold containing more CaP-coated particles (offset.50.50 scaffold) during *in vitro* osteogenic culture conditions (14). Poh et al (2015) reported similar results. Their results suggested a synergistic effect of the osteogenic supplements in the culture media and the coated particles of the PCL/10-45S5 and PCL/10-SrBG on promoting matrix mineralisation and differentiation of osteoblasts (21, 22).

Another solution for improving poor cell interactions on the PCL scaffold is by controlling the porosity of the scaffold to allow better permeability, cell infiltration and blood vessel ingrowth into the porous scaffold structure (23). The porosity of the scaffolds

increased using the MEW technique because the thin diameter of the MEW scaffold filaments enabled fabrication of larger pore sizes (24). However, although the higher porosity facilitated angiogenesis, cell penetration and subsequently better osteogenesis, the larger pores diminished the mechanical strength of the PCL scaffold (25, 26). The pore size must be optimised according to the culture condition and the cell type. Greater porosity and interconnectivity have been shown to facilitate bone-related cell movement, penetration and proliferation, and allowed more neovascularisation by improving oxygen perfusion and nutrient medium transfer (27-29). However, increasing the porosity reduces the mechanical integrity (30).

The effects of offset and gradient porous structures of MEW scaffolds on bone and vascular regeneration are not clearly understood. A focus of this project was to explore further the optimum pore size of MEW PCL scaffolds in an attempt to produce an appropriate pattern for better osteogenesis and angiogenesis. Our findings showed the scaffold designs using a 30% and 50% fibre displacement, in which the filament depositions are changed by 30% and 50% on each subsequent layer, increased the surface area and cell-seeding efficiency. In addition, the offset filament patterns overcame the mechanical limitations of the large pore size, such as the reduced ability to withstand a pressure load.

It has been shown previously that that an offset scaffold is more favourable for cell-seeding efficiency because as more junction sites between the filaments in the offset pattern decrease the flow rate of the cell medium during the seeding process. This allows greater attachment of cells within the scaffold compared with homogeneous scaffolds without any offset fibres to entrap cells (31). Our findings showed that the offset.50.50 scaffolds resulted in greater ingrowth of mineralised osteoid tissue compared with the simple porous structures and gradient scaffolds. Yeo et al (2012) also demonstrated that the offset

structures of PCL and β -tricalcium phosphate scaffolds markedly increased calcium deposition compared with no-offset scaffolds (32).

Scaffolds with a gradient in porosity may be ideal candidates for improving the mechanical integrity of the scaffold by allowing greater bone cell proliferation and ALP because it mimics the graded porous structure of natural cortical–cancellous bone. These scaffolds have variable porosity from the top to bottom by including both small and large pores in one construct. This produces a higher elastic modulus and elongation at break because of the layer of smaller pores of this scaffold, which resulted in better mechanical properties compared with homogeneous scaffold structures with large pore sizes. Although, as discussed above, offset scaffold structures function better in terms of cell-seeding efficiency, the cells tend to become entrapped in the bottom of the gradient scaffold because of the reduction in pore size in the final layer. Significant cell proliferation observed in gradient scaffolds over 30 days probably reflects the better exchange of O₂ and nutrients via the larger pore layers. A related study found similar results for human articular chondrocytes seeded on photo-polymerisable poly (D,L-lactide) macromers: the highest cell densities were in the regions of the gradient scaffold with large pores where the fluid flow was maximum (33).

Our results indicated the increase in calcium content was largest in scaffolds with smaller pore sizes, such as 250 μm , and offset structures. Luca et al. also reported that the mineralisation and ALP activity increased in scaffolds with structural porosity gradients (34). However, as shown in our study, the gradient porosity affected the cell behaviour in terms of both proliferation and ALP activity. This finding may be explained by the greater availability of oxygen and nutrients to cells localised in the larger pores and the greater tendency toward higher ALP activity in the larger pores with greater oxygen delivery, as the osteogenic differentiation process stops under hypoxic conditions (35).

In this study, the MEW PCL scaffold with gradient porosity structure provided a good support for promotion of bone growth and ossification. Although we did not evaluate specific cartilage markers, such as type II and III collagen, aggrecan or other markers, recent studies have reported that gradient structures with variation in pore size allowed better integration and transition between bone tissue and soft and cartilage tissues. They also found that the gradient structures could inhibit the degeneration of cells in the central region of the regenerated site, which resulted in the collapse and disintegration of articular cartilage, particularly when used in temporomandibular joint tissue engineering that the production of new tissue lasts a long time (36, 37).

The gradually increased density of CaP particles from the bottom to top of the scaffold allowed the coated grad.250top scaffold to generate the necessary mechanical support in the upper part of the scaffold. This upper part comprised densely distributed pores, which increased the scaffold's strength against external loads because of the higher concentration of calcium content and induced osteogenesis. On the other hand, the lower concentration of CaP together with the larger pores in the lower part of the scaffold, which was close to the dura mater in the *in vivo* studies, influenced the progression of vascular tissue. This was shown by the high expression level of VEGF, which is produced by chondrocytes and affects endochondral ossification through ECM remodelling and vessel ingrowth (38).

As a multilayered complex substitute, the gradient architecture is a new concept for osteochondral tissue engineering. Gradient architecture enables the integration of the interface between the cartilage and bone assembly by inducing the continuous gradual transformation of different types of tissues (39). This porosity pattern may help to overcome the limitation of separate cartilage and bone scaffolds that need to be connected with the use of bio-glue or bio-sealant. In separate scaffolds, the cells cannot penetrate

the clear interface between the two layers of cartilage and bone layers, which leads to the subsequent unstable combination (40-42).

In summary, the use of heterogeneous porosity is an advantageous strategy for designing a denser scaffold, which may help to improve the scaffold's mechanical properties and improve bone regeneration. The gradient MEW PCL scaffolds meet the requirements for bone tissue-engineered scaffolds; i.e., they are non-cytotoxic, have good biocompatibility, increase cell proliferation and tissue ingrowth, and produce the stable regenerated bone.

Future Directions

- Further time points after implantation (>1 year) is essential to evaluate bone remodelling and blood vessel formation while the scaffold starts degrading.
- Use of a large animal model is another critical challenge for evaluating the results, in particular the scaffold functions during the healing process, which might differ from that observed in small animals with a smaller graft size and would provide the potential use in human.
- The delivery of osteo-inductive or angiogenic growth factors should be explored to evaluate any further benefits in direction of bone regeneration.

References

1. Borrelli MR, Hu MS, Longaker MT, Lorenz HP. Tissue Engineering and Regenerative Medicine in Craniofacial Reconstruction and Facial Aesthetics. *J Craniofac Surg.* 2019.
2. Almutairi AS. A descriptive analysis of patient's preferences in bone graft therapy in dentistry. *Int J Health Sci-Ijh.* 2019;13(3):24-8.
3. Dahiya K, Kumar N, Bajaj P, Sharma A, Sikka R, Dahiya S. Qualitative Assessment of Reliability of Cone-beam Computed Tomography in evaluating Bone Density at Posterior Mandibular Implant Site. *J Contemp Dent Pract.* 2018;19(4):426-30.
4. Kim SH, Lee SJ, Lee JW, Jeong HS, Suh IS. Staged reconstruction of large skull defects with soft tissue infection after craniectomy using free flap and cranioplasty with a custom-made titanium mesh constructed by 3D-CT-guided 3D printing technology: Two case reports. *Medicine.* 2019;98(6).
5. Rindone AN, Kachniarz B, Achebe CC, Riddle RC, O'Sullivan AN, Dorafshar AH, et al. Heparin-Conjugated Decellularized Bone Particles Promote Enhanced Osteogenic Signaling of PDGF-BB to Adipose-Derived Stem Cells in Tissue Engineered Bone Grafts. *Adv Healthc Mater.* 2019;8(10).
6. Sabir MI, Xu XX, Li L. A review on biodegradable polymeric materials for bone tissue engineering applications. *J Mater Sci.* 2009;44(21):5713-24.
7. Chocholata P, Kulda V, Babuska V. Fabrication of Scaffolds for Bone-Tissue Regeneration. *Materials.* 2019;12(4).
8. Oryan A, Alidadi S, Moshiri A, Maffulli N. Bone regenerative medicine: classic options, novel strategies, and future directions. *J Orthop Surg Res.* 2014;9.
9. Nemati S, Kim SJ, Shin YM, Shin H. Current progress in application of polymeric nanofibers to tissue engineering. *Nano Converg.* 2019;6(1):36.

10. Tian T, Zhang T, Lin Y, Cai X. Vascularization in Craniofacial Bone Tissue Engineering. *J Dent Res*. 2018;97(9):969-76.
11. Felfel RM, Gupta D, Zabidi AZ, Prosser A, Scotchford CA, Sottile V, et al. Performance of multiphase scaffolds for bone repair based on two-photon polymerized poly(D,L-lactide-co-epsilon-caprolactone), recombinant hyaluronic acid hydrogel and nano-HA. *Mater Design*. 2018;160:455-67.
12. Rider P, Kacarevic ZP, Alkildani S, Retnasingh S, Schnettler R, Barbeck M. Additive Manufacturing for Guided Bone Regeneration: A Perspective for Alveolar Ridge Augmentation. *Int J Mol Sci*. 2018;19(11).
13. Jaroszewicz J, Idaszek J, Choinska E, Szlajak K, Hyc A, Osiecka-Iwan A, et al. Formation of calcium phosphate coatings within polycaprolactone scaffolds by simple, alkaline phosphatase based method. *Mat Sci Eng C-Mater*. 2019;96:319-28.
14. Abbasi N, Abdal-hay A, Hamlet S, Graham E, Ivanovski S. Effects of Gradient and Offset Architectures on the Mechanical and Biological Properties of 3-D Melt Electrowritten (MEW) Scaffolds. *ACS Biomater Sci Eng*. 2019;5(7):3448-61.
15. Chen SC, Lin SH, Chien RD, Wang YH, Hsiao HC. Chemical absorption of carbon dioxide with asymmetrically heated polytetrafluoroethylene membranes. *J Environ Manage*. 2011;92(4):1083-90.
16. Hesketh A, Bucca G, Laing E, Flett F, Hotchkiss G, Smith CP, et al. New pleiotropic effects of eliminating a rare tRNA from *Streptomyces coelicolor*, revealed by combined proteomic and transcriptomic analysis of liquid cultures. *BMC Genomics*. 2007;8.
17. Poh PSP, Hutmacher DW, Holzapfel BM, Solanki AK, Woodruff MA. Data for accelerated degradation of calcium phosphate surface-coated polycaprolactone and polycaprolactone/bioactive glass composite scaffolds. *Data Brief*. 2016;7:923-6.

18. Al-Borno A, Chen XY, Dhoke SK. Effect of High Temperature Sodium Hydroxide Immersion on Fusion Bond Epoxy Coating. *Int J Corros*. 2015.
19. Yan D, Jones J, Yuan XY, Xu XH, Sheng J, Lee JCM, et al. Plasma Treatment of Random and Aligned Electrospun PCL Nanofibers. *J Med Biol Eng*. 2013;33(2):171-8.
20. Liu WY, Yeh YC, Lipner J, Xie JW, Sung HW, Thomopoulos S, et al. Enhancing the Stiffness of Electrospun Nanofiber Scaffolds with a Controlled Surface Coating and Mineralization. *Langmuir*. 2011;27(15):9088-93.
21. Chhaya MP, Poh PSP, Balmayor ER, van Griensven M, Schantz JT, Hutmacher DW. Additive manufacturing in biomedical sciences and the need for definitions and norms. *Expert Rev Med Devic*. 2015;12(5):537-43.
22. Valainis D, Dondl P, Foehr P, Burgkart R, Kalkhof S, Duda GN, et al. Integrated additive design and manufacturing approach for the bioengineering of bone scaffolds for favorable mechanical and biological properties. *Biomed Mater*. 2019;14(6).
23. Huang SH, Hsu TT, Huang TH, Lin CY, Shie MY. Fabrication and characterization of polycaprolactone and tricalcium phosphate composites for tissue engineering applications. *J Dent Sci*. 2017;12(1):33-43.
24. Youssef A, Hrynevich A, Fladeland L, Balles A, Groll J, Dalton PD, et al. The Impact of Melt Electrowritten Scaffold Design on Porosity Determined by X-Ray Microtomography. *Tissue Eng Part C-Me*. 2019;25(6):367-78.
25. Torstrick FB, Evans NT, Stevens HY, Gall K, Guldborg RE. Do Surface Porosity and Pore Size Influence Mechanical Properties and Cellular Response to PEEK? *Clin Orthop Relat R*. 2016;474(11):2373-83.
26. Bobbert FSL, Zadpoor AA. Effects of bone substitute architecture and surface properties on cell response, angiogenesis, and structure of new bone. *J Mater Chem B*. 2017;5(31):6175-92.

27. Entezari A, Roohani I, Li GL, Dunstan CR, Rognon P, Li Q, et al. Architectural Design of 3D Printed Scaffolds Controls the Volume and Functionality of Newly Formed Bone. *Adv Healthc Mater.* 2019;8(1).
28. Park S, Kim G, Jeon YC, Koh Y, Kim W. 3D polycaprolactone scaffolds with controlled pore structure using a rapid prototyping system. *J Mater Sci-Mater M.* 2009;20(1):229-34.
29. Domingos M, Intranuovo F, Russo T, De Santis R, Gloria A, Ambrosio L, et al. The first systematic analysis of 3D rapid prototyped poly(epsilon-caprolactone) scaffolds manufactured through BioCell printing: the effect of pore size and geometry on compressive mechanical behaviour and in vitro hMSC viability. *Biofabrication.* 2013;5(4).
30. Gleadall A, Visscher D, Yang J, Thomas D, Segal J. Review of additive manufactured tissue engineering scaffolds: relationship between geometry and performance. *Burns Trauma.* 2018;6:19.
31. Sobral JM, Caridade SG, Sousa RA, Mano JF, Reis RL. Three-dimensional plotted scaffolds with controlled pore size gradients: Effect of scaffold geometry on mechanical performance and cell seeding efficiency. *Acta Biomater.* 2011;7(3):1009-18.
32. Yeo M, Simon CG, Kim G. Effects of offset values of solid freeform fabricated PCL-beta-TCP scaffolds on mechanical properties and cellular activities in bone tissue regeneration. *J Mater Chem.* 2012;22(40):21636-46.
33. Melchels FPW, Tonnarelli B, Olivares AL, Martin I, Lacroix D, Feijen J, et al. The influence of the scaffold design on the distribution of adhering cells after perfusion cell seeding. *Biomaterials.* 2011;32(11):2878-84.
34. Di Luca A, Ostrowska B, Lorenzo-Moldero I, Lepedda A, Swieszkowski W, Van Blitterswijk C, et al. Gradients in pore size enhance the osteogenic differentiation of human mesenchymal stromal cells in three-dimensional scaffolds. *Sci Rep-Uk.* 2016;6.

35. Hsu SH, Chen CT, Wei YH. Inhibitory Effects of Hypoxia on Metabolic Switch and Osteogenic Differentiation of Human Mesenchymal Stem Cells. *Stem Cells*. 2013;31(12):2779-88.
36. Xiao HL, Huang WL, Xiong K, Ruan SQ, Yuan C, Mo G, et al. Osteochondral repair using scaffolds with gradient pore sizes constructed with silk fibroin, chitosan, and nano-hydroxyapatite. *Int J Nanomed*. 2019;14:2011-27.
37. Rao RT, Browe DP, Lowe CJ, Freeman JW. An overview of recent patents on musculoskeletal interface tissue engineering. *Connect Tissue Res*. 2016;57(1):53-67.
38. Dai J, Rabie ABM. VEGF: an essential mediator of both angiogenesis and endochondral ossification. *J Dent Res*. 2007;86(10):937-50.
39. Bayrak E, Huri PY. Engineering Musculoskeletal Tissue Interfaces. *Front Mater*. 2018;5.
40. Gao JZ, Dennis JE, Solchaga LA, Awadallah AS, Goldberg VM, Caplan AI. Tissue-engineered fabrication of an osteochondral composite graft using rat bone marrow-derived mesenchymal stem cells. *Tissue Eng*. 2001;7(4):363-71.
41. Kreklau B, Sittinger M, Mensing MB, Voigt C, Berger G, Burmester GR, et al. Tissue engineering of biphasic joint cartilage transplants. *Biomaterials*. 1999;20(18):1743-9.
42. Niederauer GG, Slivka MA, Leatherbury NC, Korvick DL, Harroff HH, Ehler WC, et al. Evaluation of multiphase implants for repair of focal osteochondral defects in goats. *Biomaterials*. 2000;21(24):2561-74.